Department of Engineering Science

University of Oxford

Towards practical metal-organic framework materials:

Operando and *in situ* studies by leveraging synchrotron and neutron sources

Kirill Titov

Balliol College

Dissertation submitted for the degree of Doctor of Philosophy

Declaration

This dissertation is submitted for the degree of Doctor of Philosophy in the University of Oxford, United Kingdom. The research work described throughout this dissertation was carried out by the author in the period from October 2015 to June 2019, under the guidance of Prof. Jin-Chong Tan in the Department of Engineering Science at the University of Oxford.

To the best of my knowledge, the work described in this dissertation is original, except where due reference has been made of the work(s) of others, and nothing has been included that is the outcome of work done in collaboration of others, except where specifically noted. No part of this dissertation, or any similar to it, has been, or is currently being submitted for any degree at this or any other university.

This dissertation is less than 250 pages in length.

Kirill Titov

Oxford, UK

June 2019

Towards practical metal-organic framework materials: *Operando* and *in situ* studies by leveraging synchrotron and neutron sources

By Kirill Titov of Balliol College

Dissertation submitted for the degree of Doctor of Philosophy in Engineering Science

Abstract

Metal-Organic Frameworks (MOFs) are a new class of porous materials with dozens of potential future practical applications. This thesis strives to bring that future nearer by leveraging synchrotron and neutron sources to study MOFs for next generation dielectrics, catalysts and sensors. A novel approach to measuring broadband dielectric functions of pelletised MOF powders using specular reflectance Fourier Transform Infrared (FTIR) spectroscopy is developed. MIL-53(Al) is investigated as a model system, and *ab initio* calculations for dielectric functions of its large pore and narrow pore phases show good agreement with experimental data. Rapidly synthesised Pd@MOF composites based on the OX-1 material are developed and investigated using a combination of FTIR, inelastic neutron scattering and x-ray absorption spectroscopy. The Pd@OX-1 structure is shown as a step towards next generation heterogenous single-metal-site catalysts, where Pd atoms reside selectively on benzene rings of the linkers and are recaptured during catalytic cycles. The ZnQ@OX-1 composite is studied using *in situ* transmission FTIR spectroscopy to identify key vibrational modes responsible for its photo-chemical sensing of acetone, and to probe the limits of its sensitivity. It is shown that ZnQ@OX-1 is a promising competitor for the currently best performing metal oxide-based sensors. Quantum tunnelling methyl rotors inside ZIF-8 pores are used as more exotic sensors for gas molecules adsorbed into its pores. The importance of chemical interactions of N_2 and Ar molecules are highlighted by shifts in neutron powder diffraction patterns, while the likely importance of specific adsorption sites is brought to bear by inelastic neutron scattering spectra, which reveal shifts in energies of the quantum tunnelling methyl rotors. The ‘gate opening’ phenomenon is reclassified as ‘gate blocking’ based on these *operando* experiments. Overall, this thesis develops practical MOFs and extends the toolbox for their further advancement.

(290 words)

Acknowledgements

I am grateful to Prof. Jin-Chong Tan for his tireless guidance and support during my time at his lab for Multifunctional Materials and Composites. Prof. Tan is passionate about his research and manages to inspire that passion in those he brings on board, myself included. I have enjoyed our forays into the mysteries of MOF behaviour and hope that they will continue into the bright future of these fascinating materials.

I am eternally grateful to my wife Alina, whose love and care carried me through my time at Oxford. She provided encouragement to keep going, as well as a haven to pause and regenerate. I am an extremely lucky man to have her as my partner in life.

I am thankful to my Mother for everything I am, for she has always planted the seeds of my achievements. My Grandfather, who is no longer with us, is similarly responsible for getting me to where I find myself now. My Fathers – Pavel and Mikhail, as well as my Father-in-law Viktor have all given me incredible role models to aspire to and have provided the means for these aspirations. My wonderful sister Kristina-Tania has been an inspiration and a comfort. I also greatly appreciate all the help that my Mother-in-law Tamara continues to provide us. My extended Family has been an extremely strong and complex support network that gave me strength and depth to aspire to do more.

Dr Dmitry Eremin is a great friend who I met during the course of this work and who has been a source of inspiration and knowledge. I am grateful for our friendship and look forward to our future joint ventures.

I am similarly indebted to Dr Roberto Boada for his friendship and guidance – his work ethic and passion for his craft are unique and inspiring.

My tutors at Balliol have been instrumental to my education, and I am thankful for all the hard work that Prof. Robert Field, Prof. Dominic O'Brien and Prof. Paul Buckley

have put into my time at Oxford. I am also thankful for the spiritual guidance provided by the inspiring Prof. Alexander Korsunsky.

I am extremely grateful for the enabling work done by the scientists and engineers of Diamond Light Source and ISIS Neutron and Muon Source. I value greatly the time spent on experiments with Dr Gianfelice Cinque, Dr Mark Frogley and Dr Chris Kelley, who have all poured knowledge and experience into me without reservations. I am also grateful to Dr Svemir Rudic for an education in neutron scattering delivered with his unmistakable charm. I also count myself lucky to have absorbed some of the energy radiating from Prof. Felix Fernandez-Alonso – his dedication and spirit let nothing stand in the way of great science. My thanks go to Dr Giannantonio Cibin for his time and assistance in the dark arts of x-ray absorption spectroscopy, and to Dr Sanghamitra Mukhopadhyay for her expertise in data processing. Many thanks go to Prof. Valentine Ananikov and Dr Alexey Kashin for their guidance and hard work.

I am also grateful to all my colleagues at the MMC lab for their comradery and good humour. Special thanks go to Dr Abhijeet Chaudhari and Dr Jason Zhixin Zeng for their friendship and assistance. Special thanks also go to Bárbara Souza and Arun Babal. I thank Dr Mahmoud Mahdi, Dr Matthew Ryder, Yang Zhang, Dr Yueting Sun and Annika Möslein for their companionship.

Finally, I dedicate this dissertation to my two sons, Matvey and Robert, and to my brother Mefodiy, in the hope that they will eventually read this hefty work with ease and will be inspired to embark on their own ambitious adventures of the scientific kind.

Table of Contents

Nomenclature

°C	Degrees Celsius
μeV	Microelectronvolt
μm	Micrometre
4-MR, 6-MR	Four- and six- membered rings
8HQ	8-Hydroxyquinoline
Å	Angstrom
AFM	Atomic Force Microscopy
AP	Ambient Pressure
BDC	Terephthalic acid
BET	Brunauer–Emmett–Teller
BTC	Trimesic acid
cm	Centimetre
cm^{-1}	Wavenumber
CVD	Chemical Vapour Deposition
dba	Dibenzylideneacetone
DEF	Diethylformamide
DFT	Density Functional Theory
DGO	Dynamic Gate Opening
DMA	Dimethylacetamide
DMF	Dimethylformamide
eV	Electronvolt
EXAFS	Extended X-ray Absorption Fine Structure
FCC	Face-centred Cubic
FFT	Fast Fourier Transform
FIR	Far Infra-Red
FTIR	Fourier Transform Infra-Red
FWHM	Full Width at Half Maximum
g	Gram
GB	Gate Blocking
GC	Gas Chromatography
GC-FID	Gas Chromatography – Flame Ionisation Detector
GCMC	Grand Canonical Monte Carlo
GC-MS	Gas Chromatography – Mass Spectrometry
GHz	Gigahertz

HDPE	High Density Polyethylene
HKUST-1	Hong Kong University of Science and Technology – 1
HOMO	Highest Occupied Molecular Orbital
HP	High Pressure
HV	Healthy Volunteers
Hz	Hertz
ILD	Inter-Layer Dielectric
IM	Imidazole
INS	Inelastic Neutron Scattering
i-PrOH	Isopropanol
IR	Infrared
IRMOF	Isoreticular Metal Organic Framework
ITRS	International Technology Roadmap for Semiconductors
kHz	Kilohertz
KKT	Kramers-Kronig Transformation
kPa	Kilopascal
LOD	Limit of Detection
LP	Large Pore
LUMO	Lowest Unoccupied Molecular Orbital
m	Metre
MeIM	Methylimidazole
MeOH	Methanol
meV	Millielectronvolt
mg	Milligram
MHz	Megahertz
MIL	Materials of Institut Lavoisier
min	Minute
MIR	Mid Infra-Red
mL	Millilitre
MOF	Metal Organic Framework
mol	Mole (unit)
molec	Molecule
MOX	Metal Oxide
nm	Nanometre
NMOF	Nanoscale Metal Organic Framework

NMR	Nuclear Magnetic Resonance
NP	Narrow Pore
NPD	Neutron Powder Diffraction
OPD	Optical Path Difference
OX-1	Oxford University -1 material
PCHIP	Piecewise Cubic Hermite Interpolating Polynomial
PDF	Partial Distribution Function
ppm	Parts per million
RT	Room Temperature
s	Second
SEM	Scanning Electron Microscopy
t	Tonne
T1DM	Type 1 Diabetes Mellitus
TEM	Transmission Electron Microscopy
TGA	Thermo Gravimetric Analysis
THz	Terahertz
TON	Turnover Number
uc	Unit cell
UiO	University of Oslo
UV	Ultraviolet
VOC	Volatile Organic Compound
wt.%	Weight percent
XANES	X-ray Absorption Near Edge Structure
XAS	X-ray Absorption Spectroscopy
XRD	X-Ray Diffraction
ZIF	Zeolitic Imidazolate Framework
ZnQ	Zinc Quinoline

Chapter One

1 Introduction

This DPhil thesis strives towards novel applications of metal-organic frameworks (MOFs), all of which were made possible by access to a synchrotron radiation facility and a neutron spallation source. Three fields were targeted for potential applications: new generation dielectric materials, novel catalysts for organic synthetic reactions, and smart sensing materials. These applications are enabled by the main characteristics of MOF materials: their high porosity and tuneable physical and chemical properties.

The collection of results presented in this thesis stems from a philosophy of making most of the opportunities that arose for this candidate – both in terms of the materials that were being developed at the Multifunctional Materials and Composites (MMC) lab during this candidate's time there, and in terms of the techniques available to this candidate. These developments had historical trajectories and projects that needed to be taken to their conclusion. At first glance, this meant that some of the projects presented here appear to be quite separate from a general narrative that is expected of a thesis. Upon closer examination, however, the unifying intent of this work becomes apparent: the desire to develop practical uses for the materials studied here, but also for the techniques employed in this study. This dual focus on materials and techniques is reflected in the title of this thesis.

Another important consideration behind the way this thesis is presented is continuity. Continuity in terms of making the results presented here relevant to the field of MOF research, but also to the work undertaken by further generations of MMC lab researchers. The advances presented here build on the previous results published by MMC lab and provide a platform for further development of the materials and techniques under consideration. The literature review and experimental methods chapters are therefore written

with an underlying desire to provide context to researchers new to the field, as well as the necessary tools to engage with the work in a meaningful way. The concluding sections of each chapter and the concluding chapter are similarly intended to provide thought provoking avenues for further research, in the hope that they will be taken up by future members of MMC lab – a process that is already well under way.

The rest of Chapter 1 gives a summary of how the thesis is structured. A survey of the published literature is then presented on the application of MOFs in the three fields studied by this candidate (Chapter 2) before setting out the experimental methods employed (Chapter 3) and presenting the original experimental results (Chapters 4-7, as illustrated by Figure 1.1). Chapter 8 summarises all the important findings derived from this research and lays out the future challenges.

Chapter 4 presents the investigation of the MIL-53(Al) MOF as a model system for studying the dielectric properties of MOFs using synchrotron infrared (IR) radiation in specular reflectance mode. Here, MIL-53(Al) powder was pressed into pellets at varying levels of applied stress, triggering varying degrees of structural change in the resulting pellets, whose broadband Fourier Transform Infrared (FTIR) reflectance spectra were then measured. A custom routine was developed to apply a Kramers-Kronig transformation (KKT) to the reflectance data, which gives the real and imaginary parts of the dielectric function for the studied material in the broadband IR regime.

Chapter 5 presents the work on a catalytic guest@host MOF system developed by this candidate, termed Pd@OX-1. The structure of this system was investigated using synchrotron transmission FTIR spectroscopy, X-ray absorption spectroscopy (XAS) and inelastic neutron scattering (INS), as well as other lab-based techniques. Its catalytic properties were investigated in application to the Suzuki cross-coupling and Heck arylation

reactions, which are some of the most prominent reactions in organic synthesis. The initial structure of the Pd species and its evolution were characterised, showing that OX-1 is a robust host for the Pd catalysts.

Chapter 6 presents the results of an *in situ* synchrotron FTIR spectroscopy experiment investigating the acetone sensing behaviour of the guest@host system called ZnQ@OX-1,[1] which was recently developed in the MMC Lab. Essential details of ZnQ@OX-1 sensing functionality are uncovered, paving the way for its further development as a practical sensor for non-invasive diagnostics of Type 1 Diabetes Mellitus (T1DM).

Chapter 7 sets out a different type of sensing behaviour exhibited by Zeolitic Imidazolate Framework-8 (ZIF-8). Methyl groups present in the structure of ZIF-8 pores behave as quasi-free quantum tunnelling rotors under vacuum and at temperatures below 30 K.[2-3] The application of these quantum tunnelling rotors to sensing the interactions between adsorbed gas molecules and the framework structure was investigated by high-resolution INS spectroscopy and neutron powder diffraction (NPD). The results provide new insights into the effects of changes in local potentials of framework components on the framework's long-range order. The experimental results obtained outline a new frontier for the development of *ab initio* quantum mechanical calculations, which have yet to be able to accurately capture this level of detail.

Together these results represent a significant contribution to the field of materials engineering and take important steps towards practical applications of MOF materials in the fields of dielectrics, catalysis and sensing.

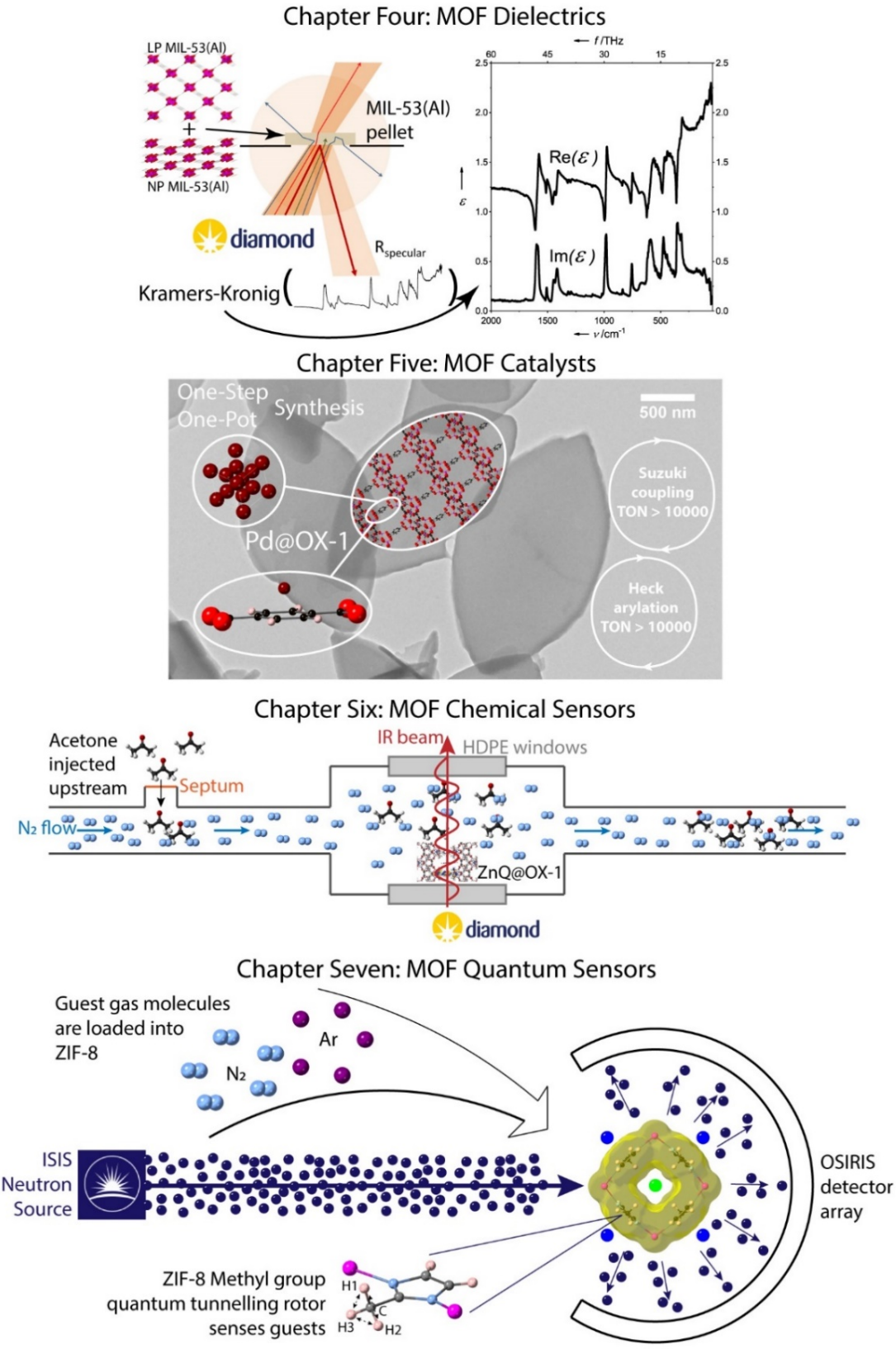

Figure 1.1 Towards practical Metal-Organic Frameworks: a graphical abstract.

Chapter Two

2 Literature Review

2.1 Introduction

Metal-Organic Frameworks (MOFs) are a relatively new class of materials, which rose to prominence together with the advent of digital imaging technology for scanning electron microscopes and other digital sensors, which dramatically sped up the development cycle of nano-scale materials. Porous MOFs are hybrid materials renowned for their large surface area,[4-5] accompanied by remarkable structural flexibility[6-7] and framework dynamics[8-10] in response to diverse physical and chemical stimuli.[11] This chapter explores the literature on MOF materials with applications in the fields of dielectrics, catalysis and sensing. The latter encompasses the more traditional chemical sensing as well as the more exotic sensing by quantum tunnelling rotors in a MOF material.

Section 2.2 presents the state of the field of next generation dielectric materials development by utilising MOF porosity.[12-13] The variety of dielectric notation conventions is consolidated before evaluating the literature on theoretical calculation of MOF dielectric properties and ways of measuring those properties experimentally. MIL-53(Al)[14-16] is explored as an opportune material for novel technique development due to its structural flexibility. A novel method for measuring dielectric properties *via* specular reflectance FTIR spectroscopy is presented in Chapter 4.

Section 2.3 delves into catalytic C-C bond formation[17] facilitated by noble metal nanoparticle catalysts and the vast body of literature on catalytic MOF systems incorporating Pd nanoparticles.[18] Some of the most established Pd@MOF systems are reviewed, together with the experimental methods employed in their development.[19-23] OX-1[1], which is rapidly

produced through a scalable synthesis route, is presented as a potentially attractive host for Pd catalysts. A novel Pd@OX-1 system is then presented in Chapter 5.

Section 2.4 outlines the challenges of non-invasive diagnostics *via* analysis of volatile organic compounds (VOCs) in exhaled breath. Acetone in particular is shown to be of interest for diagnostics of Type 1 Diabetes Mellitus (T1DM) patients, who exhale significantly higher concentrations of acetone than healthy individuals.[24] The state-of-the-art metal oxide (MOX) based sensors for acetone are then reviewed, before presenting the novel luminescent guest@host MOF system developed by Chaudhari *et al*[1] – ZnQ@OX-1 – and exploring the unanswered questions for its further development. Some of these questions are tackled in Chapter 6.

Finally, Section 2.5 explores the more exotic sensors in the form of quantum tunnelling rotors located on linkers of the much-studied Zeolitic Imidazolate Framework-8 (ZIF-8).[2-3] Such tunnelling rotors are highly sensitive to changes in surrounding potentials, which makes them excellent local probes of their environment. This provides a new approach to exploring the structure of ZIF-8, whose properties, such as chemical stability and high specific surface area, have made it a very popular material to study. One phenomenon in particular, often termed 'gate opening', has captured the community's attention in the past ten years.[8, 25-42] The evolution of approaching the understanding of 'gate opening' in ZIF-8 is explored, and an important point of possible confusion between its static and dynamic forms is identified. This sets the stage for the results presented in Chapter 7.

2.2 Dielectrics

2.2.1 Introduction: frontier for the 'dielectric constant' and difficulties of notation

Stassen *et al*[13], among others[12, 43-44], note that dielectric materials will play a decisive role in continued miniaturisation of microchips, which is driven in the electronics community by the self-imposed Moore's law, whereby the number of transistors in a dense integrated circuit doubles every two years. This miniaturisation gives rise to the problem of cross-talk between wires in integrated circuits: the shorter distances between wires increase the parasitic capacitance of the system, slowing down signal propagation and increasing power losses. Better inter-layer dielectrics (ILDs) are needed to combat this problem[12-13, 45]: less polarisable materials better resist the formation of electric fields between interconnects and decrease parasitic capacitance. The quality of a dielectric material is measured by a quantity loosely called a 'dielectric constant', or k. The lower the dielectric constant, the better the dielectric, with the lowest possible constant of $k = 1$ defined for a vacuum. "Low-k" dielectrics are defined as materials that are less polarizable than SiO_2, or $k < 4$. The current frontier in "ultra-low k" dielectrics, put forward in the International Technology Roadmap for Semiconductors (ITRS)[45] published by experts in the field, are materials with $k < 2$.

However, the dielectric 'constant' is a complex quantity, which varies with frequency of the applied electric field. There is some ambiguity of nomenclature in the literature between the lower frequency dielectric studies, done primarily in the context of capacitor design, and in the optics-related frequency ranges. Herein the definitions are set forth, in accordance with the standard conventions in the field of optics (based on 'Optical Properties of Solids' [46]) as well as in established textbooks on dielectrics (for example ref. [47]), and are further reconciled with those used by the electronics-oriented literature.

The **complex relative dielectric constant** (or **complex relative permittivity**) as a function of frequency ω is defined as:

$$\tilde{\varepsilon}(\omega) = \varepsilon'(\omega) + i\varepsilon''(\omega)$$

While the **complex refractive index** is defined as:

$$\tilde{n}(\omega) = n(\omega) + i\kappa(\omega)$$

The relationship between the two is:

$$\boldsymbol{\tilde{n}^2 = \tilde{\varepsilon}}$$

Combining these into an explicit relationship, we obtain:

$$\varepsilon' = n^2 - \kappa^2$$

$$\varepsilon'' = 2n\kappa$$

or

$$n = \frac{1}{\sqrt{2}}\left(\varepsilon' + (\varepsilon'^2 + \varepsilon''^2)^{\frac{1}{2}}\right)^{\frac{1}{2}}$$

$$\kappa = \frac{1}{\sqrt{2}}\left(-\varepsilon' + (\varepsilon'^2 + \varepsilon''^2)^{\frac{1}{2}}\right)^{\frac{1}{2}}$$

These expressions describe the propagation of the electric field E due to the incident electromagnetic wave through a medium with a complex refractive index $\tilde{n}$:

$$E(z,t) = E_0 e^{i(\frac{\omega\tilde{n}z}{c} - \omega t)} = E_0 e^{-\frac{\kappa\omega z}{c}} e^{i(\frac{\omega n z}{c} - \omega t)}$$

where E_0 is the incident electric field, z is the distance into the sample, ω is the frequency of the incident light, t is time and c is the speed of light in vacuum. It is then immediately clear that the imaginary part of the complex refractive index κ leads to losses (i.e. dissipation

term). However, many texts on dielectric behaviour (e.g. "Functional Materials vol.2" by Chung[48]) simplify their notation and simply define the relative dielectric constant as κ, which varies with frequency, in the context of discussing a parallel plate capacitor with a dielectric between the plates. The loss (imaginary) part of the dielectric constant is taken care of by modelling the capacitor as a system with an ideal capacitor (loss free) and a resistance in parallel. The loss then arises due to a phase difference between the electric displacement field D and the electric field E.

This difference in notation leads to unnecessary ambiguity and confusion. There is merit in consistently using the symbols $\tilde{\varepsilon}$ for the complex relative dielectric constant, $\tilde{n}$ for the complex refractive index and the above defined symbols for their real and imaginary parts.

2.2.2 Techniques of measuring $\tilde{\varepsilon}$ of MOF materials

Theoretical calculations[49] and a limited set of static dielectric measurements reveal that MOFs are highly promising "low-k" dielectric materials (k ~2 to 5),[43] owing to their porosity and tuneable chemical and structural versatilities. Only a few experiments have been reported to date on the dielectric behaviour of MOF-based materials. For example, Eslava *et al*[50] employed impedance spectroscopy with a capacitor arrangement to measure the dielectric constant of a micrometre-thick ZIF-8 polycrystalline film, and determined a relatively low k-value of ~2.3 across the frequencies of 100 Hz to 1 MHz. Likewise, Lu and co-workers[51] applied the impedance method to measure the dielectric constants of a Sr-based MOF, where the dehydrated sample has k ~2.4 at under 10 kHz. In addition to the examples above obtained at frequencies below 1 MHz, Redel *et al*[52] used spectroscopic ellipsometry to study the variation in the refractive index (n) of HKUST-1 films in the visible wavelength, from which the dielectric constants have been estimated by $k = n^2$. Noteworthy, frequency-dependent dielectric functions $\tilde{\varepsilon}(\omega)$ of selected Zn-based MOFs have been computed using

density functional theory (DFT) up to the near ultraviolet (UV) spectral range.[53] Yet, there are no experimental studies about MOF dielectric characteristics in the higher frequency region of ~THz (far- and mid-IR), fundamental to the development of emergent wireless communications, electronics and optical sensors.

2.2.2.1 Theoretical predictions of dielectric properties of MOFs

Ab initio calculations have been mostly focused on the family of isoreticular MOFs (IRMOFs) because of their clear possibilities for modifying the material chemistry and pore structure. This is done by considering the various organic linkers, shown in Figure 2.1, variously connected to Zn centres via Zn-O bonds. Kuc, Enyashin and Seifert[54] presented one of the first such reports exploring structural, energetic, electronic and mechanical properties of the whole array of structures (some theoretical) shown in Figure 2.1. Zagorodny, Seifert and Hermann[49] later performed similar calculations specifically for static dielectric constants of this series of IRMOFs. Their results, presented in Table 2-1, suggested that a number of these structures are promising for attaining the desired "low-*k*" behaviour for future dielectrics. However, these static theoretical values serve only as an indication of the possible behaviour of the MOFs in question. Warmbier, Quandt and Seifert[55] later extended these results by calculating the dynamic dielectric functions of selected IRMOFs using DFT methods, presented in Figure 2.2. These results indicate that the predicted ε' for these systems stays below 2 for most of the considered spectral range, further encouraging the development of IRMOFs as dielectric materials. However, these results are called into question by considering that the presented ε'' absorption bands occur at energies above 2 eV, or 16130 cm^{-1}, which is far above the expected frequencies of molecular vibrations commonly observed in IR spectroscopy. This indicates that the whole scale of the spectral range is unreliable in these predictions.

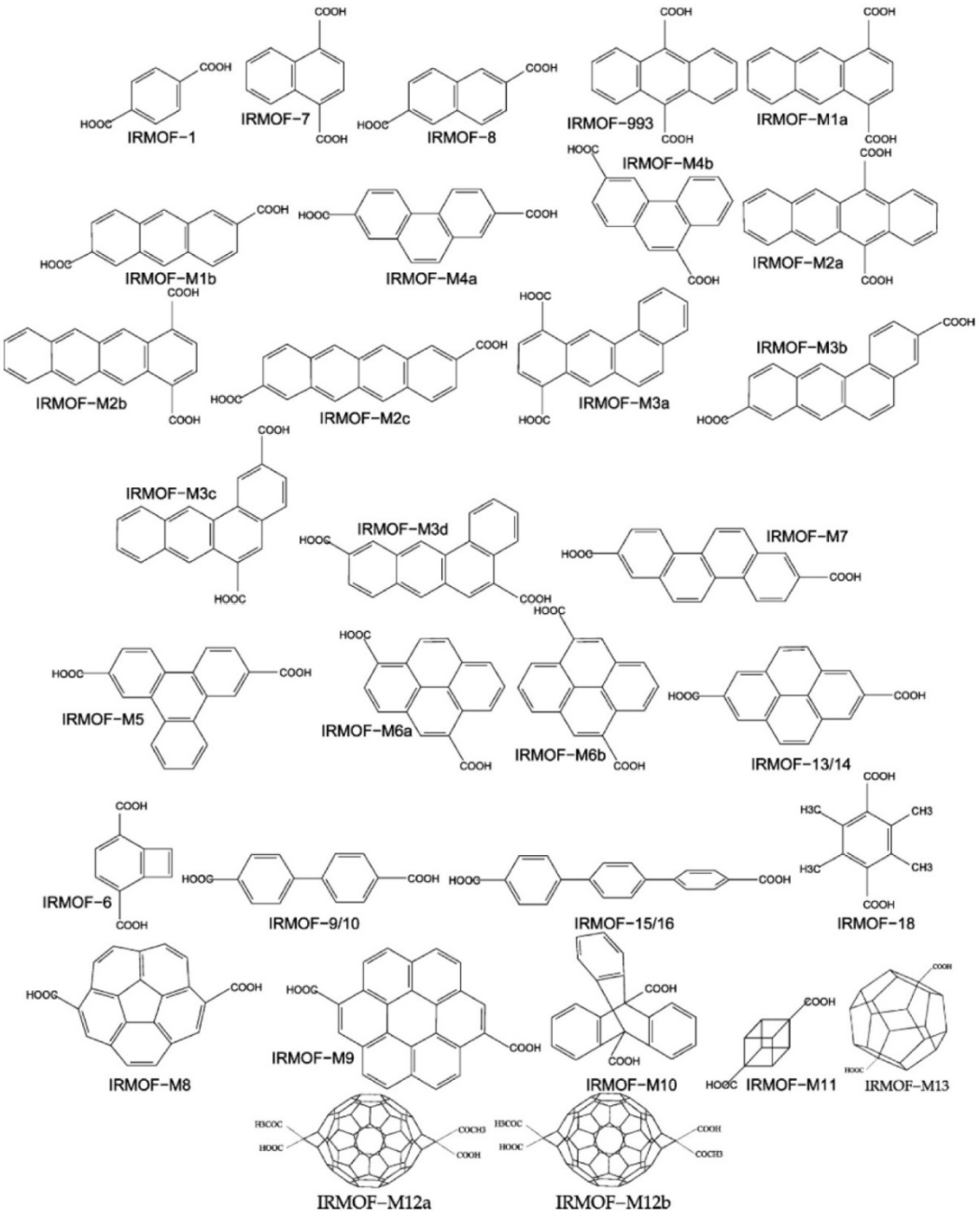

Figure 2.1 Organic linkers considered in the work of Kuc, Enyashin and Seifert[54]. For clarity, hydrogen atoms are not shown. Notation: IRMOF-x, where x is corresponding to the name given in the literature for experimentally known MOFs or IRMOF-Mn denoting the marks of the proposed linkers for hypothetical MOFs studied in Ref.[54] (a, b, c, etc. indicate different isomers for a given linker). Reprinted with permission from Ref.[54]. Copyright 2007 American Chemical Society.

Table 2-1 Static dielectric constants for the respective MOFs. Reprinted from Ref.[49], with the permission of AIP Publishing. Values for bulk modulus B and gap energy E_g are taken by Zagorodniy, Seifert and Hermann [49] from Ref.[54].

MOF	k	B (GPa)	E_g (eV)
IRMOF-M2c	1.21	2.0	1.61
IRMOF-M7	1.22	0.3	2.65
IRMOF-M3b	1.22	2.6	2.39
IRMOF-10	1.23	6.0	3.07
IRMOF-M1b	1.25	3.2	2.13
IRMOF-M4a	1.26	3.4	2.89
IRMOF-14	1.28	5.9	2.63
IRMOF-M3d	1.31	1.1	2.25
IRMOF-M5	1.32	4.2	2.90
IRMOF-8	1.32	2.4	2.83
IRMOF-1 (fcc)	1.37	8.7	3.73
IRMOF-M9	1.38	4.4	2.38
IRMOF-1 (sc)	1.39	6.3	3.66
IRMOF-M8	1.39	3.5	2.66
IRMOF-M4b	1.41	1.5	2.67
IRMOF-M6b	1.43	3.4	2.28
IRMOF-M6a	1.45	1.7	2.11
IRMOF-M11	1.45	12.6	4.91
IRMOF-M13	1.50	9.0	5.49
IRMOF-M3c	1.51	3.0	2.22
IRMOF-7	1.52	3.7	2.77
(COOH)2 (fcc)	1.62	24.3	4.17
(COOH)2 (sc)	1.62	22.3	5.56
IRMOF-993	1.65	3.6	2.16
IRMOF-M1a	1.68	4.5	2.04
IRMOF-M2a	1.84	2.4	1.50
IRMOF-M2b	1.86	6.9	1.56
IRMOF-M3a	1.88	5.1	2.15
IRMOF-M10	1.94	9.2	4.56

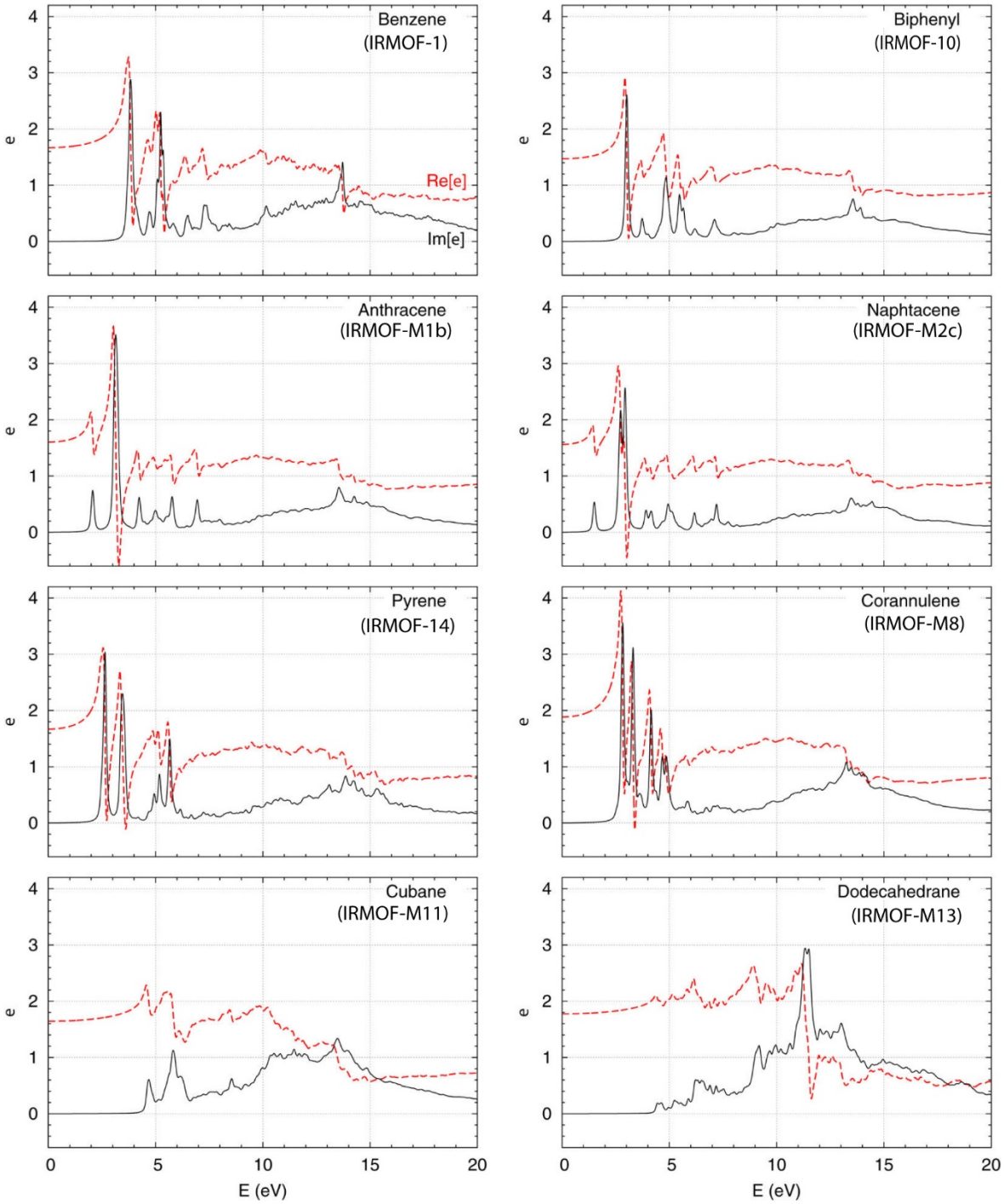

Figure 2.2 Complex dielectric function of MOFs within the independent particle model from GGA-PBE calculations. The real part $\Re[\varepsilon]$ is shown as a dashed red line, while the imaginary part $\Im[\varepsilon]$ is shown as a black line. Reprinted with permission from Ref.[53]. Copyright 2014 American Chemical Society.

2.2.2.2 ZIF-8 thin film on a Si-n chip

Eslava *et al*[56] demonstrated an approach to measuring the dielectric properties of ZIF-8 thin films, which are difficult to manufacture but are one of the most promising ways of deploying MOFs as dielectric materials. Thin films of various thicknesses were demonstrated and characterised by various methods including XRD, Gas adsorption, SEM and AFM (including nanoindentation). Most importantly, however, the authors used impedance spectroscopy to characterise various electric properties of the thin films by depositing Pt electrodes on top of the as deposited thin films (see schematic in Figure 2.3a). The results, shown in Figure 2.3, indicate that the ZIF-8 thin films have aa ε' (k) between 2.4 and 2.2 at frequencies above 100 Hz, and that these values are temperature dependent. The dissipation (loss) factor is similarly temperature dependent. These results indicate that ZIF-8 is a promising material, but that it does not quite hit the $k < 2$ target yet. The method of measurement presented is advantageous because it forces one to be able to grow a thin film of the MOF to be investigated, implying that the MOF can be incorporated into chips. On the other hand, the MOFs that cannot be manufactured as thin films by currently available methods cannot be investigated at all, limiting the usefulness of the technique.

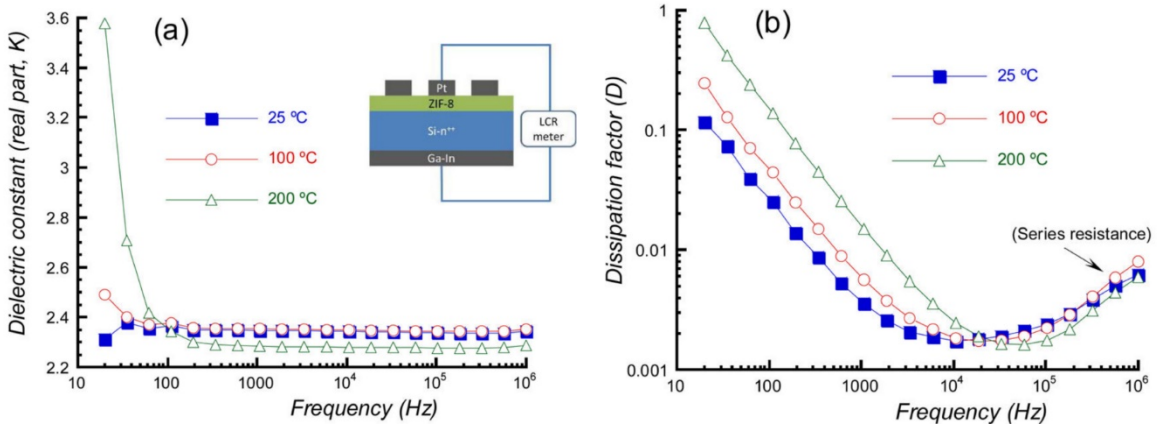

Figure 2.3 Representative (a) dielectric constant real part k and (b) dissipation factor D of a ZIF-8 film measured by impedance analysis for different frequencies and temperatures. Reprinted with permission from Ref.[56]. Copyright 2013 American Chemical Society.

2.2.2.3 Powder pellets in MIM capacitor

An approach that avoids the need for growing the MOF as a thin film on a substrate is presented by Lu and co-workers[51]. The MOF is first pressed into a pellet and then placed between two metal electrodes, again forming a metal-insulator-metal (MIM) capacitor arrangement for impedance spectroscopy (inset Figure 2.4a). The authors find a temperature dependence of the $Sr_2(1,3\text{-bdc})_2(H_2O)_2 \cdot H_2O$ material's ε', shown in Figure 2.4a. They also find a dramatically higher ε' for the hydrated material, as opposed to its activated form, which has no water molecules in the pores, as shown in Figure 2.4b. This technique lends itself to investigating all MOFs that can be pelletised without loss of crystallinity. However, the limitations include the imperfections in metal to MOF pellet contacts, which need to be mitigated by conducting pastes/inks, and the inter-crystal voids of the pellet. The latter is difficult to characterise and can lead to underestimation of the dielectric values. Nevertheless, given sufficient awareness of these factors, this is a very practicable technique for investigating dielectric properties of a wide variety of MOFs.

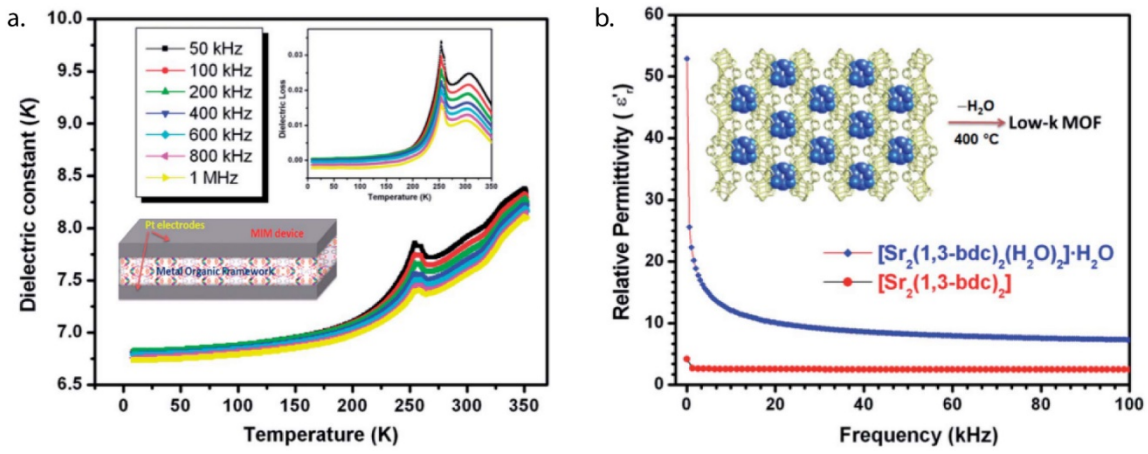

Figure 2.4 a) Temperature dependent dielectric constants from 0 to 350 K at different frequencies for $([Sr_2(1,3\text{-bdc})_2(H2O)_2]\cdot H_2O)_n$ with dielectric loss in the offset. b) Relative permittivity vs. frequency for $([Sr_2(1,3\text{-bdc})_2(H2O)_2]\cdot H_2O)_n$ and dehydrated sample $[Sr_2(1,3\text{-bdc})_2(H2O)_2]$ at room temperature. Adapted from Ref.[51] with permission from The Royal Society of Chemistry.

2.2.2.4 Spectroscopic ellipsometry on HKUST-1 and Cu-BDC thin films

Redel *et al*[52] present the method of spectroscopic ellipsometry in the visible range of wavelengths, which measures the dynamic refractive index of the material to then calculate the dielectric function. The advantage here is that the method is non-destructive and does not suffer from electrode contact problems of impedance spectroscopy. Nevertheless, the accessible frequency range is far above the MHz to GHz range of current electronics. It is useful, however, to obtain an indication of the material's behaviour even in this range, and to investigate the material's response to various stimuli. Here, for example, Redel *et al*[52] probe the temperature dependence of ε' values measured from HKUST-1 and Cu-BDC thin films. Figure 2.5 shows that both materials' ε' decreases dramatically with increasing temperature, which the authors attribute to loss of guest water molecules. Here the authors chose to demonstrate the method on thin films, emphasising the possibility of manufacturing these MOFs as such, but the method is applicable to pellets as well, which is not demonstrated.

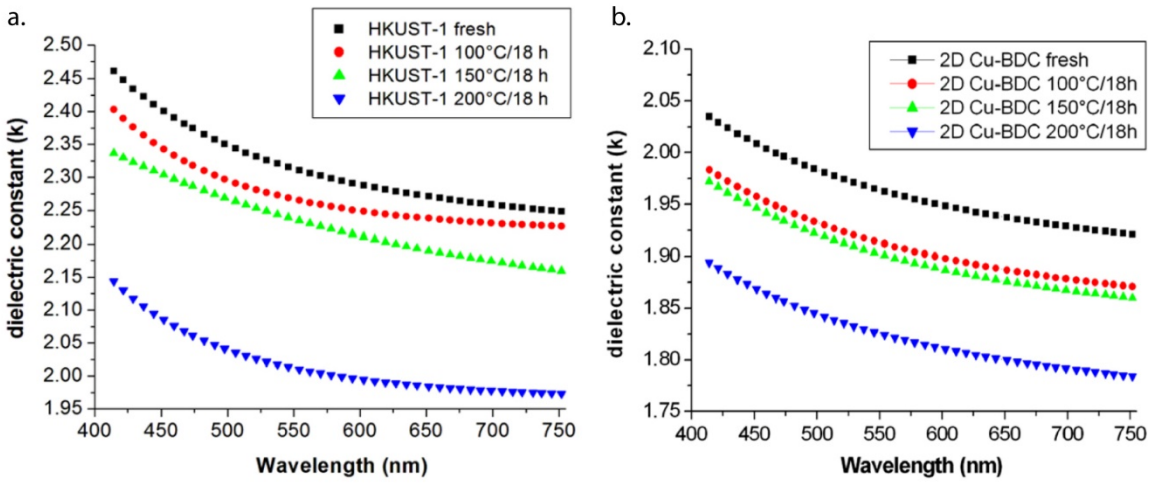

Figure 2.5 Changes in the real part of the dielectric function calculated from the refractive index measured *via* spectroscopic ellipsometry for (a) 3D HKUST-1 SURMOF and (b) laminar Cu-BDC SURMOF-2 after treatment at increasing temperatures for 18 h. The x-axis scale converts as follows: from 400 nm = 749.48 THz to 750 nm = 399.7 THz. Reprinted from Ref.[52], with the permission of AIP Publishing.

2.2.3 MIL-53(Al) – a well-studied flexible MOF

MIL-53(Al) exhibits a range of potentially useful behaviour. Ferey and co-workers[15] first published the MIL-53 framework with Cr as metal centre and subsequently published the MIL-53(Al) variant.[14] The synthesis yields crystals with a wine-rack structural motif, containing unreacted linker trapped inside the pores (Figure 2.6a), which can be removed by activation at 275°C, giving a stable large pore (LP) phase (Figure 2.6b). This LP phase then reversibly switches to a narrow pore (NP) phase upon adsorption of water molecules (Figure 2.6c). The expulsion of the disordered BDC linker from the as synthesized material and of the water molecules from NP phase crystals are well documented by thermo-gravimetric analysis (TGA) measurements (see Figure 2.6d,e respectively). Moreover, the MIL-53(Al) framework has excellent thermal stability up to 500°C, as is also shown by in situ XRD experiments presented in Figure 2.6f. The transformation from LP to NP and back is termed by Ferey and co-workers[14-15] as "breathing" behaviour, but that term is misleading. This transformation is more of a 'fold' of the framework upon water molecule uptake, whereby the 'wine-rack' pores become narrower. Interestingly, DFT calculations by Wang *et al*[57] suggest that the water molecules inside the NP phase play a structural role – they reduce anisotropy of mechanical properties and significantly increase the Young's and shear moduli of MIL-53(Al) compared to its LP guest-free phase. This is an important result, which will play a role in the pelletisation study presented in Chapter 4.

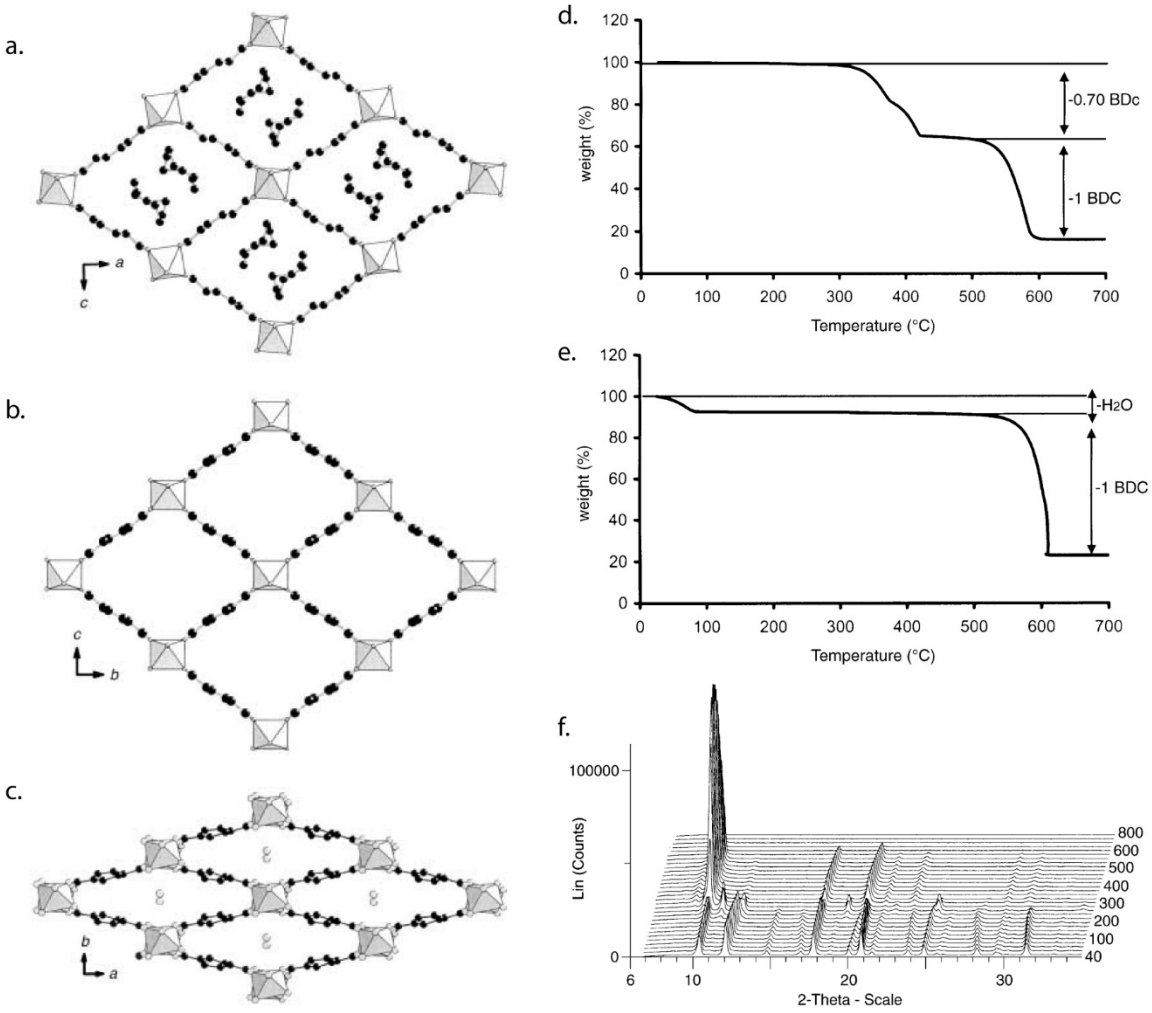

Figure 2.6 (a-c) Views of the 3D structure of MIL-53 (Al) showing the channel system: a) MIL53(Al) as synthesised, in which the channels are occupied by free disordered 1,4-benzenedicarboxylic acid molecules; b) large pore (LP) form MIL-53(Al) with empty channels; c) narrow pore (NP) form MIL-53(Al) at room temperature in which a water molecule is located at the centre of the channels. Gray octahedra: AlO_4; black circles: carbon; gray circles: oxygen. (d-e) TGA curves of as synthesised MIL-53 (Al) and hydrated narrow pore form MIL-53(Al) in air; (f) X-ray thermodiffractogram of as synthesised MIL-53(Al) in air (40-800°C). For clarity, a 2θ offset is applied for each pattern, which were collected at intervals of 20°C, except for the last two, which were collected 100°C apart. Adapted from Ref.[14], with permission from John Wiley and Sons.

The transition from LP to NP structures is also found to occur under hydrostatic pressure in mercury as the transmitting medium. Yot *et al*[58] investigated MIL-53(Al) as a mechanical energy storage medium, with a schematic of the structural transformation shown in Figure 2.7a and liquid intrusion experimental results shown in Figure 2.7b. A very similar set of experiments was earlier reported by Beurroies *et al*[59] for MIL-53(Cr), shown in Figure 2.7c. Both studies demonstrate a loading-unloading loop with a step upon loading and hysteresis upon unloading representing the reversible transition from LP (at low pressure) to NP (at high pressure) structures. It is worth noting that the term 'intrusion' here does not refer to Hg atoms entering the framework pores, but rather to Hg volume entering the sample chamber containing the MOF powder. Indeed, both studies[58-59] indicate that Hg does not penetrate micropores of the studied materials (which is a property of Hg rather than the material under question[59]). The observed hysteresis, therefore, is unambiguously attributed to the hydrostatic pressure applied to the MIL-53 crystals from the outside. Yot *et al*[60] further extend these results to show what happens to these materials under hydrostatic pressure on the order of a few GPa, rather than hundreds of MPa. They find that both the Al and Cr (as well as Fe) variants of MIL-53 further fold into a 'very narrow pore' (VNP) form, as illustrated in Figure 2.7d. Indeed, they show that the pore volume of these structures decreases significantly under GPa pressure (see Figure 2.7e,f for Al and Cr respectively), and that the manner of this decrease depends strongly on the metal centre of the MIL-53 variants.

MIL-53 is thus an interesting system to study in the context of dielectric properties: its flexible nature allows one to attempt to vary the pore size of the crystals without changing the material chemistry. However, it is important to stress that the Hg intrusion experiments shown here are under hydrostatic pressure, which is not the case for the investigations presented in Chapter 4, where uniaxial pressure is applied to MIL-53(Al) powder.

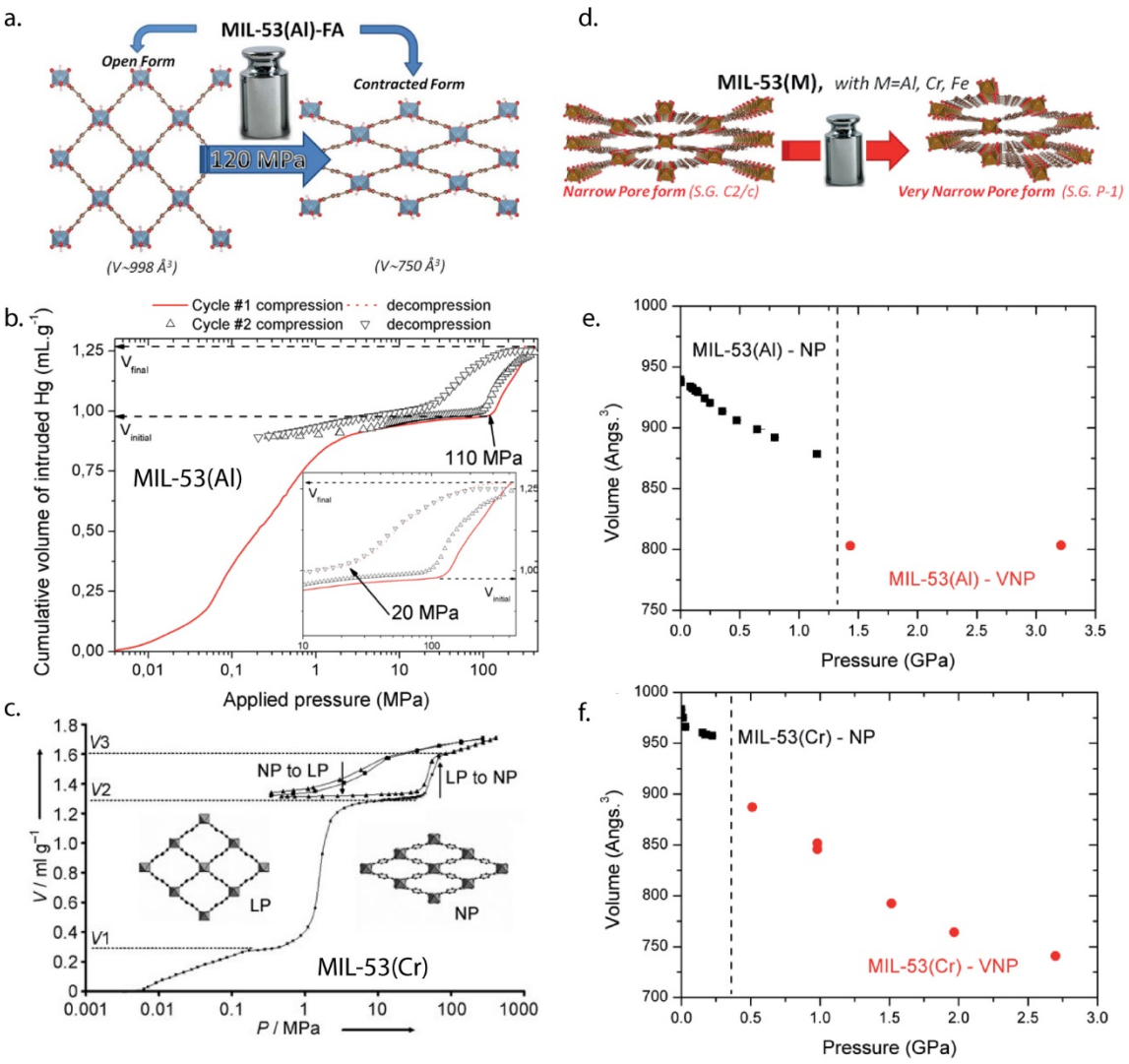

Figure 2.7 (a) Schematic of transformation of large pore (LP) MIL-53 into a compressed form (NP) under hydrostatic pressure with mercury as the pressure transmitting medium[58]; (d,c) experimental results of the hydrostatic loading cycles in mercury for MIL-53(Al)[58] and MIL-53(Cr)[59], respectively, both showing reversible switching in framework volumes; (d) schematic of transformation of narrow pore MIL-53(M) into very narrow pore form in diamond anvil cell high pressure experiments, using silicon oil (AP 100, Aldrich) as the pressure transmitting medium, followed by (e,f) the results for MIL-53(Al) and MIL-53(Cr), respectively ((d-f) from [60]). (a,b) © 2016 Royal Society of Chemistry, used under a Creative Commons Attribution-Noncommercial license: http://creativecommons.org/licenses/by-nc/3.0/. (c) reprinted from Ref.[59], with permission from John Wiley and Sons. (d-f) adapted from Ref.[60], with permission from John Wiley and Sons.

2.2.4 Conclusions and motivation for IR spectroscopy-based dielectric studies

Current state of the field of MOF dielectrics relies heavily on theoretical predictions, while facing significant challenges in the experimental arena. This is mainly due to the difficulties in synthesizing the proposed MOFs in the right forms – as precisely controlled thin films with few defects and on specific substrates. These synthetic issues are fundamental to bringing MOFs into the field of electronics as ILDs but lie outside the scope of the present thesis. Instead, the work of this candidate in furthering practical dielectric MOF deployment aims to develop a fast and relatively straightforward method of measuring the dielectric properties of MOFs without having to solve the synthetic challenges first, while providing a direct comparison to theoretically predicted values for those MOFs. FTIR spectroscopy is an advantageous technique to employ towards this aim. The FTIR frequency range is below the spectroscopic ellipsometry range (visible light), while being above the impedance spectroscopy range (kHz-MHz), thus partially filling a gap between the two. An advantage compared to those two methods is the molecular vibrational modes information inherently obtained by FTIR spectroscopy, giving a more detailed insight into the dynamics and composition of the studied systems. Dielectric property investigation through FTIR spectroscopy, therefore, is complementary to techniques described in this literature review, providing rich structural information not otherwise accessible. The choice of the MIL-53(Al) material as a model system for technique development is advantageous due to its multiple possible forms, and ability to switch between those forms under various stimuli. It will be shown that these functionalities of MIL-53(Al) allow the effects of MOF geometry and porosity to be studied, without the complications arising from varying chemistry of systems with varying linkers, such as the isoreticular MOFs[49, 54-55, 61]. Moreover, because MIL-53(Al) is a well-established system, the calculations of its properties via DFT methods can be more reliable than for less known systems.

2.3 Catalytic MOFs with Pd

2.3.1 Introduction: C-C bond formation *via* noble metal catalysts

The catalytic formation of C-C bonds is considered to be one of the key transformations in organic synthesis.[62] The use of transition metals as catalysts for these transformations is a vibrant area of research, especially involving their nanoparticles.[63-68] The precise chemical processes involved in nanoparticle catalysis are a matter of ongoing investigations,[18] while the ultimate aim is the rational design of efficient, selective and stable catalysts, with an awareness of the dynamic evolution of the active species during catalysis.[17-18, 69-71] MOF materials possess unique properties, such as tuneable porosity and the ability to fine-tune the structure of the active sites and their environments,[72] which can be utilised in achieving the above aims. MOF catalytic activity can be achieved *via* three main routes: activity at the inorganic nodes and the organic, or pseudo-organic, linkers of the framework itself; encapsulation of active species into the framework; and post-synthetic modification of the framework.[72-73] Encapsulation of active species is of particular interest, given the above mentioned intensive interest in noble metal, and palladium (Pd) in particular[17-18, 63, 68-71, 74], nanoparticle catalysis.

2.3.2 Research on MOF hosts for active Pd species

The work on Pd@MOF composites stretches back to 2005 when Fischer and co-workers[75] published their method of metal organic chemical vapour deposition (CVD) into the classical framework MOF-5 (first reported by Yaghi and co-workers[76] in 1999) and subsequent reduction of the metal organic precursor to nanoparticles inside the framework pores with H_2 gas. They also present a photochemical method for Pd deposition on MOF-5. Figure 2.8 shows a schematic of MOF-5 after CVD, XRD patterns of Pd@MOF-5 produced and a TEM image of the photochemically produced Pd@MOF-5 sample. Since this report a plethora of (Metal nanoparticles)@MOF systems have been produced, with several reviews

available on the topic[77-81]. These are classified according to nanoparticle size relative to framework pores[79], and according to where these nanoparticles reside[77] as illustrated in Figure 2.9.

Some of the most notable examples of catalytic MOFs for C-C bond formation so far have been achieved through encapsulation of active palladium (Pd) species into widely studied MOFs including MOF-5[82], the MIL family of MOFs,[19-20, 22-23, 83-86] and the UiO family,[87-89] while more exotic examples include ScBTC NMOF[90] and $Cu_2(BDC)_2DABCO$[91]. Out of all these examples MIL-101(Cr), and its amino functionalised variant MIL-101(Cr)-NH_2, stands out as most studied due to its excellent chemical and thermal stability, as well as high accessible BET area in excess of 2800 m^2g^{-1}. Martin-Matute and co-workers [19, 21-23] in particular have made significant contributions towards studying the behaviour of Pd@MIL-101(Cr)-NH_2 in Suzuki[19, 21-22] and Heck[23] coupling reactions: the ensemble of their work presents an extensive set of investigations in identifying the possibilities and limitations of a Pd@MOF material, as well as making leaps towards its practical applications.

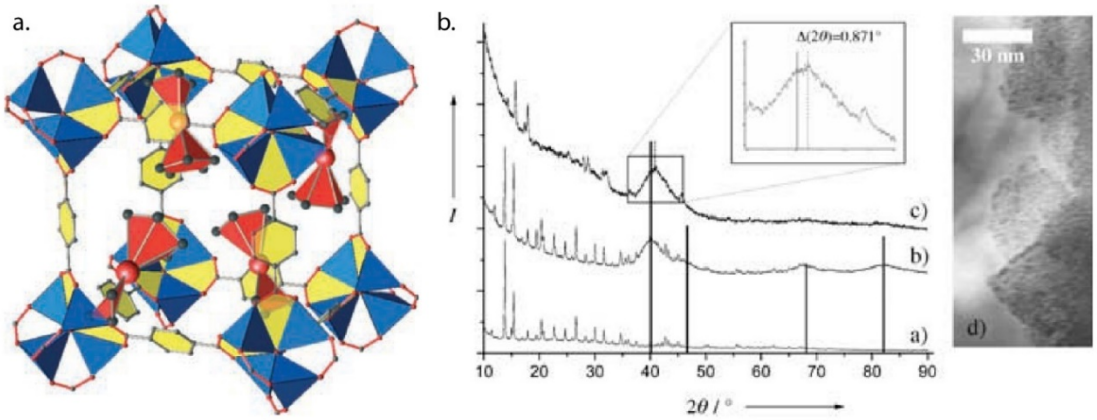

Figure 2.8 (a) MOF-5 cage (blue/yellow) with four incorporated (η^5-C_5H_5)Pd(η^3-C_3H_5) precursors (red). (b) Powder diffraction patterns of a) MOF-5, b) photolytically generated Pd@MOF-5, c) Pd@MOF-5 (reduction by H_2). The *2θ* values characteristic for palladium are highlighted. The enlargement shows the shift to higher *2θ* values, typical of small particles; d) TEM image of photolytically generated Pd@MOF-5. Adapted from Ref.[75], with permission from John Wiley and Sons.

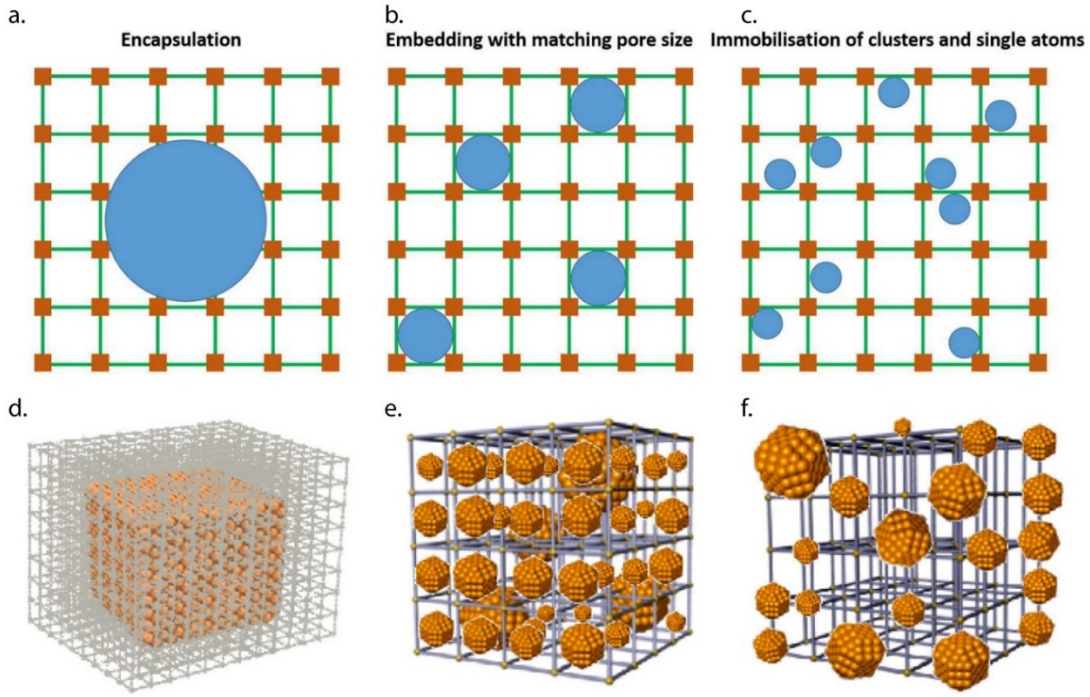

Figure 2.9 Schematic illustration of different Pd@MOF nanocomposites: (a) Pd encapsulated in the MOF matrix; (b) Pd filling the MOF's pores and (c) Pd particles that are smaller than the MOF's pore diameter, including single atoms. Reprinted from Ref.[79], with permission from John Wiley and Sons. (d-f) Metal NPs residing inside and outside MOFs as well as having different sizes. Reprinted with permission from Ref.[77]. Copyright 2016 American Chemical Society.

In their first article Martin-Matute and co-workers[19] tackled the issues of Pd particle size, closely related to the issue of particle encapsulation, and tunability of Pd loading. Figure 2.10a shows TEM images of their 4 – 16 wt.% Pd@MIL-101(Cr)-NH_2 crystals, with inset histograms tracking the size of Pd particles seen in the images. The majority of the particles in all samples are 2-3 nm in diameter, which matches the pore size of MIL-101(Cr)-NH_2. This suggests that their strategy, involving infiltration of dissolved Pd precursor into the pores of the MOF in liquid phase and subsequent reduction into Pd nanoparticles, leads to Pd particles embedded inside the individual MOF pores as schematically illustrated in Figure 2.9b. However, the scatter of particle sizes, with much larger particles (5-8 nm) detected, indicates that the realistic particle positioning is a mix of inside MOF pores, spanning several MOF pores (implying defects in crystal architecture), and outside the MOF, i.e. a mix of schematics in Figure 2.9e,f. They further recorded total x-ray scattering intensities for this series of samples and obtained the pair distribution functions (PDFs) *via* a Fourier transform, shown in Figure 2.10b. This confirmed that the amount of Pd in the samples scaled as expected. These Pd@MIL-101(Cr)-NH_2 crystals were further shown to efficiently catalyse the Suzuki reactions on a variety of substrates, and the possibility of recycling the material for as many as 10 reaction cycles was demonstrated.[19]

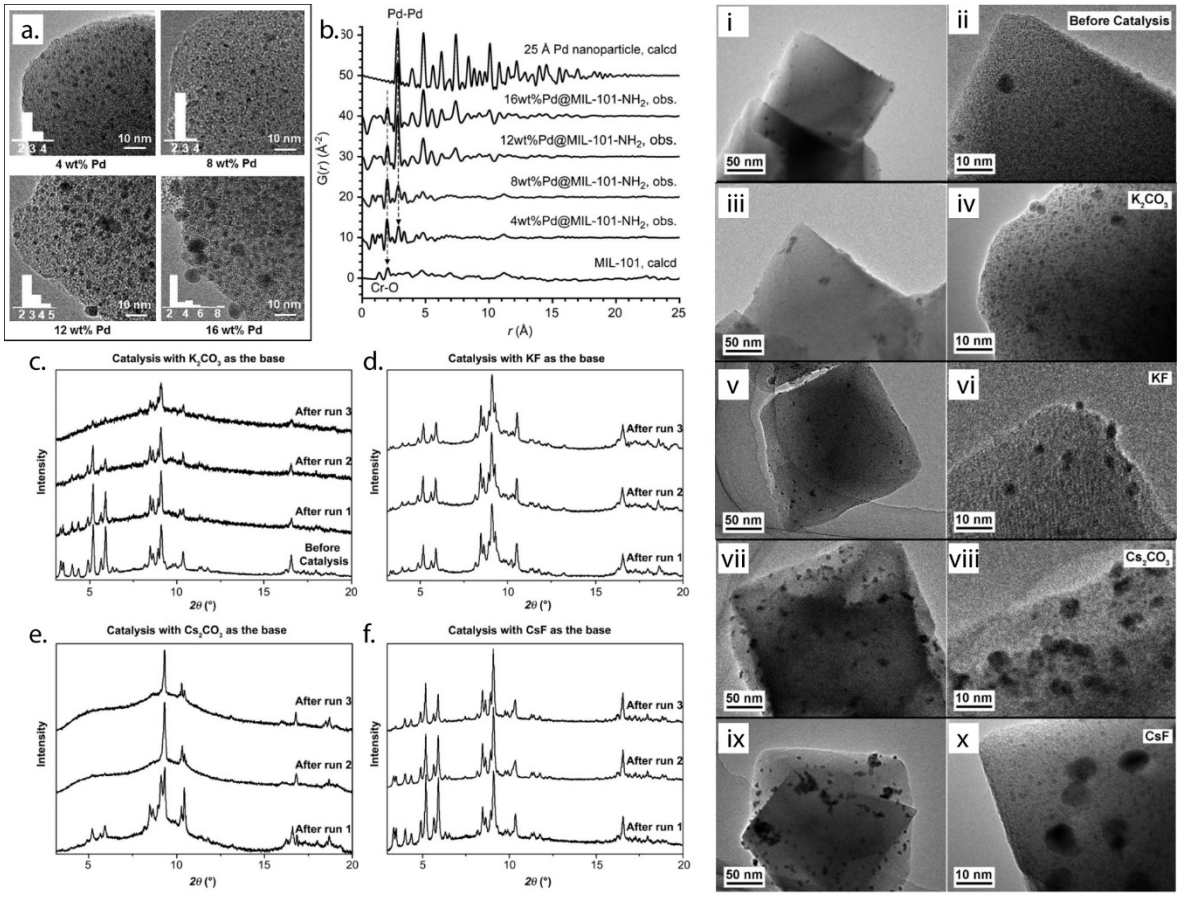

Figure 2.10 (a) TEM images of Pd@MIL-101(Cr)-NH_2 with increasing Pd loadings, and insets showing Pd nanoparticle size distribution in nm; (b) PDFs of samples of 4-, 8-, 12-, and 16 wt.% Pd@MIL-101(Cr)-NH_2 compared with the calculated PDFs of MIL-101(Cr) (bottom) and of a Pd nanoparticle (diameter: 25 Å, top). For the sake of clarity, the PDFs are vertically stacked by 10 $Å^{-2}$; (a,b) Reprinted from Ref.[19], with permission from John Wiley and Sons. (c-f) XRD patterns of 8 wt.% Pd@MIL-101(Cr)-NH_2 used to catalyse three runs of Suzuki coupling reactions with different bases, together with (i-x) corresponding TEM images of the material before and after 3 runs of catalysis with each of the bases. (c-f, i-x) Reprinted from Ref.[21], with permission from John Wiley and Sons.

In a further study Martin-Matute and co-workers[21] investigated the influence of base used in the Suzuki reactions on the stability of the MIL-101(Cr)-NH_2 framework during the reaction cycles. They compared XRD patterns of as-synthesised material with those after three cycles of Suzuki cross-coupling reactions employing potassium carbonate (Figure 2.10c), potassium fluoride (Figure 2.10d), caesium carbonate (Figure 2.10e) and caesium fluoride (Figure 2.10f). Corresponding TEM images after three cycles of Suzuki cross-coupling using those four bases are given in Figure 2.10i-x. They found that when carbonate bases were used the characteristic MIL-101(Cr)-NH_2 framework peaks eventually disappeared (faster for Cs than for K), whereas when the fluoride bases were used the framework peaks remained intact. Interestingly, their XAS data (not shown here) revealed that the Cr coordination environment remains nearly unchanged after reactions with both Cs_2CO_3 and CsF, while their gas adsorption results show a drastic drop in N_2 uptake in the case of carbonates and only a slight decrease in the case of fluorides. These three sets of results lead them to conclude that the secondary building units of MIL-101(Cr)-NH_2 survive the Suzuki reactions with both carbonate and fluoride bases, even though the framework clearly collapses when the carbonates are used. Indeed, TEM images of the material after carbonate mediated reactions (Figure 2.10iii-iv,vii-viii) show similar crystal-like particles to the pristine material (Figure 2.10i-ii). Another important observation from TEM images is made: the size of Pd particles increases in all reactions, while the Cs mediated reactions result in the largest particles, which suggests that more Pd migration occurs when Cs is present.[21] At the same time, the best catalytic results are achieved exactly when CsF is used instead of KF, which leads Martin-Matute and co-workers[21] to conclude that homogenous (atomic) Pd species contribute significantly to the material's catalytic activity. This is strongly in line with the concept of a "cocktail" of catalysts proposed by Ananikov and Beletskaya[69] and further developed by Eremin and Ananikov[18], which stresses the dynamic

nature and plurality of forms of active species in catalytic reactions involving metal atoms and particles. This is beautifully illustrated in further work by Zou, Martin-Matute and co-workers[23] employing operando XAS to study the evolutions of Pd species initially in the form of $PdCl_2$ attached to NH_2 groups of MIL-101(Cr)-NH_2. Figure 2.11a illustrates the various Pd species they discovered as the Heck reaction was carried out in the custom-made reactor for operando XAS studies, models for which were obtained by fitting the individual XANES spectra collected over time (Figure 2.11b). These results also shed light on the complexity of the transient mechanisms involved in the cycles of the Heck reaction in particular, beyond what is commonly recognised to occur.[23] The intricacies of these cycles are beyond the scope of this thesis (see references[17-18, 69, 71] for further discussion), but the before and after TEM images of the Pd@MIL-101(Cr)-NH_2 crystals used for the operando Heck reaction study show that large Pd particles form during the catalytic reaction (see Figure 2.11c,d), which further demonstrates the dynamic nature of the Pd species, even when they are initially attached to functional groups of a MOF as single Pd atoms.

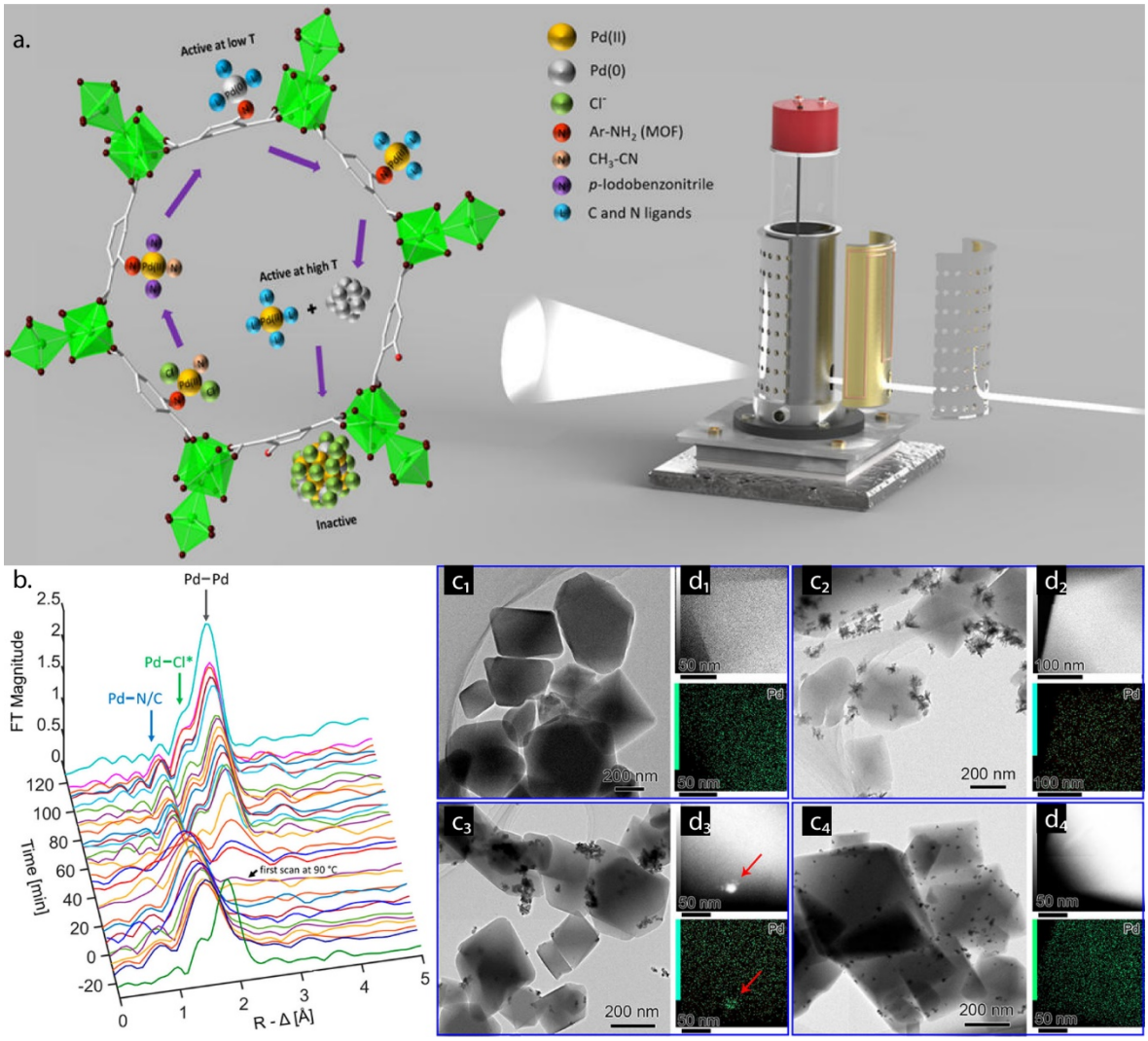

Figure 2.11 (a) Schematic illustration of the evolution of Pd species inside MIL-101(Cr)-NH_2 crystal structure, together with a drawing of the catalytic cell used for *operando* XAS studies; (b) Fourier transformed k^3-weighted EXAFS data as a function of time revealing the evolution of the Pd coordination environment in Pd(II)@MIL101(Cr)-NH_2. The spectra are not phase corrected. *The peak at ca. 1.9 Å comprises the signal of Pd−Cl single scattering and the side peak of Pd−Pd single scattering; (c) TEM images and (d) STEM image and EDS mapping of Pd(II)@MIL-101-NH2 at various stages during the Heck reaction at 0% (c_1−d_1), 25% (c_2−d_2), 54% (c_3−d_3) and >99% (c_4−d_4) conversion. While Pd nanoparticles are observed in all samples except the initial one, smaller Pd species (monomers, nanoclusters) are found to be homogeneously distributed in the MIL-101-NH_2 crystals throughout the reaction. The arrows in b3 indicate a Pd nanoparticle on the surface of the MOF. Adapted with permission from Ref.[23]. Copyright 2018 American Chemical Society.

2.3.3 Synthetic challenges of reported Pd@MOF systems

The literature summarized above presents a plethora of methods of Pd encapsulation and a wide range of impressive results on catalytic performance of the resulting Pd@MOF materials. However, the majority of these reported systems are difficult to synthesise. Some, like the first report on Pd@MOF-5[75] (Figure 2.8), require sophisticated chemical vapour deposition environments. But even those methods that are relatively easy in comparison to CVD, take a long time and require the use of sealed autoclaves for solvothermal synthesis of the MOF. Then comes a second step to actually incorporate the Pd species, and then often another to activate it. Table 2-2 gives the temperature regimes and the time required in the two (or one combined) longest steps in the synthesis of representative Pd@MOF systems, without even considering the washing and drying procedures that are similar for most MOF materials. The majority of reported Pd@MOF systems require well above 24 h of reaction and infiltration time to form. This is a major limitation of these materials in the way of their industrial applications, which the work on the Pd@OX-1 material presented in Chapter 5 sets out to overcome.

Table 2-2 Time consuming synthesis of selected Pd@MOF systems: temperature and corresponding time of heating required to obtain the reported systems. Only the longest steps are shown, without consideration of the washing and evacuation steps.

Host MOF	1st step: MOF synthesis	2nd step: Pd encapsulation
UiO-67 [87]	120°C 48 h	
UiO-66 [88]	Micrwave 100°C 2 h	RT 24 h, Microwave 30°C 20 min
$Cu_2(BDC)_2DABCO$ [91]	Ball mill RT 2 h	80°C 20 h, 130°C
NH_2-MIL-125 [92]	100°C 72 h	RT 12 h
MIL-101(Cr) [19]	180°C 96 h + 70°C 6 h	RT 18 h

2.3.4 OX-1 as a promising MOF to host Pd catalysts

Many MOFs that have been used in the Pd@MOF investigations make use of the BDC linker to produce a variety of carboxylate MOFs, which tend to exhibit good chemical and thermal stability, and are therefore attractive for catalytic applications. MOF-5, the prototypical MOF material made of Zn metal centres and BDC linkers, is a good example. Curiously, variations in the synthesis conditions can lead to different structures, as Burrows *et al*[93] discovered when attempting to synthesise MOF-5 in DEF that "has been in the laboratory for several weeks" (p.548), which resulted in a new structure distinct from MOF-5. The same structure was then synthesised in a more detailed study by Biemmi, Bein and Stock[94], who also grew large crystals of it on a ZnO tablet shown in Figure 2.12a. The crystal structure is shown in Figure 2.12b and has a wine-rack motif similar to MIL-53, but with an additional 'cross-bracing' linker in the middle of the pore. TGA and in situ thermal XRD results (Figure 2.12c,d respectively) show that this structure is thermally robust up to about 400°C, akin to MOF-5. However, between about 250°C and 450°C, the structure undergoes a transformation, which the authors attribute to a loss of one BDC linker per Zn centre, leading to a modified XRD pattern. This then decomposes to ZnO by 500°C. The authors report a modest Langmuir surface area of 66.33 m^2/g.

Upon significantly increasing the concentration of the synthesis reaction, so as to form a gel intermediate phase, Chaudhari *et al*[1] report the formation of a new structure, termed OX-1, and shown in inset of Figure 2.13a. A closer look at the structure is taken in Chapter 5. Here it is sufficient to note that OX-1 has a characteristic powder XRD pattern that is distinct from the material reported by Burrows *et al*[93] and Biemmi, Bein and Stock[94], and a TGA curve that is very similar to them, exhibiting the same excellent thermal stability. The reported BET area is 80 m^2/g, which is only marginally larger than its predecessor. It possesses the BDC linkers, which are potentially attractive structures for catalytic species

attachment. But most importantly, it is rapidly synthesised in large, scalable, amounts. Moreover, the highly concentrated synthesis route also facilitates *in situ* guest molecule encapsulation, as discussed in section 2.4.3 of this chapter. Together these properties make OX-1 a promising material for catalytic applications.

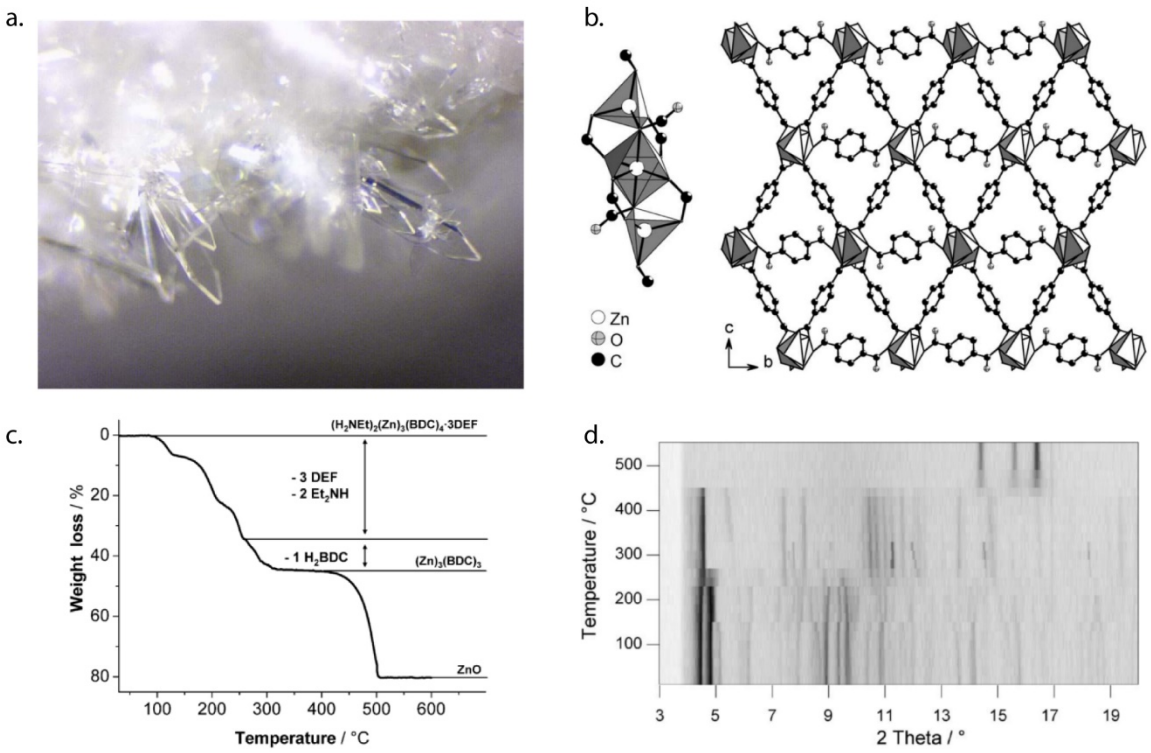

Figure 2.12 (a) Optical micrograph of $[H_2NEt2]_2[Zn_3(BDC)_4]\cdot 3DEF$ crystals covering a ZnO tablet. (b) Trimetallic zinc unit (left); BDC-units interconnecting the trimetallic units (presented in the picture as polyhedra), forming a dense layer in the b, c-plane. (c) TGA diagram of $[H_2NEt2]_2[Zn_3(BDC)_4]\cdot 3DEF$ and (d) temperature-dependent powder XRD analysis at corresponding temperatures. Reproduced from Ref.[94].

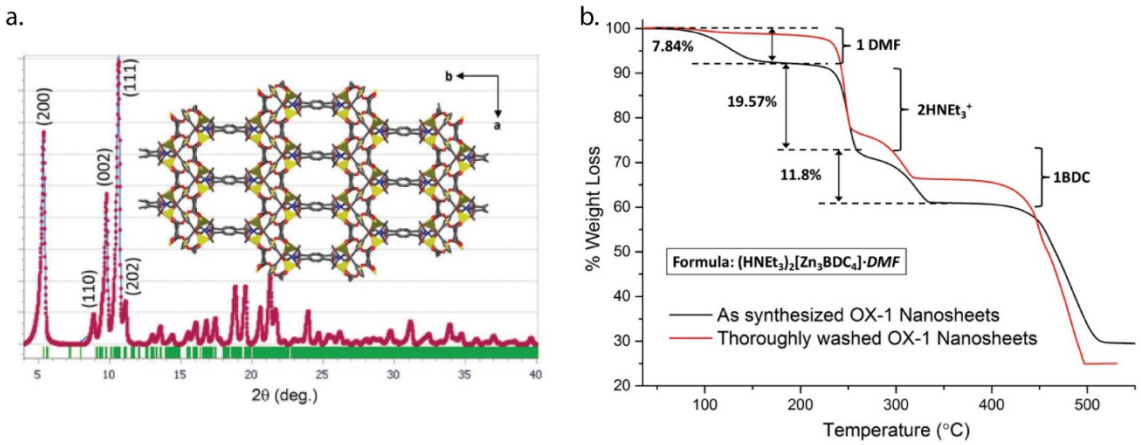

Figure 2.13 Oxford University-1 (OX-1) material structure: a) Pawley refinement of the OX-1 crystal structure incorporating Et_3N^+ charge-balancing cations (Rwp = 0.084), and crystallographic view along the c-axis showing 1D porosity (inset). Colour scheme: zinc in yellow, nitrogen in blue, oxygen in red, carbon in gray, and hydrogen in white. The traces indicate data as follows: red: experimental data, blue: calculated from structural refinement, and green: observed Bragg peak positions; b) TGA for OX-1 nanosheet material synthesized in DMF with the formula for the material which is in close agreement to the expected weight loss of the components present in the material. Adapted from Ref.[1] © 2017 John Wiley and Sons, used under a Creative Commons Attribution-Noncommercial license: http://creativecommons.org/licenses/by-nc/3.0/.

2.3.5 The catalytic frontier

The history of the study of transition-metal-catalysed reactions is comprehensively traced by Eremin and Ananikov[18], who group them into evolving attitudes towards both improving the performance of the catalysts, and also understanding the mechanisms involved. These "waves" are summarized in Figure 2.14, and the most up-to-date model of understanding is that of these catalysts possessing a dynamic nature: during the course of the reaction being catalysed, the catalyst can evolve into its various forms, i.e. nanoparticles on a surface, single atoms on a surface, single atoms in solution, as well as small clusters and nanoparticles in solution. All of these forms contribute to the catalyst's performance in the ultimately observed yields of the reactions being studied.

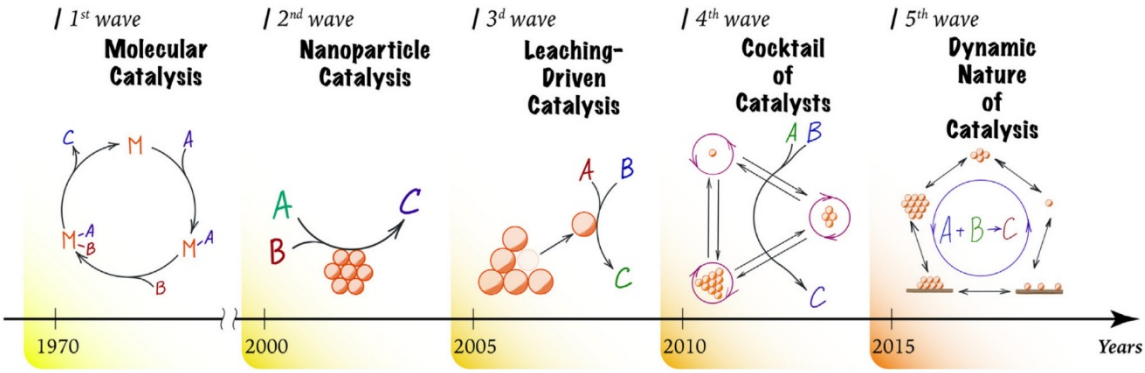

Figure 2.14 ‘‘Waves” in the mechanistic studies of the nature of transition-metal-catalysed reactions (the ‘years’ axis shows influential periods of mechanistic studies in the development of new applications in organic synthesis, rather than the year of the first mention or discovery). Reprinted from Ref.[18], with permission from Elsevier.

The design of novel and more efficient catalysts must thus thrive towards understanding what these different forms contribute to the activity of the catalyst and be aware of the evolution of the catalyst during the reactions. Beller and co-workers[95] see the frontier of such design in heterogenous single-metal-site catalysts, where single atoms of transition metals are anchored strongly on a solid support to produce a heterogenous catalyst. Zou, Martin-Matute and co-workers[23] latest work on operando XAS studies of Pd@MIL-101(Cr)-NH_2 crystals (presented in Figure 2.11) is a clear step in this direction. Pardo and co-workers[96] also present an impressive MOF material incorporating Pd_4 clusters that have excellent activity in catalytic reactions. The synthesis route to achieve these materials, however, is difficult and not immediately scaled for industrial applications. The work presented in Chapter 5 of this thesis on the Pd@OX-1 aims to strive towards single-metal-site catalysts, at least in their initial form, and to understand the evolution of the catalyst during C-C coupling reactions, while also providing a readily scalable synthesis route.

2.4 Acetone sensing for non-invasive diagnostics

2.4.1 Introduction: breath VOCs and acetone amongst them

The human body produces over 500 different volatile organic compounds (VOCs) (see Figure 2.15a) that can be found in a single breath when a person exhales. These compounds have potential to be exploited for non-invasive diagnostics of various conditions. Type-1 diabetes mellitus (T1DM) is one such condition for which data is being collected to distinguish between affected and healthy individuals based on the content of acetone in their breath. Rydosz[24] reports that healthy volunteers produce an exhaled acetone concentration below 0.8 ppm for all blood glucose levels achieved in his study. T1DM patients, on the other hand, produce concentrations of exhaled acetone in excess of 1.2 ppm, which grow with increasing blood glucose levels (see Figure 2.15b). This clear division of concentrations, with a margin of 0.4 ppm between boundary cases, can be exploited for non-invasive diagnosis of T1DM.

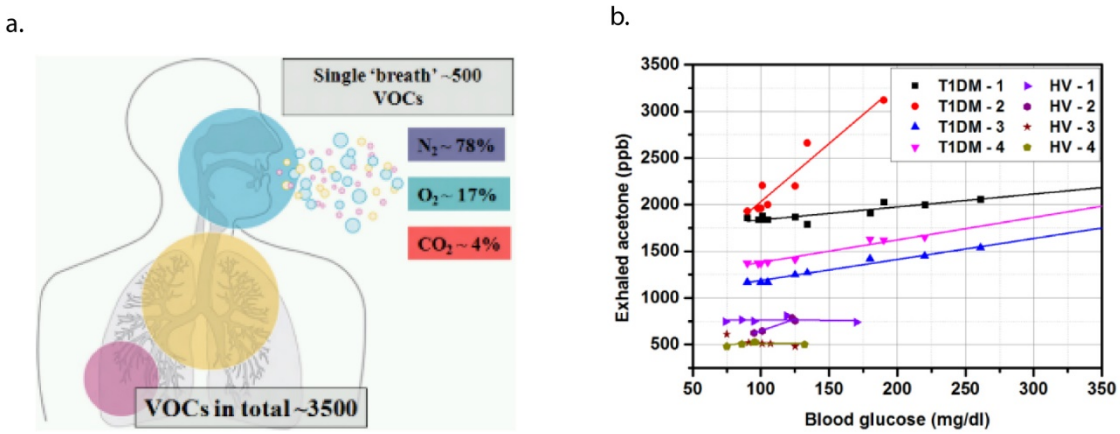

Figure 2.15 The exhaled breath: a) general overview of the exhaled breath compounds (VOCs = volatile organic compounds); b) exhaled acetone concentration vs. blood glucose concentration for selected healthy volunteers (HV) and type-1 diabetes mellitus patients (T1DM). Adapted from Ref.[24] © 2018 MDPI, used under a Creative Commons Attribution-Noncommercial license: http://creativecommons.org/licenses/by-nc/3.0/.

2.4.2 Metal Oxide (MOX) based sensors

Current state-of-the-art sensors for detection of exhaled acetone are based on metal oxide (MOX) films deposited on silicon chips. Resistance of such MOX films changes upon acetone uptake, which then results in an electric signal that can be directly measured on a chip. Figure 2.16a,b shows the schematic architecture of a sensor based on this principle, with a Pt film deposited between electrodes for improved signal amplitude produced by the InN film.[97] The response of this sensor varies with temperature of the InN film (see Figure 2.16c): an order of magnitude improvement of signal is achieved when the temperature is increased from 150 °C to 200 °C. The benefit of this relatively high operating temperature is a response that also scales with acetone concentration in the required range: from 0.4 ppm to 20 ppm (see Figure 2.16d).

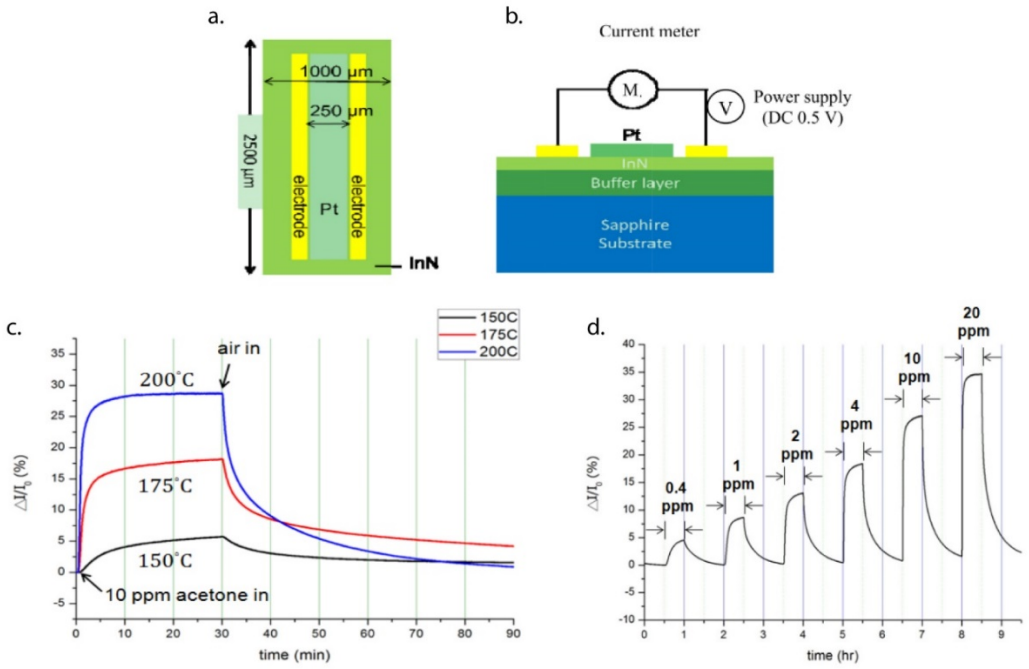

Figure 2.16 Pt-InN acetone sensor: (a) top and (b) side schematic views of the device; (c) response at various temperatures from 150 °C to 200 °C in 10 ppm Acetone/air mixture ambiance; (d) Response to increasing acetone concentrations (0.4 ppm–20 ppm), operating temperature at 200 °C. Adapted from Ref.[97] © 2012 MDPI, used under a Creative Commons Attribution-Noncommercial license: http://creativecommons.org/licenses/by-nc/3.0/.

Many variations on this sensor exist, all sharing the same basic operating principle. Rydosz[24] provides an extensive overview of the reported systems, summarized in Table 2-3. These sensors provide excellent sensitivity for acetone, with limits of detection (LOD) commonly lower than 1 ppm. These characteristics make MOX based sensors attractive because they can readily be incorporated in microchips, but they also suffer from important limitations: the high operating temperatures (commonly above 150 °C) are necessary to avoid signals from moisture uptake, while the mechanisms for selectivity against the numerous other exhaled VOCs are unclear. These two design criteria are exactly where MOFs are advantageous – they respond to gases at ambient temperatures and can provide selectivity based on pore size and chemical composition design.

Table 2-3 Summary of selected metal-oxide based sensors for acetone detection with special emphasis to exhaled acetone measurements in terms of diabetes monitoring. Reproduced from [24]. Reference numbers refer to references in the source review article [24]. This table is © 2018 MDPI, used under a Creative Commons Attribution-Noncommercial license: http://creativecommons.org/licenses/by-nc/3.0/.

Material	Max. Response	Temp. (°C)	Acetone (ppm)	LOD [1] (ppm)	Reference
NiO/SnO_2	20.18 R_a/R_g [2]	300	50	0.01	[42]
$NiFe_2O_4$	30.4 R_g/R_a	160	200	0.52	[52]
SnO_2/SiO_2	2193.7 $R_a/R_g - 1$	270	300	0.5	[46]
TiO_2/In_2O_3	33.34 R_g/R_a	250	10	0.1	[53]
Sb/In_2O_3	64.3 R_a/R_g	240	50	-	[54]
C_3N_4-SnO_2	11 V_g/V_a [3]	380	20	0.087	[43]
GO-SnO_2-TiO_2	60 R_a/R_g	200	5	0.25	[46]
ZnO:Pt	188.0 R_a/R_g	400	1000	1	[55]
ZnO:Nb	224.0 R_a/R_g	400	1000	1	[55]
$Pd/LaFeO_3$	1.19 R_g/R_a	200	1	1	[57]
$Pt_{0.3}Au_{0.7}$–In_2O_3	40 R_g/R_a	160	50	0.3	[58]
$CuFe_2O_4/\alpha$-Fe_2O_3	14 R_a/R_g	275	70	0.1	[59]
ZnO–Fe_3O_4	47 R_a/R_g	475	50	0.15	[60]
$ZnCo_2O_4$	38 R_g/R_a	200	500	0.5	[61]
Co_3O_4	17 R_g/R_a	111	1000	-	[62]
$Co_{1-x}Zn_x$ Fe_2O_4	−112 mV	650	50	0.3	[63]
TiO_2	25.97 R_a/R_g	370	500	-	[64]
Ru/WO_3	7.3 R_a/R_g	300	1.5	0.5	[47]
WO_3 NFs	90 R_a/R_g	350	5	0.4	[48]
WO_3/Pt-GNs	12 R_a/R_g	200	10	1	[49]
In/WO_3-SnO_2	66.5 R_a/R_g	200	50	1	[45]

[1] LOD—Limit of Detection. [2] R_a/R_g—electrical resistance under exposure to air and target gas (acetone), respectively. [3] V_a/V_g—electrical voltage under exposure to air and target gas (acetone), respectively.

2.4.3 ZnQ@OX-1 acetone sensing MOF

The ZnQ@OX-1 guest@host MOF system developed by Chaudhari *et al*[1] is an excellent candidate for chemical sensing applications. The ZnQ guest complex consists of a single Zn centre, to which two 8-hydroxyquinoline (8HQ) aromatic molecules are coordinated. This assembly is a highly flexible one, allowing for other molecules to coordinate to the Zn centre. It is also a luminescent complex whose emission changes depending on its structure and surroundings, which opens the door for opto-chemical sensing based on the emission spectrum under UV light. Chaudhari *et al*[1] report simulations of different spatial arrangements of the 8HQ aromatic rings when DMF solvent molecules are coordinated to ZnQ (Figure 2.17a), compared to the arrangements when DMA molecules are coordinated (Figure 2.17b) and when no solvent molecules are attached to ZnQ (Figure 2.17c). The latter is also reported to have weak interactions with the OX-1 pore – more specifically with the aromatic rings of the BDC linkers. This configuration is illustrated in Figure 2.17d,e with the highest occupied molecular orbital (HOMO) and the lowest unoccupied molecular orbital (LUMO), respectively. Importantly, the luminescent emission of the ZnQ@OX-1 system is drastically different to the emission of solid ZnQ crystals, the latter producing dark yellow emission with low quantum yields.[1] The luminescent emission from the guest@host system, on the other hand, produces a range of colours depending on the solvent used in synthesis and processing steps. The nominal emission is taken to be that from the system synthesised in DMF, designated as ZnQ_{DMF}@OX-1, which produces bright light-blue emission in its dried solid state. This emission is retained when the powder is suspended in DMF and shifts colour in response to other solvents, as illustrated in Figure 2.18. This colour shift-based sensing is highly advantageous compared to intensity quenching-based sensing more commonly reported for luminescent MOF sensors, as set out in numerous reviews on the topic.[13, 98-99]

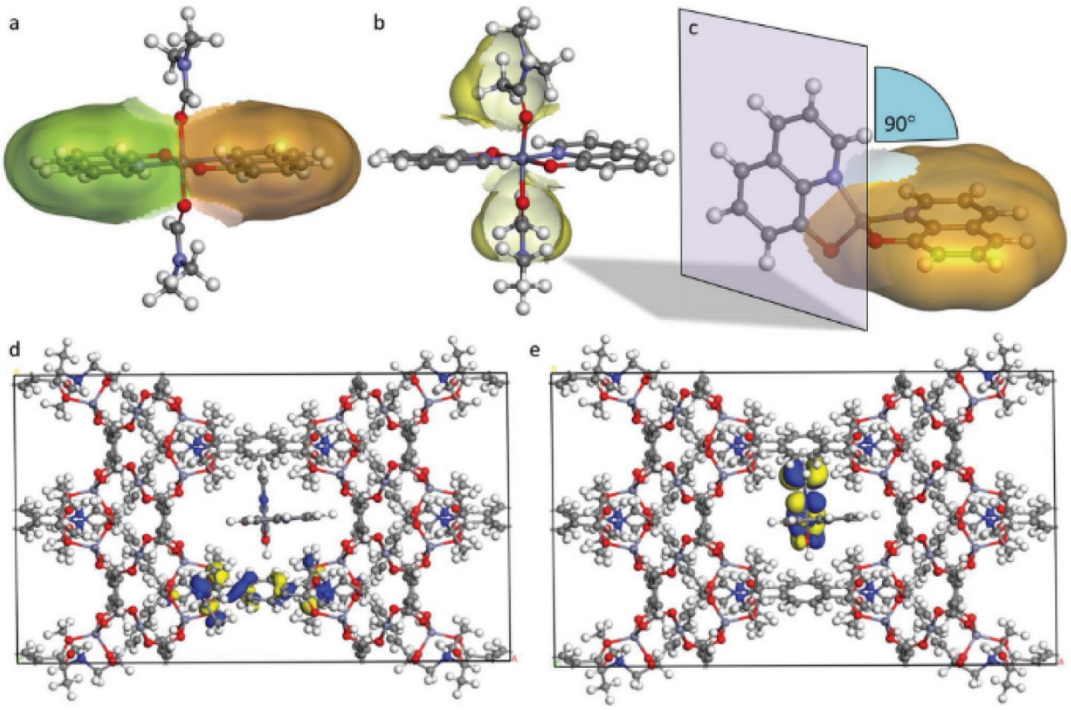

Figure 2.17 Optimized geometries of the ZnQ guest in three different structural configurations: a) DMF solvent molecules coordinated axially to the Zn^{2+} octahedral centre; less steric DMF molecule allowing planar spatial arrangement of the 8HQ aromatic rings (indicated by green and orange van der Waals surfaces). b) Steric hindrance from axially coordinated DMA solvent molecules deforming the planarity of 8HQ aromatic rings; yellow surfaces represent CH_3 groups of the coordinated DMA. c) Tetrahedral configuration achieved upon removal of the two axially coordinated DMA molecules, permitting a 90° rotation of one of the two 8HQ aromatic planes. ZnQ@OX-1 assembly in which d) HOMO located on the BDC linker of the host framework, while e) LUMO on the aromatic rings of ZnQ guest molecule confined within an OX-1 pore. Blue and yellow isosurfaces are positive and negative charges, respectively. Adapted from Ref.[1]

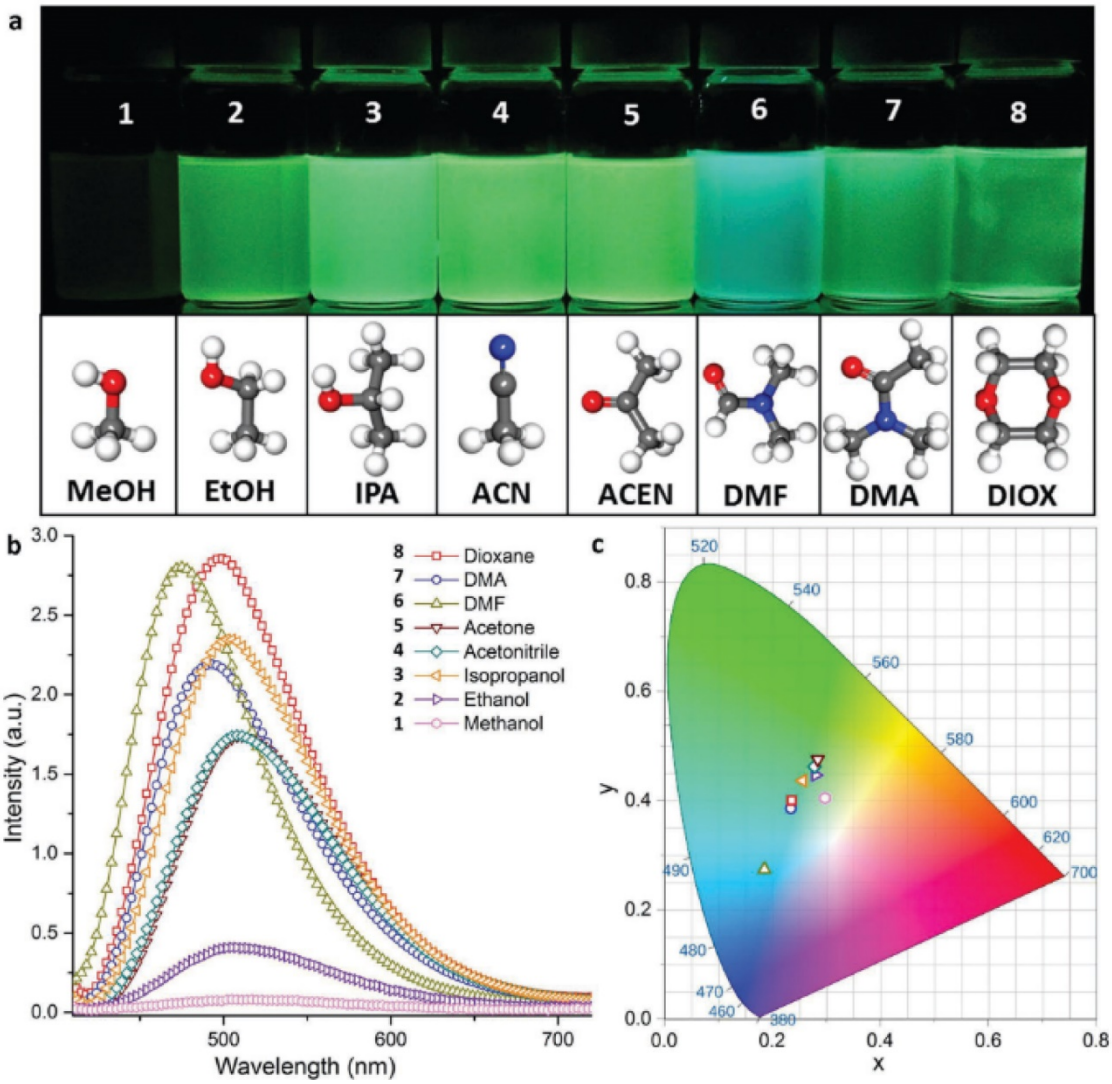

Figure 2.18 Optochemical responses of ZnQ_{DMF}@OX-1 nanosheets: a) visible to naked eye are distinct modulations in emission properties of dispersions of functionalized nanosheets in a range of small-molecule solvents (each comprising 5 mg of active material in 15 mL solvent); b) emission profiles and emission intensities of respective dispersions showing different levels of blue or red shifts; c) chromaticity plot (CIE 1931) indicating the emission colour coordinates of the respective dispersions. Adapted from Ref.[1] © 2017 John Wiley and Sons, used under a Creative Commons Attribution-Noncommercial license: http://creativecommons.org/licenses/by-nc/3.0/.

Chaudhari *et al*[1] further report a simple device for acetone vapour sensing: it consists of a piece of filter paper onto which ZnQ@OX-1 is drop cast from a suspension in Hexane. Once the hexane evaporates, the ZnQ@OX-1 crystals produce bright blue emission under a 365 nm UV source in ambient lab air. When acetone vapour is introduced, the emission rapidly shifts to a dark green colour. The emission then recovers when acetone vapour is removed. This process is illustrated in Figure 2.19a, together with the corresponding emission spectra in Figure 2.19b. After a number of cycles the emission is reported to get stuck in the green state centred around 507 nm, which then requires a re-activation step – soaking the material in DMF – to recover the 476 nm blue emission. The authors postulate that the emission gets locked in the green state due to increased host-guest interactions between the ZnQ guests and OX-1 pores as DMF molecules slowly get displaced from the pore during acetone adsorption and desorption. During the re-activation step the DMF molecules slowly leach back into the channel-like pores, breaking the host-guest interactions and interacting with the ZnQ guests as in the freshly synthesised material. This re-activation process is schematically summarized in Figure 2.19c. It is important to stress, however, that this process is postulated based on qualitative observations of the luminescent emission during the re-activation step, and so must be considered with caution. A similar note can be made on the sensing mechanism: while the phenomenological observations are substantiated by visible emission spectra measurements, the underlying mechanisms remain to be discovered.

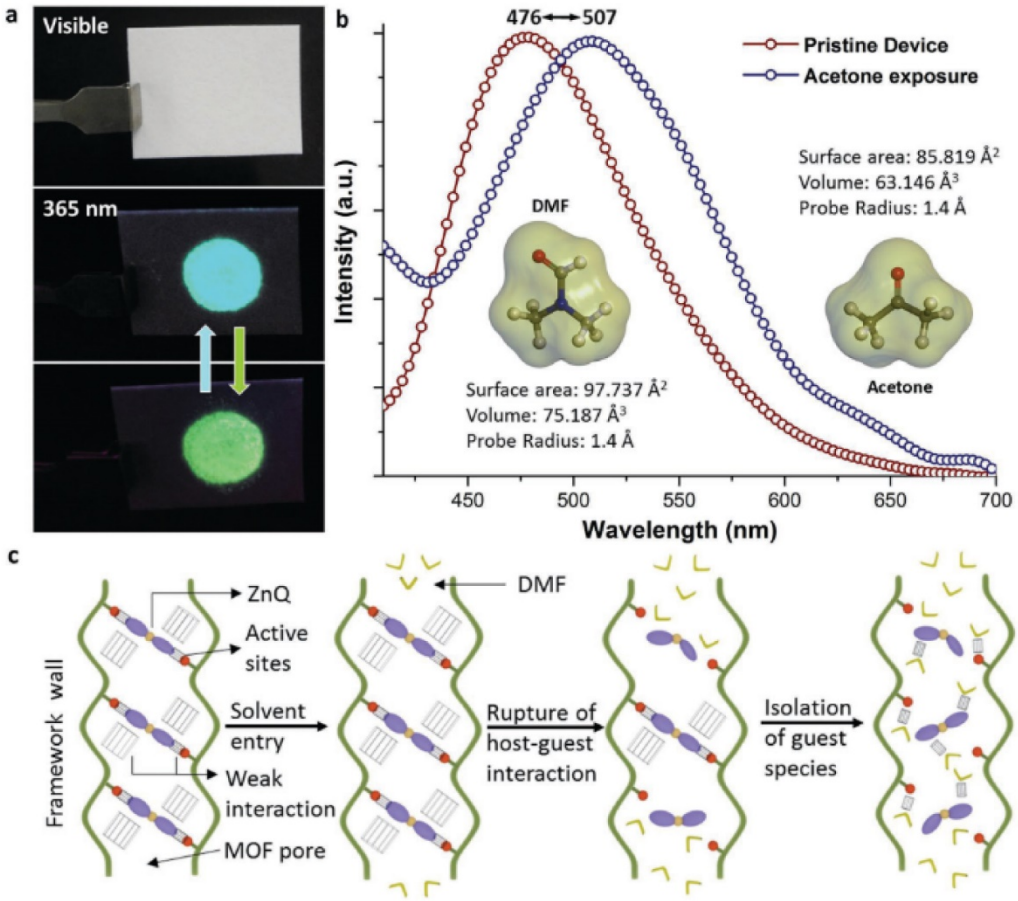

Figure 2.19 Optochemically active sensory materials comprising ZnQ_{DMF}@OX-1 nanosheets. a) Paper-based optochemical sensor demonstrating reversible acetone sensing ability. b) A 31 nm red shift upon acetone exposure and recovery to its original emission wavelength upon DMF exposure. Inset shows chemical structures of DMF and acetone analytes and their differential molecular sizes. c) Proposed mechanisms involving multiple host–guest interactions under the nanoscale confinement of 1D undulating (tortuous) channels of the OX-1 host framework (vertical: c-axis, corresponding to the 1D channels in Figure 2c), and upon the introduction of a DMF analyte triggering a blue shift transformation. Adapted from Ref.[1] © 2017 John Wiley and Sons, used under a Creative Commons Attribution-Noncommercial license: http://creativecommons.org/licenses/by-nc/3.0/.

2.4.4 Conclusion: missing knowledge of ZnQ@OX-1 functionality

ZnQ@OX-1 is a prime candidate for outperforming the MOX based sensors as it is shown to detect acetone in real time at ambient temperature and pressure, while also producing a readily observable signal. These are positive initial results, but more evidence is needed to understand the full potential of the material. The crucial questions to ask of ZnQ@OX-1 at this stage in development are the following:

1. What concentrations of acetone can it detect and how does the material response vary with those levels of concentration?
2. After what amount of acetone does the material lock into its green state?
3. How selective is the material?

Given satisfactory answers to the above questions, ZnQ@OX-1 can be a very attractive material for non-invasive diagnostics of T1DM cases. Chapter 6 begins to tackle these questions.

2.5 Quantum tunnelling 'sensors' in ZIF-8

2.5.1 Introduction: Quantum tunnelling of -CH_3 groups in ZIF-8

Rotational tunnelling is the phenomenon of the librational states of a molecule whose rotating atoms, in this case the three H atoms, are indistinguishable.[2] The phenomenon of quantum rotational tunnelling has long held the promise to shed light on the subtle effects of chemical interactions in materials, which are undetectable via conventional techniques, as discussed at length by Eckert[100] and Prager and Heidemann[2]. Yildrim and co-workers[3] show that under high vacuum and at temperatures below 30 K, high resolution inelastic neutron scattering (INS) spectra of the Zeolitic Imidazole Framework - 8 (ZIF-8) MOF show a well-defined peak at 0.33 meV (see Figure 2.20a), which corresponds to rotational tunnelling transitions of hydrogen atoms on the -CH_3 groups of the 2-methylimidazolate (MeIM) linkers, which make up the pores of ZIF-8. The ZIF-8 crystal structure and its MeIM linkers are variously illustrated later in this section (see for example Figure 2.21c-f,k) along with the discussion of the dynamic nature of ZIF-8 structure. Yildrim and co-workers[3] further report that at increasing temperatures this tunnelling disappears and gives way to classical jump reorientations, seen as quasi-elastic scattering of neutrons in INS spectra (see Figure 2.20b). Most importantly, however, the work of Yildrim and co-workers[3] shows that the tunnelling peak is sharp and singular, with no peak splitting, implying that there is no coupling between neighbouring methyl rotors. Therein lies the key to the usefulness of tunnelling spectroscopy on ZIF-8: the -CH_3 rotors can be used to detect guest molecules adsorbed into the pores of ZIF-8, as more generally mentioned by Prager and Heidemann[2] (p. 2942) - "tunnelling molecules can be used as probes to study the local potentials of adsorption sites". Tunnelling spectroscopy can thus shed new light onto the much-contested phenomenon in ZIF-8 commonly called 'gate opening', which is the subject of the next subsection.

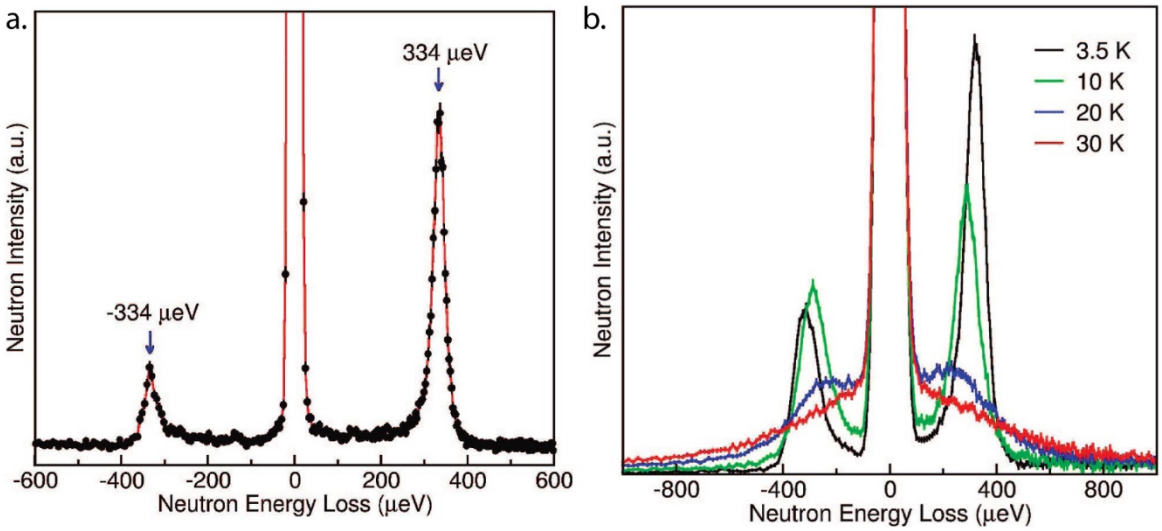

Figure 2.20 a) Tunnelling spectrum of ZIF-8 at 1.4 K. Vertical error bars denote ±1σ. The relatively high energies [at ±334 ± 1 μeV] imply a low rotational barrier. b) Temperature evolution of the tunnelling spectrum of ZIF-8. Vertical error bars denote ±1σ. At higher temperature, classical jump reorientation leads to quasi-elastic scattering. Adapted from Ref.[3]. Copyright 2008 American Chemical Society.

2.5.2 A brief history of gate opening in ZIF-8

The existence of two phases of ZIF-8 – ambient pressure (AP) and high pressure (HP), illustrated in Figure 2.21a-f – was first published in 2009 by Moggach, Bennett and Cheetham[25], who performed single crystal XRD on ZIF-8 in a diamond anvil cell, using a mixture of methanol and ethanol as a pressure transmitting fluid. They found that the structure of the single crystal changed substantially at 1.47 GPa, most notably expressed in the rotation of the MeIM linkers so as to create a channel through the 4-MRs, accessible to guest molecules. This "swing effect", as well as a swelling of the unit cell was attributed to the packing of methanol and ethanol molecules inside the ZIF-8 cages. The high external pressure applied to the crystal makes the experiment ambiguous: do the structural changes occur due to external pressure or due to chemical changes induced by the guest molecules?

Following this first report, Fairen-Jimenez *et al* [26] used the two structures to simulate the step-wise N_2 gas adsorption isotherm in ZIF-8 at 77 K shown in Figure 2.21g. They

found that the AP structure results in a simulated isotherm, which fits well to the experimental data up to gas doses of about 20 molec/uc and significantly underestimates the experimental data beyond that point. The HP structure, on the other hand, gives a close match to experimental data from about 25 molec/uc onwards. Fairen-Jimenez *et al*[26] therefore argue that both structures are required to understand the observed adsorption behaviour of ZIF-8, and, by implication, that the same structural transition occurs during N_2 adsorption at 77 K. They later expanded this reasoning to other gases (such as CO_2 and CH_4), and argued that both the AP and HP forms were needed to simulate gas adsorption even when no 'steps' are present in the isotherms.[28] Their calculations also suggested that the N atoms of MeIM linkers were important for interactions with CH_4 guest molecules, and that these binding sites near the imidazole (IM) rings played a role in the GO behaviour. Almost simultaneously, Ania *et al*[27] published their results attempting to model gas adsorption isotherms of ZIF-8 for CO, N_2, O_2 and Ar gases. They attempted to identify regions with common features in isotherms of all four gases, shown in Figure 2.21h, where similar transitions happen during adsorption. Their findings support the notion of structural changes taking place during gas adsorption but reject the notion of different adsorption sites playing a role in the multistep adsorption behaviours of these gases. Instead, they make a distinction between polar and non-polar gas molecules and argue that this is the key determining factor in adsorption behaviour. The observed hysteresis in desorption of all the gases is vaguely associated with a structural transition back to a closed form (AP) of ZIF-8 and the associated reorganization of the remaining gas molecules.[27] This last point is further complicated by the already mentioned rejection of the possible existence of preferential adsorption sites, whose interaction energies could have a role to play in the hysteresis behaviour.

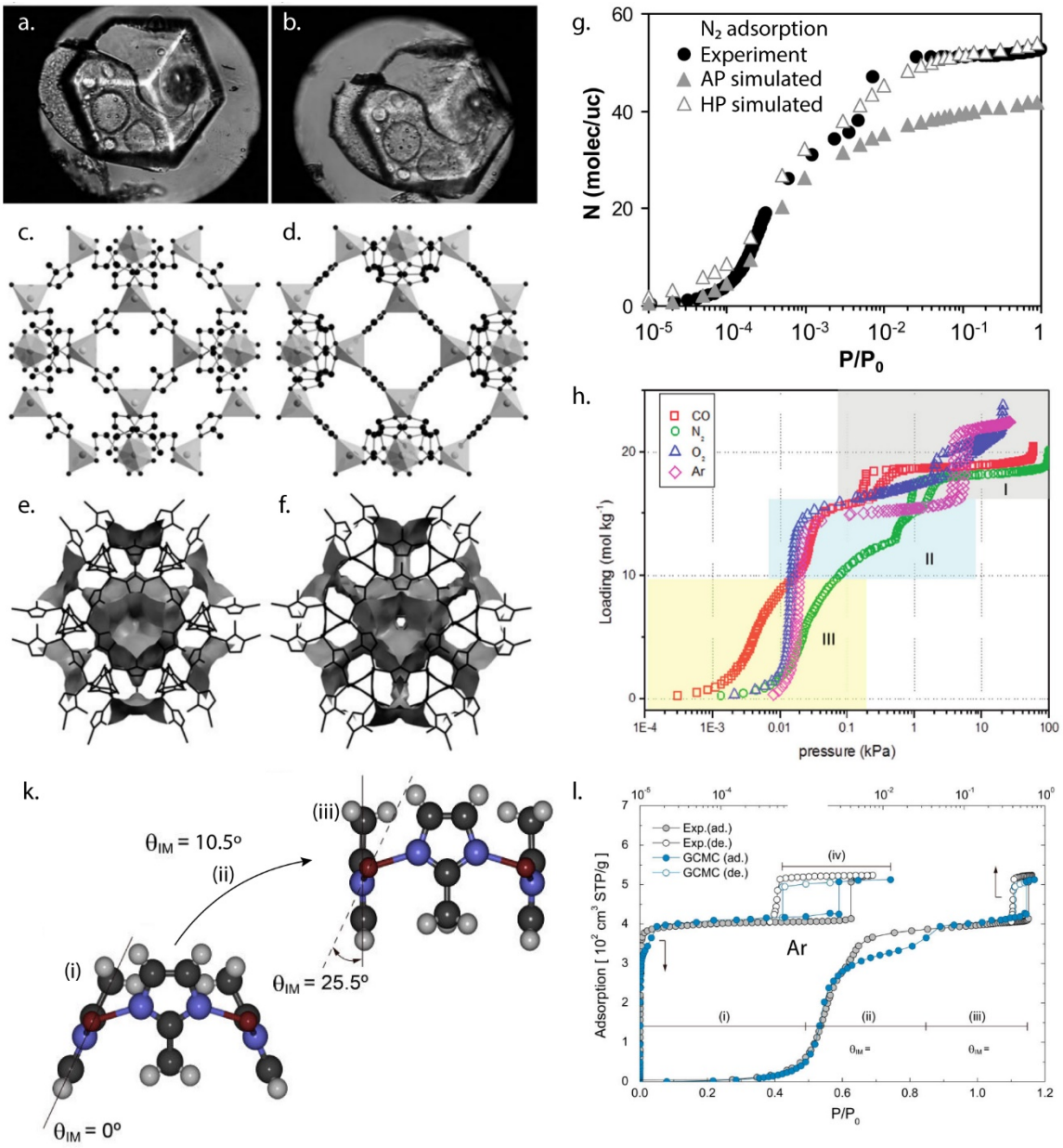

Figure 2.21 (a, b) Optical microscope images of a ZIF-8 single crystal in the AP (atm.) and HP (1.47 GPa) phases, respectively, with corresponding (c, d) crystal structures and (e, f) void surfaces; (a-f) Adapted from Ref.[25], with permission from John Wiley and Sons. (g) Experimental and simulated N_2 adsorption isotherms of ZIF-8; Reprinted with permission from Ref.[26]. Copyright 2011 American Chemical Society. (h) Experimental adsorption isotherms of ZIF-8 for various gases, with postulated marked zones corresponding to crystal structures shared in all cases; Reprinted with permission from Ref.[27]. Copyright 2012 American Chemical Society. (k) Schematic illustration of calculated MeIM linker rotation at stages (i-iii) marked in the (l) experimental and calculated using Grand Canonical Monte Carlo (GCMC) methods Ar adsorption isotherms of ZIF-8. (k-l) Adapted with permission from Ref.[30]. Copyright 2014 American Chemical Society.

A study published two years later by Tanaka *et al*[30] further explored Ar adsorption in ZIF-8, by taking a more detailed look at the rotation of the MeIM linkers beyond the two discrete states of AP and HP. They conclude that the linkers go through a transition state roughly between the AP and HP, illustrated in Figure 2.21k, and divide the Ar adsorption isotherm into regions with the three orientations of the linkers (see Figure 2.21l). Their simulated isotherm, however, deviates from experimental data in the transition region (ii), suggesting that the model is incomplete. Their explanation is the possible existence of further degrees of freedom, which were not captured by the rotation of a rigid MeIM linker.

A further detailed study appearing in 2016 by Fairen-Jimenez and co-workers[34] investigated N_2 adsorption by ZIF-8 crystals of drastically different sizes: from around 140 nm to around 98 μm (see SEM images in Figure 2.22i-vi). Interestingly they found that the adsorption isotherms for all crystal sizes were nearly identical up to about 300 cm^3/g, or in other words up to the second step in the isotherm. This second step was significantly shorter for larger crystals (Figure 2.22a) than for smaller crystals (Figure 2.22b). They further attempted *in situ* high resolution powder XRD dosing experiments to experimentally prove structural changes in ZIF-8. Figure 2.22c-d shows results for the large and small crystals, respectively: gas uptake is plotted together with linker rotation (illustrated in Figure 2.22e) and an additional degree of freedom, namely the bend of the methyl groups of MeIM linkers (illustrated in Figure 2.22f). However, the values for gas uptake appear to be problematic: the pressure range would place these experiments near the second step in the isotherms and above in terms of gas dose, but the gas uptake in Figure 2.22c appears to jump from nearly 0 molec/uc to 40 molec/uc between 0.05 and 0.06 bar, which in no way resembles the respective isotherms presented in Figure 2.22a. This calls into question the values obtained for linker rotation and methyl group bending. Nevertheless, the variations in gas adsorption data with increasing crystal size poses an interesting challenge.

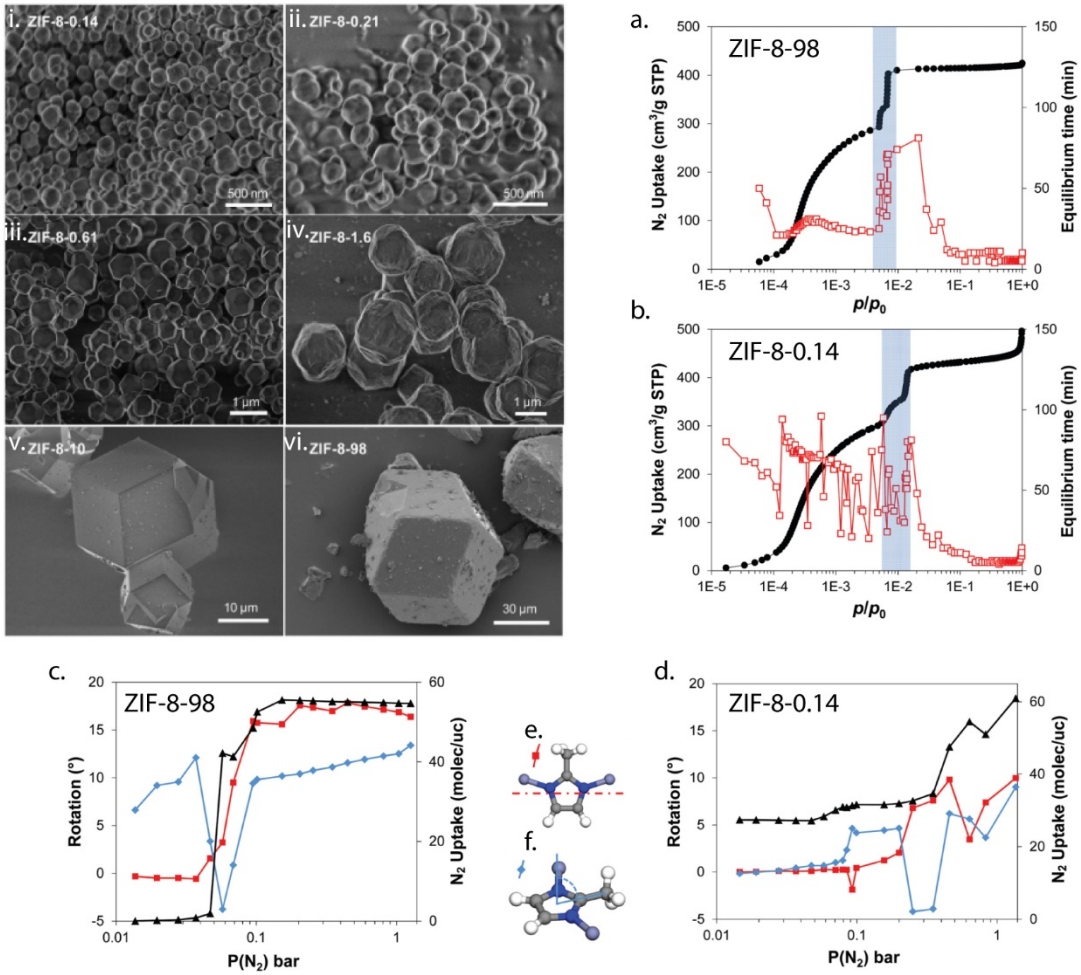

Figure 2.22 (i-vi) SEM images of ZIF-8 samples with increasing crystal sizes together with the corresponding (vi-a, i-b) high resolution N_2 adsorption isotherms and the respective (c, d) plots of gas uptake (black triangles), as well as MeIM linker rotation angles (red squares, illustrated in (e)) and -CH_3 group bend angles (blue diamonds, illustrated in (f)) obtained from high resolution powder XRD experiments. Adapted from Ref.[34]

In 2014, the dynamic nature of the MeIM linker 'swing' motions was beginning to be recognized, as opposed to the static 'positions' of the linkers discussed earlier. Tan and co-workers[8] published their density functional theory (DFT) predictions for the terahertz vibrational modes of ZIF-8 (as well as ZIF-4 and ZIF-7). These are illustrated in Figure 2.23a, where the MeIM linkers indeed undergo more complex motions than a simple rotation. Importantly, the 'gate opening', or the rotation of the MeIM so as to open the 4-MR channels, is described as one of the vibrational modes of the framework, which are then observed in experimental inelastic neutron scattering spectra (Figure 2.23b). This stresses the dynamic nature of the framework's structure, which plays an important role in the ability of ZIF-8 to adsorb various guest molecules – even those, whose size is larger than the nominal diameter of the channels through 6-MRs, and which would be expected to not penetrate into ZIF-8 crystals.[32, 37] Kolokolov *et al*[31] later observed swing and twist motions of the MeIM linkers *via* ^{2}H NMR, similar to those described by Tan and co-workers[8]. Moreover, they distinguished two types of swing motions: 2-site flips, where the linker average position rotates by 34°, and librational rotations around those positions of about ±17° (see Figure 2.23c). Their data further suggests that these motions persist even with benzene adsorbed inside the ZIF-8 pores (presented in Figure 2.23d).

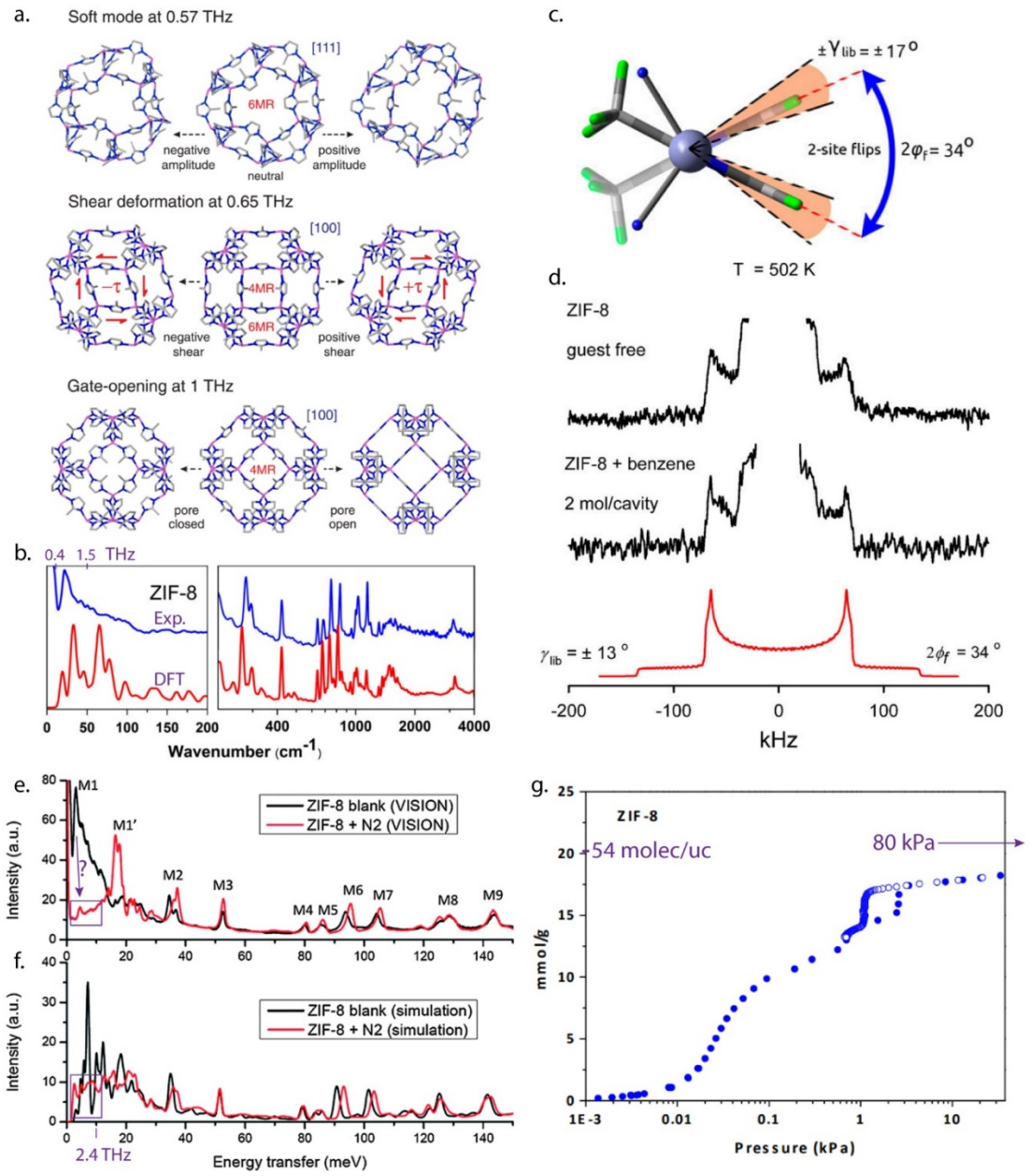

Figure 2.23 (a) Illustrations of THz vibrational modes in ZIF-8 obtained *via* DFT calculations together with (b) experimental and calculated INS spectra of ZIF-8 powder; Adapted figure with permission from Ref.[8]. Copyright 2014 by American Physical Society. (c) Schematic illustration of MeIM rotational motions obtained from modelling (d) experimental ^{2}H NMR spectra of ZIF-8; Adapted with permission from Ref.[31]. Copyright 2015 American Chemical Society. (e) Experimental INS spectra of ZIF-8 at high vacuum and ZIF-8 exposed to N_2 gas at 80 kPa for 10 min, together with (f) calculated spectra for corresponding samples and (g) experimental N_2 adsorption isotherm for the sample in (e). (e-g) Adapted from Ref.[33] © 2016 Royal Society of Chemistry, used under a Creative Commons Attribution-Noncommercial license: http://creativecommons.org/licenses/by-nc/3.0/.

Casco *et al*[33] published a study in 2016 repeating some of the INS measurements reported by Tan and co-workers[8], and providing further data on *in situ* N_2 dosing of ZIF-8, as well as further DFT simulations on both empty and N_2 loaded ZIF-8 structures (see Figure 2.23e-f). The results for pure ZIF-8 reproduce those published by Tan and co-workers[8] very well, lending further credibility to their measurements and simulations. Upon dosing with N_2, however, drastic changes occur in the experimental INS spectra, especially below about 5 THz – i.e. in the region where the various collective modes highlighted by Tan and co-workers[8] are observed. The interpretation of these changes by Casco *et al*[33] is problematic. They attribute the 3.08 meV (0.74 THz) band, labelled M1 in Figure 2.23e, to "free rotation of the -CH_3 group" (p. 3640), which apparently shifts to about 16.4 meV (3.97 THz) upon N_2 adsorption for 10 min at 80 kPa. They maintain that their simulations support this claim, arguing that the large shift results from a change in the molecular environment of the methyl groups, and that this change results from increased steric hindrance of the methyl groups caused by the swing of the MeIM linkers upon N_2 uptake. This, to them, constitutes "the first in situ experimental evidence of the rotation of the imidazolate rings in ZIF-8 upon exposure to N_2" (p. 3640). There are a number of claims to deconvolute here. The dose of N_2 they load into ZIF-8, about 54 molec/uc (see Figure 2.23g and previous gas adsorption results in Figure 2.21g,h and Figure 2.22a,b), is indeed expected to catapult the sample to an 'open gate'(HP) configuration[26-28, 34], which would significantly alter the environment of the -CH_3 groups of MeIM linkers. However, the peaks below 2.4 THz do not disappear entirely in the dosed spectrum, and it could be argued that the magnitudes of the original peaks are simply diminished by N_2 uptake (see purple annotations in Figure 2.23e and discussion of other THz results by Tanno *et al* [37] discussed below and presented in Figure 2.24h-l). This is, in fact, supported by Casco *et al*'s simulated dosed spectrum – the peaks below 2.4 THz are still there, albeit with lower magnitudes (see Figure 2.23f). Nor does the simulated spectrum

predict the large magnitude of the dosed experimental peak marked as M1'. Finally, as detailed by Tan and co-workers[8], there is a number of modes below 2.4 THz and the resolution of the spectra, as well as the reliability of theoretical calculations, do not permit such selective assignments of the observed bands as to say that the peak marked M1 indeed corresponds solely to the (free or otherwise) rotations of the -CH_3 groups.[32] Overall, however, the experimental results published by Casco *et al* [33] (Figure 2.23e) are valuable because they provide evidence for how the terahertz modes identified by Tan and co-workers[8] are affected by adsorbed N_2 gas: the modes do not disappear, but are somewhat suppressed by the presence of the guest gas molecules, showing that the dynamic vibrations of the framework and the MeIM linkers in particular are still present even at high loadings of N_2 gas.

Simulations and experimental terahertz spectroscopy by Tan *et al*[32] and later simulations by Formalik *et al*[39] are further building blocks in the understanding of ZIF-8 as a dynamic, rather than static, structure. Tan *et al*[32] predicted a strong vibrational mode at 1.89 THz arising from rotational motions of MeIM linkers, among mostly shearing and torsional terahertz modes, which they also observed in experimental terahertz time-domain spectra closer to 2 THz (Figure 2.24a). The advantage of this technique over INS is the ability to measure spectra at temperatures as high as 300 K (see Figure 2.24b), which allowed Tan *et al*[32] to observe changes in this mode at increasing temperatures from 80 K up to room temperature, showing that the rotations of MeIM persist across the whole range, albeit with slight shifts in frequency (see inset of Figure 2.24b). Formalik *et al*[39], following Coudert's[35] suggestion that chemical modification of the linkers have consequences for their rotations (discussed below), carried out comparative simulations of the terahertz vibrational modes (illustrated in Figure 2.24c) for ZIF-8 and its ZIF-8_amino and SALEM-2 modifications (distinguished graphically in Figure 2.24d). Their results, summarised in Table 2-4, and

plotted in Figure 2.24e-g, suggest that the chemical modification indeed shifts the frequency of swing motions of the linkers, but that those motions persist after the chemical modifications.

Tanno *et al*[37] provide further experimental evidence of these terahertz modes at room temperature and in N_2 atmosphere intermittently dosed with ethane, butane and CO2 (see Figure 2.24h-l). They attribute the mode near 2 THz to the 'gate opening' motions, as described by the simulations and experiments discussed above.[32] These results show the linker swing motions occur even in a saturated N_2 atmosphere, and in the presence of bulky molecules: ethane and butane appear to hinder the 2 THz mode but not completely extinguish it (Figure 2.24h,k), while CO_2 appears to have no effect on the swing motions (Figure 2.24l). This evidence would support the alternative explanation to the changes in INS spectra observed by Casco *et al*[33] (Figure 2.22e): the peaks below 2.4 THz most likely diminish in magnitude but do not disappear altogether.

Table 2-4 Predicted terahertz vibrational modes, illustrated in Figure 2.24c, of the three isostructrural frameworks distinguished in Figure 2.24d.[39] Units: cm^{-1} (THz).

	ZIF-8	SALEM-2	ZIF-8_amino
Symmetric gate opening	40 (1.19)	43 (1.29) 46 (1.38)	50 (1.49)
Asymmetric gate opening	67 (2.01)	37 (1.11)	58 (1.74)
6-MR breathing	100 (2.99)	105 (3.15)	97 (2.91)
Shear-like mode	22 (0.66)	23 (0.69)	37 (1.11)

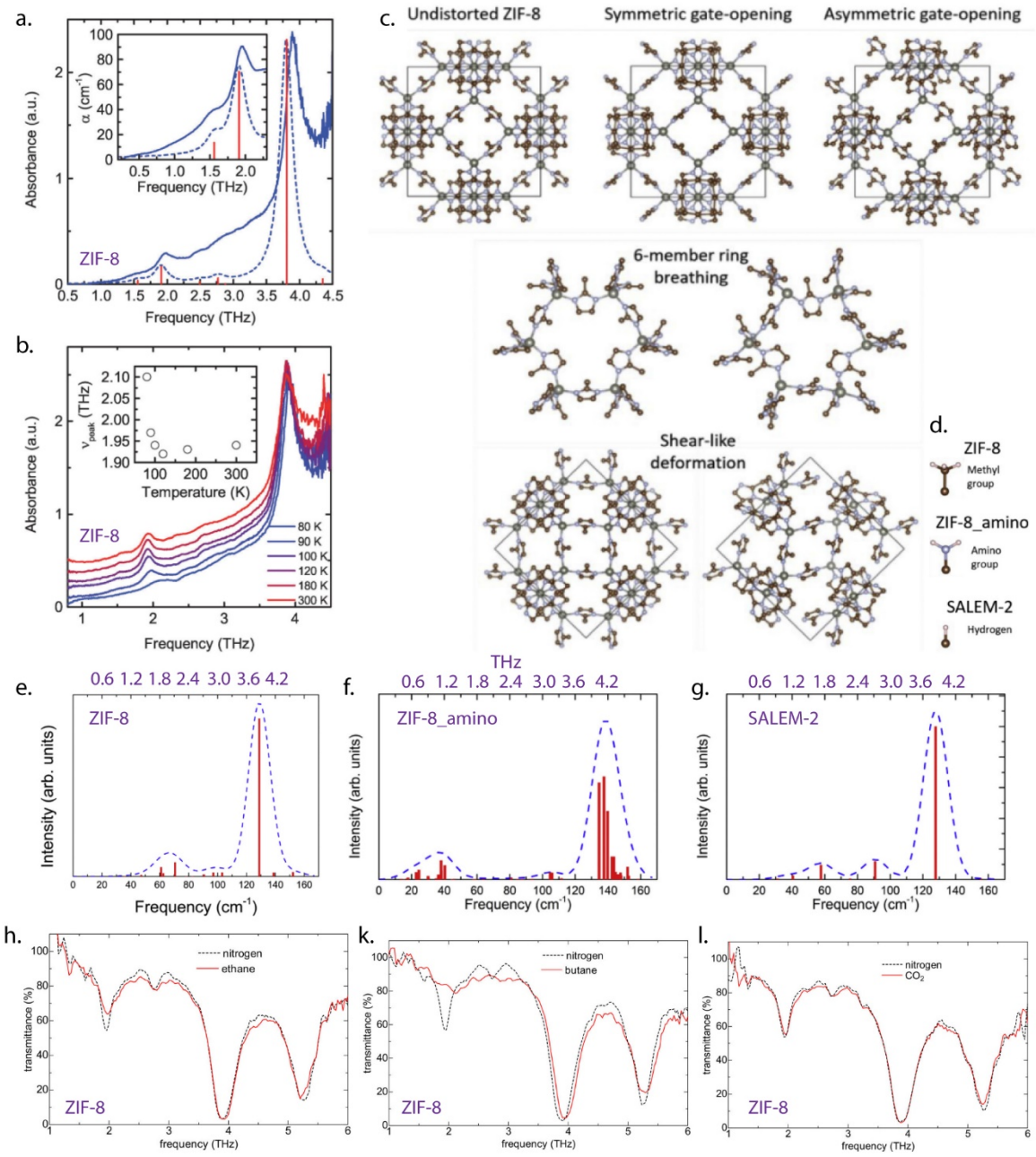

Figure 2.24 (a) Experimental and simulated terahertz spectra of ZIF-8 (inset showing spectrum obtained from a higher concentration pellet) and (b) experimental terahertz spectra of ZIF-8 at increasing temperatures (inset showing the positions of the peak associated with 'gate opening' modes at increasing temperatures); Adapted from Ref.[32], with permission from the Royal Society of Chemistry. (c) Illustrations of the various vibrational modes simulated from ZIF-8, ZIF-8_amino and SALEM-2 structures (linker variants illustrated in (d)) and the (e-g) corresponding simulated terahertz spectra; Adopted from Ref.[39], with permission from Elsevier. (h-l) Experimental terahertz spectra of ZIF-8 in N_2 atmosphere (black) subsequently dosed with ethane, butane and CO_2, respectively; Adopted with permission from Ref.[37]. Copyright 2017 American Chemical Society.

In 2017 Coudert[35] published his work employing quantum chemistry and first-principles molecular dynamics calculations, in which he argued that GO is a gradual effect, which corresponds well to amount of gas adsorbed, and showed that the 'open gate', or HP, is not a meta-stable structure in the absence of adsorbed gas molecules. The results of his dynamic simulations are summarized as histograms of MeIM linker orientations relative to their nominal AP ('closed gate') reported positions, presented in Figure 2.25a,b. These histograms can be thought of as "snapshots" of the dynamically rotating linkers at a point in time, when the angles all the MeIM linkers make to their AP position are measured. Figure 2.25a thus shows that the empty framework is predicted to have linker swing motions that do not go beyond about 15°, while addition of increasing numbers of N_2 molecules shifts the mean orientation of the linkers, in what is assumed (based on discrete data) to be a gradual transition, without significantly increasing the maximum amplitude of linker rotation about the mean position (or librational vibrations after Kolokolov *et al*[31]). This dynamic is in broad agreement with the bulk of the literature discussed above[26-28, 30-31, 34, 37] in terms of the starting and final mean orientations of the linkers, as well as the amount of gas doses at which these orientations are observed. However, the degree to which this transition is 'gradual' is hard to gauge due to the limited number of doses presented: it is difficult to visualize the step sizes in the amount of gas between the individual histograms. The results could therefore be missing details of when this transition is slow or fast with increasing gas dose: such detail could provide better explanations to the step-like adsorption isotherms.

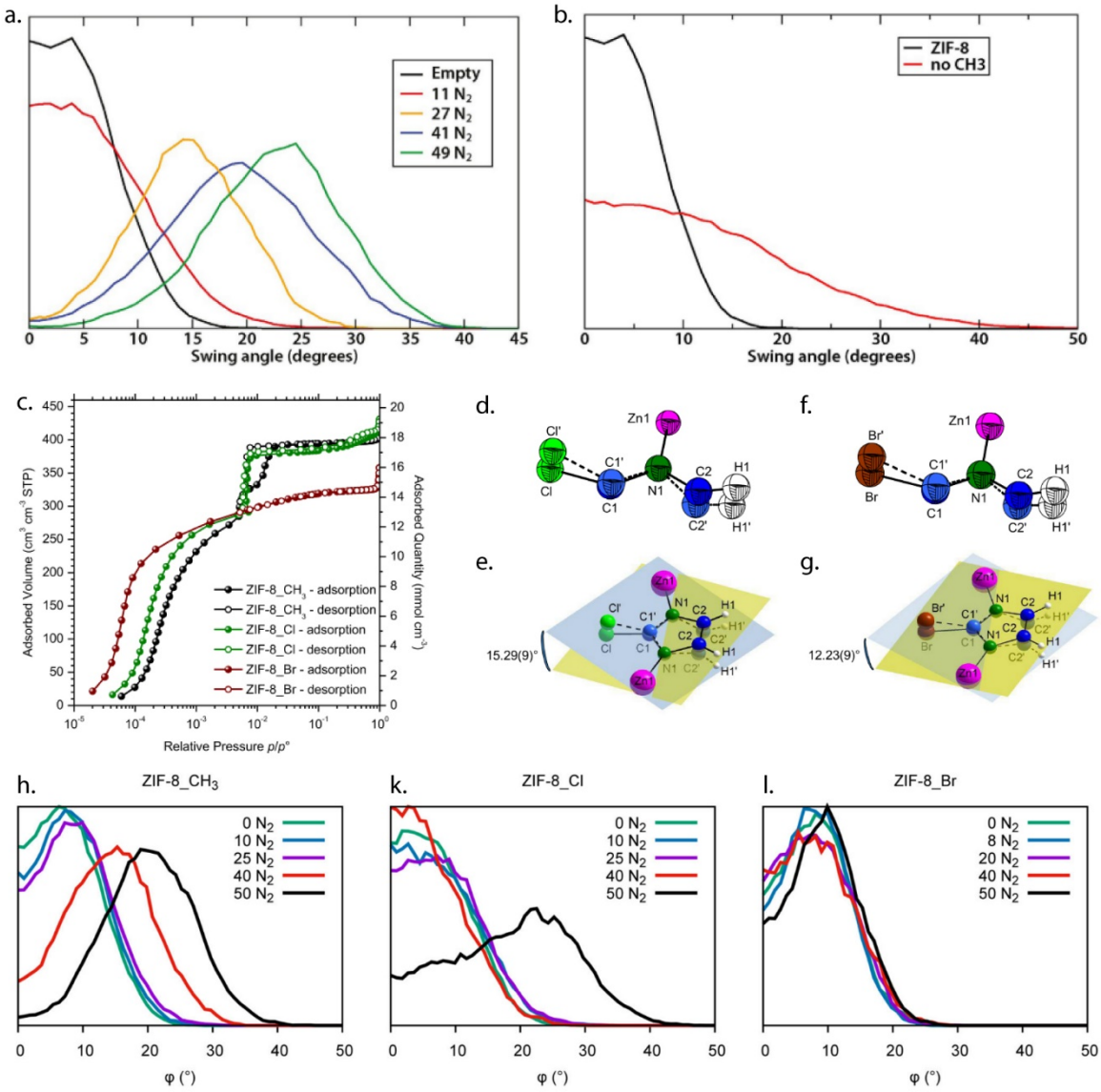

Figure 2.25 Theoretically calculated histograms of MeIM linker 'swing' angles relative to the AP ZIF-8 crystal structure with (a) increasing doses of N2 gas inside the crystals and (b) a comparison of ZIF-8 to a structure with no -CH_3 groups on the MeIM linkers; Adapted from Ref.[35], with permission from John Wiley and Sons. (c) Experimental N_2 adsorption isotherms for ZIF-8 and its variants with Cl and Br atoms on MeIM linkers illustrated in (d-g), together with (h-l) corresponding calculated histograms of MeIM rotation angles as in (a, b); Adapted with permission from Ref.[38]. Copyright 2018 American Chemical Society. (e, g) Illustrate the dihedral angles between disordered IM linkers in the ZIF-8_Cl and ZIF-8_Br structures, respectively.

Coudert's[35] calculations also suggest that chemical modification of the MeIM linker would have a significant effect on its 'swing' motions: Figure 2.25b shows that taking the -CH_3 group away from the MeIM linker significantly increases the amplitude of linker rotations. This latter result appeared to capture the research community's attention, and in 2018 three studies were published on tuning the swing effect. Chaplais *et al*[38] studied gas adsorption behaviours of ZIF-8 with modified linkers, while Moggach and co-workers[40] performed high-pressure single crystal XRD on isostructural ZIF-8 variants, and Formalik *et al*[39] expanded the community's scope of theoretical simulations of vibrational modes to two further modified ZIF-8 structures (as discussed above).

Chaplais *et al*[38] synthesised ZIF-8 variants with Cl (Figure 2.25d-e) and Br (Figure 2.25f-g) atoms substituting the -CH_3 groups on the MeIM linkers and compared their N_2 adsorption characteristics *via* experimental gas adsorption measurements (Figure 2.25c). They also presented revised simulation results after Coudert[35] for all three structures (Figure 2.25h-l). They found that the ZIF-8_Cl variant adsorbs about the same amount of N_2 as ZIF-8 but lacks the second 'step' in the adsorption isotherm, whereas the ZIF-8_Br adsorbs about 4 mmol/cm^3 (about 12 molec/uc) less and has no steps in the isotherms. The corresponding simulations of the linker rotations for the three structures attempt to explain these differences: the shift in mean linker orientation of ZIF-8_Cl (Figure 2.25k) is presented as more sudden than the shift in ZIF-8 (Figure 2.25h), while ZIF-8_Br shows no shift in mean linker position whatsoever. It is worth noting that the simulated behaviour of ZIF-8 presented in these revised results (Figure 2.25h) differs significantly from the previous version (Figure 2.25a), making the claim of a 'gradual' transition more ambiguous since the mean position of linkers in the revised version barely shifts until a dose of 40 molec/uc – a much more 'sudden' change.

Moggach and co-workers[40] performed single-crystal XRD experiments, similar to the original Moggach, Bennett and Cheetham[25] report, to track unit cell volume changes and linker rotation in the isostructural ZIF-8, ZIF-90 and ZIF-65 (see Figure 2.26a-d) under hydrostatic pressure in a 4:1 methanol:ethanol hydrostatic medium. They find that ZIF-8 and ZIF-90 exhibit similar behaviour under stress (see Figure 2.26e,f) – with a swelling of the unit cell and an initial 'closing' (decrease in MeIM angle as defined in Figure 2.26b) and subsequent 'opening' (increase in MeIM angle). The ZIF-65 variant, however, exhibits a steady shrinkage of the unit cell as well as an accompanying 'closure' of the gate. It is important to note here, in light of the dynamic nature of the framework modes, including the linker rotations, that the XRD based techniques provide information on the mean linker positions, and do not capture the extent of the dynamic rotations. Nevertheless, the differences in behaviour of the isostructural ZIFs captured by Moggach and co-workers[40] indicate that the specific chemical structure of the linker plays a crucial role in the behaviour of the structure. The ambiguity around the unit cell expansions and contractions, however, remain as in the case of the original publication[25] discussed above: it is unclear what causes the changes in unit cell volume – the hydrostatic pressure, or the chemical interactions of guest molecules with the framework. The differences in responses of the isostructural ZIFs would suggest that the chemical effects are more important.

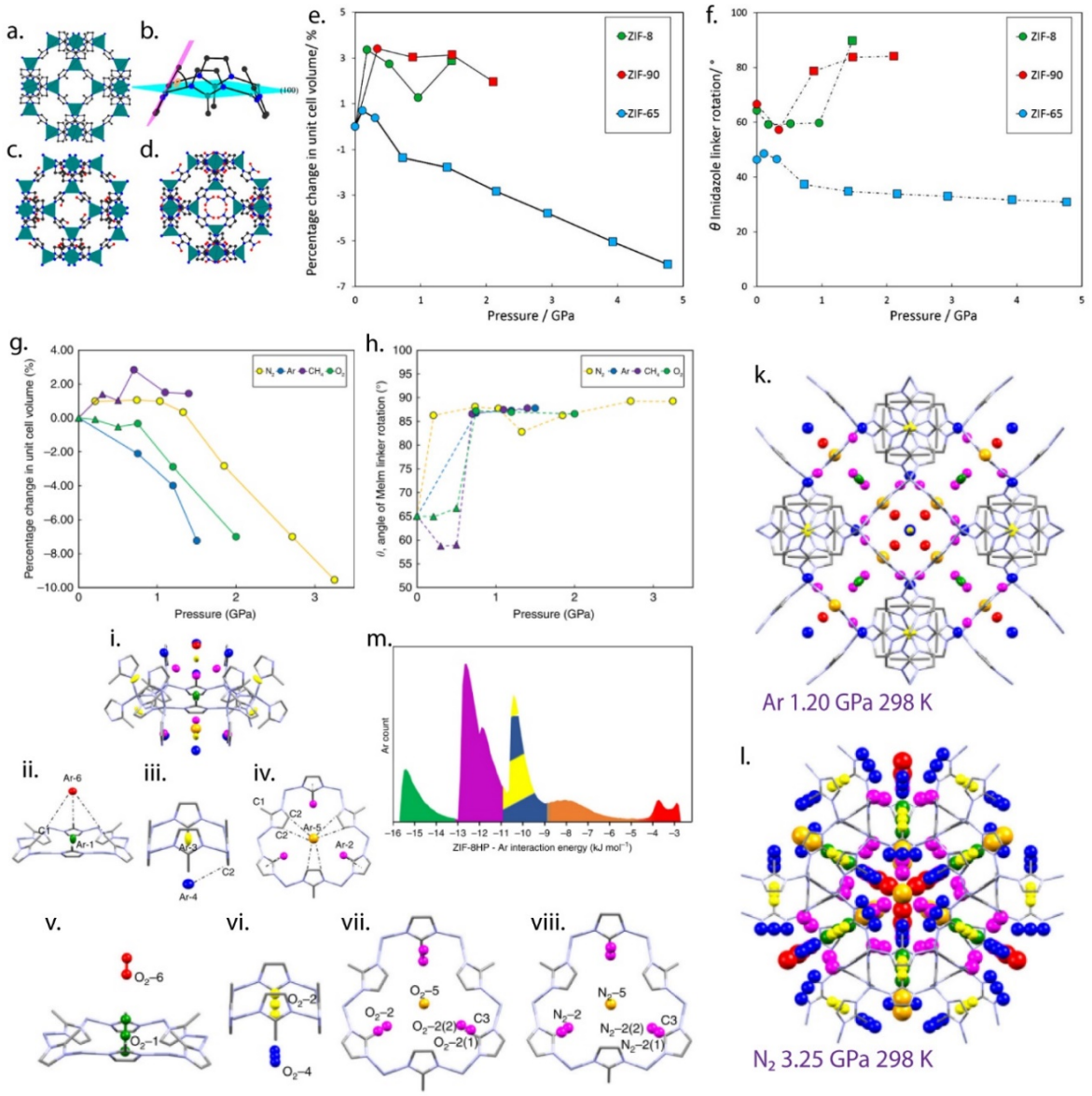

Figure 2.26 (a) ZIF-8 crystal structure, (b) angle of MeIM ring rotation relative to the 100 (hkl) crystallographic plane through a 4MR, crystal structures of the isostructural (c) ZIF-90 and (d) ZIF-65 (Zn tetrahedra, cyan; C, black; N, blue; O, red) and the experimentally obtained data for (e) changes in unit cell volume and (f) MeIM linker orientation in the three isostructural ZIFs under hydrostatic pressure in a 4:1 methanol:ethanol hydrostatic medium; Adapted with permission from Ref.[40]. Copyright 2018 American Chemical Society. (g,h) Unit cell volume and MeIM linker rotation, respectively, under hydrostatic pressure in N_2, Ar, CH_4 and O_2 media obtained from single crystal XRD experiments, which also determined symmetry-independent adsorption sites in the ZIF-8 unit cell for (k) Ar and (l) N_2, with (m) theoretical calculations of Ar energies of interactions with the framework at the different sites yielding their hierarchy: sites 1-6 are labelled and colour coded according to their increasing attractiveness for (k, i-iv) Ar and (l, v-viii) N_2 (O_2) guest molecules. Note

that where sites are labelled as O2 (in v-vi) the N_2 positions are the same. Adapted from Ref.[41] © 2018 Springer Nature Limited, used under a Creative Commons Attribution-Noncommercial license: http://creativecommons.org/licenses/by/4.0/.

In a later publication Moggach and co-workers[41] took important steps towards understanding the specific chemical effects, by crystallographically determining positions of all adsorption sites inside ZIF-8 pores for various gases (N_2, Ar, CH_4 and O_2) *via* high pressure single crystal XRD using those gases as the hydrostatic media. They loaded the gases at 77 K in the respective gases' liquid phases and subsequently let the sealed system warm up to room temperature. The resulting GPa hydrostatic pressure ensures full occupancy of the ZIF-8 pores, facilitating high accuracy of the XRD data. They again tracked unit cell volume changes and linker rotations (Figure 2.26g,h) and found different responses to different gases. This further establishes that the chemical/physical interactions of the guest molecules with the framework are more important than the externally applied pressure. They found that the average linker orientation (Figure 2.26h) reaches the same HP configuration for all gases, and which matches their previously reported values for ZIF-8[25, 40]. More importantly, they were able to determine symmetry independent adsorption sites for the studied gases. Curiously, all gases appeared in very similar sites. Ar sites are shown in Figure 2.26k with a view into 4-MRs (individual site positions are given in Figure 2.26i-iv) and N_2 sites are shown in Figure 2.26l with a view into 6-MRs (individual site positions given in Figure 2.26v-viii). Furthermore, single point DFT calculations provided Moggach and co-workers[41] with estimates of interaction energies of guest molecules with the framework at the different adsorption sites (Figure 2.26m), which they used to build a hierarchy of the adsorption sites. They label the sites 1-6 according the magnitude of interaction energies at those sites, and colour code the various guest molecules according to this hierarchy (Figure 2.26k-m,i-viii). This hierarchy goes against Ania *et al*'s[27] earlier simulations, which yielded no preferential adsorption sites, and led them to seek explanations for stepwise adsorption

isotherms in the polarity of molecules being adsorbed. It could be argued that such distributional order of molecules inside ZIF-8 pores as Moggach and co-workers[41] observe is a result of the forced hydrostatic packing. Nevertheless, the emerging understanding of the significance of linker chemistry[35, 38-40], as well as the drastically different responses of the unit cell swelling and contraction under hydrostatic pressure in different media (Figure 2.26e,g)[40-41], makes it more likely that the hierarchy detailed by Moggach and co-workers[41] is applicable to gas adsorption in typical BET conditions as well as under GPa pressures. This last observation gives overwhelming support to revisiting the community's understanding of ZIF-8 adsorption behaviour, which manifests itself in the step-wise experimental adsorption isotherms.

2.5.3 Conclusion: possibilities of *operando* tunnelling spectroscopy with gas dosing

In conclusion it is important to make an observation regarding the terminology used to describe structural transformations of ZIF-8, which are commonly observed *via* x-ray diffraction techniques,[25, 34, 40-41] as opposed to the intrinsic dynamic vibrational modes of ZIF-8, predicted by DFT simulations[8, 31-33, 39] and observed *via* INS,[8, 33] ^{2}H NMR[31] and terahertz spectroscopy.[32, 37] Specifically the term "gate opening" is loosely used to describe both the structural shifts, manifested in the change of mean linker orientation as detected by XRD, and the rotational motions around those mean positions detected by spectroscopic methods. This duality obscures the dynamic nature of the ZIF-8 structure and hampers understanding of its gas adsorption behaviour, which has important practical implications.

Operando tunnelling spectroscopy with gas dosing of ZIF-8 powder can aid in understanding this complex behaviour of the MeIM linkers, whose tunnelling -CH_3 rotors are extremely sensitive local probes of the potentials around them. The changes in the tunnelling behaviour are an indication of the changes in local potentials, which are induced by the introduction of guest gas molecules. Coupled with simultaneous neutron powder

diffraction (NPD) measurements, such data can provide a rich addition to the understanding of ZIF-8 structural dynamics. This is the subject of Chapter 7.

2.6 Summary and challenges

This chapter takes a slice through the field of MOF research for practical application of the novel materials in the three fields that this thesis engages with: dielectric MOFs, catalytic MOFs and sensing MOFs. The review of this literature provides perspective necessary to carve out a niche for the results presented in the remainder of this thesis and to direct the reader's attention to the subtleties of those results that may not stand out at first but are relevant to the wider context of MOF research.

Section 2.2 of this chapter explores the potential of MOFs as next generation dielectric materials. And it shows that for all the promise that this holds, reliable data on MOF dielectric properties is still rare. The development of an attractive technique to measure those properties is therefore a worthwhile exploit at this stage. Chapter 4 presents one take on such a technique based on reflectance FTIR spectroscopy, which has its advantages and limitations.

Section 2.3 hones in on Pd@MOF composites for the catalytic formation of C-C bonds. Research in this field has already been extremely productive with a myriad of attractive and effective systems reported. The set-back for most of these materials are the complex and therefore expensive production routes necessary for achieving the reported structures. Chapter 5 presents the Pd@OX-1 material developed by this candidate, which appears to have highly competitive catalytic properties, but whose synthesis route is fast and simple.

Section 2.4 outlines the possibility of non-invasive diagnostics of diabetes *via* exhaled acetone sensing. It presents the current best sensors based on the variable resistivity

of metal oxides (MOX) upon exposure to ppm levels of acetone in surrounding atmosphere. The ZnQ@OX-1 material developed by Chaudhari *et al*[1] is then explored as a prime MOF competitor for these MOX sensors, whose performance limits have not been explored so far. Chapter 6 begins to chip at this latter challenge by employing *in situ* Fourier Transform Infrared (FTIR) spectroscopy.

Finally, section 2.5 presents the exotic phenomenon of quantum tunnelling -CH_3 rotors in the architecture of ZIF-8. Such tunnelling rotors have long held promise as sensitive local probes for exploring novel materials. By the standard of the MOF research community, ZIF-8 is far removed from being novel – much has been published on various aspects of its functionality. Indeed, this section traces the finer points of the rich literature on the phenomenon often termed 'gate opening' exhibited by ZIF-8. This review concludes that there are points of confusion when it comes to understanding the structure in 'static' terms, as captured by techniques such as x-ray diffraction, and in 'dynamic' terms, as illuminated by various spectroscopic techniques. This entanglement of understanding makes the topic ripe for disruption, as Chapter 7 attempts to proceed by employing tunnelling spectroscopy together with neutron powder diffraction.

Chapter Three

3 Experimental Methods

3.1 Introduction

Chapter 2 explores the current literature on MOFs in the areas of interest for this thesis and carves out niches that research presented in Chapters 4-7 aims to fill. This chapter in turn details the experimental methods employed in achieving that aim. First point of departure are the materials themselves – their synthesis and verification routes, as well as details of procurement where the commercially available materials were used. It is important to know what these materials look like, so the relevant imaging techniques are detailed next. These are followed by the spectroscopic techniques utilised to discover many of the phenomena that constitute the novel findings in this thesis. Fourier transform infrared spectroscopy, inelastic neutron scattering, and x-ray absorption spectroscopy are given particular attention due to their importance for this thesis. Exploration of Pd@OX-1 catalytic potential is then elucidated, followed by the details of various computational methods employed in calculating material properties, as well as handling and interpreting the experimental data.

3.2 Materials preparation and characterisation

This section first details the synthesis routes taken to produce OX-1 and its composites – Pd@OX-1 and ZnQ@OX-1. It then gives details of procured materials MIL-53(Al) and ZIF-8, and the method for preparing MOF pellets. Finally, it details the crucial X-Ray Diffraction (XRD) technique for sample validation and characterisation carried out on two types of instruments during the course of this study. Considerations regarding gas adsorption measurements conclude the section.

3.2.1 OX-1 synthesis procedure

3 mmol of benzene-1,4-dicarboxylic acid (BDC) are dissolved in a mixture of 6 mmol of Et_3N in 3 mL of DMF. This mixture is then combined with 1.5 mmol of $Zn(NO_3)_2$ in 4 mL of DMF, at which stage a gel is observed and OX-1 crystals are formed. The gel is then transferred to a 50 mL centrifuge tube, with 43 mL of DMF added in the process. This mixture is sonicated for 10 min to break down the gel and ensure good exfoliation of the OX-1 nanosheets. It is then centrifuged for 5 min at 8000 rpm to separate the nanosheets from solvent containing excess linker and Et_3N. The crystals are then washed twice in acetone and dried overnight at 100 °C (yield ~500 mg).

3.2.1.1 Pd@OX-1

To incorporate 0.1 – 1 wt.% of Pd into OX-1, 5-50 mg of the precursor $Pd_2(dba)_3$ complex [dba = dibenzylideneacetone] is dissolved in 2 mL of DMF and added to 3 mmol of benzene-1,4-dicarboxylic acid and 6 mmol of Et_3N in 3 mL of DMF. This mixture is then combined with 1.5 mmol of $Zn(NO_3)_2$ in 2 mL of DMF, at which stage a gel is observed and OX-1 crystals are formed. The gel is then transferred to a 50 mL centrifuge tube, with 43 mL of DMF added in the process. This mixture is sonicated until it loses its pink colour, becoming grey-greenish. It is then centrifuged for 5 min at 8000 rpm, to separate the light grey crystals from the light marsh solution of dba and excess BDC in DMF. The crystals are

then washed twice in acetone and dried overnight at 100 °C (yield ~500 mg). The colour change from pink to green-grey during the first sonication step is evidence of dissociation of the Pd complex. During this step Pd atoms break free of the $Pd_2(dba)_3$ complex and bind onto OX-1. Figure 3.1 illustrates the above described synthesis route up to the washing steps.

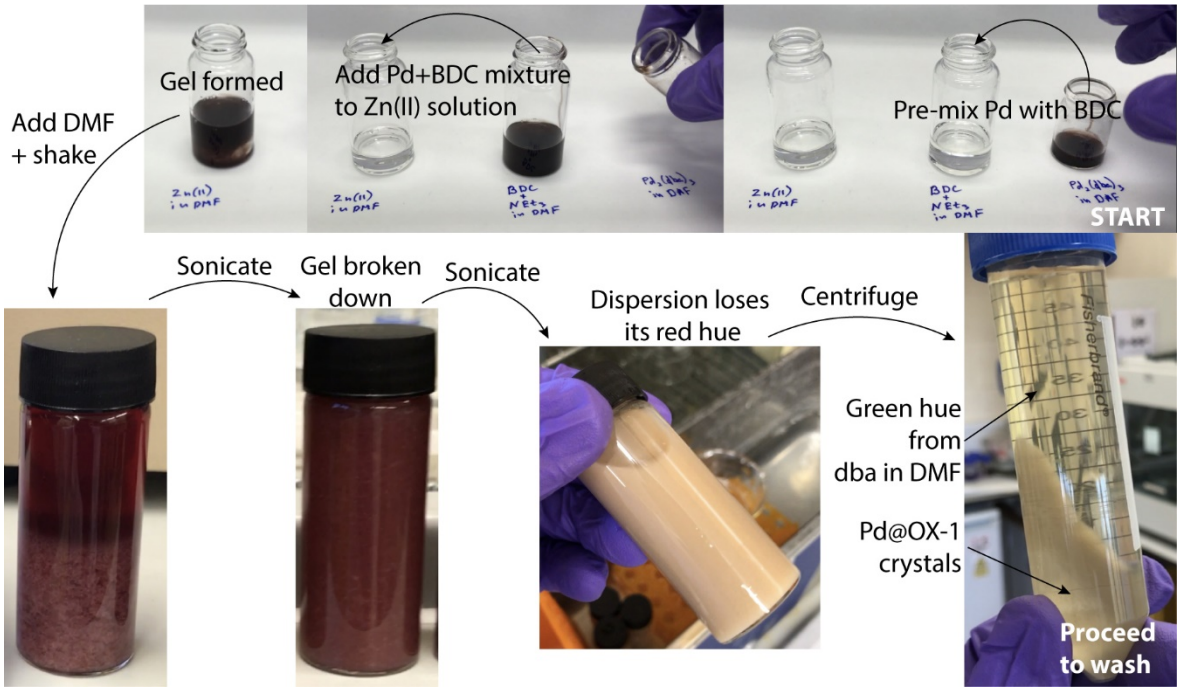

Figure 3.1 Pd@OX-1 synthesis route illustrated.

3.2.1.2 ZnQ@OX-1

To incorporate ZnQ into OX-1, 0.5 mmol of $Zn(NO_3)_2$ and 1.0 mmol of 8-hydroxyquinoline (8HQ) are dissolved in 1 mL of DMF and added to the already prepared BDC solution, which contains 3 mmol of benzene-1,4-dicarboxylic acid (BDC) dissolved in a mixture of 6 mmol of Et_3N in 3 mL of DMF. This mixture is then combined with 1.5 mmol of $Zn(NO_3)_2$ in 2 mL of DMF, at which stage a gel is observed and ZnQ@OX-1 crystals are formed. The gel is then transferred to a 50 mL centrifuge tube, with 43 mL of DMF added in the process. This mixture is sonicated for 10 min to break down the gel and ensure good exfoliation of the ZnQ@OX-1crystals. It is then centrifuged for 5 min at 8000 rpm, to separate the crystals from the yellow solution containing excess ZnQ and BDC in DMF. The

subsequent washing steps are important and determine whether the resulting material will possess sensing functionality. The crystals need to be washed with DMF until the residue solvent loses its yellow hue, indicating that all ZnQ that has not been incorporated into OX-1 pores has been washed away. This may take as many as 7 wash cycles with DMF. (Sometimes the material retains its functionality after as few as 2 washes with DMF, but this is not guaranteed.) The crystals are then washed once with MeOH and dried at ambient conditions (under a fume hood) for 24 hours. The material is sensitive to applied heat and vacuum, but the investigations into those mechanisms have not yet yielded systematic understanding of the material's behaviour. So far, therefore, the material has been simply dried at ambient conditions before being used for acetone sensing experiments.

To prepare ZnQ@OX-1 for sensing experiments, a small amount (typically ~10mg) of powder is dispersed in 3 ml of Hexane, whose large molecules do not enter the pores. This dispersion is then drop cast onto a piece of filter paper (or optical windows for FTIR experiments, as discussed in section 3.4.1.2). The Hexane quickly evaporates, and the material becomes active. Figure 3.2 illustrates a quick procedure to validate the acetone sensing functionality of the prepared ZnQ@OX-1.

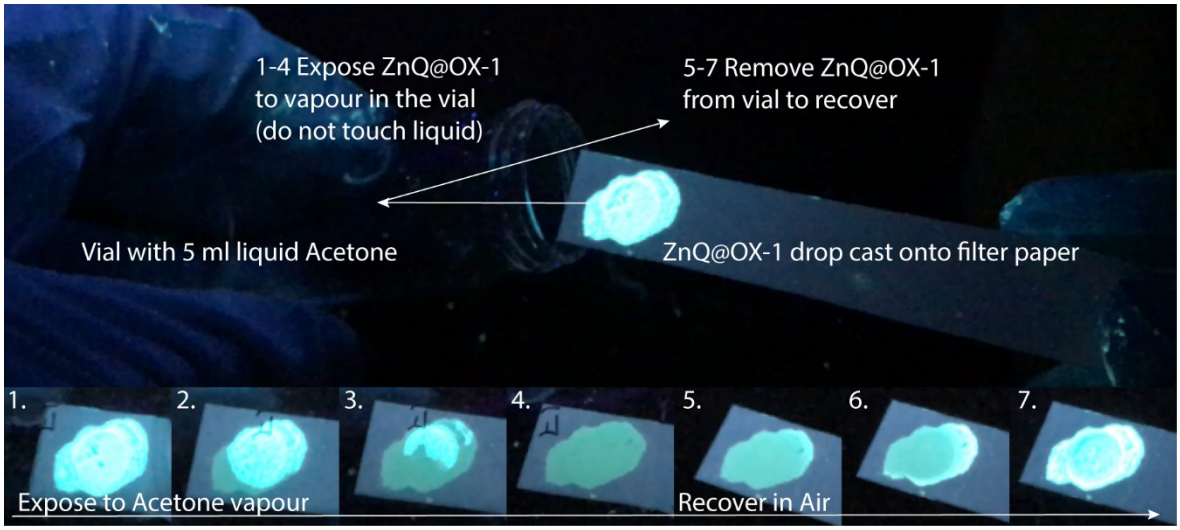

Figure 3.2 Stop-frame illustration of ZnQ@OX-1 acetone sensing test under UV.

3.2.2 Purchased materials

3.2.2.1 MIL-53(Al)

Activated MIL-53(Al) polycrystalline powder (Basolite A100) was purchased from Sigma-Aldrich and used as received in preparation of pellets for reflectance FTIR measurements, as described below. For further investigations of its behaviour under uniaxial stress in a pellet press, detailed in section 4.2, the MIL-53(Al) powder was first activated at 315 °C for 20 h to obtain purely large pore (LP) phase powder.

3.2.2.2 ZIF-8

ZIF-8 polycrystalline powder (Basolite Z1200) was purchased from Sigma Aldrich. For a typical sample 1.2 g of ZIF-8 were loaded into a perforated Al sachet and evacuated at 200 °C overnight to ensure the sample was desolvated prior to the *operando* gas loading experiments at the OSIRIS instrument of ISIS neutron source described in Chapter 7.

3.2.3 Pellet pressing

MOF pellets were pressed under uniaxially applied pressure using a 13 mm diameter dye in a Specac Manual Hydraulic Press with loading capacity up to 25 tonnes (t). It is important to have a well homogenised powder, which is evenly distributed inside the dye before pressing the pellet. Otherwise stress concentrates in regions with higher amounts of powder. This happens to a varying degree for all powder pellets and serves as a reminder that the stress applied in this way is by no means hydrostatic. A very rough rule of thumb observed in this work is that 100 mg of MOF powder produces a 13 mm diameter pellet with thickness of about 1 mm. This, of course, varies with MOF density and crystal size, and exact density of each pellet must be measured *ex post*.

3.2.4 X-Ray Diffraction (XRD)

X-Ray Diffraction (XRD) is an essential tool for working with MOF materials. It is the simplest, fastest way of analysing the crystal structure of a powder or pellet MOF sample. Two types of instruments were employed in the course of all the work presented in this thesis: Rigaku MiniFlex and Xenocs NanoInXider. The MiniFlex is a simpler system convenient for powders, while the InXider is a more sophisticated system most suitable for pellets because the measurements are done in transmission. Figure 3.3 illustrates the principle behind the two machines. While the InXider provides an added bonus of small angle x-ray scattering (SAXS) data, its resolution for wide angle x-ray scattering (WAXS = XRD) is not as good as can be achieved in the MiniFlex machine. Given a known crystal structure, XRD patterns are easily simulated and compared to experimental data, providing a way of inferring structural changes in the sample. The subsections below give details of experimental conditions used for the two machines and of software used for simulating the XRD patterns.

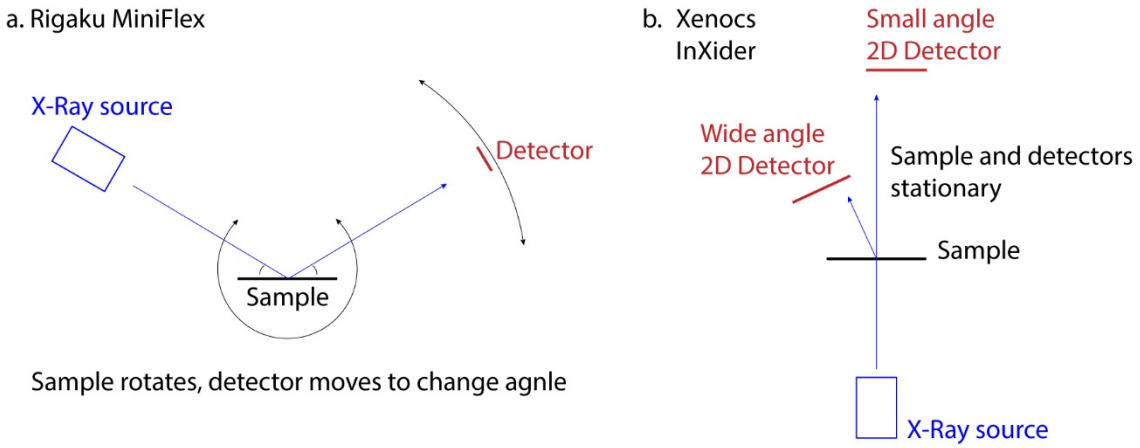

Figure 3.3 Schematics of the two types of XRD machines used in this thesis.

3.2.4.1 Rigaku Miniflex

Powder X-ray diffraction (PXRD) patterns were collected using a benchtop Rigaku MiniFlex diffractometer with a 1D scintillation counter detector and a Cu Kα X-ray source. Samples were loaded into a 20×20×0.5 mm sample holder and weighed before measurement. The measurements were carried out with a step size of 0.02° at a speed of 1°min^{-1}. The patterns were then normalised by the mass of the samples, so that patterns collected using the same holder and settings could be compared quantitatively.

3.2.4.2 Xenocs NanoInXider

All pellets were characterized *via* X-ray scattering in transmission mode using the Xenocs NanoInXider (R53 Materials Characterization Laboratory, ISIS) equipped with two 'Pilatus 3' 2-D detectors for SAXS and WAXS. All X-ray spectra were collected for 300 s under high-resolution beam settings: 400 μm spot size on sample and 15 Mphs^{-1} typical flux. The physical density of each pellet was determined by weighing each pellet and dividing this quantity by its nominal volume (dimensions *via* a micrometre). The collected X-ray scattering intensities were normalized by density×thickness of the corresponding pellets, making the obtained patterns comparable quantitatively when collected using the same settings.

3.2.4.3 Simulating XRD patterns

CrystalMaker and CrystalDiffract software version 9 provide functionality to read in CIF crystal structure files and simulate the powder XRD and NPD patterns given properties of the incident x-rays or neutrons. It also allows to adjust the volume of the unit cell of a given crystal structure and observe the resulting shifts in the diffraction patterns. These changes in unit cell volume can then be expressed as a percentage.

3.2.5 Gas adsorption and BET

Brunauer–Emmett–Teller (BET) theory explains the adsorption of gas molecules onto solid surfaces and is the basis for the technique used to estimate the specific surface areas of porous solids like MOFs. It has been a well-established method for characterizing MOF materials for more than ten years now[101] and detailed treatments of pitfalls to be avoided when treating gas adsorption data are available.[102] Where gas adsorption was employed in this thesis, N_2 and Ar isotherms were obtained at 77 K using the Quantachrome Autosorb iQ-Chemi machine according to reported best practices.[102] For ZIF-8 adsorption isotherms, the data was converted from cubic centimetres of gas per gram to molecules of gas per unit cell of ZIF-8 using a value for ZIF-8 density simulated in CrystalMaker software version 9, using the AP model of ZIF-8 reported by Moggach *et al*[25].

3.3 Imaging techniques

Four main imaging techniques were employed in the course of the work presented in this thesis, dictated by the need to study micro- and nano-scale structures of the materials investigated. These are illustrated schematically in Figure 3.4.

The go-to technique to begin understanding a material that was synthesised in the lab or acquired from outside sources is scanning electron microscopy (SEM), which achieves a wide range of magnification and is therefore ideal for getting a sense of both the sub-micron features of crystals and for looking at a large number of those crystals for some sort of statistically significant understanding of the sample.

Transmission electron microscopy (TEM) is a more challenging technique, which requires the sample to be sufficiently thin for the electron beam to penetrate all the way through. However, TEM achieves resolution on the nanometre scale, allowing for imaging of very fine features such as nanoparticles inside of or on MOF surfaces (such as in

Chapter 5). TEM, however, does not allow for as wide a view of a sample as SEM and so needs to be used as a complementary method.

Atomic Force Microscopy (AFM) is competitive with TEM in terms of achievable resolution but provides a topographical image of the sample surface. This is useful, for example, in measuring the thickness of MOF nanosheets. The limitation lies in its constrained spatial range – it is even more limited than TEM in terms of looking at samples larger than a few microns wide.

The Alicona Infinite Focus profilometer does away with this spatial constraint at the expense of resolution. Like any optical microscope it is limited by the diffraction limit of light. However, its images are highly advantageous for understanding the larger scale profiles, such as those of MOF pellets in Chapter 4.

When used together, the above four techniques provide a complete picture of MOF features spanning the micro- and nano-scales. Specific experimental details for each of the techniques used are given below.

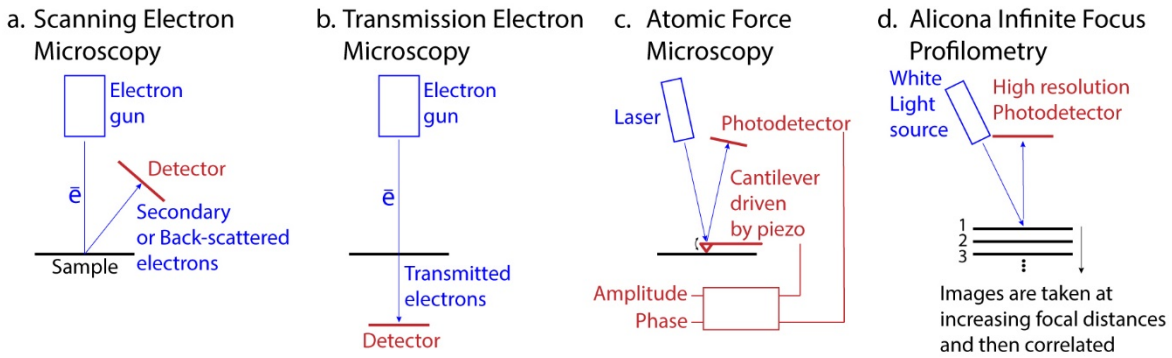

Figure 3.4 Schematics of the imaging techniques employed in this thesis.

3.3.1 Scanning Electron Microscopy (SEM)

SEM images of MIL-53(Al) powder were acquired on a Carl Zeiss Merlin Scanning Electron Microscope with a field emission gun and back-scattered electron detector at

10 mm working distance. The powder was dispersed in ethanol and drop cast onto polished Al stubs. The samples were carbon coated in an Ar atmosphere.

SEM images of MIL-53(Al) pellet surfaces were acquired on a Carl Zeiss Evo LS15 VP-Scanning Electron Microscope with a secondary electron detector, 15 kV accelerating voltage and 8 mm working distance. The pellets were not coated before imaging to retain their dielectric properties.

SEM images of Pd@OX-1 samples were also acquired on a Carl Zeiss Evo LS15 VP-Scanning Electron Microscope with a secondary electron detector, 15 kV accelerating voltage and 8 mm working distance. The crystals were sampled before the final centrifugation step of the synthesis and drop cast onto polished Al stubs. The samples were gold coated with a sputter coater in an Ar atmosphere.

3.3.2 Transmission Electron Microscopy (TEM)

Before TEM observations the samples of Pd@OX-1 were deposited on 3 mm carbon-coated copper grids (200 mesh) from suspension in isopropyl alcohol. Samples morphology was studied using a Hitachi HT7700 transmission electron microscope. Images were acquired in bright-field TEM mode at 100 kV accelerating voltage.

3.3.3 Atomic Force Microscopy (AFM)

AFM images of MIL-53(Al) pellet surfaces and Pd@OX-1 nanosheets were obtained on the Veeco Dimension 3100 instrument with Tap300Al-G tapping mode AFM probes. The MIL-53(Al) pellets were imaged as prepared and as used for the dielectric measurements without any surface modifications. The Pd@OX-1 crystals were sampled before the final centrifugation step of the synthesis, sparsely dispersed in acetone and drop cast onto polished Al stubs.

3.3.4 Alicona InfiniteFocus Profilometer

The profiles of MIL-53(Al) were acquired on an Alicona Infinite Focus Profilometer with a 50× objective aperture. Three different measures of surface roughness of the pellets at two different magnifications of 20× and 50× were taken to make sure the different lenses and calculation routes did not affect the measurements. The vertical resolution achieved by the instrument is 20 nm. The pellets were imaged as prepared and as used for the dielectric measurements without any surface modifications.

3.4 Spectroscopic techniques

Various forms of spectroscopy – the study of a material's interaction with a source of varied radiative energy – are instrumental in studying novel materials. This section goes to some lengths to provide understanding of the principles behind, and to detail specific experimental conditions used in spectroscopic techniques employed in this thesis based on infrared light, neutrons and x-rays as sources of the radiative energy.

3.4.1 Fourier Transform Infrared (FTIR) spectroscopy

Fourier transform infrared (FTIR) spectroscopy is an extremely useful technique because its spectral range encompasses a large proportion of molecular vibrational modes that are found in chemical compounds. For MOFs it can be a rich source of information when coupled with *ab initio* predictions of those vibrational modes. FTIR spectra are acquired relatively quickly due to the broadband nature of signal modulation, which is schematically illustrated in Figure 3.5. Before reaching the sample, the infrared beam from the source enters a device called a Michelson Interferometer. In its simplest form this consists of a beam splitter and two mirrors – one fixed and one oscillating. The beam splitter, as the name suggests, splits the beam in two, sending one part of the beam to the fixed mirror and the other to the moving mirror. The moving mirror, by changing the distance the beam has to travel, introduces a delay in its phase which is continuously adjusted due to the

mirror's movement. The two parts of the beam then travel back towards the beam splitter where they are recombined. But the varying phase shift of one half of the beam relative to the other leads to various patterns of constructive and destructive interference in the recombined beam. These patterns are dependent on the optical path difference (OPD) introduced by the moving mirror, and produce a signal often called an interferogram, which is recorded by the detector.

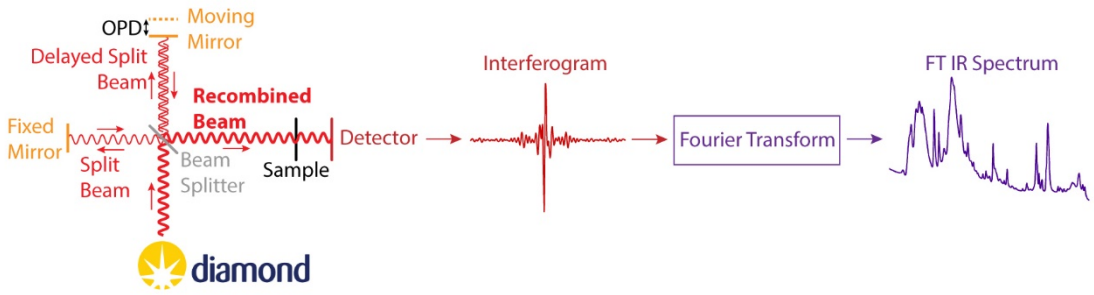

Figure 3.5 FTIR spectroscopy: behind the scenes.

The interferogram is then transformed into an IR spectrum by means of a Fast Fourier Transform (FFT) – a computationally inexpensive special case of the more general analytical Fourier transform. The FFT routine puts certain constraints on the way data is recorded and processed. More important considerations in practical terms, however, are those of background interferograms to which sample interferograms are compared. The incident beam has varying intensity at the different frequencies contained within the beam. This is due to the nature of the source used and the optics between the source and the sample. When a synchrotron is used as a source this is especially important because parts of the beam come out of the optics with more power than others and the beam may vary due to a variety of factors. The following subsections provide specific experimental details for the specular reflectance FTIR measurements, from which dielectric properties were calculated in Chapter 4 and Chapter 5, and for the transmission FTIR measurements used to study ZnQ@OX-1 acetone sensing behaviour in Chapter 6.

3.4.1.1 Specular Reflectance FTIR for Dielectric measurements

The specular reflectance experiments were conducted at Beamline B22 MIRIAM in the Diamond Light Source synchrotron. Specular reflection measurements were carried out in a Bruker Vertex 80V FTIR interferometer, equipped with the Pike Technologies VeeMAX II variable angle specular reflectance accessory (Figure 3.6).

Synchrotron IR reflectivity spectra were collected on samples of pressed-powder pellets (diameter = 13 mm, thickness ~1 mm) prepared under uniaxial compression varied from 0.1-10 ton (see section 3.2.3). Specular reflection was obtained at an angle of 30° from the normal to the pellet's surface, where IR spectra were collected with a resolution of 2 cm^{-1} and 512 scans per spectral scan. Vacuum was pumped to better than 10^{-5} bar and maintained at room temperature (21°C). The synchrotron far-IR (FIR) measurements were performed for the spectral range 1000-0 cm^{-1} while the mid-IR (MIR) for the range 10000-0 cm^{-1}. It is noted that the useable data reached as low as 40 cm^{-1}. The background spectra were collected by measuring the reflectance from a mirror once before the FIR measurements and once before the MIR measurements.

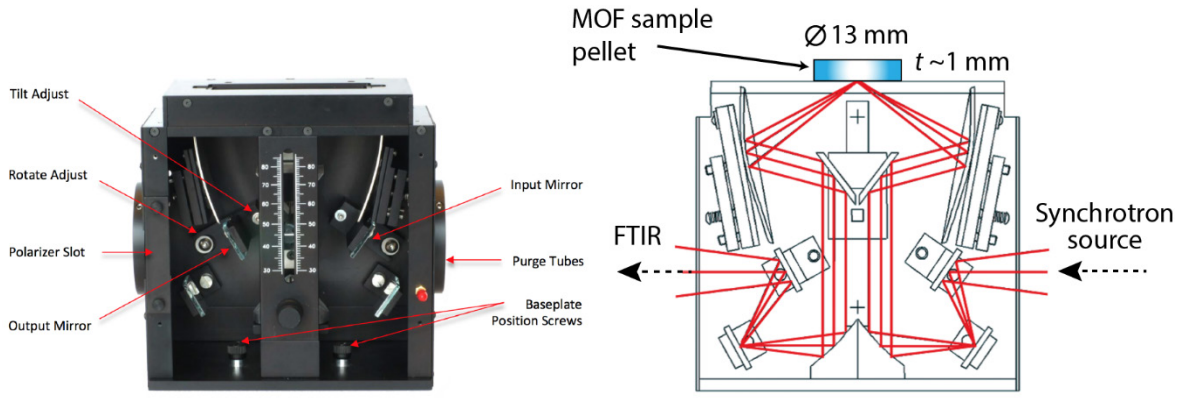

Figure 3.6 a) VeeMAX II variable angle specular reflectance accessory, and (b) its optical diagram. Adapted from [103].

3.4.1.2 Transmission FTIR for in situ acetone sensing

The transmission FTIR experiments were also conducted at B22 MIRIAM. A flow cell was used for *in situ* gas flow acetone dosing experiments. To allow for broadband measurements, this called for special high-density polyethylene (HDPE) windows and an Al disc spacer to be made. HDPE was chosen due to its transparency for IR in the full spectral range of these experiments, despite being opaque to visible light (which would be a limitation in an experiment under an IR microscope). HDPE also allows the use of an Al spacer, which would be problematic with brittle crystal windows. Figure 3.7a shows schematic views of the windows and spacer assembly of the sample environment. ZnQ@OX-1 samples were drop cast onto the bottom HDPE window from a dispersion in Hexane (as described in section 3.2.1.2). The thickness of the sample layer had to be experimented with because the poor compatibility between crystals and Hexane meant that the dispersion was not homogenous, and the crystals sank rapidly. This resulted in a hit-and-miss process, where the thickness of the sample could only be found suitable or otherwise once the measurement was started (if it wasn't, a new sample was prepared).

Figure 3.7b shows a photo of the Harrick gas flow cell used in these experiments, and Figure 3.7c shows the septum assembly through which the gas from mass flow controllers was dosed with liquid Acetone using an SGE 50 µl gas chromatography syringe. Gas was initially flowed at 1 cubic centimetre per minute (ccpm), which resulted in very slow, but well time-resolved experiments. The flow was then increased to 5 ccpm, and once it was verified that this did not disturb the sample, this volumetric flow was used for the remainder of the experiments. The sample chamber volume was approximately 50 µl, which meant that at 5 ccpm the environment in the chamber renewed at a rate of 100 min^{-1}. During runs with an empty sample environment, the cell was flushed at rates as high as 100 ccpm to speed up extraction of Acetone from the system.

IR spectra were collected with a resolution of 2 cm^{-1}. The number of scans per spectral scan varied. For far-IR (FIR) measurements 128 scans were initially collected per spectral scan, which was then reduced to 64 scans to improve time resolution. Similarly for mid-IR (MIR) 64 scans were initially used, which was reduced to as low as 32 scans. Vacuum was pumped to better than 10^{-5} bar and maintained at room temperature (21°C). The synchrotron far-IR (FIR) measurements were performed for the spectral range 1000-0 cm^{-1} while the mid-IR (MIR) measurements were done using a Globar IR source for the range 10000-0 cm^{-1}. Curiously, when a highly focused beam (used for micro FTIR experiments) is not required, the Globar source provides more power than the synchrotron, and has the added benefit of not contingent on the synchrotron beam being available to users. The background spectra were collected through the same flow cell assembly, with gas flowing through the cell, but without a sample. Care was taken to take a background before each new sample because the dosing runs took a long time – on the scale of a few hours each.

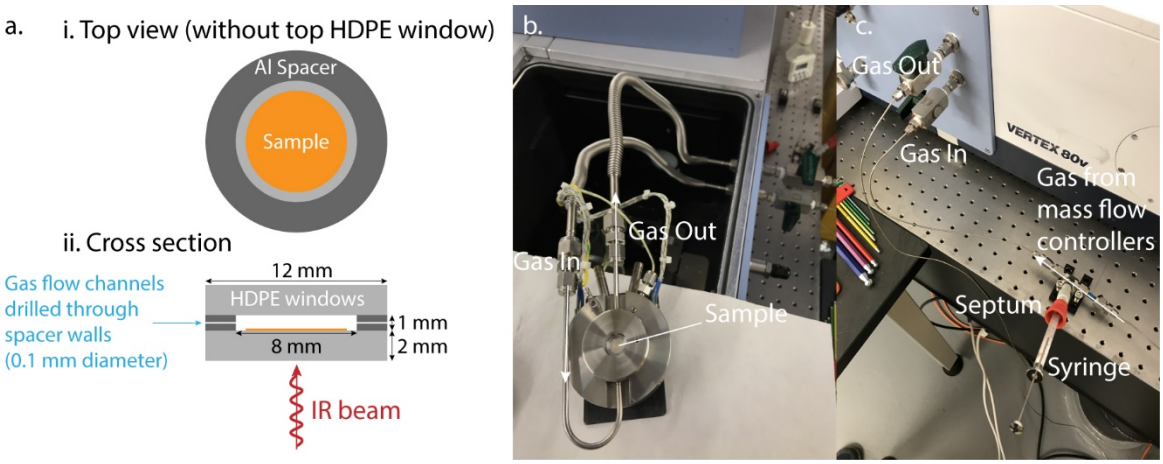

Figure 3.7 Gas flow cell for *in situ* FTIR: a) schematics of the sample environment assembly drawn to scale; b) photograph of the flow cell with the top off, showing the gas tube connections and sample position (the cell has heating and cooling jackets, but these were not used); c) photograph of the septum assembly through which the gas flow was dosed with liquid Acetone using a syringe.

3.4.2 Neutron Spectroscopy

Inelastic Neutron Scattering (INS) spectroscopy is a technique that probes atomic and molecular motions, and which does not suffer from optical selection rules of FTIR spectroscopy. It is also a highly penetrating technique, requiring large amounts of sample – on the order of 1 g for MOF materials. It is especially sensitive to hydrogen motions because hydrogen atoms have large neutron cross sections – a property that determines how likely a neutron is to scatter off a given atom.

Figure 3.8 illustrates the basic principle of INS. A beam of incident neutrons with momentum $\mathbf{k}_i$ and wavelength ω_i hits a sample, neutrons exchange momentum with atoms inside the sample, and travel towards the detector with their final momentum $\mathbf{k}_f$ and wavelength ω_f. These quantities are recorded by various detectors around the sample in the form of time of flight data (time it takes a neutron to travel a fixed distance). This data is then reduced to the scattering function $S(Q, \omega)$, where Q is momentum transfer and which is also a function of energy since $E = \hbar\omega$. Instrument geometries determine their spectral range and resolution. TOSCA has a very wide spectral range, but lower resolution than OSIRIS. The latter's detector arrays, on the other hand, in addition to its high resolution, give it the ability to convert the time of flight data to d-spacing, meaning that it functions simultaneously as an INS and a diffraction instrument. The following subsections provide experimental details specific to TOSCA and OSIRIS.

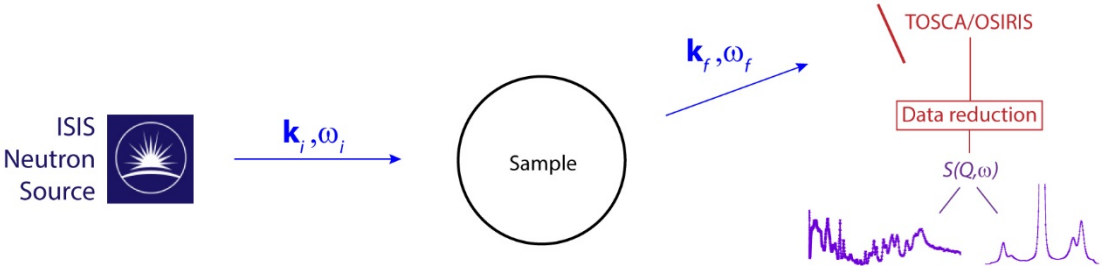

Figure 3.8 Inelastic Neutron Scattering: the basics.

3.4.2.1 Inelastic Neutron Scattering on TOSCA

INS measurements of Pd@OX-1 samples were performed using the TOSCA spectrometer[104-105] at the ISIS Pulsed Neutron and Muon Source. The high-resolution ($\Delta E/E \sim 1.25\%$) and broadband (0 – 4,000 cm^{-1}) spectra of each sample (~1 g) were collected at approximately 10 K. TOSCA is an indirect geometry time-of-flight spectrometer where a pulsed, polychromatic beam of neutrons collide with the sample at a distance of ~17 m from the source. The scattered neutrons are then Bragg-reflected by a pyrolytic graphite analyser, and higher-order reflections beyond (002) are suppressed by a cooled (T < 50 K) beryllium (Be) filter, to selectively analyse neutrons of a consistent final energy. Therefore, neutrons with a final energy of approximately 32 cm^{-1} (~1 THz) are passed towards the ^{3}He detector bank. The detector array consists of a total of ten banks each having thirteen ^{3}He tubes with an effective length 250 mm. Five banks are located in the forward direction (scattering angle ~45°) and five in the backwards direction (~135°).

The use of a low (fixed) final energy translates into a direct relationship between energy transfer (E_T, cm^{-1}) and momentum transfer (Q, $Å^{-1}$) such that $E_T \approx 16Q^2$. Energy transfer and spectral intensity i.e. $S(Q, \omega)$ can then be obtained using the Mantid software.[106] A disc chopper is positioned to prevent frame overlap at a distance of 9.455 m from the moderator centre. The sample was wrapped in a 4×4 cm^2 aluminium foil sachet and placed in a 2 mm spaced stainless steel cell. To reduce the impact of the Debye–Waller factor on the observed spectral intensity the sample was cooled to approximately 10 K by a closed cycle refrigerator, and the spectra were recorded for 4-6 hours.

The neutron guide upgrade of the TOSCA spectrometer was completed in 2017, which has increased the neutron flux at the sample position by as much as 82 times.[107] This enables faster INS measurements and the use of a smaller sample mass.

3.4.2.2 Inelastic Neutron Scattering and Neutron Powder Diffraction on OSIRIS

The high-resolution INS and NPD data for ZIF-8 were collected on the OSIRIS spectrometer at the ISIS Pulsed Neutron and Muon Source. OSIRIS is a high resolution (25.4 μeV) indirect-geometry neutron spectrometer with long-wavelength diffraction capabilities. The secondary spectrometer sits at ~34 m from a 25 K liquid hydrogen cooled moderator. Optimised for low-energy, high-resolution inelastic neutron-scattering studies, OSIRIS uses a broadband of incident wavelengths which are Bragg-scattered from a crystal analyser array following interaction with the sample. For the INS experiment the (002) plane of the pyrolithic graphite analyser was used defining the single final energy of detected neutron as 1.84 meV. The installed cooled beryllium filter between the sample and the analyser suppressed higher order reflections of the graphite analyser. Due to utilising a pulsed neutron source, time-of-flight methods are used to determine energies at each particular scattering angle. Using the repetition rate of 16 Hz, which is one third of the repetition rate of ISIS target station I, an energy transfer range of 20 meV (~5 THz) was achieved. The scattered neutrons were detected in an angular range corresponding to momentum transfer range 0.42-1.82 $Å^{-1}$. the scattered data from all Q values in this range were summed up to produce the INS spectrum. The diffraction data were obtained from the instrument as a by-product of the spectroscopy experiments from diffraction detectors in its backscattering geometry. It's resolution amounts to $\Delta d/d = 2.5 \times 10^{-3}$, where Δd is the resolution in d-spacing.[108]

The sample was loaded into a cylindrical vanadium can connected to a gas handling system. N_2 and Ar gas loading was done volumetrically at 77 K. The sample was degassed at 10^{-7} bar between gas dosing experiments. At each gas dose the system was allowed to equilibrate for at least 30 min.

3.4.3 X-Ray Absorption Spectroscopy (XAS)

XAS is perhaps the technique with the highest resolution of material structure on the scale of single atoms. It probes the local environments of metal atoms in a sample, like the environments of individual Pd atoms in a Pd@OX-1 MOF system – the subject of Chapter 5. Figure 3.9 gives an overview of the principle behind XAS and the workflow that is involved in the process of using it for understanding a material's structure. The following discussion aims to give a very brief overview of the difficulties involved and possibilities to be realised. For an excellent practical manual the reader is referred to the book by Calvin[109].

When an x-ray of the right energy is incident on a metal atom, a photoelectron from the 1s orbital of the atom is emitted. This photoelectron propagates out of the atom as a spherical wave. When this photoelectron wave meets a neighbouring atom, there is a probability that it will scatter off that neighbour elastically. When it does, it travels back to its origin at the absorbing atom with a phase shift and interferes with itself. The likelihood of this interference of the photoelectron with itself in turn modulates the probability that the x-ray is absorbed. Likelihood of constructive interference increases the probability of x-ray absorption, whereas likelihood of destructive interference decreases it. This leads to the structure of the XAS spectra measured by detectors.

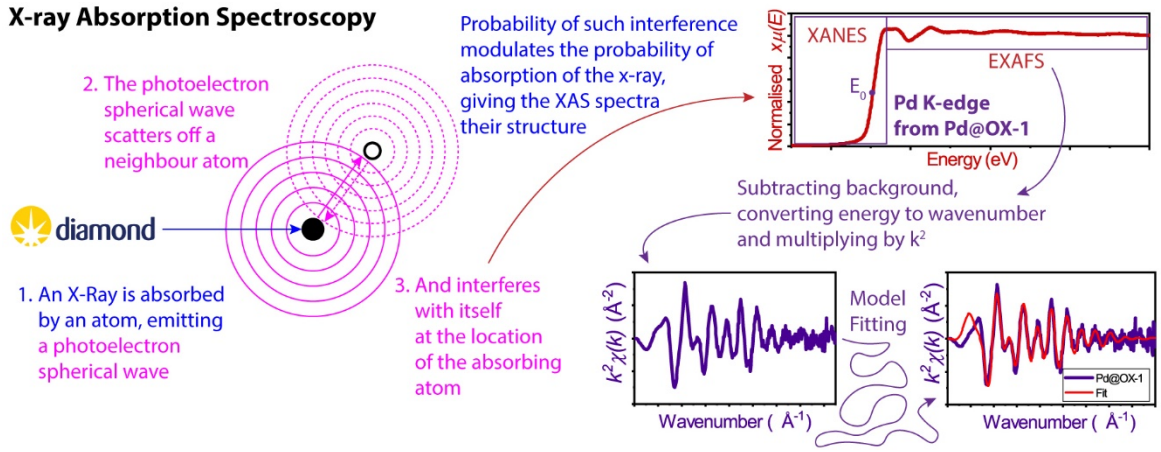

Figure 3.9 The principles and process of X-ray Absorption Spectroscopy

Two areas of the XAS spectrum are identified and analysed in different ways. One is the X-ray Absorption Near Edge Structure (XANES), where the 'edge' is the rapid rise in absorption near the binding energy (E_0) of the electron being emitted. This contains information about the atom's electronic state. The other region, containing the structural information originating from the interference effects described above, is referred to as Extended X-ray Absorption Fine Structure (EXAFS). This region of data is more challenging to collect with good quality and requires synchrotron sources to provide excellent signal to noise ratios for the data to be useful.

Upon background subtraction and conversion from energy to wavenumber (k), a function $\chi(k)$ emerges that describes the probability of the photoelectron scattering off neighbouring atoms and interfering with itself. The fitting of this function by means of a structural model of the sample ultimately provides the investigator with the desired structural information. To a first approximation, $\chi(k)$ can be expressed in the form of what is commonly referred to as 'the EXAFS equation', although many forms of this equation exist based on preferences of notation and form. Here the EXAFS equation is given in the form described by Calvin[109]:

$$\chi(k) = S_0^2 \sum_i N_i \frac{f_i(k)}{kD_i^2} e^{-\frac{2D_i}{\lambda(k)}} e^{-2k^2\sigma_i^2} \sin(2kD_i + \delta_i(k))$$

This equation describes $\chi(k)$ to be a sum of contributions from the photoelectrons of wavenumber k scattering off all neighbouring atoms i, each a distance D_i away from the absorbing atom. $\chi(k)$ is enhanced by the number of identical neighbour atoms N_i and is modulated by the probability $f_i(k)$ of the photoelectron scattering elastically off those neighbours, which drops as D_i^2. The equation also accounts for the atom becoming more positive as the photoelectron is emitted using the amplitude reduction factor S_0^2, as well as

making sure that EXAFS is a local phenomenon using the mean free path travelled by the photoelectron $\lambda(k)$ in the exponential $e^{-\frac{2D_i}{\lambda(k)}}$. The exponential term $e^{-2k^2\sigma_i^2}$ accounts for a mean square radial displacement of each neighbour σ_i^2 across all the metal sites in the sample. Finally, because the photoelectron wave is periodical, so is $\chi(k)$, with the main driving term $\sin(2kD_i + \delta_i(k))$, where $\delta_i(k)$ is the phase shift acquired by the photoelectron as it scatters off each neighbour.

This EXAFS equation, in one form or another, is at the heart of all software packages that fit EXAFS data, including the Demeter package[110] used in this thesis. Demeter takes in models of the environment of the absorbing atoms and attempts to fit it to the experimental data by adjusting parameters of the EXAFS equation that arise from that model. This process can be fraught with challenges and is very difficult indeed for a completely unknown system, because the possible structure of the system needs to first be postulated with some degree of probability before it can be fitted to the experimental data.

The following subsection provides specific experimental details for the XAS measurements carried out for this thesis at the B18 beamline of Diamond Light Source.

3.4.3.1 XAS spectroscopy at B18 of Diamond Light Source

XANES and EXAFS spectra of Pd@OX-1 were acquired on B18, the Core XAS beamline at Diamond Light Source.[111] Data at the Zn K-edge were acquired in transmission mode with ionization chambers filled with Ar and pressure adjusted to absorb 10% and 70% of the beam before and after the sample, respectively. B18 Double Crystal Monochromator was equipped with Si(111) crystal pair, and Pt-coated mirrors were inserted in the beam path to remove high energy harmonics.

For Pd K-edge, Si(311) crystals were used. Data were acquired in fluorescence mode using a 36-element monolithic Ge detector (Canberra) with XSPRESS2 acquisition

electronics. For both experiments, the beam was partially defocused to obtain a beam footprint on the sample of approximately 1×1 mm^2.

Samples were pressed into 8 mm pellets at 0.5 ton applied weight using a standard Specac benchtop hydraulic press. For transmission Zn K-edge measurements 10 mg of MOF powder was mixed with 35 mg of cellulose binder. For fluorescence Pd K-edge measurements 50 mg of MOF powder was used without binder, while the PdonC sample required 120 mg of pure material. $Pd_2(dba)_3$ was measured in transmission through a pellet pressed from 45 mg of pure material.

The Demeter software package[110] was used to process the raw data and subsequently fit the Pd K edge EXAFS spectra for the Pd@OX-1 samples before and after the Heck and Suzuki reactions.

3.4.4 X-Ray Photoelectron Spectroscopy (XPS)

X-ray photoelectron spectroscopy (XPS) is a technique whose principle is simple: x-rays hit a sample and photoelectrons are emitted from its surface; the photoelectrons are then counted, and their energy determined by the analyser/detector assembly. This provides information about the electronic states of metal atoms in a sample. This does not require a synchrotron source and many lab-based machines exist. The XPS measurement for Pd@OX-1 in Chapter 5 was done on a Thermo Scientific K-Alpha machine equipped with a 180° double focussing hemispherical analyser-128-channel detector.

Figure 3.10 XPS in a nutshell.

3.4.5 X-Ray Fluorescence (XRF) Spectroscopy

X-ray fluorescence (XRF) spectroscopy is an even simpler technique than XPS, performed on a table top PANalytical Epsilon 3 XL machine. X-rays are fired at the sample, whose atoms' electrons are excited to higher energy states and then emit photons upon relaxation to the lower states. These photons are analysed, and a spectrum compiled of the elements present in the sample. This is used to quantify the amount of Pd present in a series of Pd@OX-1 samples in Chapter 5.

3.5 Catalytic studies

Prediction of a material's catalytic activity is difficult with the currently available computational techniques. To understand a new material's utility as a catalyst, therefore, many experiments need to be conducted in a trial and error fashion. This section provides details of techniques used to analyse the reaction outcomes before elucidating the procedures followed to establish the initial scope of Pd@OX-1 catalytic functionality.

3.5.1 General considerations – analysing yield via NMR and GC

The NMR measurements were performed using a Bruker DRX 500 spectrometer operating at 500.1 MHz for ^{1}H spectra; chemical shifts were measured relative to TMS as internal standard; all the measurements were performed at room temperature and processed using TopSpin 4.0 software package.

The GC measurements were performed with an Agilent 7890 GC system equipped with an Agilent 5977A mass-selective detector (electron ionization, 70 eV) or with a SCION 436-GC system with a flame ionization detector. Both systems were equipped with HP-5MS column (30 m × 0.25 mm × 0.25 μm film) using He as the carrier gas at a constant linear velocity of 30 $cm \times s^{-1}$. The following temperature program was used in all the GC-MS measurements: initial temperature: 60 °C, hold for 2 min, then 20 $°C \times min^{-1}$ to 300 °C and hold for 6 min. Data processing was conducted using Bruker Data Analysis 4.0 (GC-MS) or CompassCDS (GC-FID) software packages.

3.5.2 Suzuki reaction

3.5.2.1 General procedure for the Suzuki reaction

For all the reactions 0.2 wt.% Pd@OX-1 was used as a catalyst source. A screw-top reaction tube was charged with aryl halide (5×10^{-4} mol), Pd@OX-1 (from 1 to 100 mg; 1×10^{-8} to 1×10^{-6} mol in Pd), phenylboronic acid (73.2 mg, 6×10^{-4} mol), potassium carbonate

(110.6 mg, 8×10^{-4} mol), and 1 mL of MeOH:H_2O (1:1) or *i*-PrOH:H_2O (1:1). The tube was equipped with magnetic stirring bar, then sealed tightly, and placed into a hot plate (from 100 ºC to 150 ºC) with continuous stirring. After specified time (from 1 h to 24 h) reaction mixture was cooled to room temperature and analysed by GC-MS.

3.5.2.2 Variation of palladium loadings in the Suzuki reaction

A screw-top reaction tube was charged with iodobenzene (102.0 mg, 5×10^{-4} mol), Pd@OX-1 (from 1 to 100 mg; 1×10^{-8} (0.002 mol%) to 1×10^{-6} mol (0.2 mol%) in Pd), phenylboronic acid (73.2 mg, 6×10^{-4} mol), potassium carbonate (110.6 mg, 8×10^{-4} mol), and 1 mL of MeOH:H_2O (1:1). The tube was equipped with magnetic stirring bar, then sealed tightly, and placed into a hot plate (from 100 ºC to 150 ºC) with continuous stirring. After specified time (from 4 h to 24 h) reaction mixture was cooled to room temperature and analysed by GC-MS.

3.5.2.3 Recycling of Pd@OX-1 in the Suzuki reaction

A screw-top reaction tube was charged with iodobenzene (102.0 mg, 5×10^{-4} mol), Pd@OX-1 (25 mg; 2.5×10^{-7} mol (0.05 mol%) of Pd), phenylboronic acid (73.2 mg, 6×10^{-4} mol), potassium carbonate (110.6 mg, 8×10^{-4} mol), and 1 mL of *i*-PrOH:H_2O (1:1). The tube was equipped with magnetic stirring bar, then sealed tightly, and placed into a hot plate at 100 ºC with continuous stirring. After 1 h reaction mixture was cooled to room temperature and analysed by GC-FID. Product was extracted with acetone (5 mL), material was washed with 5 mL of water, and washed with additional 5 mL of acetone. Dried material was used under exactly the same conditions.

3.5.2.4 Optimization for Ar-Br activation in the Suzuki reaction

A screw-top reaction tube was charged with 4-bromoanisole (93.5 mg, 5×10^{-4} mol), Pd@OX-1 (1 mg; 1×10^{-8} mol (0.002 mol%) of Pd), phenylboronic acid (73.2 mg, 6×10^{-4}

^{4} mol), potassium carbonate (110.6 mg, 8×10^{-4} mol), and 1 mL of *i*-PrOH:H_2O (1:1). The tube was equipped with magnetic stirring bar, then sealed tightly, and placed into a hot plate at 150 ºC with continuous stirring. After 24 h reaction mixture was cooled to room temperature and analysed by GC-MS.

3.5.2.5 Substrate scope examination for Pd@OX-1 in the Suzuki reaction

A screw-top reaction tube was charged with aryl halide (5×10^{-4} mol), Pd@OX-1 (10 mg; 1.0×10^{-7} mol (0.02 mol%) of Pd), aryl boronic acid (6×10^{-4} mol), potassium carbonate (110.6 mg, 8×10^{-4} mol), and 1 mL of *i*-PrOH:H_2O (1:1). The tube was equipped with magnetic stirring bar, then sealed tightly, and placed into a hot plate at 100 ºC with continuous stirring. After 1 h reaction mixture was cooled to room temperature and yield was analysed by GC-MS. Then, 1 mL of dichloromethane was added to extract the product and the product yield was analysed by ^{1}H NMR in $CDCl_3$.

3.5.2.6 Catalyst isolation for XAS study for the Suzuki reaction

For all the reactions 0.2 wt.% Pd@OX-1 was used as a catalyst source. Four parallel reaction were conducted to receive enough amount of the material. A screw-top reaction tube was charged with iodobenzene (102.0 mg, 5×10^{-4} mol), Pd@OX-1 (100 mg; 1×10^{-6} mol of Pd), phenylboronic acid (73.2 mg, 6×10^{-4} mol), potassium carbonate (110.6 mg, 8×10^{-4} mol), and 1 mL of *i*-PrOH:H_2O (1:1). The tube was equipped with magnetic stirring bar, then sealed tightly, and placed into a hot plate at 100 ºC with continuous stirring. After 4 h reaction mixture was cooled to room temperature, yield was determined by GC-MS. Product was extracted with acetone (5 mL), material was washed with 5 mL of water, and washed with additional 5 mL of acetone. Dried material was subjected to the XAS study.

3.5.3 Heck reaction

3.5.3.1 General procedure for the Heck reaction

For all the reactions 0.2 wt.% Pd@OX-1 was used as a catalyst source. A screw-top reaction tube was charged with aryl halide (5×10^{-4} mol), Pd@OX-1 (from 1 to 100 mg; 1×10^{-8} to 1×10^{-6} mol of Pd), butyl acrylate (76.9 mg, 6×10^{-4} mol), triethylamine (81.0 mg, 8×10^{-4} mol), and 1 mL of DMF. The tube was equipped with magnetic stirring bar, then sealed tightly, and placed into a hot plate (from 100 ºC to 150 ºC) with continuous stirring. After specified time (from 1 h to 24 h) reaction mixture was cooled to room temperature and analysed by GC-MS.

3.5.3.2 Variation of palladium loadings in the Heck reaction

A screw-top reaction tube was charged with iodobenzene (102.0 mg, 510^{-4} mol), Pd@OX-1 (from 1 to 100 mg; 110^{-8} (0.002 mol%) to 1×10^{-6} mol (0.2 mol%) of Pd), butyl acrylate (76.9 mg, 6×10^{-4} mol), triethylamine (81.0 mg, 8×10^{-4} mol), and 1 mL of DMF. The tube was equipped with magnetic stirring bar, then sealed tightly, and placed into a hot plate (from 100 ºC to 150 ºC) with continuous stirring. After specified time (from 4 h to 24 h) reaction mixture was cooled to room temperature and analysed by GC-MS.

3.5.3.3 Recycling of Pd@OX-1 in the Heck reaction

A screw-top reaction tube was charged with iodobenzene (102.0 mg, 5×10^{-4} mol), Pd@OX-1 (100 mg; 1×10^{-6} mol (0.2 mol%) of Pd), butyl acrylate (76.9 mg, 6×10^{-4} mol), triethylamine (81.0 mg, 8×10^{-4} mol), and 1 mL of DMF. The tube was equipped with magnetic stirring bar, then sealed tightly, and placed into a hot plate at 100 ºC with continuous stirring. After 4 h reaction mixture was cooled to room temperature and analysed by GC-FID. Product was extracted with DMF (5 mL), material was washed with 5 mL of DMF, followed by 5 mL of acetone. Dried material was used under exactly the same conditions.

3.5.3.4 Ar-Br activation in the Heck reaction

A screw-top reaction tube was charged with 4-bromoanisole (93.5 mg, 5×10^{-4} mol), Pd@OX-1 (25 mg; 2.5×10^{-7} mol (0.05 mol%) of Pd), butyl acrylate (76.9 mg, 6×10^{-4} mol), triethylamine (81.0 mg, 8×10^{-4} mol), and 1 mL of DMF. The tube was equipped with magnetic stirring bar, then sealed tightly, and placed into a hot plate at 150 ºC with continuous stirring. After 24 h reaction mixture was cooled to room temperature and analysed by GC-MS.

3.5.3.5 Substrate scope examination for Pd@OX-1 in the Heck reaction

A screw-top reaction tube was charged with aryl iodide (5×10^{-4} mol), Pd@OX-1 (10 mg; 1.0 10^{-7} mol (0.02 mol%) of Pd), acrylate (6×10^{-4} mol), triethylamine (81.0 mg, 8×10^{-4} mol), and 1 mL of DMF. The tube was equipped with magnetic stirring bar, then sealed tightly, and placed into a hot plate at 100 ºC with continuous stirring. After 4 h reaction mixture was cooled to room temperature and yield was analysed by GC-MS. Then, the product yield was analysed by ^{1}H NMR in $CDCl_3$.

3.5.3.6 Catalyst isolation for XAS study for the Heck reaction

For all the reactions 0.2 wt.% Pd@OX-1 was used as a catalyst source. Four parallel reaction were conducted to receive enough amount of the material. A screw-top reaction tube was charged with iodobenzene (102.0 mg, 5×10^{-4} mol), Pd@OX-1 (100 mg; 1×10^{-6} mol of Pd), butyl acrylate (76.9 mg, 6×10^{-4} mol), triethylamine (81.0 mg, 8×10^{-4} mol), and 1 mL of DMF. The tube was equipped with magnetic stirring bar, then sealed tightly, and placed into a hot plate at 100 ºC with continuous stirring. After 4 h reaction mixture was cooled to room temperature, yield was determined by GC-MS. Product was extracted with DMF (5 mL), material was washed with 5 mL of DMF, followed by 5 mL of acetone. Dried material was subjected to the XAS study.

3.6 Computational methods

This section details the various computational methods employed in analysing and simulating some of the data presented in Chapters 4-7. It also outlines the data treatment strategies employed to handle the vast amounts of data collected during the acetone sensing experiments of Chapter 6 on the one hand, and the sparse data obtained from the quantum tunnelling experiments of Chapter 7.

3.6.1 Kramers-Kronig Transform (KKT)

The basis of the transformation from FTIR specular reflectance spectra to dielectric and optical properties used in Chapter 4 are the Kramers-Kronig relations, which are themselves based on the principle of causality of physical systems and connect the real and imaginary parts of many complex quantities in physics.[112] In particular, the much studied Kramers-Kronig transform (KKT) between $\frac{1}{2}\ln[R(\nu)/R_\infty]$ and the phase change upon reflection $\varphi(\nu)$ is the key to computing the optical and dielectric properties. Here R stands for reflectance and ν stands for wavenumber. In the case of external reflection at normal incidence (experimental conditions are an approximation of these) the following relation holds[112]:

$$\varphi(\nu_a) = \frac{-2\nu_a}{\pi} P \int_0^\infty \frac{\frac{1}{2}\ln[R(\nu)/R_\infty]}{\nu^2 - \nu_a^2} d\nu$$

where the P designates the Cauchy principle value of the integral. It is important to note here that this integral considers reflectance data from zero to infinity for each individual value of phase change being calculated. From this stem the problems with the Kramers-Kronig transform built into the Brucker software called OPUS (version 7.2): the transform only takes as input the necessarily limited piecewise measurements (in this case 40-600 cm^{-1} for far IR measurements and 600-4000 cm^{-1} for mid IR measurements). This problem results in

physically intractable negative values for the imaginary parts of the complex refractive index and complex dielectric function: the imaginary part is the loss coefficient, and negative loss implies a gain, which is impossible in the absence of a power source (as is the case for a passive material). The Matlab code given in Appendix 1 solves this problem by smoothly joining the far and mid IR spectra and extrapolating to 0 wavenumber to get a single continuous reflectance spectrum, which does a much better job of approximating an infinite dataset. The reflectance is assumed to remain constant from the lowest wavenumber reflectance value measured, while reflectance at infinity R_∞ is assumed to be the highest wavenumber reflectance value measured. Obeserving that the complex refractive index is given by [112]:

$$n = \frac{1 - R}{1 + R - 2\sqrt{R}\cos\phi}, k = \frac{-2\sqrt{R}\sin\phi}{1 + R - 2\sqrt{R}\cos\phi}$$

and then using the relation to the complex dielectric function given in section 2.2.1 above, the Matlab code in Appendix 1 calculates both properties given experimentally measured reflectance spectra. The KKphase function was inspired by the algorithms given as supplementary code with the book by Lucarini *et al*[113]. To use the code, save the functions in a single .m file with the KKtransform_Publish function on top and call it in accordance to instructions contained within the header comments.

Figure 3.11 compares the output of this code to the output of OPUS built-in transform to demonstrate the former's advantages over the latter.

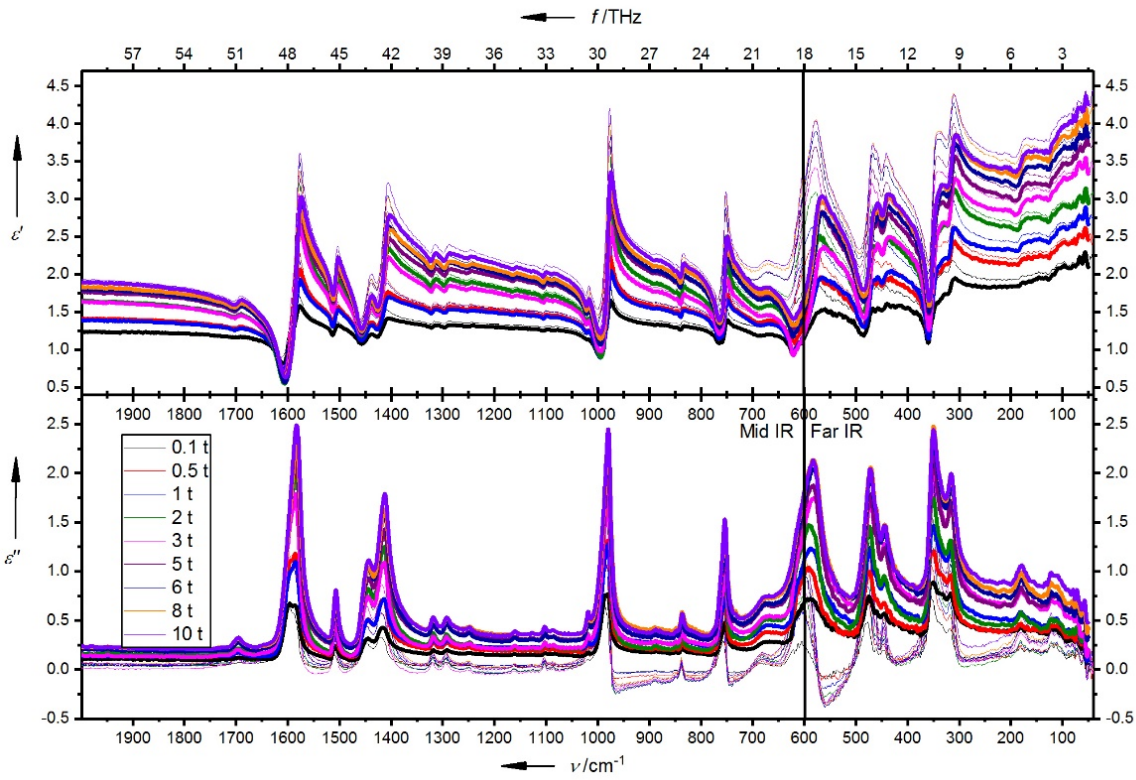

Figure 3.11 Opus transform output (thin spectra) versus own transform output (thick spectra) of the complex dielectric function. Note the physically intractable negative values in the imaginary part of Opus output and the corresponding higher peaks of the real part.

3.6.2 Density functional theory (DFT) calculations of frequency-dependent dielectric properties of MIL-53(Al) NP and LP crystal structures

Density functional theory (DFT) calculations were performed using a development version of the ab-initio periodic program CRYSTAL14[114]. The B3LYP hybrid exchange-correlation functional augmented with the Grimme's dispersion correction D3 (i.e. B3LYP-D3)[115] were used in combination with an Alhrichs' triple-zeta quality (TZP) basis sets.[116] The MIL-53 LP and NP structures have been geometrically optimized in accordance with Walker *et al*[117]. The vibrational frequency calculations were performed with additional CRYSTAL keywords (listed below), to incorporate the contributions of nuclear motions to the static dielectric constants.

FREQCALC
NUMDERIV
2
INTENS
INTCPHF
END
IRSPEC
REFRIND
DIELFUN
DAMPFAC
5.0
GAUSS
ENDIR
END

The computed data provide a prediction of the reflectance spectrum and the complex dielectric function at 0 K, for an idealized (defect free) MIL-53 LP/NP structure of well-defined symmetry, namely: orthorhombic (*Imma*) and monoclinic (*C2/c*), respectively. The three values (*x*, *y*, *z*-directions, due to tensorial property) of the real and imaginary parts of the dielectric function were obtained through Kramers-Kronig relations[118], then averaged, and plotted as the resultant Re($\tilde{\varepsilon}$) and Im($\tilde{\varepsilon}$) values as a function of frequency. Thus, the DFT results presented in Chapter 4 correspond to the behaviour of a polycrystalline material with randomly oriented crystallites, as found in a pressed powder pellet. The position, but not the height, of the peaks between 1000-2000 cm^{-1} has been scaled by applying a factor of 0.98. This scaling factor was implemented so as to empirically compensate for the well-known overestimation in the computed harmonic frequencies, with respect to the fundamental frequencies determined from experiments.

3.6.3 Schrödinger equation calculations for -CH_3 quantum rotational tunnelling energy estimation

In a single particle model, the quantised rotational energy levels are calculated for a molecule with a rotational constant B, under the assumption that the environment of that molecule can be represented by a simple harmonic potential $V(\omega)$.[2] The energy levels of the molecular rotor are then given by the solutions E_i of the stationary Schrödinger equation:

$$H\Phi_i = E_i\Phi_i$$

with the Hamiltonian:

$$H = B\nabla^2 + V(\omega)$$

where H and the spatial wavefunction Φ_i depend on angular variables ω. The rotational constant B of a -CH_3 rotor is ≈ 0.655 meV[3], and the external potential $V(\omega)$ is assumed to have the simple harmonic form:

$$V(\omega) = U(1 - \cos 3\omega)/2$$

where U is the potential barrier height in units of meV and the factor of 3 in the simple harmonic term represents the three-fold symmetry of the rotor.

This system is then solved in Mathematica using the built-in NDEigensystem solver (code is provided in Appendix 2) to get energy levels E_i for increasing barrier heights U in the range 0-32 meV. Results of the calculation are shown in Figure 3.12. The energy of the quantum tunnelling transition is then the difference between ground state (0) and first excited state (1 or 2), and the energy of the first librational transition is the difference between states (1 or 2) and (3 or 4), for any given barrier height.

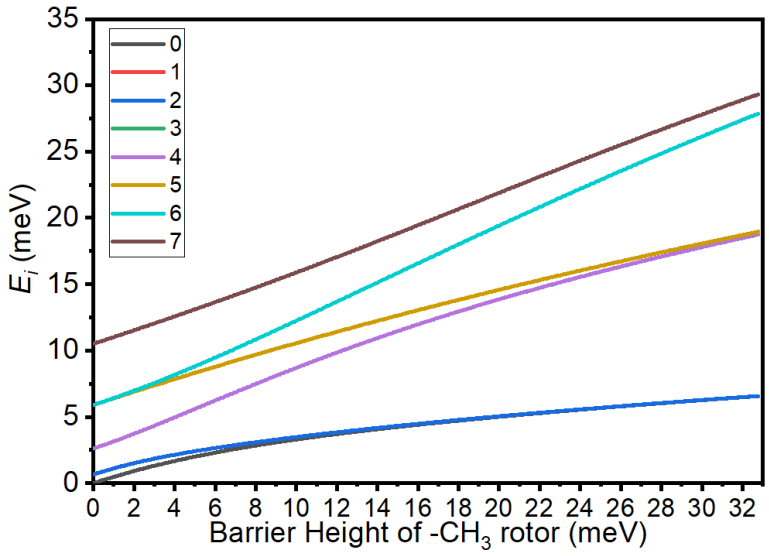

Figure 3.12 Quantised rotational energy levels given by solutions E_i of the stationary Schrödinger equation for varying barrier heights of a -CH_3 rotor. Note that levels 1 and 2, as well as 3 and 4, overlap exactly.

3.6.4 Data array handling and formatting for 3D plotting

3.6.4.1 Acetone sensing FTIR data

Large amounts of data were collected in the acetone sensing experiments presented in Chapter 6 – the need to capture dynamics of the material's response to acetone necessitated continuous data collection. This data accumulated into arrays of more than 500 individual spectra for some of the dosing runs. Due to limitations of the OPUS software, in which data was collected, new ways of handling the data had to be developed. This led to Matlab code presented in Appendix 3, which automates and standardises data handling. It also facilitates fast and reliable ways of producing 3D time-resolved plots of the data, which are vital to understanding the sensing dynamics. The code assumes that the individual spectra are taken at regular intervals and generates a time sequence based on that assumption. This, however, is not always the case during data collection, which is sometimes interrupted during measurements in the far IR due to synchrotron electron beam top-ups. However, these exceptions do not introduce a large error into the final data and are absent all together from mid IR data measured with a Globar source, which is not interrupted in that way.

3.6.4.2 Interpolating OSIRIS INS and NPD spectra

The INS and NPD spectra collected during the OSIRIS experiments were taken at specific levels of gas dose loaded into the ZIF-8 sample. Due to the necessarily long time it takes to accumulate statistically reliable neutron data, the number of levels, at which measurements can be carried out, are limited by the time allocated to the experiment. It is therefore necessary to interpolate this discrete data along the gas dose dimension to better understand and analyse the data. This extrapolation is done in Matlab, making use of the built-in Piecewise Cubic Hermite Interpolating Polynomial (PCHIP) function, which preserves the shape of the data. It fits the discrete data with a piecewise cubic polynomial $P(x)$ with the following properties[119]:

- On each subinterval $x_k \leq x \leq x_{k+1}$, the polynomial $P(x)$ is a cubic Hermite interpolating polynomial for the given data points with specified derivatives.
- $P(x)$ interpolates y, that is, $P(x_i) = y_i$, and the first derivative $\frac{dP}{dx}$ is continuous. The second derivative $\frac{d^2P}{dx^2}$ is probably not continuous, so jumps at the x_i are possible.
- The cubic interpolant $P(x)$ is shape preserving. The slopes at the x_i are chosen in such a way that $P(x)$ preserves the shape of the data and respects monotonicity. Therefore, on intervals where the data is monotonic, so is $P(x)$, and at points where the data has a local extremum, so does $P(x)$.

This interpolation provides a powerful way of visualising the discrete data with wide gaps between gas doses presented in Chapter 7. This aids understanding and analysis. However, care is taken to stress the discrete nature of the collected data, and, where possible, the doses at which measurements were taken are identified for the reader's attention.

3.7 Summary of the experimental approach

This chapter presents the experimental techniques used as part of the wider experimental approach to understanding and developing practical MOF materials in this thesis:

1. Once the materials are procured or synthesised and appropriately processed, they are characterised by XRD and gas adsorption (section 3.2), as well as the combination of imaging techniques spanning the appropriate length scales (section 3.3). This establishes a level of certainty about the material structure required to proceed with subsequent experiments.
2. Appropriate spectroscopic techniques are then used to explore the materials' behaviours (sections 3.4 and 3.5).
3. Experimental data acquired through those techniques is handled and complemented using the appropriate computational methods (section 3.6).

The results of these experiments are presented in Chapters 4-7 of this thesis.

Chapter Four

4 Investigating dielectric properties of MOFs using specular reflectance FTIR spectroscopy

4.1 Introduction

This Chapter describes the novel application of a high-resolution synchrotron specular reflectance FTIR method to study the dynamic dielectric characteristics of the MIL-53(Al) polycrystalline powder, encompassing the broad spectral range of 1.2 to 120 THz. The structural bistability of MIL-53(Al) is well-documented (see section 2.2.3 of this thesis), commonly existing in two structural configurations: large pore (LP) and narrow pore (NP) architectures (see Figure 4.2a). Switching between the LP ⇌ NP structures can be triggered by water/solvent uptake, temperature swing or mechanical stress (pressure). This structural transformation provides an opportunity to monitor the variation in dielectric properties of samples, in which the ratio of LP:NP phase mixtures can be modified by controlling the externally applied stress.

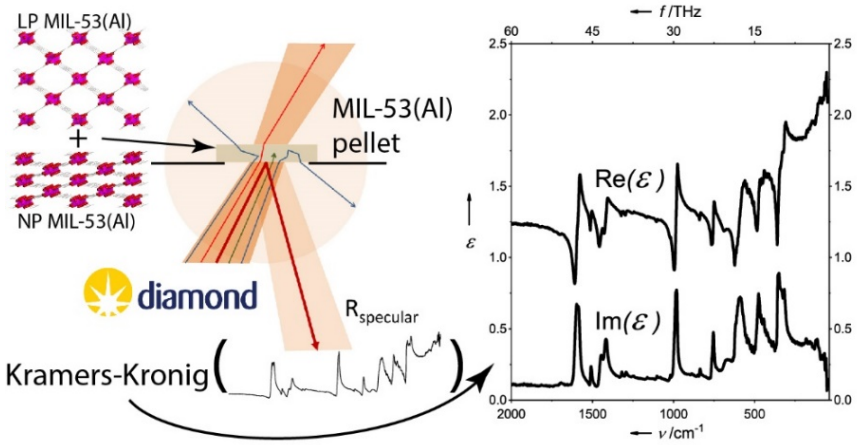

Figure 4.1 Schematic of the workflow involved in measuring the dynamic dielectric function of MOF pellets using synchrotron IR radiation at the B22 beamline of Diamond Light Source.

4.2 Pelletisation of MIL-53(Al) powder

The Al-O octahedral sites in MIL-53(Al) have a strong affinity towards water, which results in LP to NP (see Figure 4.2a for schematics of the two crystal phases) transformation when water molecules enter the pore. It is thus difficult to obtain purity of phase of MIL-53(Al) under ambient conditions – the moisture in the atmosphere is adsorbed, resulting in a mixture of LP and NP configurations even if the material is converted to pure LP (activated) phase through heating and evacuation prior to exposure to atmosphere. Indeed, because the pellets in this study were all prepared under ambient conditions, the precursor MIL-53(Al) powder contained an amount of its NP phase. After the pellets were prepared they were only exposed to controlled laboratory air, so no increased amount of moisture interacted with the crystals.

The as received MIL-53(Al) powder was subjected to several tests to determine its behaviour under lab atmosphere conditions and its response to moisture and mechanical stress. As received powder was activated at 315 °C for 20 hr to obtain mostly LP phase powder (obtaining pure LP phase proved to be difficult). Figure 4.2 shows subsequent powder XRD measurements taken using the MiniFlex X-ray diffractometer at increasing times after the activated powder was exposed to the lab's ambient conditions (which are kept relatively dry). The LP content does not appear to dramatically change even after 72 hr of exposure – all the measurements up to this time agree very well. However, as soon as the sample is exposed to water vapour, the XRD pattern changes dramatically (see the 'MintyBreath', i.e. exposed to moisture, patterns in Figure 4.2).

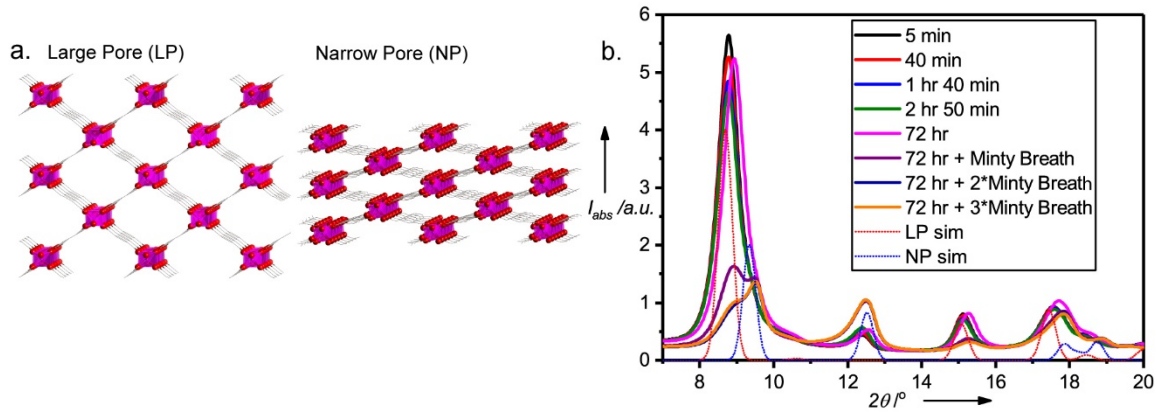

Figure 4.2. (a) LP and NP crystal structures colour code: Zn pink, O red, C black; (b) Powder XRD patterns measured from the same activated MIL-53(Al) mostly LP powder at increasing times after the powder was exposed to the ISIS R-53 laboratory air (see legend); after 72 hr the powder was exposed to increasing amounts of water vapour.

This evidence shows that the as-received MIL-53(Al) LP phase powder is stable under the relevant lab conditions but converts to NP when water vapour is incident. Thus, it is viable to measure a powder sample's XRD pattern, then press a pellet from the same sample and assume that the phase content of the powder remained unchanged up until the time at which stress was applied, so long as no moisture was actively applied to the powder sample.

More powder was activated to further test its response to mechanical stress in the manual hydraulic pellet press. See Figure 4.3a for powder XRD of the activated powder collected on the MiniFlex instrument. One of the samples was exposed to water vapour so that a portion of crystals converted to NP phase by adsorbing water molecules – see pattern 4_MintyBreath compared to the initial pattern 4. These powder samples were then subjected to loads (in metric tonnes, t) from 0.5 t up to 10 t and the resulting pellets studied using transmission WAXS on the InXider diffractometer. It is convenient to refer to the pellets in terms of the mass applied to press each pellet, *i.e.* the 0.1 t pellet or the 10 t pellet, rather than the uniaxially applied nominal stress (force/area) 7.39 MPa and 739 MPa, respectively. The results are presented in Figure 4.3b. For clarity of comparison all the data is further

plotted in Figure 4.4 to juxtapose the starting powder XRD patterns with the patterns collected from the resulting pellets. It is important to note that the powder XRD curves in Figure 4.4 (black and blue curves) were normalised 0 to 1 while the pellet WAXS curves were all normalised by density×thickness of the pellets. Thus, only like-for-like measurements can be compared numerically between themselves: the powder XRD collected using MiniFlex and the pellet WAXS collected using InXider (this is how they are grouped in Figure 4.3).

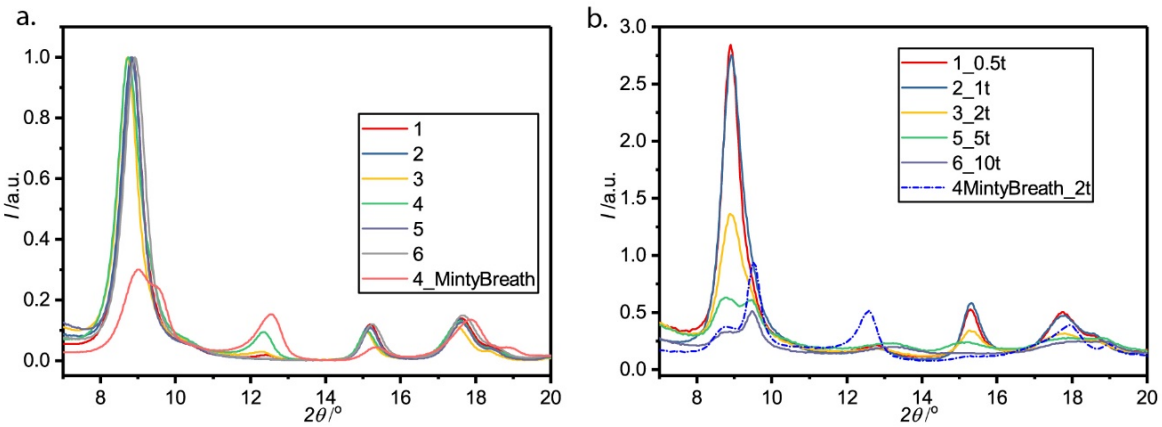

Figure 4.3. Showing a) the activated MIL-53(Al) powder XRD collected on MiniFlex; b) WAXS patterns of pellets pressed from the activated powder in (a). Legend gives sample numbers and where appropriate the load applied during pelletisation. 'MintyBreath' sample was subjected to water vapour before pelletisation.

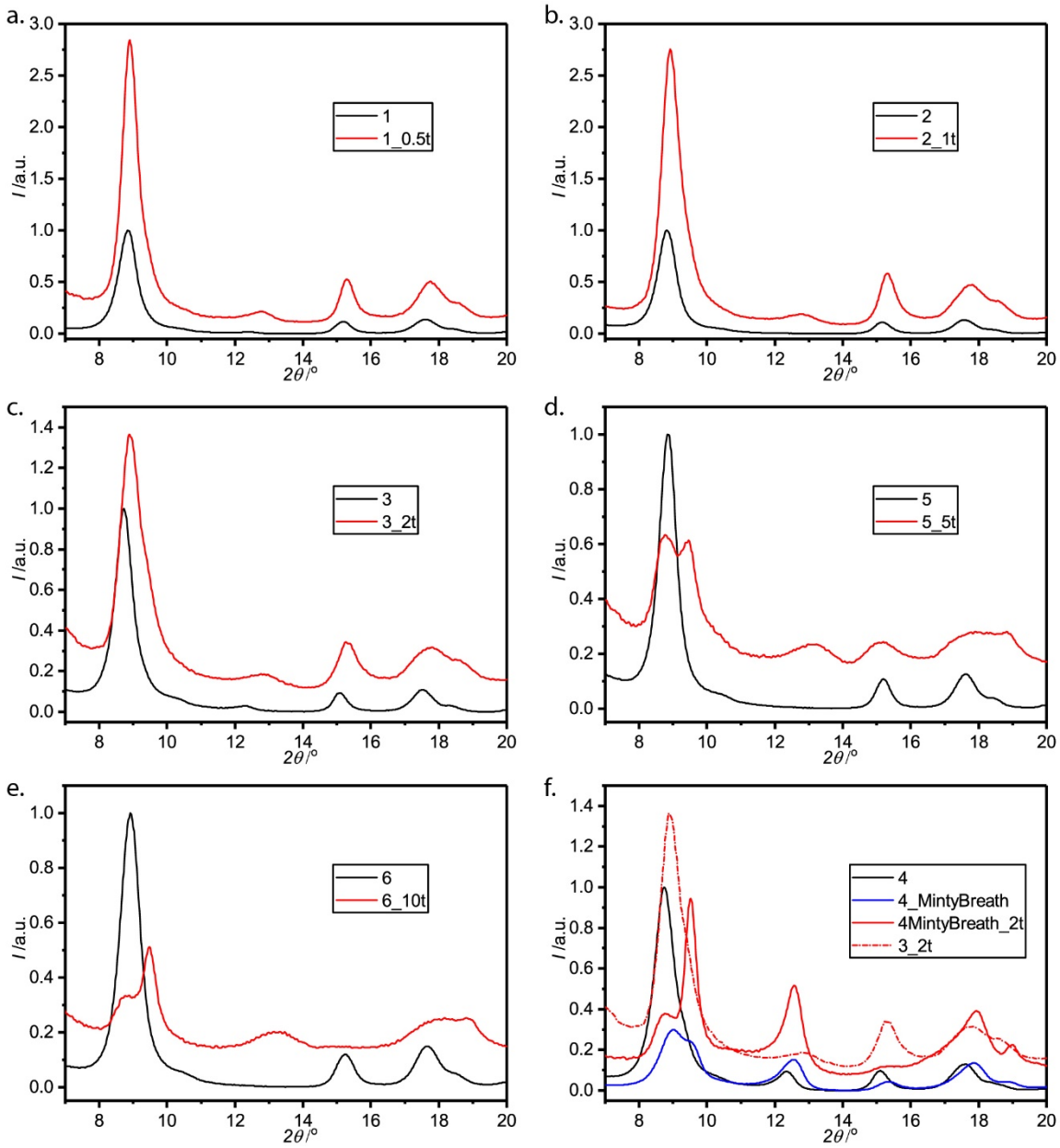

Figure 4.4. Comparing the (normalized 0 to 1) activated powder XRD with the WAXS pattern of the pellet pressed from that powder. Panel (f) aims to highlight the difference in resulting pellet composition when the starting powder has almost no NP phase (3, see panel c) versus the large starting NP content (4_MintyBreath panel f): the NP content of sample 3_2t is nowhere near that of sample 4MintyBreath_2t (simply comparing the magnitudes of the NP peaks of the two red curves at 9.8°) in panel f.

The most important evidence in all this data lies in the comparison between the pellets pressed from pure LP powders and the pellet pressed from the powder exposed to water vapour. The WAXS patterns show that pressing LP phase powder does not produce anywhere near the same magnitude of NP WAXS peaks (2θ = 9.8° and 12.5°) compared to magnitudes of those peaks in the pellet made from powder with significant initial NP phase content (the 4_MintyBreath sample). This can be clearly seen in Figure 4.3b, where the 12.5° peak of sample 4MintyBreath_2t is much more intense than any of the other samples; and also in Figure 4.4f where the high NP phase content pellet is compared to the pellet also pressed under 2 t but from purely LP powder. It is also important to note that the LP peaks (8.9° and 15.2°) have drastically diminished in the NP pellet (4MintyBreath_2t) in terms of their relative intensity to the NP peaks compared to the starting powder (4_MintyBreath).

Together the above discussed evidence demonstrates that subjecting MIL-53(Al) to uniaxial mechanical stress in a closed cylindrical vessel leads to the collapse of LP phase crystals, and only a limited fraction of those LP crystals can be assumed to convert to NP phase. At the same time, the NP phase crystals appear to survive the stresses applied in this study, which makes them mechanically more robust compared to their LP counterparts.

4.3 Pellet composition for FTIR spectroscopy

The as-received MIL-53(Al) powder containing the LP and NP phases (see Figure 4.5a) was used to make 9 pellets at increasing pressures, see Figure 4.5b. Figure 4.5c shows the nominal density of the pellets as a function of the applied stress. The pellet density appears to follow a logarithmic law (with the 8 t pellet being an outlier as a result of part of the pellet being chipped off), and approaching ~90% of the theoretical single-crystal density of NP MIL-53(Al) at ~800 MPa. This increase in density indicates a drastic decrease in void size and better packing of the crystals inside the pellets (see Figure 4.5d,e for SEM images of the as-received powder, and Figure 4.5f,g for a schematic representation of pellet

composition). Crystal size is an important consideration here and it is noted that the supplied MIL-53(Al) crystals vary in size from 50 nm up to 2 μm, This distribution of crystal sizes is comparable to the wavelength of incident light within the spectral region of interest, thus some diffraction of the incident beam can be occurring; see Figure 4.5h for a breakdown of what happens to various parts of the incident beam. Here it is noted that it is predominantly the specular reflected light that was measured.

Specular reflectance measurements are contingent on the surface quality of the sample. Therefore, the surfaces of each of the prepared pellets were characterized by SEM and quantified using the Alicona profilometer and AFM (see Figure 4.6 and Figure 4.7). Figure 4.7 shows the three different measures of roughness (mean, rms and mean depth) determined using the 20× and the 50× optics on the profilometer to ensure that the optics were not affecting accuracy of the measurements. It is evident that the surface roughness of the pellets was low, showing less than 100 nm rms roughness across all the pellets. This is important for comparing the measured optical and dielectric properties: because the surface quality is unchanged across the pellets prepared under increasing applied stress, it is concluded that the observed changes in the measured properties arise from evolution in the underlying framework structure of MIL-53(Al), as well as the increasing density of the pellets, but independent of sample surface quality.

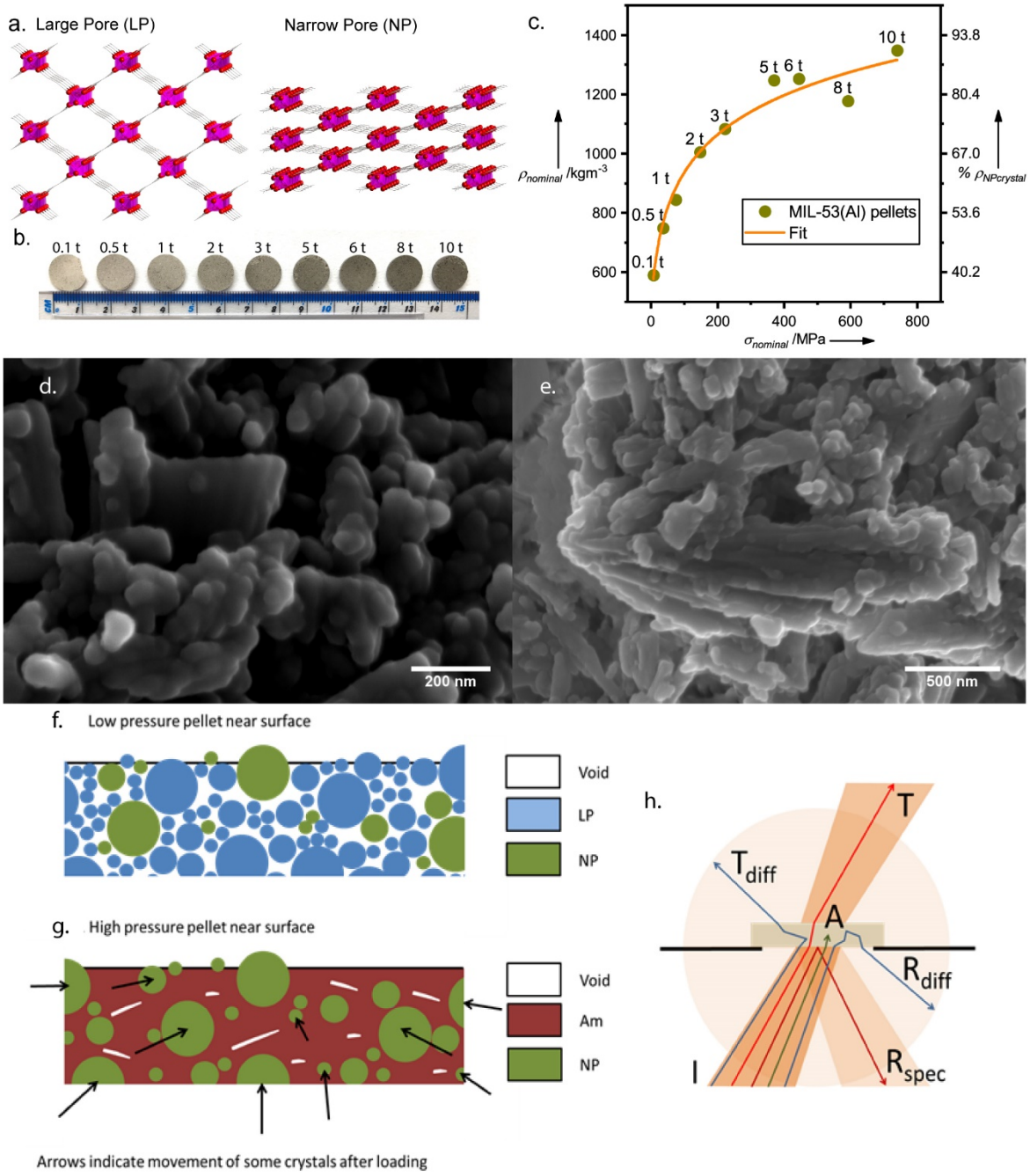

Figure 4.5. MIL-53(Al) pellet composition: (a) Schematic illustration of the crystal structure of MIL-53(Al) large pore (LP) and narrow pore (NP) configurations; (b) photographs of the pellets studied in this work; (c) the measured density of pellets as a function of applied nominal stress ($\sigma_{nominal}$), labels on data points correspond to the applied weight reading on the press gauge. (d,e) SEM images of the MIL-53(Al) crystal powder supplied by Sigma Aldrich, showing a size distribution of ~50 nm to ~2 μm. (f,g) Schematic of the postulated composition of the prepared pellets. The lower pressure pellets (f) consist of LP and NP crystals as well as some internal voids due to imperfect packing, while the higher pressure pellets (g) consist of the much better packed amorphized LP crystals (note that these still

have porosity, but lack long range periodicity, hence ‘amorphized’), NP crystals and fewer voids. (h) Showing a schematic of the various paths taken by parts of the incident (I) IR beam from the synchrotron source: (A) is absorbed, (T) is transmitted, (T_{diff}) is diffracted and transmitted, (R_{diff}) is diffracted and reflected, and (R_{spec}) is the specular reflected part of the incident beam that was measured in the experiments.

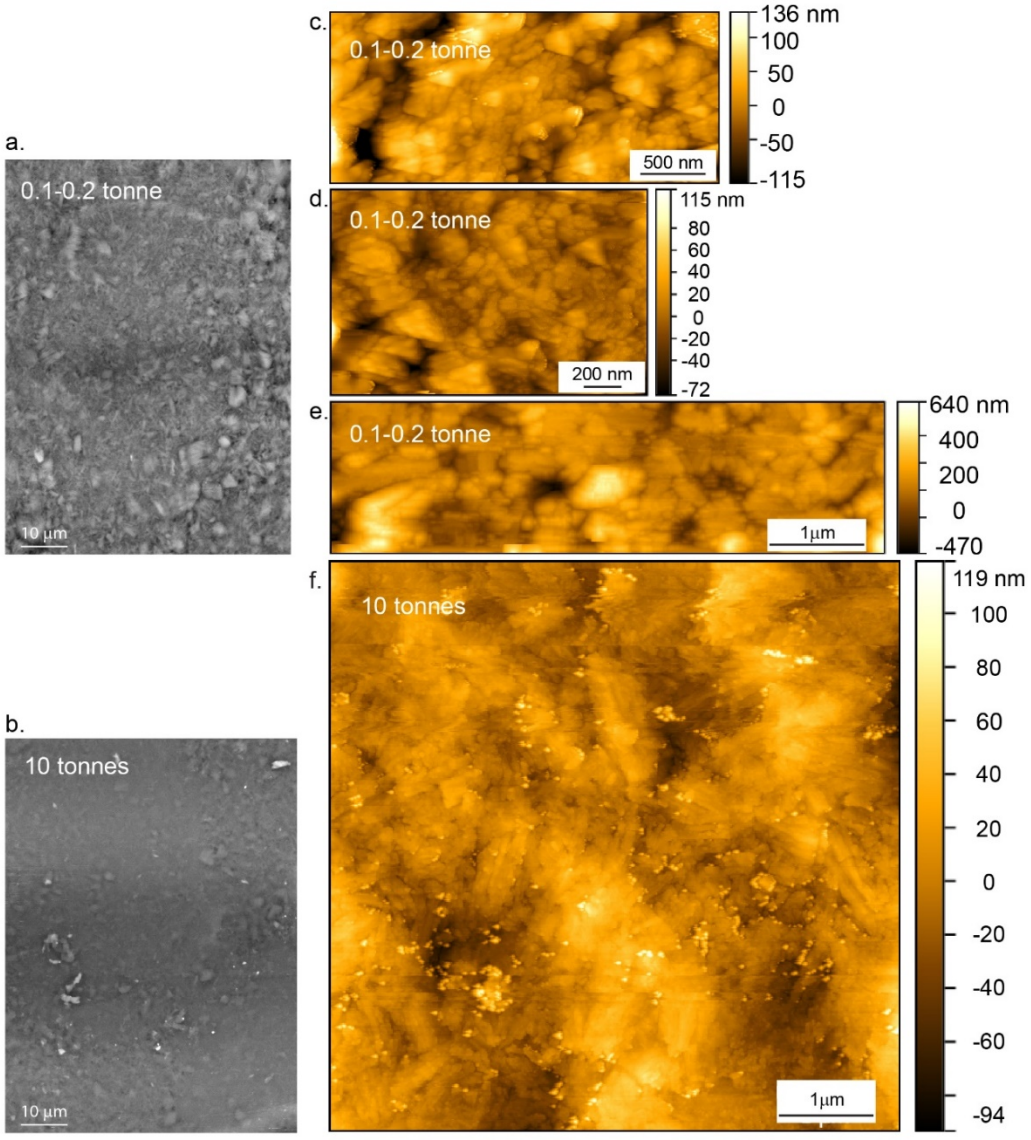

Figure 4.6. Scanning electron microscopic (SEM) images of MIL-53 pellets moulded under loads (a) 0.1 – 0.2 t and (b) 10 t; Atomic force microscopic (AFM) images of MIL-53 pellets moulded under loads (c-e) 0.1 – 0.2 t and (f) 10 t.

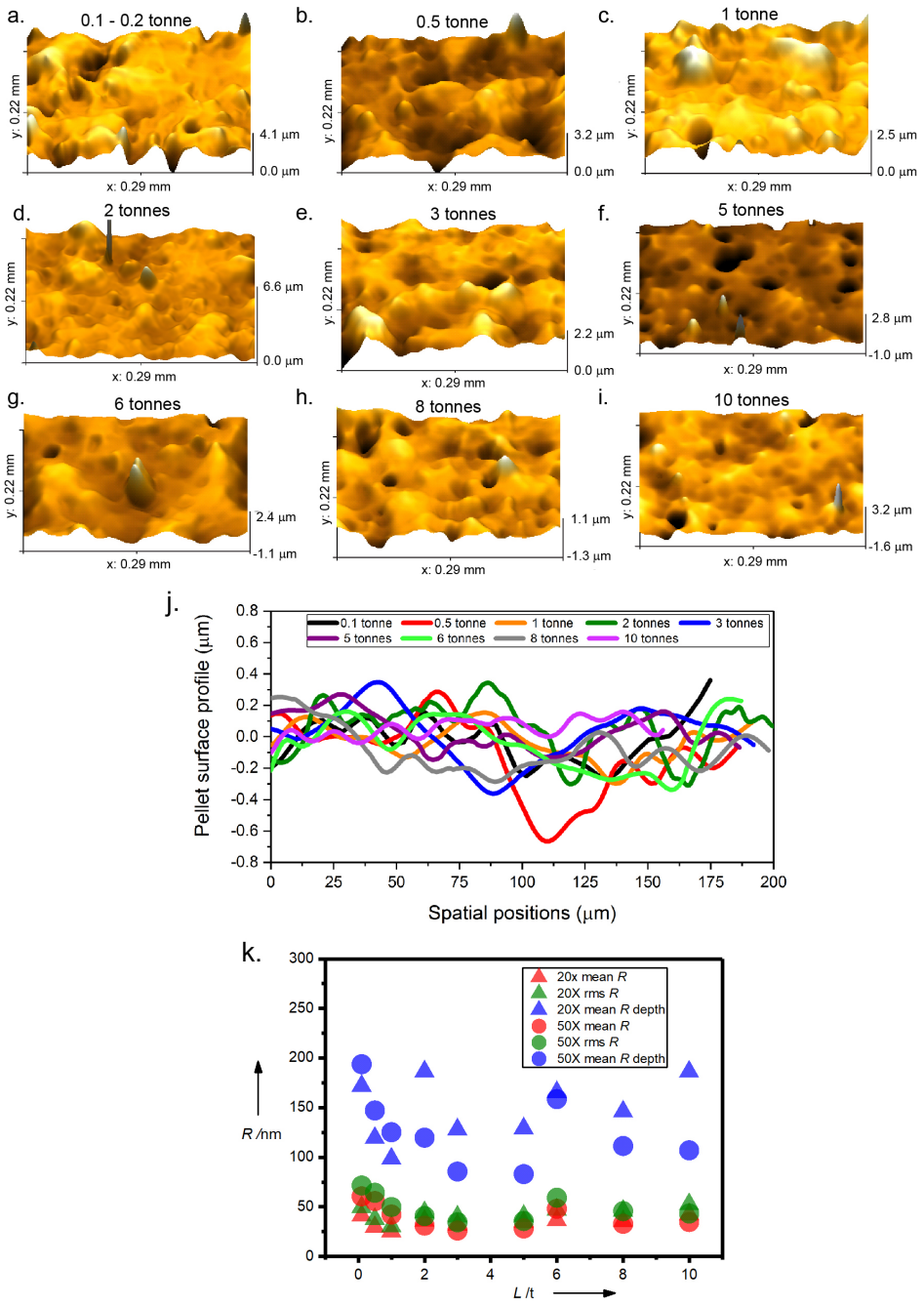

Figure 4.7. Reconstructed 3D surface profiles of pellets pressed under loads (a) 0.1 – 0.2 t, (b) 0.5 t, (c) 1 t, (d) 2 t, (e) 3 t, (f) 5 t, (g) 6 t, (h) 8 t, (i) 10 t; (j) Representative cross-sectional profiles of pellets under various loads; (k) three different measures of surface roughness of the pellets at two different magnifications of 20× and 50× on the Alicona Infinite Focus profilometer employing the optical focus-variation technique with 20 nm vertical resolution (50x objective magnification).

The pellets were then studied using wide-angle X-ray scattering (WAXS – see Figure 4.8), to determine the crystal structure of the MIL-53(Al) inside the pellets as a function of pelletising pressure. With increasing pelletisation stress the remaining crystalline material inside the prepared pellets approached purely NP phase plus the amorphized LP crystals. The LP and NP powder diffraction patterns were simulated using the CrystalMaker and CrystalDiffract software (see section 3.2.4.3 for details) Figure 4.8b shows the results of integration of the area underneath the largest LP and NP XRD peaks centred on 9° (see inset marked # in Figure 4.8a), which were used to track the changing amounts of the LP and NP phases with increasing stress. This analysis shows that the amount of LP phase decreases rapidly with increasing stress, whereas the NP content appears to remain constant. Based on the investigation described in section 4.2 above, it was found that LP phase simply collapses under stress while NP phase withstands the level of stress applied here; it was also found that this amorphous phase is not reversible. This finding is in line with theoretical studies showing improved mechanical properties of NP compared to LP.[57] It is therefore likely that LP crystals under stress are converted to an amorphous LP phase. Literature on amorphous MOFs[120] has shown that they lose long-range periodic order, but retain the basic building blocks and connectivity,[121] including some porosity[122] of their crystalline counterparts. As a result, the pellets studied using synchrotron IR radiation in this study appear to have the same amount of NP phase, but progressively less LP phase and more amorphous LP phase develops as the applied stress increases.

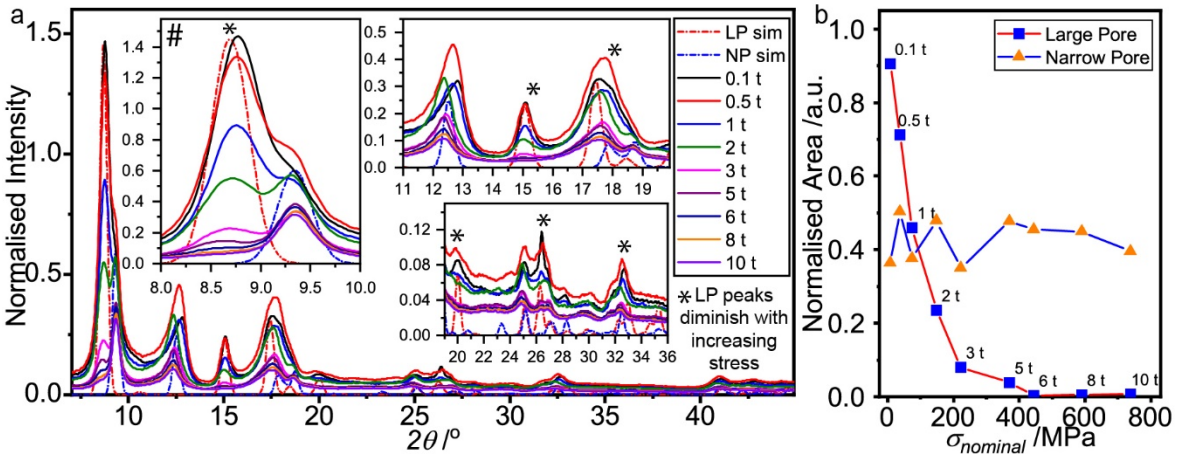

Figure 4.8 X-ray analysis of MIL-53(Al) pellets: (a) WAXS (XRD) patterns normalized to the product of density×thickness for all the pellets, with simulated powder XRD patterns for both the LP and NP crystal structures; the NP was simulated with a preferred orientation on the (200) plane with a factor of 0.524 in the CrystalDiffract software; (b) variation with applied stress of the areas of peaks fitted to the double peak marked # in (a) associated with the LP and NP structures, respectively.

4.4 Properties glimpsed from IR spectroscopy

Drastic changes in the IR reflectance data, and the calculated dielectric properties, are observed as a result of the above described composition changes in the MIL-53(Al) pellets. Figure 4.10 shows the collected reflectance (R) spectra and Figure 4.11 shows the complex dielectric functions of frequency obtained by applying the Kramers-Kronig Transform (KKT): $\tilde{\varepsilon}(\omega) = \varepsilon'(\omega) + i\varepsilon''(\omega)$, for each pellet, shown in the component form of spectra of its real (ε') and imaginary (ε") parts (see Figure 4.14 for the complex refractive index). Section 2.2.1 discusses the dielectric notation used here, while section 3.6.1 deals with the KKT. It can be seen that there is a stepwise decrease in ε' with increasing frequency of excitation. Specifically, each transition step exhibits a peak of varying magnitude associated with it, accompanied by distinct peaks in ε", the latter describing dielectric losses. These steps are resonant vibrational responses of the material to the applied electromagnetic field. The orientational responses are detected at lower frequencies (THz phonons),[8, 10] while the electronic responses are observed at higher frequencies beyond ~20 THz. It is important

to note here that the spot size of the beam is of the order of $(100\ \mu m)^2$, such that the measured reflectance spectrum is an average across this area, thus making the calculated properties the linear combination of properties of all the crystals and voids sampled in that area.

Each of the loss ε'' peaks grows with increasing pelletizing pressure and thus, as the above analysis of the pellet composition shows, with decreasing content of LP phase and increasing pellet density. These changes in amplitude are accompanied by changes in the shape of the peaks, which are indicative of changes occurring in the structure of the MIL-53(Al) crystals. Inset of Figure 4.11c shows one example of this transformation in the imaginary part of the dielectric function: the double peak around 1590 cm^{-1} (47.7 THz) grows dramatically with increasing applied stress as well as shifting the dominant peak area from 1600 cm^{-1} (48 THz) down to 1585 cm^{-1} (47.6 THz). These changes are predicted by *ab initio* density functional theory (DFT) calculations of NP versus LP structures as can be seen in the same inset (for details of DFT calculations, see section 3.6.2). Detailed views of the other peaks of ε'' are presented in Figure 4.12, which show similar shifts and intensity increases agreeing with DFT predictions of NP versus LP structures. Note that the DFT predicted ε'' were scaled down so that they could be plotted together with the experimental spectra in an informative way while preserving the shape and relative intensities of the computed peaks.

The ε'' peaks grow rapidly from 0.1 t to 5 t applied load and level off, which is consistent with the decline in the LP fractional content in Figure 4.8b up to 5 t followed by a complete loss of the LP phase. This spectroscopic evidence suggests that the amorphous LP phase has a structure resembling the NP phase, but without long-range periodicity (commonplace in amorphous MOFs[120]). Pellet density also increases rapidly over the same range before levelling off after 5 t and approaching 90% of the theoretical NP crystal density. This finding suggests that the porosity of the amorphous LP phase is similar to the porosity

of the NP phase. Meanwhile, the theoretical unit cell volume of a LP crystal is 1411.95 Å^3 and only 946.7 Å^3 in a NP crystal. Furthermore, the void space in those cells reduces from 54.4% of a LP unit cell to just 17.6% of a NP unit cell (these values are calculated using the Mercury CSD software). Gas adsorption measurements were also performed on pieces of the pellets used in the reflectance measurements. The calculated BET areas are shown in Figure 4.9. Just how accurately these gas adsorption measurements capture the porosity of the pellets is unclear, but they do further demonstrate that there is, in fact, a significant decrease in porosity of pellets prepared under increasing pressure.

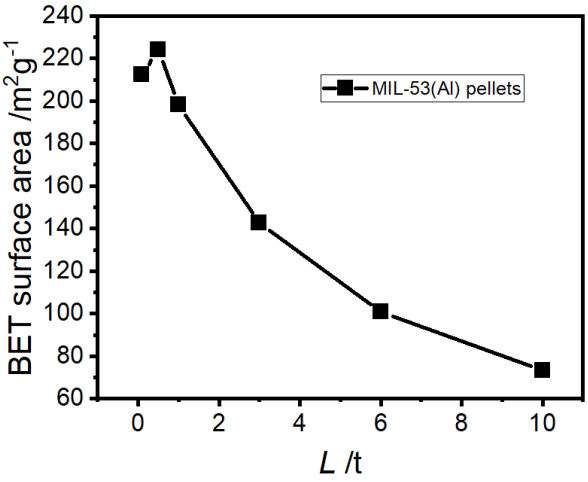

Figure 4.9 BET area of MIL-53(Al) pellets pressed under increasing loads and used for the FTIR reflectance measurements.

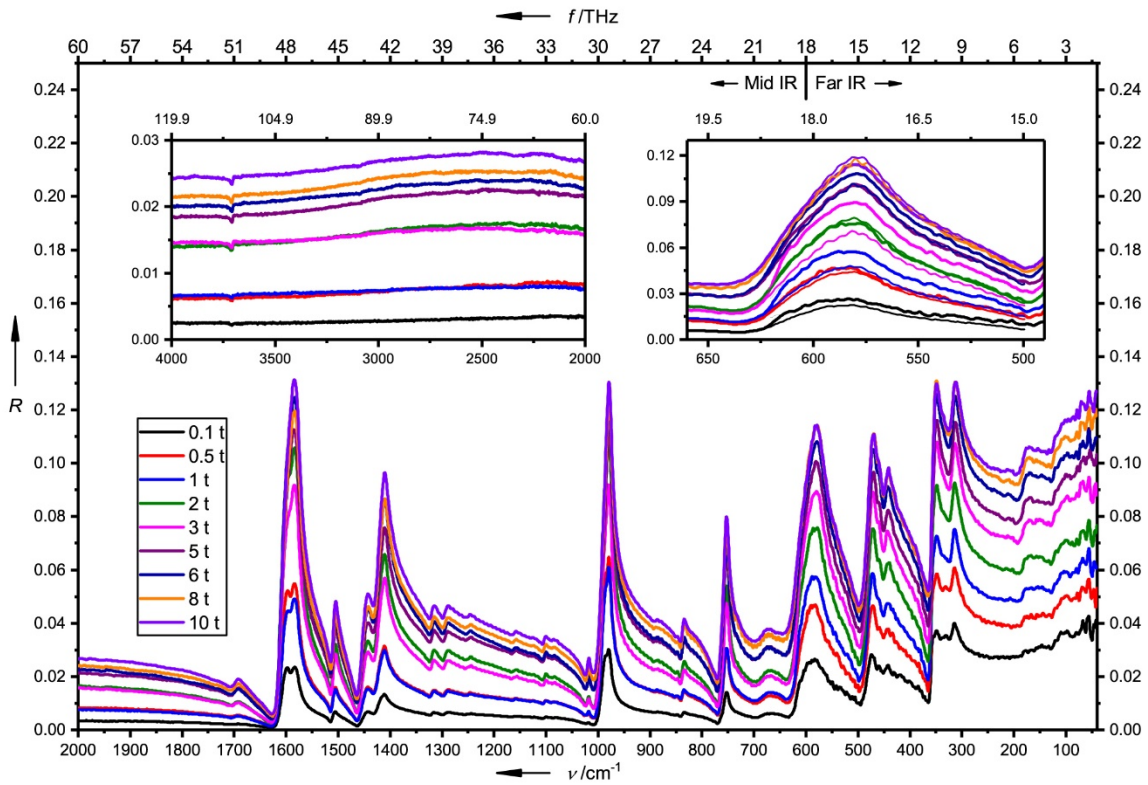

Figure 4.10 Showing the measured reflectance spectra of MIL-53(Al) pellets. The spectra for the far-IR region have been joined with the mid-IR spectra at 620 cm^{-1} (see the code in Appendix 1 on details of joining the spectra using Matlab). Inset b) shows the joined curves (thick) with the as measured (thin) mid-IR spectra to demonstrate the good agreement of far- and mid-IR measurements.

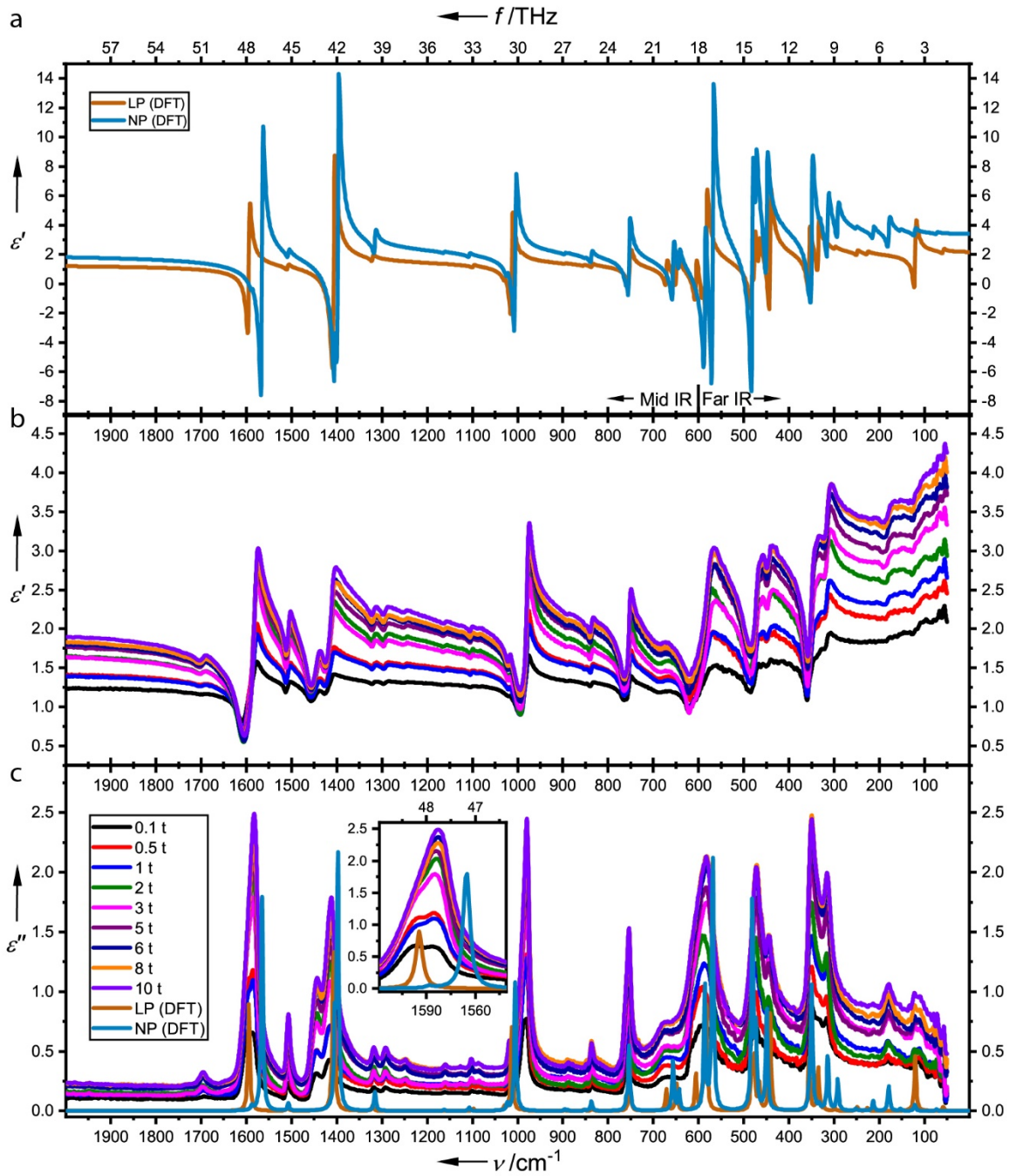

Figure 4.11 Complex dielectric functions of the MIL-53(Al) pellets: (a) real (ε') and (c) imaginary (ε") parts of the DFT-calculated complex dielectric function of purely LP crystals and purely NP crystals. Experimentally obtained (b) real part (ε') and (c) imaginary part (ε'') of the complex dielectric functions of pellets pressed under increasing loads. Note that ε" of the DFT spectra here are scaled down to be comparable with the experimental data, so it is the positions and the relative intensities of the peaks that are important, not the absolute intensities.

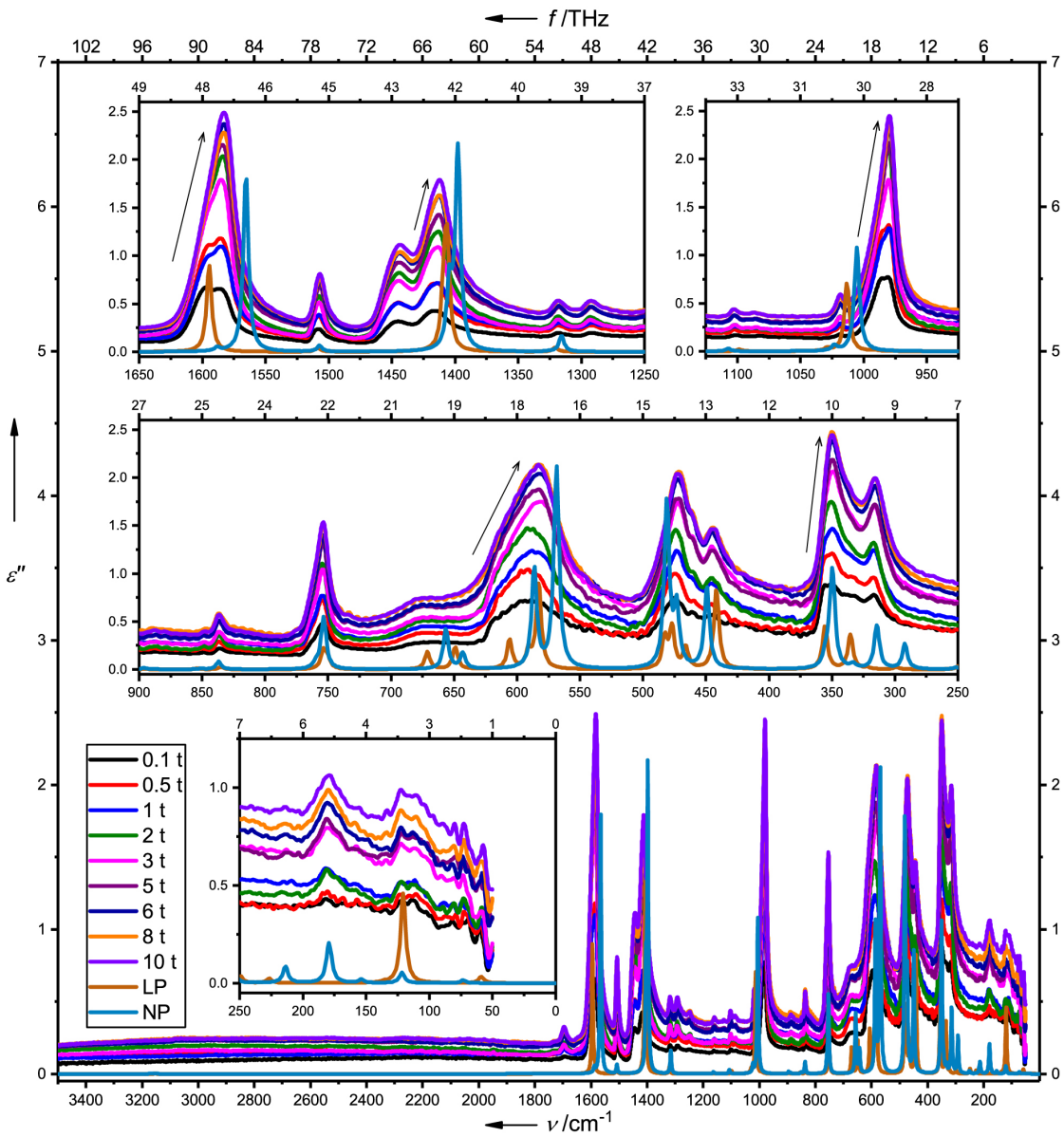

Figure 4.12. The imaginary part of the complex dielectric function obtained experimentally and *via* DFT simulation. Insets show a closer view of the various absorption peaks. Importantly, experimental data shows marked shifts and increases in intensity of peaks with decreasing LP content, which are predicted by the DFT simulations of LP versus NP crystals. These shifts are indicated with arrows in the insets. Note that the DFT spectra are scaled down to be comparable with the experimental data, so it is the positions and the relative intensities of the peaks that are important, not the absolute intensities.

The real part of the dielectric function is tied to the imaginary part by Kramers-Kronig relations, so the factors affecting ε' are the same as those affecting ε''. Figure 4.11 shows the experimental ε' spectra as well as the ε' values predicted by DFT for LP and NP (see Figure 4.13 for an overlapping ε' plot of DFT *vs*. experimental data). The predicted NP ε' is higher than that of LP and has higher amplitude resonances. The positions and relative intensities of the resonances captured by experiment agree well with the DFT predictions. Moreover, and most importantly, the rise in the values of ε' of the pellets with decreasing amounts of LP phase agrees with DFT predictions. This increase is attributed to the decrease in porosity of the MIL-53(Al) pellets from LP+NP to an (amorphized LP)+NP structure. Likewise, the transformation from LP to amorphous phase is essentially causing a fall in porosity of the crystals, thus further decreasing the porosity of the pellet. This is an important outcome: a decrease in void volume significantly increases ε' of pellets with the same chemical composition of initial MIL-53(Al).

Above findings are of importance for the design of "low-*k*" MOFs (*k* here is interchangeable with ε' as used by various conventions, see discussion in section 2.2.1) with the design aim (among others) of keeping the real part of the complex dielectric function below 2.[13] While the spectral range measured in the present experiments lies beyond the range of interest for current electronic technology (MHz-GHz), it is plausible to postulate that the observed effect of decreased porosity is similar beyond the range studied here, and possibly stronger at frequencies below 1 THz since there appears to be a diverging trend being observed in the value of ε' with decreasing frequency of the applied electromagnetic field.

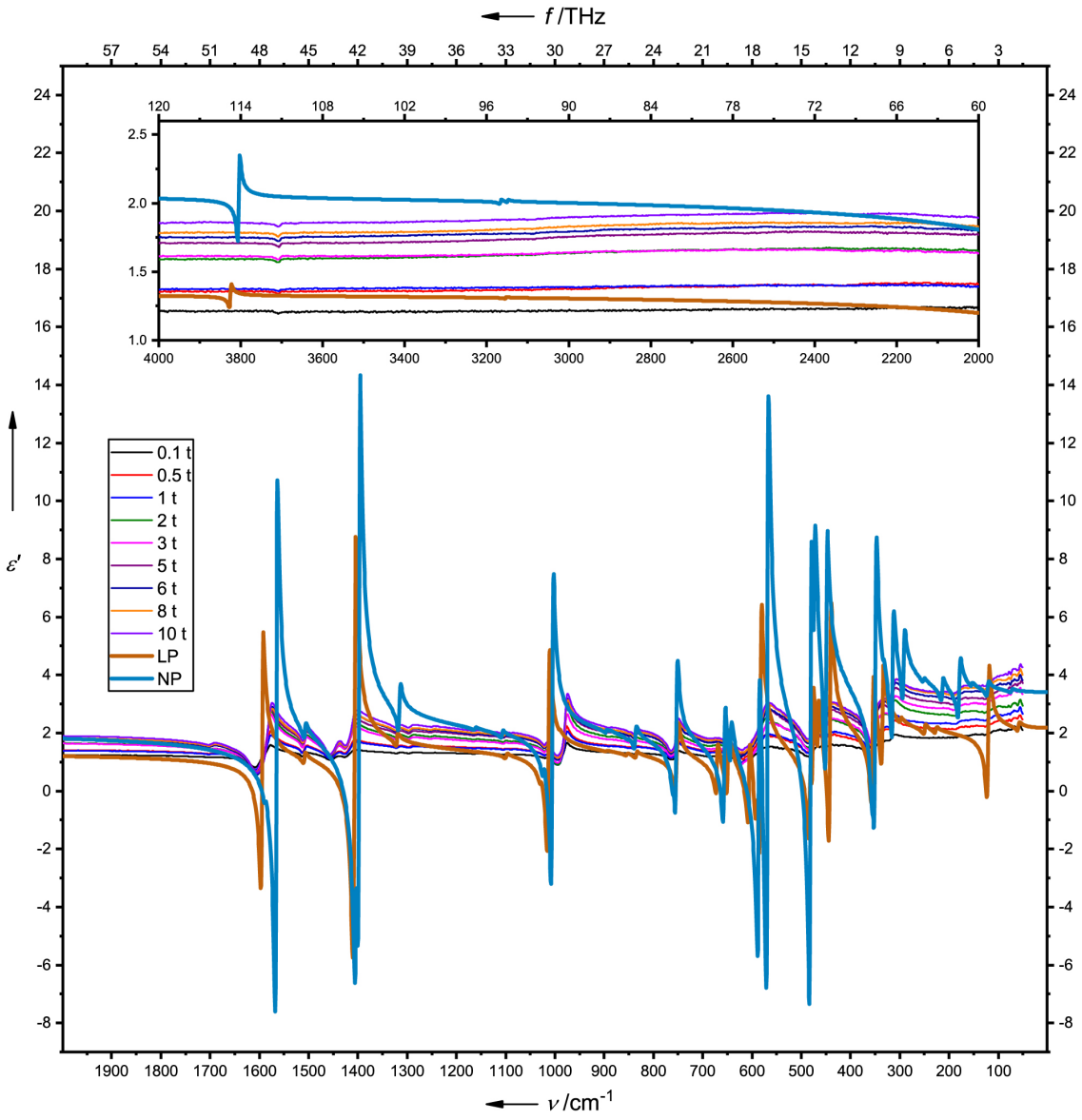

Figure 4.13. The overlap of the values simulated *via* DFT versus experimental values. The agreement is superb: all the oscillatory transitions are predicted *via* DFT and the values rise with increasing NP fraction. The inset shows the datasets up to 4000 cm^{-1}.

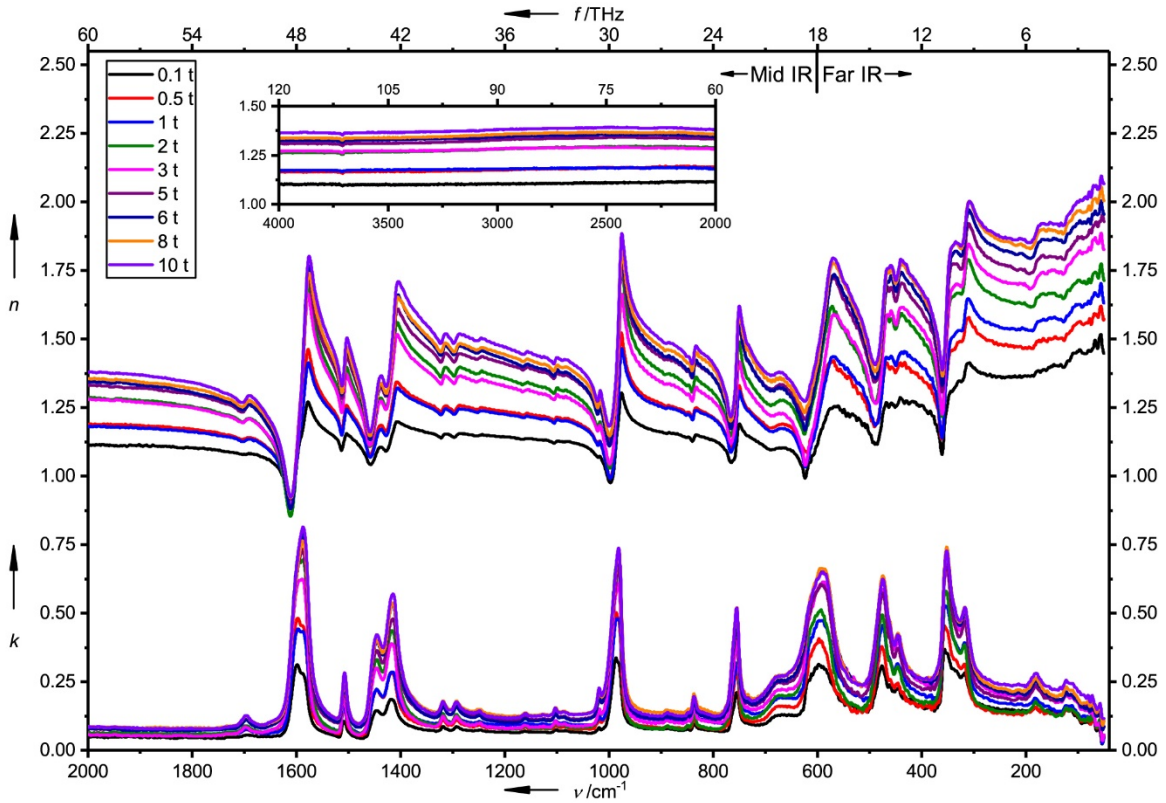

Figure 4.14. Complex refractive indices of MIL-53(Al) pellets in the form of their real (n) and imaginary (k) parts. The inset shows data for n up to 4000 cm^{-1}.

4.5 Summary and Conclusions

This chapter shows that the larger pore size of a MOF material results in a lower real part of the complex dielectric function ε' (or k as in other literature[13, 43]). Therefore, when searching for "low-k" dielectrics, it is prudent to explore those MOF variants, which maximise the pore size. Conversely, for "high-k" dielectrics, the MOF variants that minimise pore size are likely to yield the best performance. In light of this, a MOF structure that could reversibly and controllably switch between the LP ⇌ NP configurations would open the door to a new generation of tuneable dielectrics. The results suggest that MIL-53(Al) is an unlikely candidate for practical deployment in conventional electronics because it has a strong affinity to moisture uptake[7] and due to synthetic challenges.[123] Nevertheless, it was established that in the region of 50-120 THz, the ε' of all prepared MIL-53(Al) pellets is strictly less than 2, and reaching a value as low as ~1.25 for the pellet with the largest fraction

of LP phase (0.1 t). This result is remarkable and the reader is urged to be aware of the possible issue of inter-crystal voids, discussed in detail above, that might affect these figures. Furthermore, the bi-stability of MIL-53(Al) and the achievable high quality of pellets prepared from its powder are advantageous for further development of the method demonstrated in this chapter for studying dielectric properties of MOFs *via* specular reflectance broadband FTIR spectroscopy. This progress opens the door to future studies to accomplish "designer" MOF dielectrics and composite systems.

This chapter demonstrates the efficacy of the specular reflectance method in conjunction with the use of a synchrotron light source for quantifying the dielectric and optical properties of porous framework materials. The proposed approach will be applicable to polycrystalline powders, nanocrystals, nanosheets, etc. Fast acquisition of high-quality spectra is feasible (~minutes), making it possible to rapidly screen a large number of pelleted samples, which can accelerate the development of MOF dielectrics.

Excellent agreement of experimental complex dielectric function data with theoretical DFT calculations has also been achieved, which paves the way towards advancing MOF designs, from the bottom-up in the important field of dielectrics.

Chapter Five

5 OX-1 metal-organic framework nanosheets as robust hosts for highly active catalytic palladium species

5.1 Introduction

This Chapter presents a new catalytic system based on OX-1 nanosheets, incorporating catalytically active Pd species. This Pd@OX-1 guest@host system is rapidly synthesised *via* a one-step single-pot supramolecular assembly, with the possibility of controlling the Pd loading. The structures of the resulting framework and of the active Pd species before and after catalytic reaction are studied in detail using a wide variety of techniques including synchrotron radiation FTIR spectroscopy, inelastic neutron scattering (INS) and X-ray absorption spectroscopy (XAS). Pd@OX-1 is shown to be a highly efficient catalyst of the Suzuki coupling and Heck arylation reactions, with the possibility of recycling the material for at least five cycles of each reaction. Furthermore, OX-1 is shown to possess active sites for Pd attachment, which are not deactivated in the process of the Heck reaction and even survive a complete transformation of crystal structure during the Suzuki reaction.

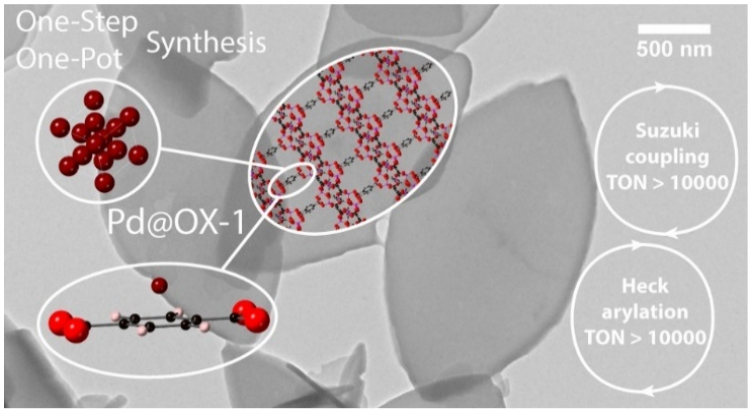

Figure 5.1 Pd@OX-1 catalytic MOF at a glance: TEM image of leaf shaped nanosheets with overlaid OX-1 crystal structure and Pd species. Turn Over Number (TON) is defined as the number of reactions catalysed by each atom of Pd.

5.2 Facile synthesis of Pd@OX-1

A series of OX-1 materials were synthesised with varying loadings of palladium (Pd), whose zero valency form, Pd(0), is an active catalyst for a variety of important organic synthesis reactions. Palladium is embedded in the material during OX-1 synthesis and does not affect the processing time. To incorporate 0.1 – 1 wt.% of Pd into OX-1, 5-50 mg of the precursor $Pd_2(dba)_3$ complex [dba = dibenzylideneacetone] was dissolved in 2 mL of DMF and added to 3 mmol of benzene-1,4-dicarboxylic acid and 6 mmol of Et_3N in 3 mL of DMF. This mixture was then combined with 1.5 mmol of $Zn(NO_3)_2$ in 2 mL of DMF, at which stage a gel was observed and OX-1 crystals were formed. The gel was then transferred to a 50 mL centrifuge tube, with 43 mL of DMF added in the process. This mixture was sonicated until it lost its pink colour, becoming grey-greenish. It was then centrifuged for 5 min at 8000 rpm, to separate the light grey crystals from the light marsh solution of dba and excess BDC in DMF. The crystals were then washed twice in acetone and dried overnight at 100 °C (yield ~500 mg). The colour change from pink to green-grey during the first sonication step is evidence of dissociation of the Pd complex. During this step Pd atoms break free of the $Pd_2(dba)_3$ complex and bind onto OX-1. Gas chromatography - mass spectrometry (GC-MS) and ^1H nuclear magnetic resonance (NMR) spectroscopy measurements were carried out to confirm the presence of free dba in solution, showing that Pd has been dissociated from the $Pd_2(dba)_3$ complex. It is important to note that it was not possible to reproduce the Pd@OX-1 material by dispersing pre-synthesised OX-1 crystals in DMF, adding only $Pd_2(dba)_3$ to the mixture and sonicating – in this case the white OX-1 turned black, indicating that large Pd particles formed over an extended period of suspension in DMF.

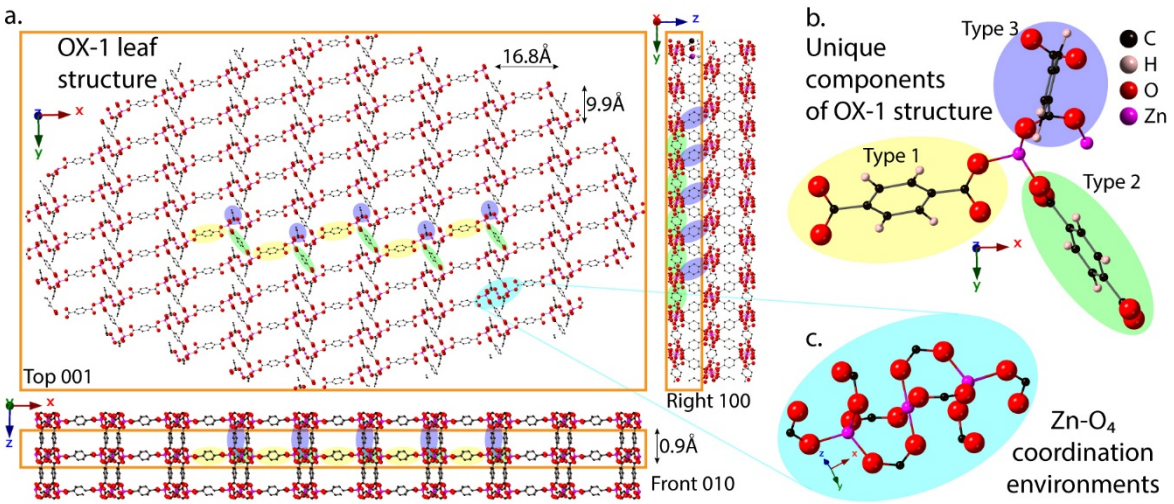

Figure 5.2 Crystal structure of OX-1 nanosheets exhibiting a leaf-shaped morphology: (a) views of a selected 2-D layer (bound by the orange box) making up the 3-D sheet structure; (b) details of the unique components of the structure – 2 unique Zn centres and 3 possible orientations of BDC linker; (c) detail of the Zn coordination environments. Coloured ovals highlight the positions of the different types of structural motifs in the crystal structure.

OX-1 crystal structure[1], shown in Figure 5.2, gives rise to 3D leaf-shaped sheet formation in the one-pot supramolecular synthesis. Single layers of Zn metal centres and BDC linkers (Figure 5.2a) are stacked with an offset of half pore width and a reflection to create the sheets seen in Figure 5.4a-c, e-f. This structure is built up using just five unique components (see Figure 5.2b): two different Zn centres and three different orientations of BDC linkers. Type 1 linkers connect the metal nodes along the x-axis and type 2 linkers connect the metal nodes along the y-axis – together they create the 2D layers of the structure. Type 3 linkers act as spacers and cross-bracing between the 2D layers. Each metal node (see Figure 5.2c) is made of three Zn centres, to which eight BDC linkers are coordinated. Two of the Zn centres have tetrahedral coordination environments and one has a square planar coordination environment.

OX-1 is a highly attractive material for practical applications: the rapid high yield synthesis route (detailed above) is readily scaled – while the nominal reported yield is about 500 mg, as much as 3 g of OX-1 powder was obtained from a single reaction as part of this work with an insignificant increase in processing time. Moreover, OX-1 is readily functionalised: guest species can be incorporated *via* the same single pot method. The possibility of pelletising OX-1, and its functionalised variants, without loss of crystallinity (see Figure 5.3), is also shown in this work, making it even more practicable.

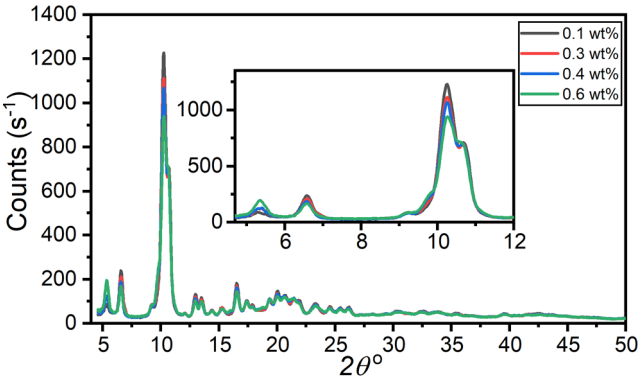

Figure 5.3 XRD patterns of Pd@OX-1 pellets pressed at 50 MPa showing retained structure of OX-1.

5.3 Capture of Pd onto OX-1 active sites

The chemical reaction described above produced leaf-shaped crystals with sizes varying between 5 and 100 μm in length and between 100 nm and 2 μm in thickness. Figure 5.4a-c shows SEM images of pure OX-1 crystals and Pd@OX-1 crystals, while Figure 5.4e-f shows AFM images with an edge detection filter applied and some extracted height profiles. These show that the smaller crystals do not change morphology when increasing amounts of precursor $Pd_2(dba)_3$ complex are added to the gel synthesis. The larger crystals, however, undergo a change: Figure 5.4c shows that the shape of the leaves changes to a more hexagonal geometry and additional smaller layers are seen appearing on top of the large plates upon introduction of 50 mg of $Pd_2(dba)_3$ into the reaction gel. These changes in morphology are captured by XRD patterns shown in Figure 5.4d. The numbers of Bragg reflections between various crystallographic planes changes, seen most strikingly in the changing magnitude of the 5.25° peak corresponding to the (200) crystallographic planes, but the distances between planes do not change because the peaks do not shift to higher or lower angles. The presence of Pd thus does not distort the underlying structure of host OX-1 crystals, but the presence of $Pd_2(dba)_3$ in the gel during synthesis affects their morphology. X-ray photoelectron spectroscopy (XPS) measurement (Figure 5.4g) of 0.2 wt.% Pd@OX-1 (used for all catalysis experiments in this chapter) reveals the predominance of Pd(0) phase of palladium in the material. X-ray fluorescence spectroscopy (XRF) measurements (Figure 5.4h) of a series of variously loaded Pd@OX-1 crystals reveal a linear relationship between the amount of $Pd_2(dba)_3$ added to the reaction gel and the amount of Pd detected in the washed and dried product.

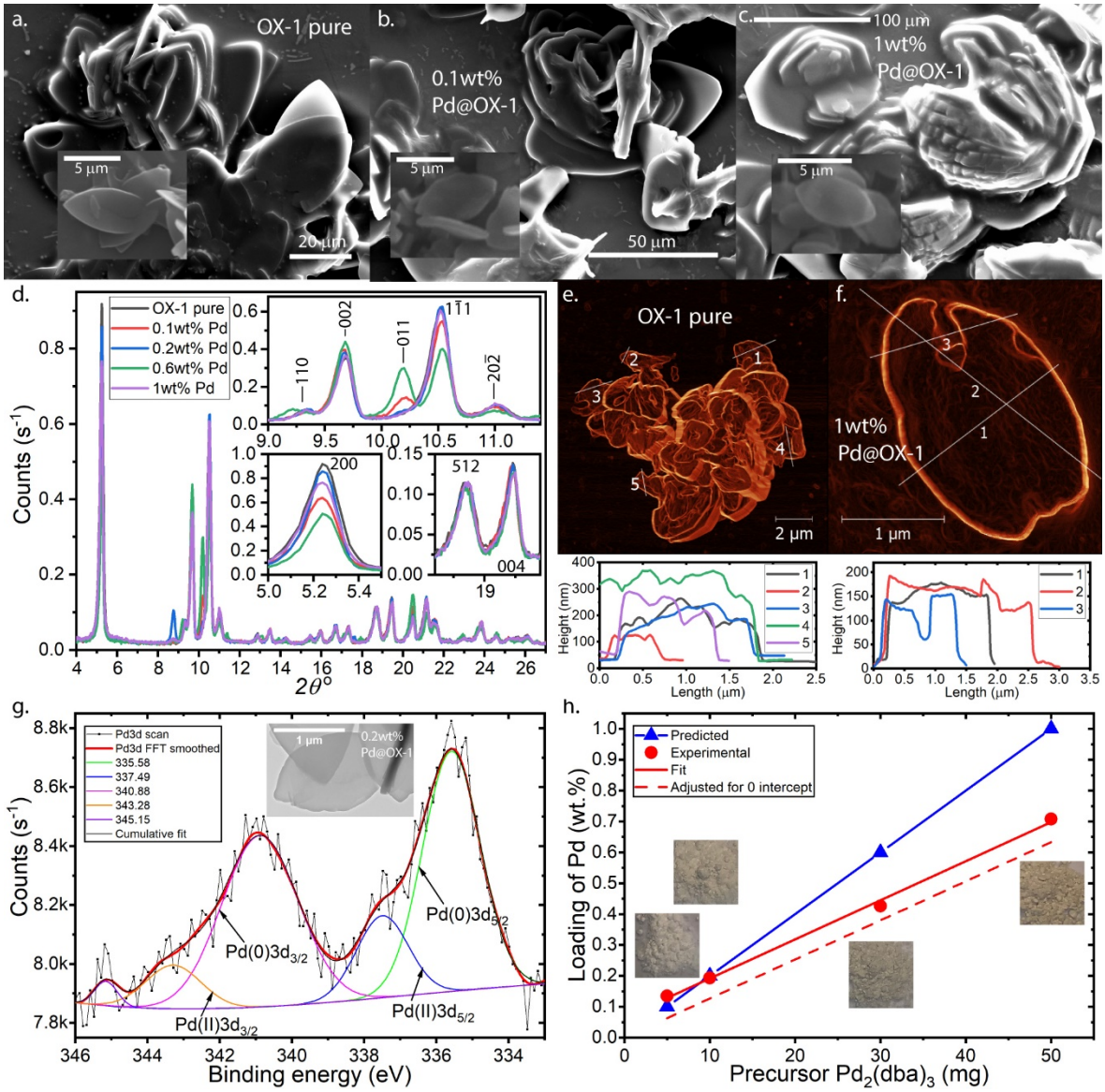

Figure 5.4 OX-1 and Pd@OX-1 crystals: SEM (a-c) and AFM images (e-f) of pure OX-1 (a,e) and Pd@OX-1 (b,c,f); PXRD patterns (d) of a series of Pd@OX-1 materials with different Pd loadings; XPS spectrum (g) of the 0.2 wt.% Pd@OX-1 with a TEM image of the crystal inset; theoretical and experimental Pd content in Pd@OX-1 measured by XRF (h) for the same series of samples as (d), with photos of the respective powders.

Figure 5.5 shows FTIR absorption spectra derived from specular reflectance measurements of pelletised Pd@OX-1 samples *via* the Kramers-Kronig transformation (see section 3.6.1). Raw reflectance spectra and the full derived dielectric function are shown in Figure 5.6. This method of IR spectroscopy provides information on IR active vibrational modes of compounds near the surface of the samples, with depth of penetration of IR beam being material dependent and not easily determined (see section 3.4.1 for details on FTIR). Figure 5.5 also shows inelastic neutron scattering (INS) spectra taken at the TOSCA beamline of ISIS neutron source. INS is a highly penetrating non-selective technique, which provides information on all vibrational modes of the sample (no optical selection rule), probing the whole volume of the material and thus averaging across all local environments and especially sensitive to modes involving hydrogen motions (see section 3.4.2 for details on INS).

The modes probed in FTIR absorption spectra are all detected in INS spectra, but the relative intensities of those peaks do not match. Furthermore, INS spectra also contain IR inactive modes. The spectra for the pristine OX-1 material thus resemble each other but do not match exactly, which might be due to the different penetration depth and selection rules of the two techniques. When Pd is introduced, dramatically different changes are observed by the two methods, which emphasises the complementarity of FTIR and INS spectroscopies.

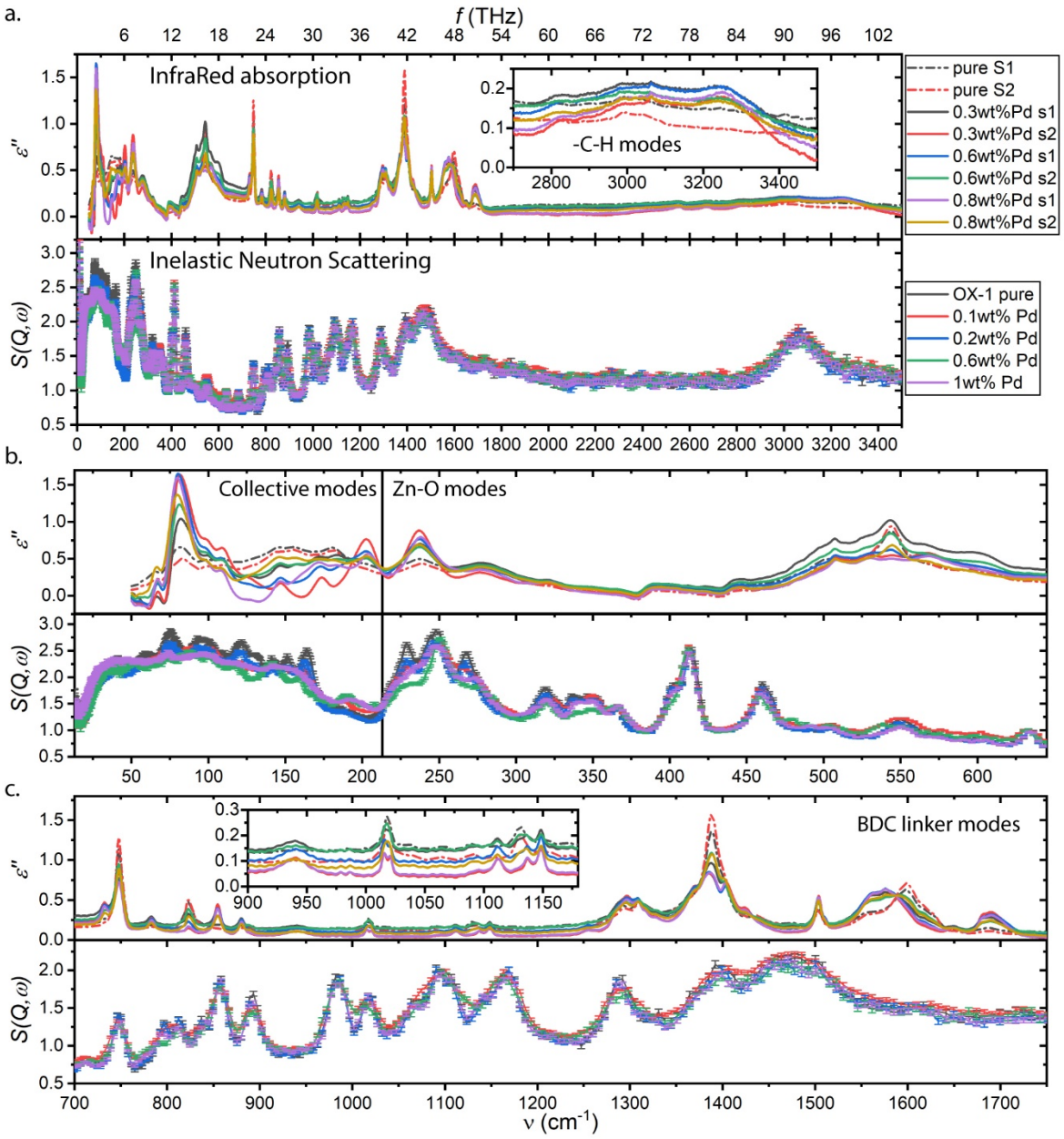

Figure 5.5 Infrared absorption spectra (top of each panel) and inelastic neutron scattering spectra (bottom of each panel) of Pd@OX-1 materials with various Pd loadings. These measurements were carried out on two separately synthesised series of materials as part of two separate beam times.

Ab initio density functional theory (DFT) calculations for a very similar material, MOF-5, were reported by Civalleri and co-workers[124] and can serve as a rough guide for vibrational mode assignment in spectra for OX-1. As indicated in Figure 5.5, collective modes of the framework are present below 200 cm^{-1}, various Zn-O bond modes appear between 200 and 650 cm^{-1}, and the various modes of BDC linkers, or their components, appear above 700 cm^{-1}. Both IR and INS spectra show significant changes in collective modes and Zn-O bond modes, but only IR spectra show noticeable changes in the BDC linker modes. Closer examination also reveals that the changes below 700 cm^{-1} are different for IR and INS spectra. IR reveals a dramatic enhancement of the collective mode at 80 cm^{-1}, and noticeable enhancement of bands at 200 and 280 cm^{-1}. INS spectra, on the other hand, show dampening of most collective modes up to 175 cm^{-1}, as well as the sidebands of the triple peak in the region 213-280 cm^{-1}. The BDC linker modes are also affected differently. IR spectra show dramatic changes in practically all BDC modes, whereas INS spectra show minor changes, which are difficult to attribute to introduction of Pd in the sample. Moreover, none of the changes in IR spectra appear to scale with the amount of Pd loaded into the samples. This is most clearly seen in the shift of peaks from around 1600 cm^{-1} down to about 1575 cm^{-1}: all studied loadings appear to have the same step-like effect. However, the changes in INS spectra appear to follow the same trend as the changes in magnitudes of XRD peaks, most notably the (200) peak, shown in Figure 5.4d. The significantly lower frequency (<700 cm^{-1}) changes in INS spectra can be attributed to the changes in morphology of the crystals discussed above. These INS spectra therefore suggest that most modes in Pd@OX-1 composites are not significantly affected in the presence of Pd. The IR spectra, however, identify the BDC linkers of OX-1 as primary interaction sites between Pd guests and the host framework. The BDC linkers are thus the most likely active sites for attachment of Pd species in the Pd@OX-1 composite system.

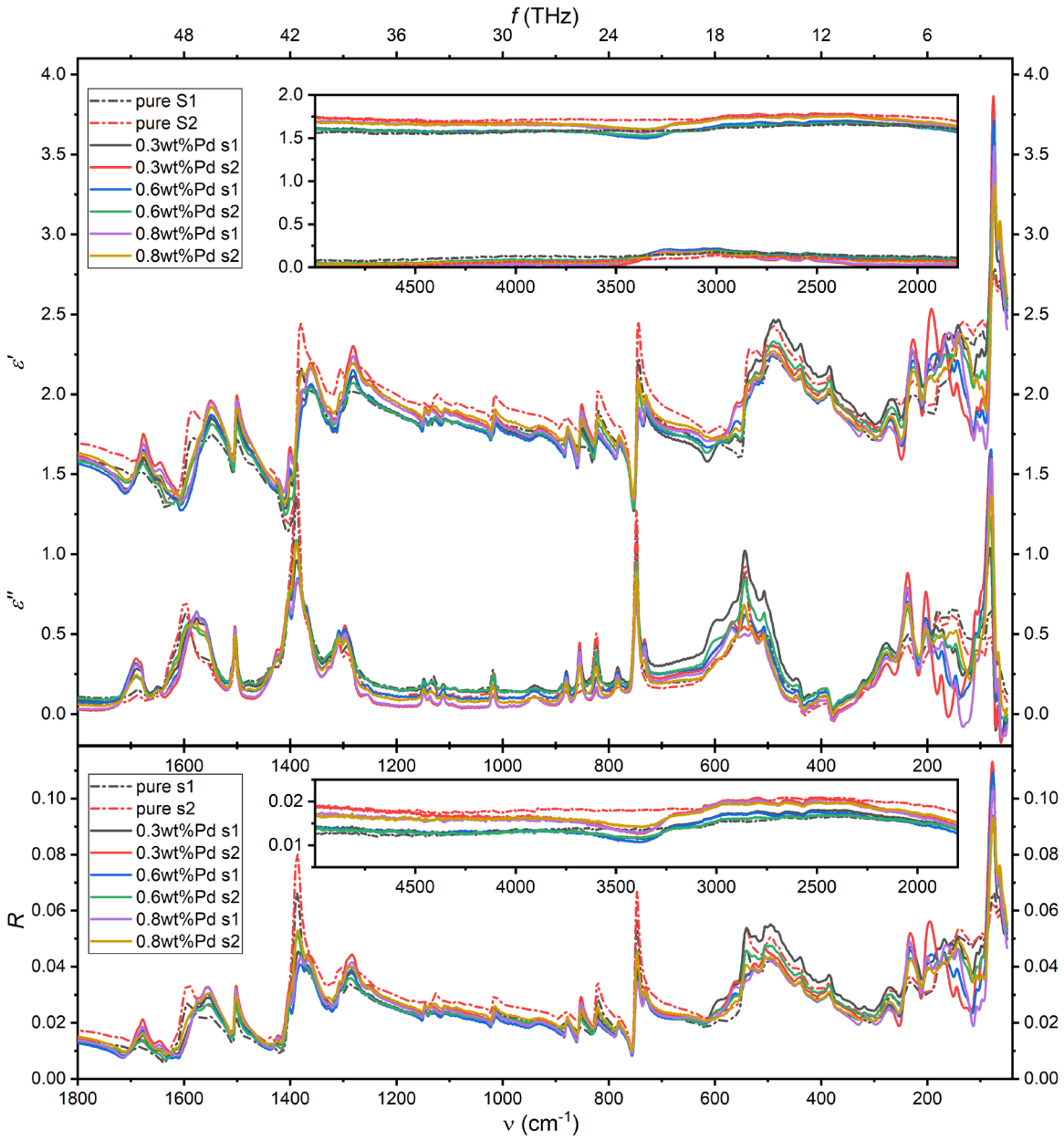

Figure 5.6 Specular reflectance FTIR results: reflectivity spectra (*R*) and its Kramers-Kronig transformation into the real (ε') and imaginary (ε'') parts of the complex dielectric function.

5.4 Catalytic performance of guest Pd species

Catalytic performance of 0.2 wt.% Pd@OX-1 was studied in the Suzuki cross-coupling and the Heck arylation reactions, as they are well known to be efficiently catalysed by multiple palladium species.[17-18, 69] All catalytic studies were performed under air in order to examine the robustness of the material.

In the Suzuki coupling of phenylboronic acid with iodobenzene (Figure 5.7a) catalyst activity was studied by decreasing the Pd loading from 0.2 mol% down to 0.002 mol%, where the latter corresponds to 20 ppm loading relative to PhI. The reaction was conducted in *i*-PrOH:H_2O (1:1) media and the product formation was analysed by GC-MS. In all three cases > 99% quantitative yields of biphenyl were reached (Figure 5.7b). Because of the high yields with PhI, Ar-X (which is of lower reactivity) was used to address the material activity: 4-bromoanisole with 20 ppm catalyst loading. After 3 hours of the reaction at 100 °C, 120 °C, and 140 °C the product yield grew from 55% up to 82%. Moreover at 150 °C 91% yield was achieved already after 1 hour, and after 4 hours reached 97% of the 4-methoxybiphenyl product (Figure 5.7c). These results are also summarised in Table 5-1. Following these results, preliminary scope studies were conducted, using 0.05 mol% of Pd at 100 °C. Both aryl iodides and bromides gave yields from good to excellent (see Figure 5.8). Electron properties of the substituents in aryl halide or aryl boronic acid have no significant effect on the outcome of the reaction. Steric bulkiness provided by *orto*-substituent (2-iodobenzaldehide) also did not affect an excellent product yield. Even though visually the microstructure of the catalyst material changed after the reaction, seeming to be more agglomerated, the possibility of catalyst recycling with PhI was investigated, which is usually problematic because the freed iodide species in the solution are known to poison heterogeneous catalysts. The reaction was stopped after 2 hours (98%

yield), material was centrifuged, washed and re-used for another four cycles without significant loss of activity (see Figure 5.7d).

Next, the catalyst behaviour in the Heck reaction was studied (Figure 5.7e). The approach was similar, butyl acrylate arylation with PhI was investigated with decreasing Pd loading. The outcome was roughly the same as for the Suzuki coupling. Butyl cinnamate was obtained with > 99% yield after 24 hours at 150°C with only 20 ppm of Pd (Figure 5.7f). Although the catalyst was active towards iodide, when switching to 4-bromoanisole only traces of the reaction product were detected after 24 hours at an elevated temperature of 180 °C for either butyl acrylate or styrene. However, as with Suzuki coupling, the material could be recycled for five times, showing only slight loss of activity for PhI conversion (Figure 5.7g). These results are also summarised in Table 5-2. Even though the medium in which the Heck reaction is performed is strikingly similar to the medium in which Pd@OX-1 is synthesized (DMF, Et_3N), the MOF appeared visually unchanged after the reaction except a slight change in colour. Substrate scope was evaluated for the Heck reaction. Yields from good to excellent were obtained for all substrates (see Figure 5.8) with either electron withdrawing or electron donating groups. Utilisation of an *orto*-substituted iodotoluene resulted in lower yield of 81%. Comparing different acrylates it was observed that longer chain provides higher yield (Me- – 84%, Et- – 87%, *n*-Bu- – 98%); while with increasing steric bulkiness the yield of the product was slightly lowered (*t*-Bu- – 92%).

This ensemble of results demonstrates the high catalytic activity of Pd@OX-1 in a broad variety of conditions, as well as retainment of catalytic properties after both the Suzuki coupling and the Heck reactions.

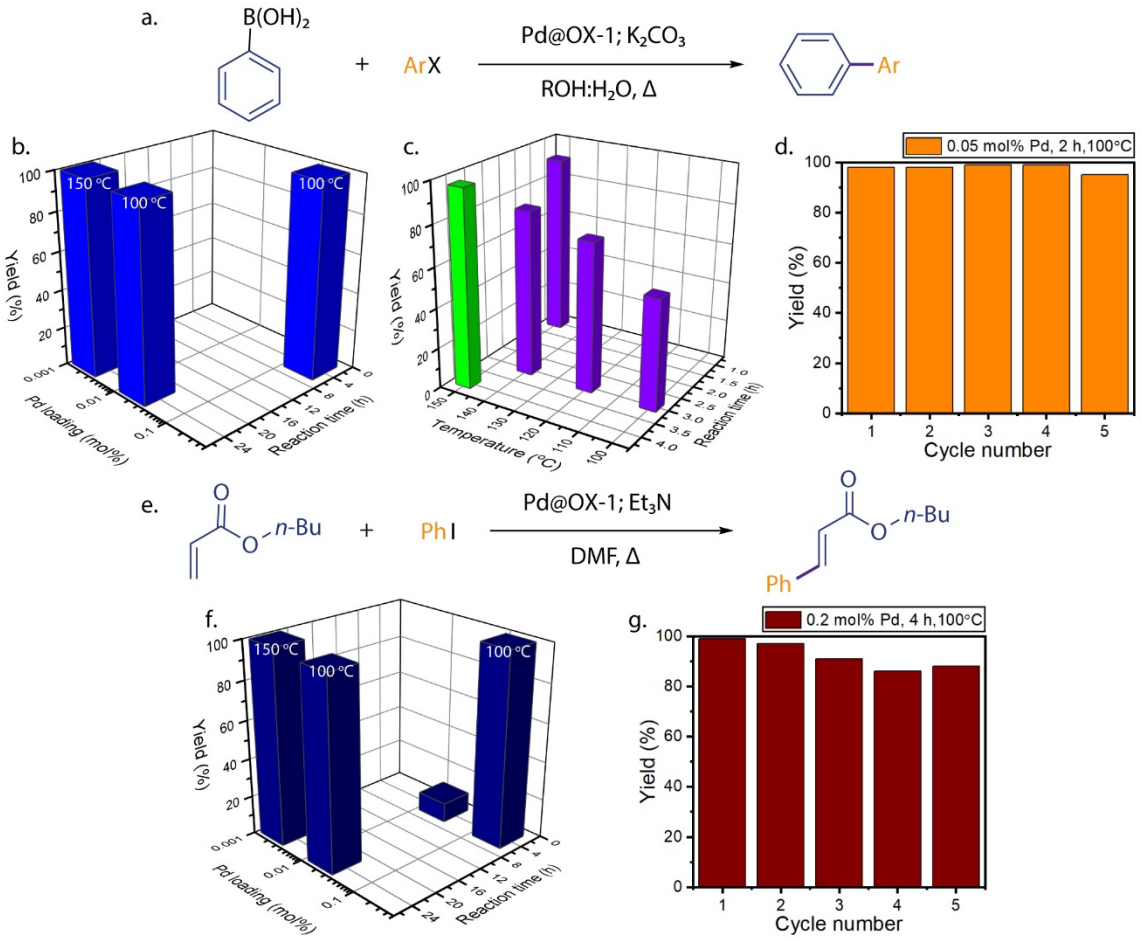

Figure 5.7 Pd@OX-1 catalytic performance in the Suzuki and Heck reactions. (a) Model Suzuki reaction; (b) variation of Pd loading for the reaction, ArX = PhI, ROH = MeOH; (c) optimization of the reaction conditions, ArX = 4-bromoanisole with 0.002 mol% of Pd, ROH = *i*-PrOH; (d) recycling of the material, ArX = PhI with 0.05 mol% of Pd at 100 °C, ROH = *i*-PrOH. (e) Model Heck reaction; (f) variation of Pd loading; (g) recycling of the material, 0.2 mol% of Pd at 100 °C. This data is also given in Table 5-1 and Table 5-2.

Table 5-1 Pd@OX-1 performance on the Suzuki reaction

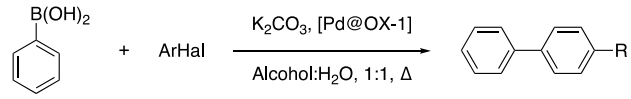

ArHal	[Pd], mol%	Solvent	Temperature, °C	Time, h	Yield, %
Activity of various Pd loadings					
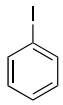	0.2	MeOH:H_2O	100	4	> 99
	0.02		100	24	99
	0.002		150	24	> 99
Conditions optimization					
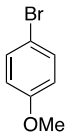	0.002	*i*-PrOH:H_2O	100	3	55
			120	3	74
			140	3	82
			150	1	91
			150	4	97
Recycling possibility					
	0.05 (Cycle 1)	*i*-PrOH:H_2O	100	2	98
	0.05 (Cycle 2)			2	98
	0.05 (Cycle 3)			2	99
	0.05 (Cycle 4)			2	99
	0.05 (Cycle 5)			2	95

Table 5-2 Pd@OX-1 performance on the Heck reaction

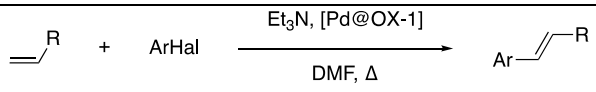

Olefin	ArHal	[Pd], mol%	Solvent	Temperature, °C	Time, h	Yield, %
Activity of Various loadings						
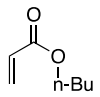	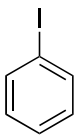	0.2	DMF	100	4	> 99
		0.02	DMF	100	4	10
		0.02	DMF	100	24	98
		0.002	DMF	150	24	> 99
Recycling possibility						
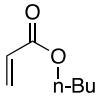	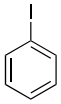	0.2 (Cycle 1)	DMF	100	4	> 99
		0.2 (Cycle 2)	DMF	100	4	97
		0.2 (Cycle 3)	DMF	100	4	91
		0.2 (Cycle 4)	DMF	100	4	86
		0.2 (Cycle 5)	DMF	100	4	88

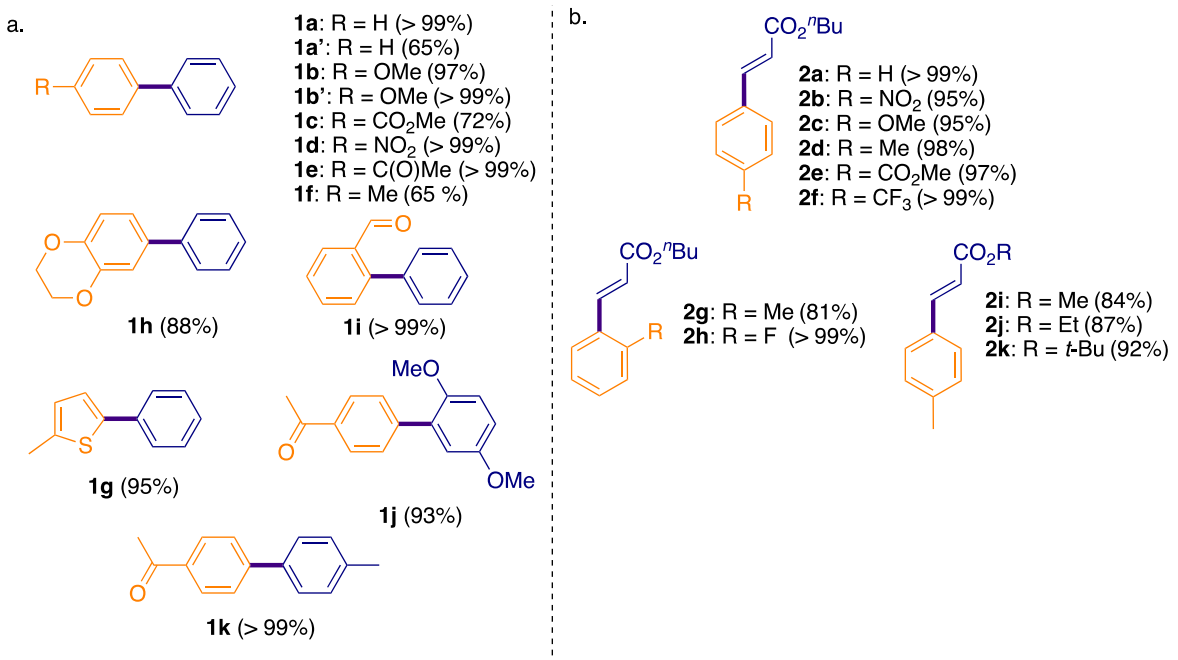

Figure 5.8 Pd@OX-1 catalysed Suzuki and Heck reactions: Yields determined by ^{1}H NMR; Aryl iodide used as substrate: **1a-c**,**1g**,**2a-k**; aryl bromide used as substrate: **1a'**,**b'**,**d-f**, **h-k**

5.5 Local structure and persistence of active sites

In recent decades diverse catalytic applications of Pd nanoparticles in cross-coupling reactions were facilitated by release of highly active Pd species to solution *via* leaching.[19] However, leaching of Pd species to solution often leads to dramatic loss of catalytic activity on the next cycle due to metal losses. Re-capture of metal species from solution back to the surface of support after completing the catalytic process is the key challenge for retaining activity and avoiding contamination of reaction products with palladium traces. Support materials do not routinely retain the ability to re-capture metal species from solution after catalytic transformation under harsh conditions, causing significant reconstruction of surface. Thus, the observed performance of the material developed here prompted more detailed characterization to be conducted.

Pd@OX-1 owes its good catalytic performance and the possibility of recycling the material to the structure and persistence of its BDC active sites for Pd attachment. These are

studied by probing the structure and local environments of Zn centres of OX-1 and of the various Pd species.

TEM imaging detects the presence of fine scale Pd nanoparticles on as synthesised 0.2 wt.% Pd@OX-1 crystals (Figure 5.9a) with a size range of *ca.* 2-5 nm. Smaller particles were not detected at this microscope's resolution. After the Heck reaction (see section 3.5.3 for reaction details) the morphology of the crystals appears to be unchanged, but most of the Pd nanoparticles appear to have grown in size, with particles as large as 10 nm (Figure 5.9b). After the Suzuki reaction (see section 3.5.2 for reaction details), however, the shape of the recovered crystals changes dramatically to oblong particles. The size of Pd nanoparticles became even larger than in the case of the Heck reaction reaching 15-20 nm, seen in TEM images (Figure 5.9c). XRD measurements (Figure 5.9d) reveal that crystal structure of Pd@OX-1 does not change during the Heck reaction but is completely different after the Suzuki reaction. This is remarkable: not only can OX-1 survive in DMF at 100°C for at least 4 hours for the Heck reaction and recapture[18, 125-129] the active Pd species, but even after a dramatic change in microstructure during the Suzuki reaction it retains the Pd species and is still active in following cycles. This is a rare example of Pd recapture after total reconstruction of the material.

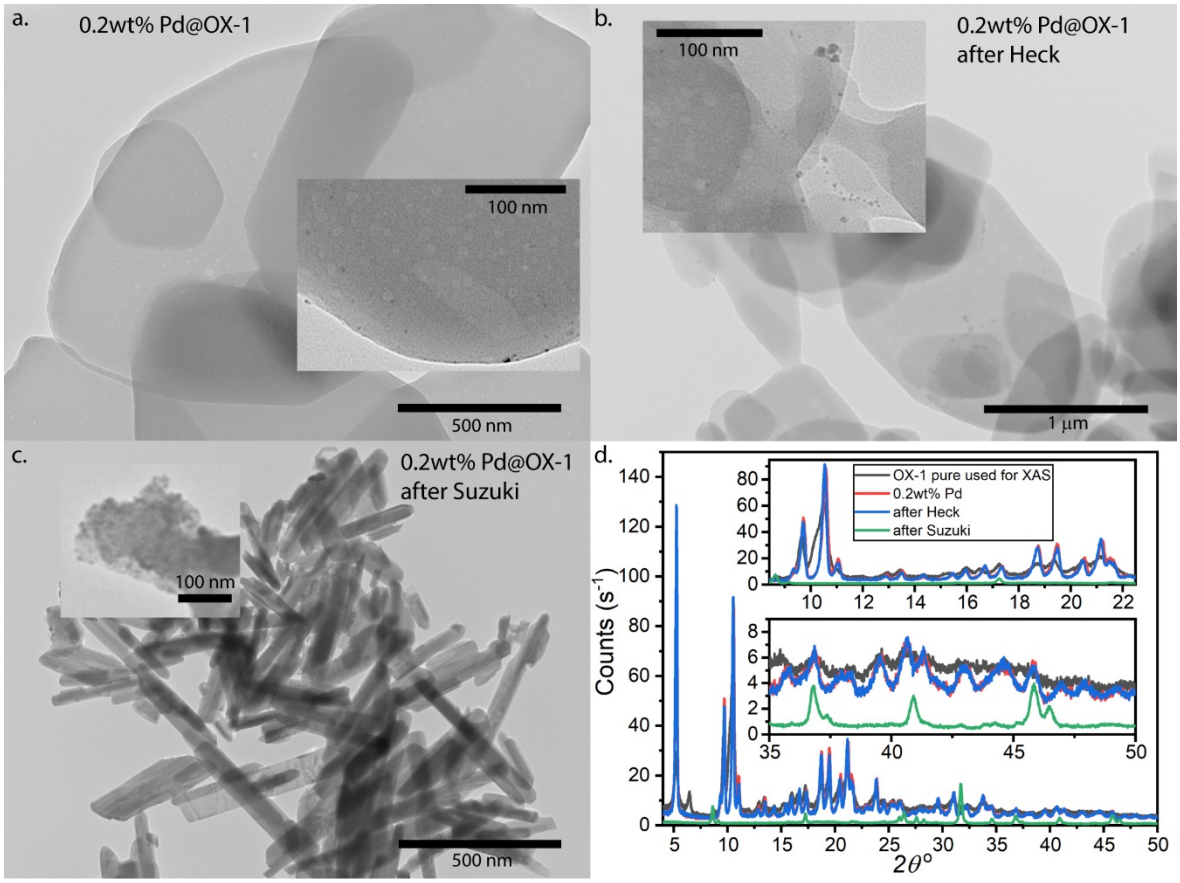

Figure 5.9 TEM images of (a) as synthesised Pd@OX-1 crystals and the same crystals after the (b) Heck and (c) Suzuki reactions. (d) XRD patterns for of the same set of samples.

X-ray Absorption Spectroscopy (XAS) experiments were performed at the B18 beamline[111] of Diamond Light Source to study the possible changes in OX-1 crystal structure, as well as the structure and location of the attached Pd species, with results shown in Figure 5.10. X-ray Absorption Near Edge Structure (XANES) and Extended X-ray Absorption Fine Structure (EXAFS) data were collected at the Zn and Pd K-edges for the 0.2 wt.% Pd@OX-1 as synthesised sample, a sample that was used to catalyse the Heck reaction, and a sample that was used to catalyse the Suzuki reaction. Moreover, precursor $Pd_2(dba)_3$ crystals and a sample of Pd nanoparticles on graphite[130] derived from $Pd_2(dba)_3$ were measured at the Pd K-edge for reference. This XAS data reflects the local structure around Zn and Pd atoms in the Pd@OX-1 system.

Zn K-edge measurements reveal that the introduction of $Pd_2(dba)_3$ into the synthesis does not change the framework structure around the Zn centres of OX-1. The spectra for OX-1 and Pd@OX-1 coincide almost exactly. There is only a slight increase of the white-line intensity when loading Pd into the host framework. This can be ascribed to a subtle enhancement of the localisation of the final electronic states of Zn. This difference is negligible in the EXAFS signal. Thus, the local structure around Zn can be considered not affected by the loading of Pd.

Zn K-edge data further shows that the Zn environment of Pd@OX-1 does not change at all during the Heck reaction, confirming TEM and XRD observations discussed above. During the Suzuki reaction, however, the Zn environment is significantly altered: the profile of the XANES changes drastically, becoming more structured. On the other hand, the pseudo radial distribution function $|\chi(R)|$ of the sample after Suzuki reaction, in particular the first coordination shell is similar to the one obtained for the pristine Pd@OX-1 sample, thus the short-range order appears to be preserved. The changes in the XANES may be due to distortions in the bond angles which influences mainly the multiple scattering contributions. Indeed, the EXAFS signal for the sample after Suzuki reaction is more complex than the one for the original compound. This again confirms TEM and XRD observations and identifies this new structure as a new MOF-type material with long range periodicity with a consistent local environment.

Pd K-edge data, Figure 5.10b, d, f, shows that the XANES of the samples after catalytic reactions are similar to the one obtained from the pristine Pd@OX-1 sample. The only difference is that the broad white-line of the pristine sample, characteristic of low order environments, splits into two structures after the reaction. This XANES profile with the two structures is very similar to the one obtained for Pd/C sample which agrees with the observation of having larger Pd nanoparticles than the pristine sample.

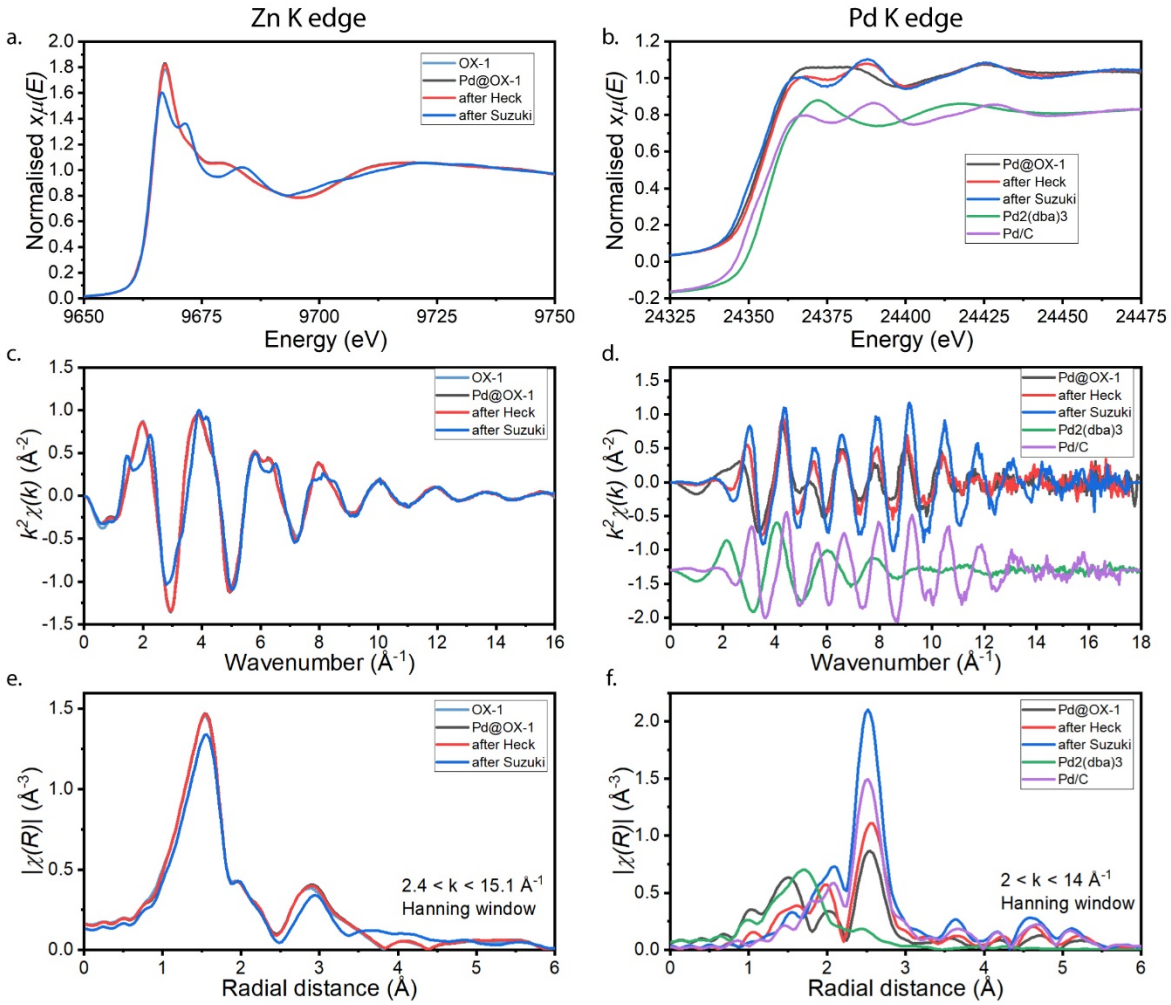

Figure 5.10 X-ray absorption spectra at the Zn (a,c,e) and Pd (b,d,f) K-edge of pure OX-1, pristine 0.2 wt.% Pd@OX-1, Pd@OX-1 after the Heck and Suzuki reactions, of $Pd_2(dba)_3$ crystals and of Pd nanoparticles on graphite. In panels (b) and (d) the spectra of $Pd_2(dba)_3$ and Pd/C have been shifted vertically for sake of comparison. Data processing and fitting were done in Demeter.[110]

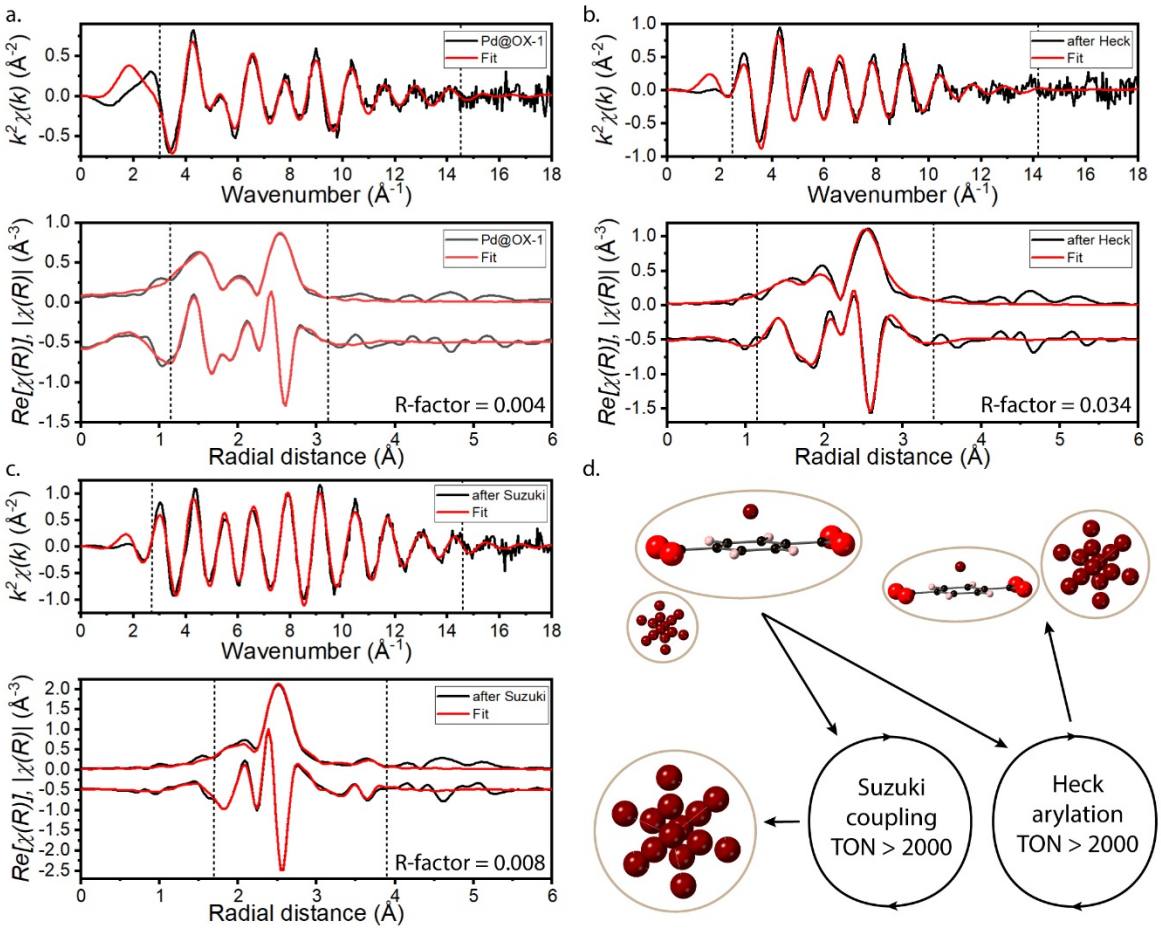

Figure 5.11 Fitting of EXAFS spectra for the as synthesised (a) 0.2 wt.% Pd@OX-1, (b) Pd@OX-1 after the Heck reaction and (c) Pd@OX-1 after the Suzuki reaction using models of Pd environments given in (d). The "Turn Over Number" (TON) is defined as the number of reactions catalysed per Pd atom. Data processing and fitting were done in Demeter.[110]

The model used for performing the fitting analysis of the EXAFS data considered the Pd-C scattering path to the carbon atoms of benzene rings on BDC linkers, where Pd is assumed to be equidistant from all six members of the ring, and the Pd-Pd scattering paths characteristic of the face-centred cubic (FCC) Pd bulk. The fits can be seen in Figure 5.11 and the results from the fit are given in Table 5-3. The model seems to agree reasonably well with the experimental data despite its simplicity. A very low coordination number of Pd in as synthesised Pd@OX-1 is obtained from the fit, which suggests that the clusters of Pd inside the composite are very small, reflecting that a very high number of Pd atoms belong to surfaces of Pd particles. It is therefore likely that the as-synthesised Pd@OX-1 contains atomic Pd and Pd in small clusters coordinated to the π-system of the benzene rings of BDC linkers. Only a small number of particles are as big as those seen in the TEM images, while most of Pd in the sample is not resolved. After both catalytic reactions, the coordination number of the Pd-Pd contribution increases, which indicates that the size of Pd nanoparticles grows, in agreement with the TEM images. In the case of the after Suzuki sample in particular, the contribution of the Pd on ligand component of the model was found to be negligible, so it was excluded from the fit.

Some recent results[64-65] also show that a shift to lower energy and a sharpening of the first near-edge peak of the XANES region are indicative of palladium hydride formation. In addition, this hydrogen bonding is accompanied by an elongation of the Pd-Pd distance (see Table 5-3). It is thus possible that during the Suzuki reaction some heteroatom insertion of hydrogen into the Pd nanoparticles may take place.

Table 5-3 EXAFS fitting parameters for Pd@OX-1 as synthesised, after Heck and after Suzuki reactions. S_0^2 was fixed to a value of 0.88 obtained from the fit for the EXAFS spectrum of reference Pd foil measured simultaneously with the samples. Correlation between variables is less than 90% for all fits reported.

Pd@OX-1 as synthesised				
k-range	3-14.5	Independent points	14.3	R-factor
R-range	1.15-3.15	Number of variables	7	0.004
Path	N	ΔE_0 (eV) (E_0 = 24355)	R (Å)	σ^2 (Å^2)
Pd.1	4.3 ±0.3	-2.8 ±0.4	2.798 ±0.003	0.009 ±0.0004
C7.1	4.0 ±0.3	-2.8 ±0.4	2.037 ±0.004	0.005 ±0.0009
Pd@OX-1 after Heck				
k-range	2.5-14.2	Independent points	16.4	R-factor
R-range	1.15-3.4	Number of variables	7	0.034
Path	N	ΔE_0 (eV) (E_0 = 24355)	R (Å)	σ^2 (Å^2)
Pd.1	10.4 ±0.9	-3.5 ±0.6	2.774 ±0.008	0.014 ±0.001
C7.1	1.2 ±0.7	-3.5 ±0.6	2.003 ±0.025	0.005 ±0.005
Pd@OX-1 after Suzuki				
k-range	2.7-14.6	Independent points	16.4	R-factor
R-range	1.7-3.9	Number of variables	6	0.008
Path	N	ΔE_0 (eV) (E_0 = 24353)	R (Å)	σ^2 (Å^2)
Pd.1	10.6 ±0.6	-2.1 ±0.4	2.766 ±0.003	0.009 ±0.0004
Pd.2	5.3 ±0.3	-2.1 ±0.4	3.847 ±0.02	0.008 ±0.002

5.6 Summary and Conclusions

This chapter presents a method of rapid *in situ* functionalisation of OX-1 metal-organic nanosheets with catalytically active Pd species, obtained *via* a one-step one-pot supramolecular synthesis route. The loading of Pd can be controlled by adjusting the amount of $Pd_2(dba)_3$ added to the synthesis. The resulting Pd@OX-1 composite crystals contain predominantly atomic and small cluster Pd species, which selectively reside on benzene rings of the BDC linkers. The composites are shown to efficiently catalyse the Suzuki coupling and the Heck arylation reactions under a variety of conditions. The material retains the ability to recapture active Pd species during the reactions, which is not a routine property of common substrates for Pd nanoparticles. This enables the demonstrated potential for Pd@OX-1 to be recycled in reaction cycles of either type without loss of activity. More detailed studies are warranted to fully explore catalytic potential of the developed material as follow-on work, to systematically investigate the influence of various reaction conditions and substrates, amongst others. Undoubtedly, with its variety of Pd species and tunability of Pd loading, Pd@OX-1 shows promise as an attractive system for further study, with potential industrial applications in organic synthesis.

Chapter Six

6 Acetone sensing behaviour of ZnQ@OX-1 *via in situ* transmission FTIR spectroscopy

6.1 Introduction

This chapter presents advances on the current understanding of the ZnQ@OX-1 composite sensing MOF system reported by Chaudhari *et al* [1] and discussed in literature review section 2.4. In their report Chaudhari *et al* [1] provide phenomenological observations of acetone vapour sensing by ZnQ@OX-1, but the mechanism behind acetone vapour sensing in air is not explored in great detail. This chapter presents results from operando transmission FTIR experiments and elucidates the response of several key vibrational bands of ZnQ@OX-1 to acetone vapour, as well as identifying which bands are lost when the material stops reverting to its initial state after acetone exposure. The experiments were performed using a sample cell through which N_2 gas was continuously passed, while acetone was intermittently injected into the system upstream of the sample cell. The FTIR spectra were continuously measured, giving time-resolved data. Moreover, by varying the amount of acetone injected into the system it was possible to vary the concentration of acetone in the carrier gas reaching the sample cell, thus starting to quantify the material's response.

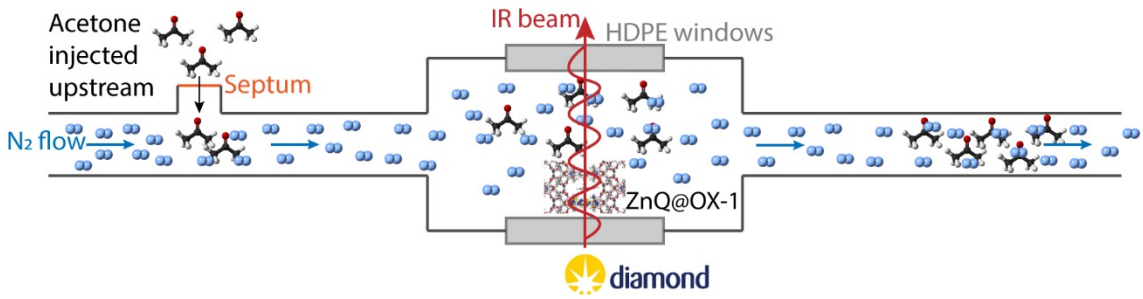

Figure 6.1 Schematic of the operando transmission FTIR experiments at the B22 MIRIAM beamline of the Diamond Light Source.

6.2 Acetone propagation through sample cell

It is first necessary to establish the positions of acetone absorbance peaks with respect to the ZnQ@OX-1 IR active modes, as well as establishing what peaks are unique to the composite material as opposed to pure OX-1. Figure 6.2a shows the FTIR spectra of both pure OX-1 and ZnQ@OX-1 guest@host crystals under dry N_2 gas flow, as well as the maximum measured acetone vapour spectrum. The acetone vapour bands are of comparable magnitudes to the smaller peaks in the MOF spectra, while most bands corresponding to ZnQ@OX-1 do not coincide with the Acetone vapour bands. Moreover, the peaks of ZnQ@OX-1 marked with an asterisk (*) likely originate from ZnQ guests inside OX-1 and will be seen to respond to acetone vapour. Some of the OX-1 peaks detected in the pure sample also appear to be altered in the ZnQ@OX-1 composite, but there is a multitude of factors possibly driving these changes, which are difficult to ascertain without complex *ab initio* simulations.

Figure 6.2b shows a 2D projection of a 3D surface of one of the acetone vapour triple bands (1710-1800 cm^{-1}) from the moment acetone is injected into the system upstream of the sample cell. At 5 ccpm of N_2 flow through the system, acetone vapour starts reaching the sample cell roughly 3 min after injection upstream of the cell, reaching maximum concentration about 4 min after injection. The maximum concentration is maintained for about 4 min (depending on the amount of acetone injected) before it suddenly drops and then gradually decays. This gives an indication of when the material sees acetone after it is injected into the system. On the question of acetone concentration, one useful assumption to make is that all the liquid acetone injected into the system vaporizes and passes through the sample cell, although some trace amounts likely remain on the metal surfaces of the pipes leading up to the sample cell. For a first approximation this assumption allows for a calculation of acetone concentration: if the total volume under the surface of the time-

resolved acetone vapour spectra corresponds to the amount of acetone injected, then the volume element at any point in time under these spectra corresponds to a proportional fraction of the total volume of acetone injected. Figure 6.2c shows the result of this calculation for varying doses of acetone injected: from 1 µL to 50 µL. Importantly, Figure 6.2c shows that the concentration of acetone vapour in the cell stays below 10 ppm for all investigated doses of liquid acetone. Moreover, the lower doses result in concentrations comparable to those in single breath samples from healthy individuals (below 0.8 ppm) and from T1DM patients (1.2-3 ppm) reported by Rydosz [24] and given in Figure 2.15b. This makes it possible to provide some assessment of ZnQ@OX-1 as a sensor for these low concentrations based on results presented in this Chapter.

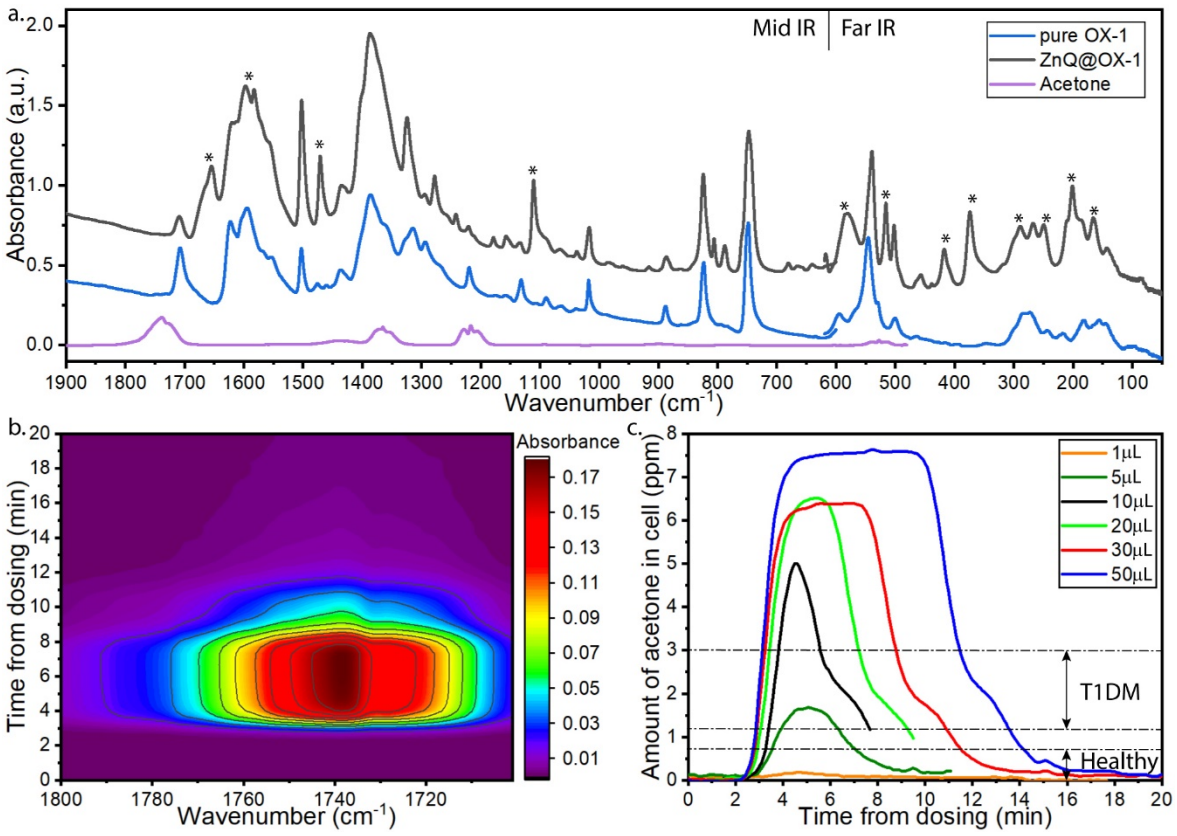

Figure 6.2. (a) FTIR spectra of Acetone vapour with respect to spectra of pure OX-1 and ZnQ@OX-1 crystals; (b) time-resolved FTIR spectra of a 30 µL dose of Acetone vapour travelling through the empty sample cell, and (c) the calculated time-resolved concentration of Acetone vapour in the sample cell for the set-up used in this experiment.

6.3 Material response to acetone vapour and testing to failure

The *in situ* dosing experiments show excellent agreement with the expected acetone dynamics. Figure 6.3a shows a single spectrum comparison of pure OX-1 and ZnQ@OX-1 under continuous flow of N_2 and N_2 dosed with Acetone. No changes are observed in the spectrum of pure OX-1 crystals, apart from the increases in absorbance corresponding to acetone vapour triple bands. In case of ZnQ@OX-1, however, drastic changes are observed. Table 6-1 details the most noticeable changes and likely assignments of the affected peaks to specific vibrational modes (based on MOF-5 vibrational bands reported by Civalleri *et al*[124]). Figure 6.3b shows the time-resolved effects of acetone vapour passing through the sample cell. These follow the expected dynamics of acetone vapour content in the cell and show that acetone is adsorbed by ZnQ@OX-1 as soon as it enters the cell (at t ~ 4 min), followed by desorption as the acetone content in N_2 flow drops (at t ~ 12 min).

The bands revert to the pre-acetone state as the vapour leaves the cell, but this switch is not ideal – some bands loose intensity in the process, indicating some aging. The material was studied to the point of failure: upon continued exposure to N_2 flow and several acetone doses (250 μL split into 7 doses) amounts of acetone, the switching mechanism observed in Figure 6.3 deteriorated and the bands permanently switched. Figure 6.4 shows the initial and final FTIR spectra to highlight the permanent changes in vibrational modes, as well as the time-resolved spectra of the extended dosing experiment. Five bands, at frequencies of 201, 250, 289, 374 and 1656 cm^{-1} appear to be most important for the sensing mechanism of ZnQ@OX-1. These modes switch most noticeably during acetone doses and appear to fade away as the time progresses: by 150 min into the experiment they all diminish, beyond which point the material does not respond to acetone in the same way as depicted in Figure 6.3. Importantly, all five of these bands can be argued to originate from vibrations in the ZnQ guests. Drastic changes observed at these frequencies indicate that the structure of the guest

ZnQ complex undergoes a transformation in the presence of acetone, substantiating hypotheses put forward by Chaudhari *et al* [1] (see page 49 for the relevant literature review section 2.4.3). They argue that blue light emission of the system arises due to a specific orientation of the 8HQ ligands arising from DMF molecules coordinating to the Zn centre. It is further argued that when acetone enters the framework, it changes the environment around ZnQ, changing the ligand orientation, and thus the electronic structure of the complex, which leads to a shift in the wavelength of emitted light. The data presented in this chapter does not conflict with this hypothesis. Indeed, the bands at 201, 250 and 289 cm^{-1} associated with ZnQ, likely originate from bending and stretching of Zn bonds with its surrounding atoms, and a postulated change in the geometry of Zn coordination is consistent with the observed changes in those bands. The bands at 374 and 1656 cm^{-1} likely originate with deformations and bond stretches respectively of benzene rings of the 8HQ ligands and can be significantly affected by a change in the conformation of those ligands. Furthermore, the 'ageing' of the material observed in Figure 6.4b can be indicative of DMF molecules leaving the ZnQ@OX-1 system, preventing the relevant vibrational modes from recovering because the bonds giving rise to those modes no longer form. This, however, is still a theory and more proof is needed to substantiate its validity. For instance, it is unclear whether it is the successive doses of acetone, or simply the continuing exposure to N_2 gas flow, that is responsible for the disappearance of the above discussed vibrational modes.

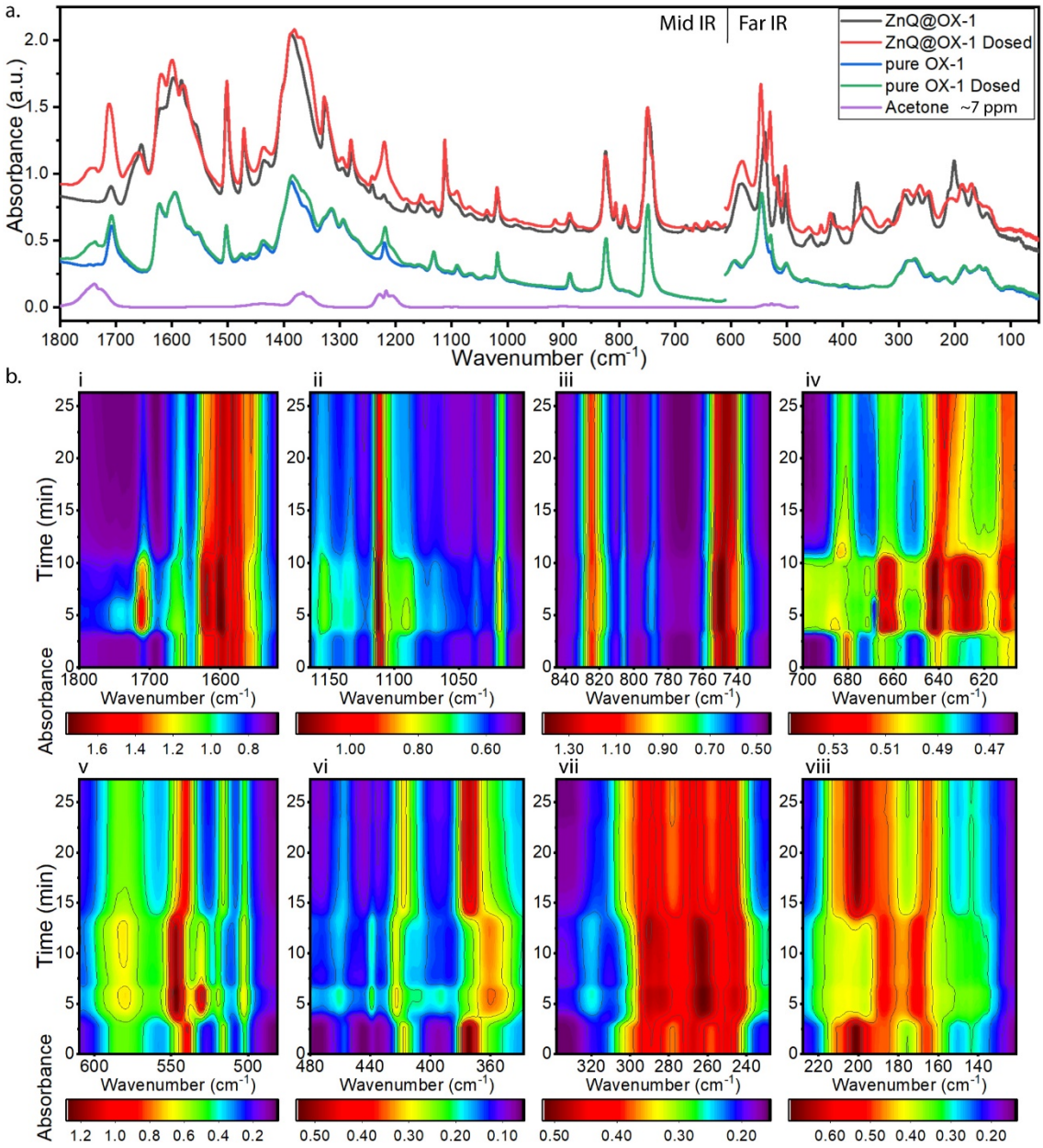

Figure 6.3. Dosing with acetone: (a) single FTIR spectra of ZnQ@OX-1 and pure OX-1 under dry N_2 flow and under N_2 dosed with acetone; (b) 2D projections of time-resolved FTIR spectra of ZnQ@OX-1 responding to a single 30 µL (~6.5 ppm max) dose of acetone flowing through the sample cell.

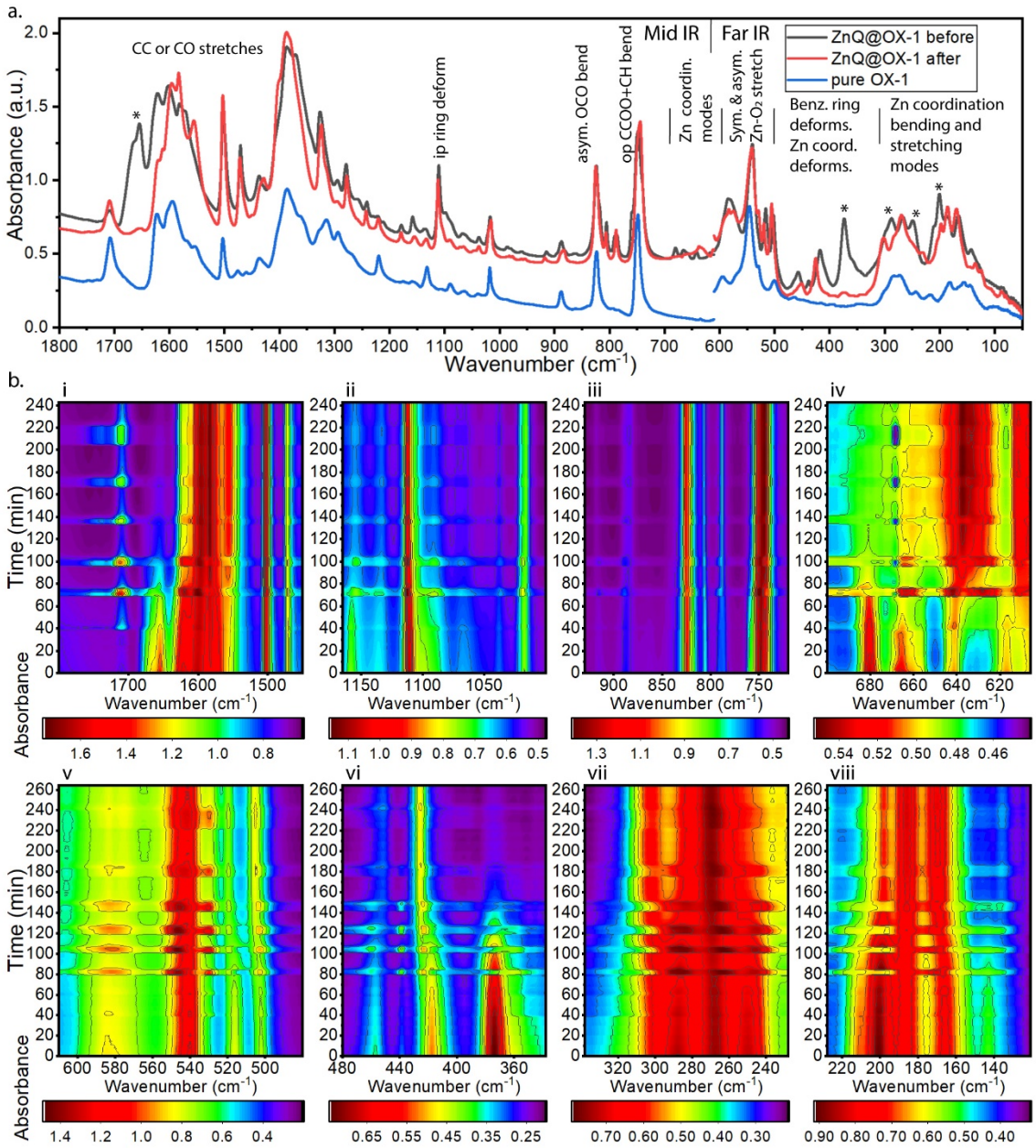

Figure 6.4. Loss of sensing behaviour: (a) single FTIR spectra for ZnQ@OX-1 before and after exposure to copious amounts of acetone vapour, plotted together with pure OX-1 spectra for reference; (b,c) 2D projections of time-resolved FTIR spectra of ZnQ@OX-1 responding to several doses of acetone, as well as residual acetone in the system, leading to the loss of sensing behaviour.

Table 6-1. Vibrational modes exhibiting response to acetone, and their possible assignment to ZnQ or OX-1. Frequencies in bold (also marked with * in Figure 6.4) show the biggest changes – both reversible and permanent.

Vibrational frequency (cm^{-1})	Magnitude change and/or Blue/Red shift for single dose (Permanent change, if different)	Possible Band Assignment
166	+B	ZnQ: Zn coordination bends and stretches
188	+	
201	-B	
210	-R	
250	+R (-)	
268	+R (+B)	
289	+R (-)	
298	+R (none)	
374	-R (-)	ZnQ: Benzene ring deformations Zn coordination deformations
417	-B	
439	+ (-)	
456	-B (-R)	
502	+B	
516	-B	
540	+R (none)	OX-1 or ZnQ: Symmetric and asymmetric Zn-O2 stretches
546	+ (-B)	
580	+ (-)	
604-682	various	ZnQ: Zn coordination
748	+B (+R)	OX-1: out of plane CCOO+CH bend
824	-	OX-1: asymmetric OCO bend
1090	+	ZnQ: in plane ring deform
1219	+	OX-1: CC stretches
1598	+B (R)	OX-1 or ZnQ: C-C or CO stretches
1619	+ (-)	
1656	-B (-)	ZnQ: CC or CO stretches
1710	+	OX-1: uncertain

6.4 Towards quantifiable sensing

For ZnQ@OX-1 to become a diagnostic tool, ways must exist to quantify its response to acetone vapour such that acetone content could be determined with sub ppm precision. It also must be able to detect as little as 0.5 ppm of acetone selectively. Even leaving the question of selectivity aside for the moment, the above are difficult design criteria to achieve. Nevertheless, some promising steps are taken here with the results presented in Figure 6.5, which shows overlapping time-resolved spectra of a single sample of ZnQ@OX-1 responding to successive increasing doses of acetone. At least three important conclusions can be drawn from these results:

- First, the greater the acetone concentration, the greater the detected response.
- Second, some form of proportionality likely exists between acetone concentration and the magnitude of response. The beginnings of such proportionality can be seen in Figure 6.5. But proportionality is also to be expected because ZnQ@OX-1 is a sensor that can be thought of as having discrete switches: each ZnQ guest is switched independently by a fixed number of acetone molecules (the number depends on how many molecules can be accommodated inside the pore).
- Third, the limit of detection for ZnQ@OX-1 is at least as low as about 1.5 ppm when deposited on a flat surface exposed to the gas mixture being analysed. This can likely be improved by changing the thickness of the ZnQ@OX-1 layer exposed to the gas mixture.

These three observations make ZnQ@OX-1 a very promising material for further development as a substitute for metal oxide-based sensors described in Chapter 2.

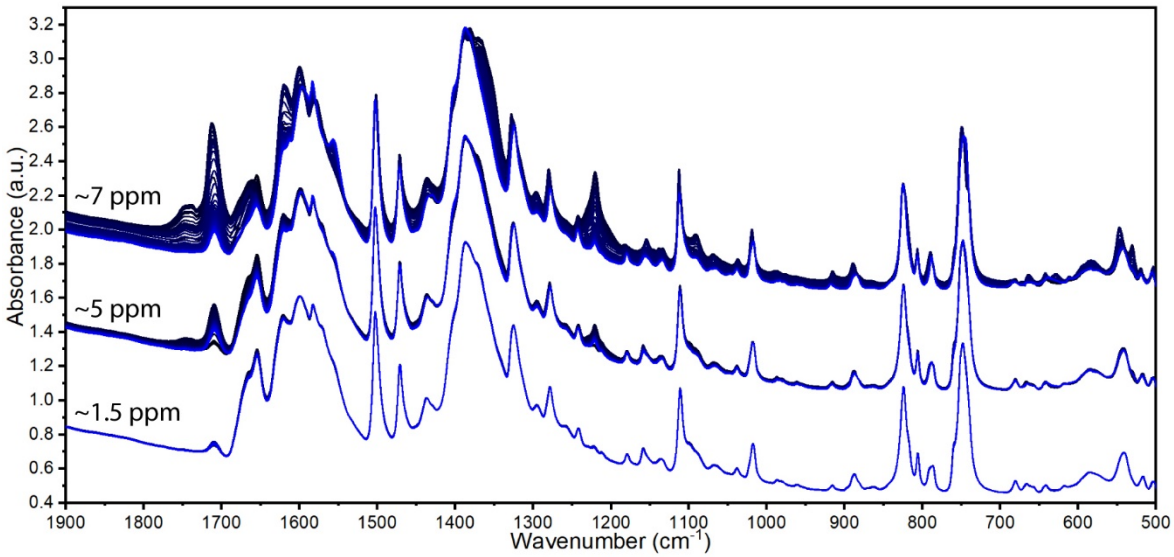

Figure 6.5. ZnQ@OX-1 response scales with increasing doses of acetone: showing successive runs of the *in situ* FTIR sensing experiment for the same sample responding to increasing concentrations of acetone. Labels designate the maximum estimated concentration achieved in the cell during the experiments. Colour scheme progresses from dark to lighter blue with time.

6.5 Summary and outstanding challenges for ZnQ@OX-1

This chapter takes some important steps towards understanding the mechanisms behind the ability of ZnQ@OX-1 composites to sense acetone vapour in the surrounding atmosphere. Broadband transmission FTIR spectra are presented and key vibrational modes of ZnQ guests are identified. The responses of these vibrational modes to the presence of acetone in the surrounding atmosphere are elucidated in detail. The links between certain vibrational modes and the material's sensing capabilities are established. The potential for quantification of the material's response is demonstrated. Finally, an *in situ* experimental method is demonstrated based on transmission FTIR spectroscopy, which has potential to tackle some of the further challenges. The most pressing of these challenges refer to the material's selectivity, stability and limits to quantification of its response. All three of these can be addressed by careful design of further *operando* transmission FTIR experiments.

Chapter Seven

7 Quantum tunnelling rotors sensing guests in ZIF-8

7.1 Introduction

This chapter presents a set of new results on the well-established Zeolitic Imidazolate Framework-8 (ZIF-8). The literature on this material is comprehensive and nuanced, as section 2.5 of this thesis illustrates. However, ambiguities and misconceptions around the material's behaviour persist. This chapter takes an aggregated view of the published literature discussed in section 2.5 and proposes an improved view of ZIF-8 adsorption and lattice dynamics. Tunnelling spectroscopy *via* inelastic neutron scattering (INS), coupled with neutron powder diffraction (NPD), obtained simultaneously at the OSIRIS instrument of the ISIS Neutron and Muon Source, provide new insight on the local potentials of ZIF-8 structure as well as the accompanying changes in long-range order of the crystals. When considered in conjunction with ZIF-8 adsorption isotherms of the same gases, the triumvirate of these results paint a picture of the adsorption process that is rich in previously unexplored detail.

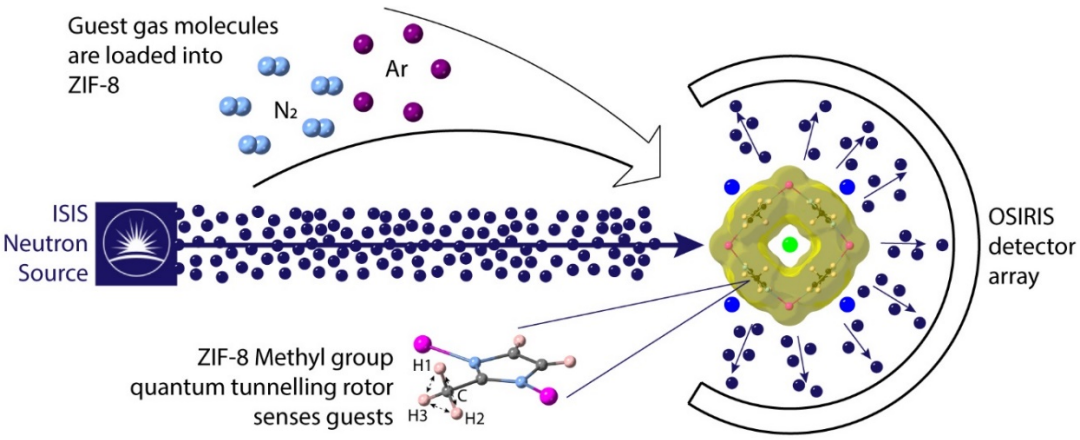

Figure 7.1 Schematic of tunnelling spectroscopy experiments at the OSIRIS instrument of the ISIS Neutron and Muon Source.

Quantum rotational tunnelling of -CH_3 groups is the phenomenon of librational states of its H atoms, where the three are indistinguishable[2] (see schematic in Figure 7.2c). These quantum rotors are highly sensitive to surrounding potentials, so to observe the rotors is to observe the surrounding potentials. A crucial piece for understanding this puzzle is the view of ZIF-8 pores as possessing preferential adsorption sites for guest molecules. Moggach and co-workers[41] recently experimentally determined the positions of these adsorption sites for a number of gases, including N_2 and Ar. They also constructed a hierarchy of these sites based on single-point DFT calculations. This chapter builds on these results to analyse the new triumvirate of Gas adsorption-INS-NPD results presented here. It also takes a dynamic view of the ZIF-8 pores, and in particular the 'gate opening' motions of its MeIM linkers. This wide-angle view of the processes involved in gas adsorption by ZIF-8 crystals leads to a reclassification of the 'static gate opening' – the shift in mean position of MeIM linkers from a 'gate closed' to a 'gate open' configuration, which is traditionally dealt with in simulation studies – as more of a 'gate blocking' phenomenon achieved by gas molecules occupying specific adsorption sites. The chapter then takes a step further by presenting some INS-NPD results from dosing ZIF-8 with one gas after another, which may give an indication of how N_2 and Ar gases compete for adsorption sites when adsorbed sequentially.

7.2 Guests induce changes in potentials: a first look

Individual tunnelling spectra for increasing doses of the respective gases are shown in Figure 7.2a-b. These were used to fit piecewise cubic hermite interpolating polynomial (PCHIP) lines through individual energy transfer data points along the gas dose dimension to construct 3D surfaces (see section 3.6.4.2 for details), which reveal the evolution of the tunnelling peak with increasing gas doses. These are seen Figure 7.2d-e, together with their 2D projections onto an energy transfer (meV)-gas dose (molecules/unit cell) plane.

Up to 51 molec/uc of N_2 and up to 71 molec/uc of Ar were loaded into the sample and two opposite effects triggered by the two gases were observed. The -CH_3 rotors in empty ZIF-8 have a tunnelling transition that appears in neutron scattering spectra as a peak at 0.33 meV with a FWHM of 0.06 meV, which corresponds to a barrier height of about 5.9-7 meV (see Figure 7.3a). Details of the barrier height calculations are given in section 3.6.4.2 of the experimental methods chapter. These values match well with those calculated by Yildirim and co-workers[3] but are slightly below the *ab initio* predictions of Ruggiero and co-workers[131]. This barrier height is also expected to produce a peak corresponding to the first librational transition (illustrated schematically in Figure 7.3b) of the -CH_3 rotor at ≈ 4 meV (see Figure 7.3). Peaks at this energy are indeed observed in reported INS spectra of ZIF-8[8, 33] (shown in Figure 2.23b,e on p. 62 of this thesis). N_2 molecules shift the tunnelling peak to lower values of energy transfer, thus decreasing the rotational energy of the tunnelling rotor, before the peak vanishes entirely by 48 molec/uc. At the same time, N_2 molecules broaden the tunnelling peak, which indicates a range of rotational energies of the -CH_3 rotors and thus an increase in heterogeneity of their environments. The N_2 dosed tunnelling peak (at 36 molec/uc) has position 0.21 meV and a FWHM of 0.18 meV, which corresponds to barrier heights of about 7-13 meV (see Figure 7.3a). On the other hand, Ar molecules act to shift the tunnelling peak to higher energy transfer levels, increasing the rotational energy of the -CH_3 rotors, without broadening the peak. This latter observation indicates that the environments of the individual -CH_3 rotors remain largely uniform. Ar (at 42 molec/uc) raises the peak to 0.426 meV with a FWHM of 0.065 meV, which corresponds to barrier heights of 4-5 meV (see Figure 7.3a) and does not appear to inhibit the tunnelling even at doses of 71 molec/uc.

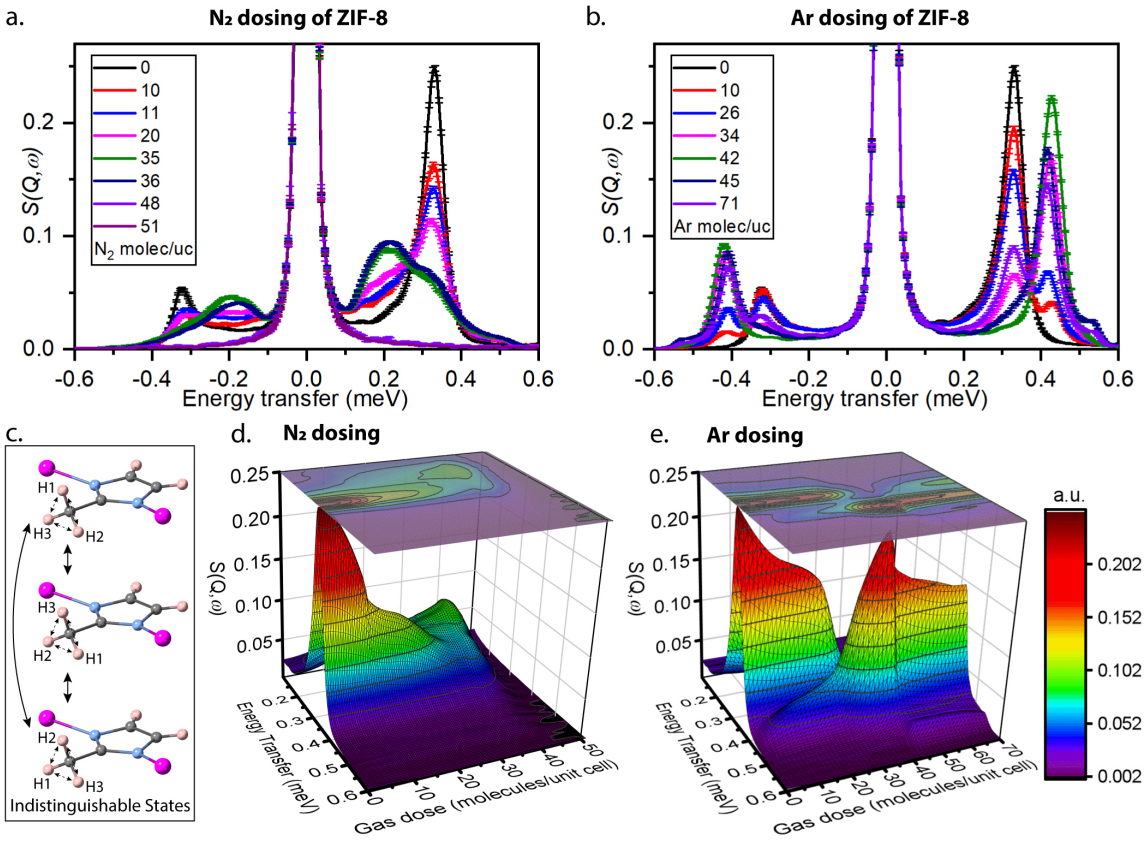

Figure 7.2 Methyl tunnelling in ZIF-8 with guests measured at 3 K: (a,b) As measured INS spectra of ZIF-8 powder dosed at 77 K with varying amounts of N_2 and Ar gas respectively; (c) the indistinguishable librational states of -CH_3 rotors in ZIF-8 under quantum rotational tunnelling [2], colour scheme: Zn (pink), C (grey), N (blue), H (beige); (d,e) 3D interpolated surfaces of spectra in (a,b), respectively.

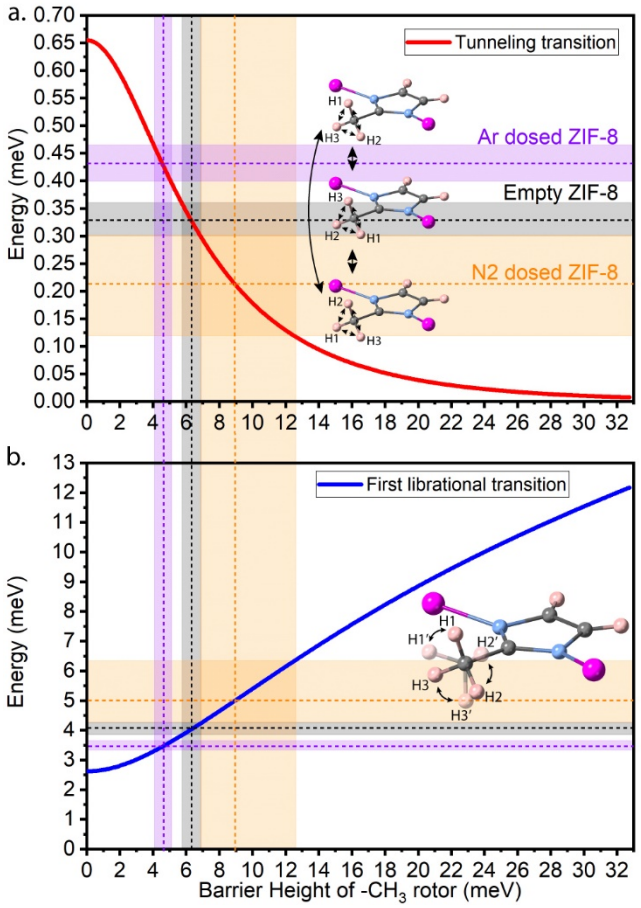

Figure 7.3 Energies of the (a) tunnelling transition and the (b) first librational transition as a function of barrier height. Inset schematics illustrate the respective transitions. Experimentally measured tunnelling peak positions (dotted lines) and the FWHM (transparent rectangles) are constructed to determine the barrier height of the -CH_3 rotors in these conditions and the first librational transition energies for empty, N_2 and Ar dosed ZIF-8.

7.3 Adsorption sites: a closer look at ZIF-8 structure

To analyse the tunnelling spectra, it is first necessary to understand the structure of ZIF-8 and its adsorption sites, as elucidated by Moggach and co-workers [41]. The first five adsorption sites of ZIF-8 (site 6 is analogous to site 5, and so is omitted for clarity) are shown in Figure 7.4a. ZIF-8 is constructed using just one unique organic MeIM linker (highlighted in yellow in Figure 7.4a-c), which connects two Zn metal centers on either side of the imidazole ring via Zn – N bonds. Each Zn centre is bonded to four MeIM linkers in a tetrahedral coordination environment. This results in a structure consisting of 6-membered rings (MRs) and 4-MRs, where each MeIM linker is part of two 6-MRs and one 4-MR simultaneously – this assembly is shown in Figure 7.4a. Adsorption sites 1 are in the middle of the 6-MRs and are the most preferable for guest molecules. Sites 2 are located on alternating sides of the imidazole rings of MeIM linkers with reference to 6-MRs and are predicted to be more preferable than sites 3 and 4. The latter are located on the centre axis of each 4-MR with a single site 3 in the middle of the 'gate' and one site 4 on either side. These sites are not clearly energetically differentiated by theoretical calculations.[41] Sites 5 are less preferable still and are located under sites 1 inside the sodalite pore, with the closest distance to the pore being the distance to the C-C part of imidazole rings. Sites 6 are analogous to sites 5, located on the other side of sites 1, with closest distances to the $-CH_3$ rotors as opposed to the C-C ends of MeIM linkers. Figure 2.26i-viii (p. 71) shows the original[41] illustrations of these sites.

To start tackling the quantitative Gas adsorption-INS-NPD results through this adsorption sites lens, it is also necessary to understand how many adsorption sites there are within a given volume of ZIF-8. Here a cubic unit cell of ZIF-8 is taken as the unit of analysis because cubes are easy to stack and gas adsorption data is often reported in molecules per

unit cell. Refer to Figure 7.4b-c for illustrations of the unit cell and its components, referred to in the following calculation.

A single unit cell of ZIF-8 contains eight 6-MRs, which are fully contained within the boundaries of the unit cell. The number of adsorption sites 1, which are located in the middle of the 6-MRs, within a unit cell is thus 8. Sites 2 are located near each imidazole ring, of which there are six in a 6-MR, but each ring is shared between two 6-MRs, so the number of sites 2 in a unit cell is $\frac{6}{2} \times 8 = 24$.

Sites 3 and 4 are located in 4-MRs, which are located at the extremities of the unit cell – on each face of the cube and on each edge. The 4-MRs on the six faces of the cubic unit cell are shared between two unit cells, while the 4-MRs on the twelve edges are shared between four unit cells, which brings the total number of 4-MRs associated with a single unit cell to $\frac{6}{2} + \frac{12}{4} = 6$. There is just one site 3 and two sites 4 in a single 4-MR, therefore there are 6 sites 3 and 12 sites 4 in a unit cell.

Finally, there is one site 5 and one site 6 per 6-MR, which are not shared with neighbouring rings, therefore there are 8 sites 5 and 8 sites 6 per unit cell. This brings the total number of adsorption sites to $8 + 24 + 6 + 12 + 8 + 8 = 66$.

Thus a total of 66 molec/uc are accommodated by a unit cell of ZIF-8. This is true for both N_2 and Ar gases [41], which have similar kinetic radii [132]: 364 pm for N_2 and 340 pm for Ar. However, the homonuclear diatomic N_2 is reported to have a scatter of possible orientations relative to the framework at all the different sites, whereas the monatomic Ar has much more precisely defined positions and symmetry.[41] This distinction between the two gases is important as it likely explains the higher FWHM of the N_2 dosed tunnelling peak: the scatter of orientations likely gives rise to a scatter of rotational barrier heights for the -CH_3 tunnelling rotors.

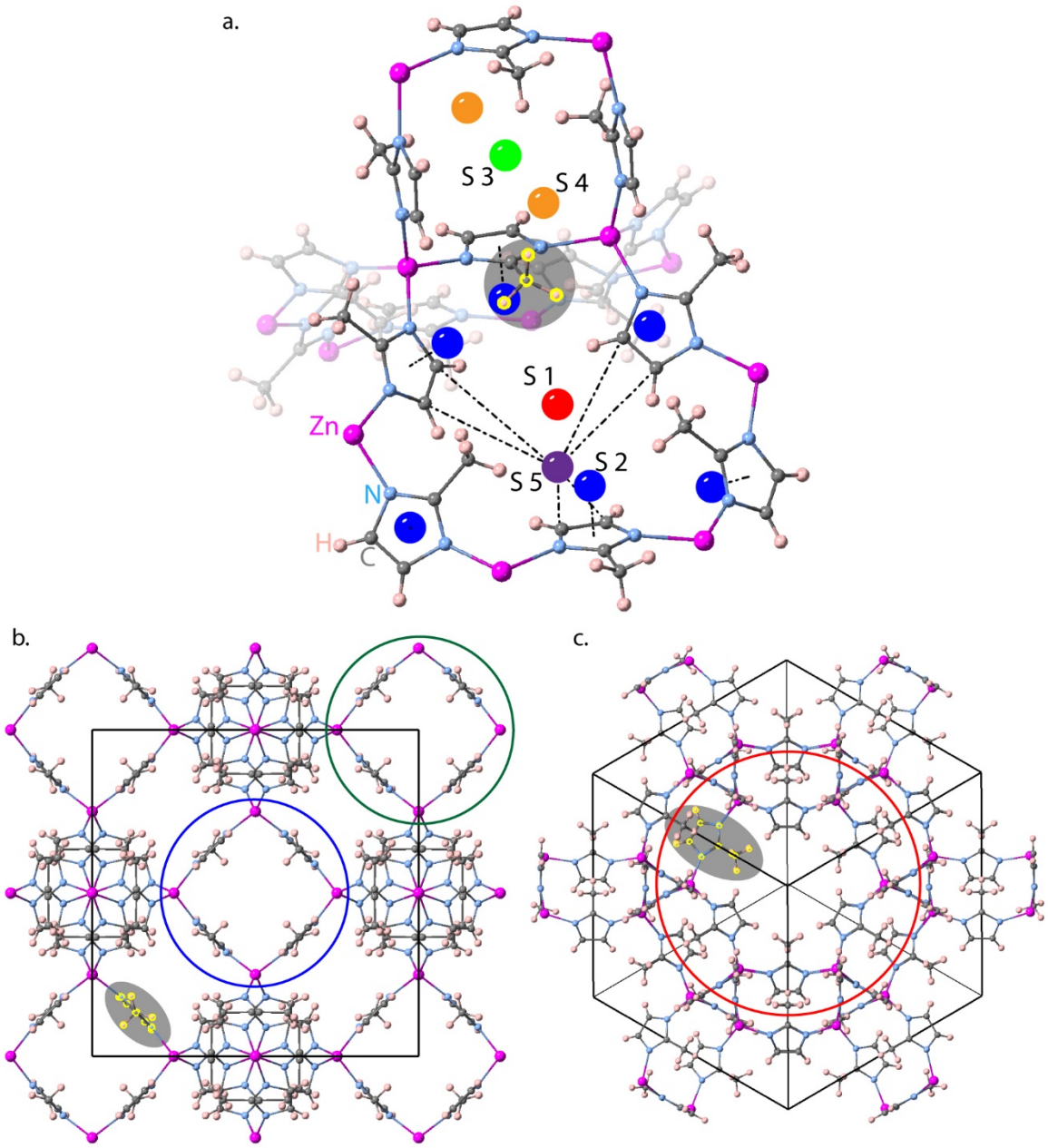

Figure 7.4 Adsorption sites in ZIF-8: a) The unique -CH_3 group of ZIF-8, highlighted in yellow, as part of two 6-MRs (second 6-MR is translucent, extending into the page) and one 4-MR, with schematic positions of adsorption sites marked in order of preference (S 1-5) (after Moggach and co-workers[41]); (b,c) unit cell of 'open gate' ZIF-8 (reported by Moggach *et al*[25]) is marked by black bounding box with views into 4-MRs and into 6-MRs respectively. Circles indicate examples of 4-MRs on the edges of the unit cell (green) and on the faces of the unit cell (blue), as well as a 6-MR contained fully inside the unit cell (red).

7.4 Gate Opening vs Gate Blocking: Gas adsorption-INS-NPD triumvirate of results through the adsorption sites lens

Taking the above calculated numbers of adsorption sites for ZIF-8, and assuming that these are filled in order of preference, while also building on the numerous theoretical papers discussed in section 2.5 of this thesis, it is possible to postulate new detailed theories of ZIF-8 adsorption dynamics. To this end, NPD patterns, collected together with the INS spectra, are interpolated in the same way and plotted as 2D projections of 3D surfaces. Both INS and NPD data are then plotted on a common gas dose axis with corresponding adsorption isotherms for the same sample. Figure 7.5 shows these results for N_2 and Ar dosed ZIF-8 respectively.

Introducing 10 molec/uc (see both Figure 7.2 and Figure 7.5 for the following discussion) of either gas leads to the creation of a second species of methyl rotors: in addition to the 'empty' tunnelling peak, an extra peak appears at a lower (for N_2) or higher (for Ar) energy. The existence of isosbestic points in the spectral plots for both gases indicates an exchange of intensities: the 'dosed' peaks grow as the 'empty' peak diminishes with increasing gas doses. This exchange, however, only occurs up to the level of dosing sufficient for full occupancy of sites 1, 2 and 3 (38 molec/uc in total) and breaks down after that level. This dose is also just below the second (for N_2) and first (for Ar) plateau in the respective gas adsorption isotherms. No accompanying shifts in long-range order are observed at this level of N_2 dosing, whereas for Ar dosing there is a clear transition of all recorded NPD peaks to lower *d*-spacing values, corresponding to a 2.2% volumetric contraction of the unit cell (simulation of the contraction is discussed in section 3.2.4.3). It is noted that such shifts in NPD are not caused by increasing the temperature of the sample, even though the tunnelling peaks are significantly affected (see Figure 7.6).

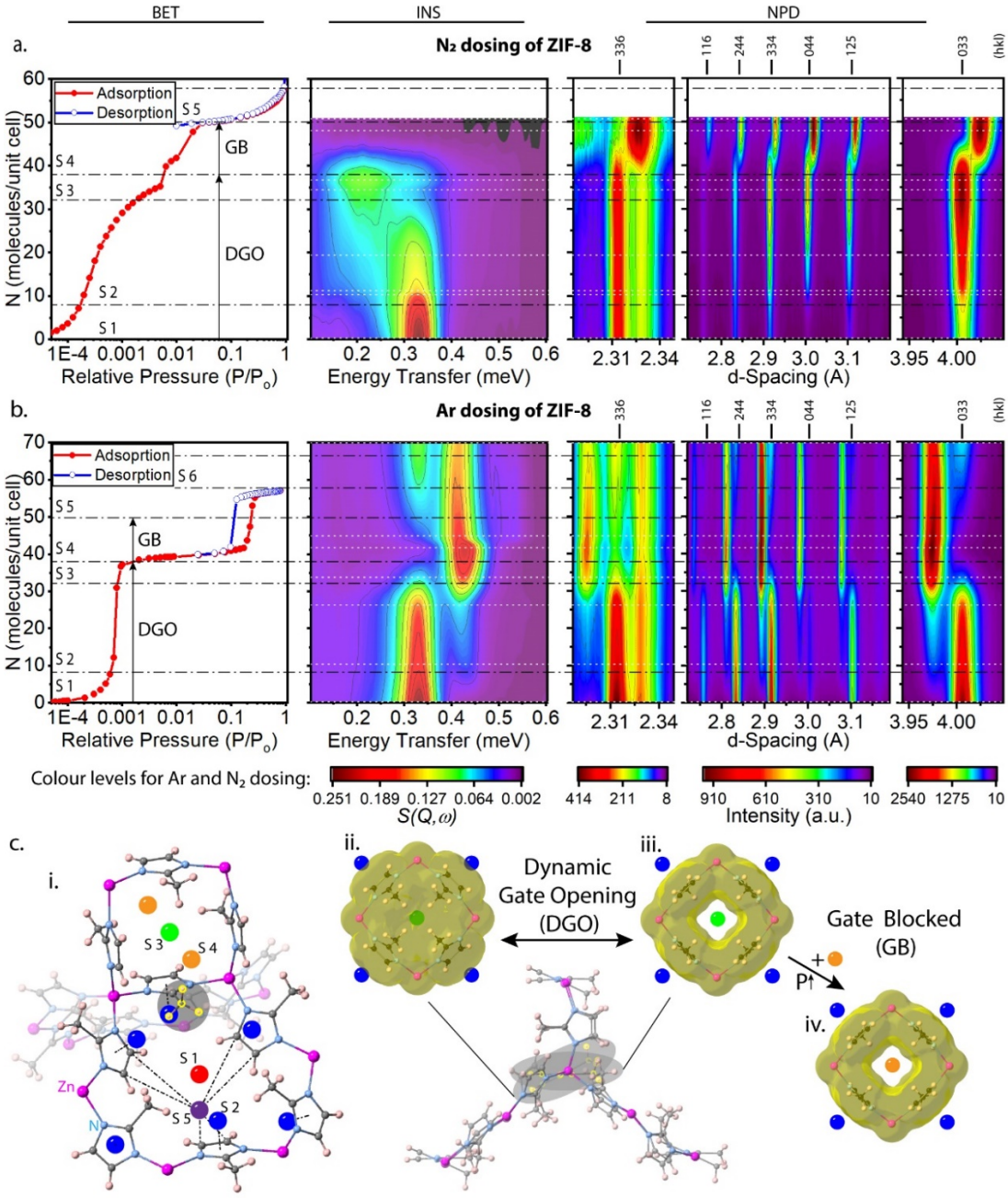

Figure 7.5 a,b) Gas adsorption measurements correlated with the interpolated INS spectra and interpolated NPD patterns of ZIF 8 dosed with N_2 and Ar gas respectively. The gas adsorption measurements were done at 77 K while the neutron measurements were done at 2 K. Dosing with gases for neutron experiments was done at 77 K. Black dash-dot lines mark levels of full cumulative occupancy of adsorption sites (S1-S6); white dotted lines mark levels at which individual spectra were recorded. ci) Adsorption sites positions are reproduced for reference, together with illustrations of the average (cii) 'closed' and (ciii) 'open' states (CIFs reported by Moggach *et al*[25]) reached by 4-MRs as they undergo dynamic gate opening motions. civ) The 'gate blocked' state is illustrated with sites 4 occupied as a result of higher external pressure applied to the sample.

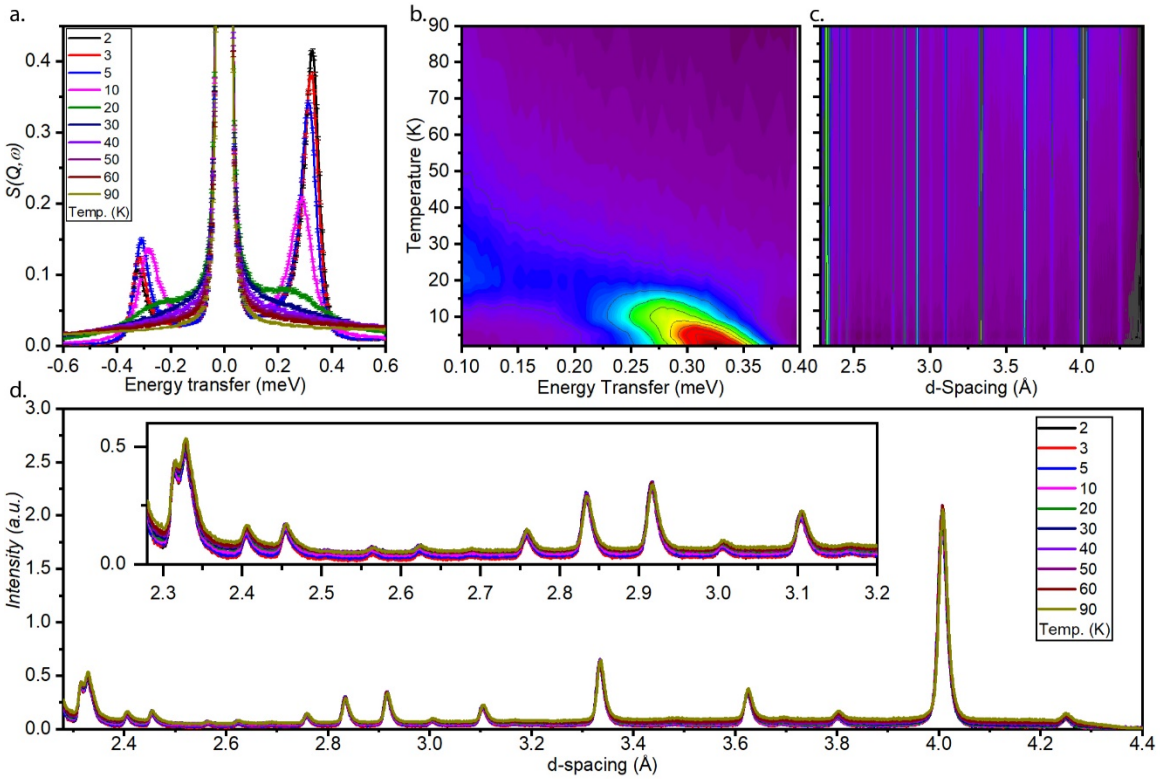

Figure 7.6 Temperature ramp study of methyl tunnelling of ZIF-8. (a) Individual INS spectra of ZIF-8 at increasing temperatures showing excellent agreement with data reported by Yildirim and co-workers[3] (reproduced in Figure 2.20 on p. 56 of this thesis); (b,c) projections of interpolated INS and NPD data onto the energy transfer – temperature and *d*-spacing – temperature planes, respectively; (d) individual NPD patterns of ZIF-8 at increasing temperatures.

These observations show that the local interactions of increasing amounts of gas molecules in the pores of the framework have a cumulative effect. Moreover, the gradual transition from the 'empty' to 'dosed' INS and NPD peaks indicates that the distribution of gas molecules inside the crystals is not uniform, with some cells shifting before others. This non-uniformity of distribution is somewhat offset by the averaging nature of neutron spectroscopy: neutrons penetrate easily into the sample and thus the resulting measurements are representative of the whole volume of the sample, which means that the changes observed in these measurements are representative of the sample as a whole. It is thus unclear if the gradual transitions occur due to some cells in a given crystal switching before the rest, or due to some crystals (smaller or larger) switching before others (as some literature[34] shows is possible – see Figure 2.22 on p. 60).

The gradual transition is completed by 38 molec/uc, at which point both N_2 and Ar dosed spectra show well-defined 'dosed' peaks. However, a scatter of orientations of adsorbed N_2 molecules likely leads to the much broader dosed peak, whereas the precisely defined positions of Ar molecules produce a peak as sharp as the original homogenous 'empty' quasi-free -CH_3 rotors. The reasons for N_2 molecules increasing the barrier height for quantum tunnelling rotations of the -CH_3 rotors, while Ar decreases that barrier, are likely subtler than the diatomic-monatomic distinction between N_2 and Ar made here. The contraction of the unit cell upon adsorption of Ar is a clear indication of this, demonstrating that the specific physical/chemical local interactions of the two gases are drastically different, with different consequences for the long-range order of the framework. Despite this difference in direction in which the tunnelling peaks shift, the well-defined 'dosed' INS and NPD peaks at around 38 molec/uc of both N2 and Ar are evidence in favour of adsorption site hierarchy being adhered to. This is based on the following argument:

The 4-MRs should not be accessible to gas molecules in the 'gate closed' state, as illustrated by the van der Waals surface construction in Figure 7.5cii based on the CIF reported by Moggach *et al*[25]. And yet, the homogeneity of tunnelling rotors reached by 38 molec/uc necessitates homogeneity of gas molecule positions across all unit cells in the sample. Therefore, since at 38 molec/uc there are just enough molecules to occupy sites 1,2 and 3, it is highly likely that sites 3 are indeed occupied. If this is so, then sites 3 must be accessible before the 'static' gate opening occurs. This can be a result of 'dynamic' gate opening: each 4-MR (gate) continuously oscillates between the 'closed' (Figure 7.5cii) and 'open' (Figure 7.5ciii) states, allowing access to sites 3 located in the middle of the gate.

Taking this argument further, these dynamic gate opening motions also resist adsorption of additional gas molecules giving rise to the plateaus observed in gas adsorption isotherms: to significantly increase amounts of adsorbed gas beyond 38 molec/uc, it is necessary to increase external gas pressure by a factor of 10 in the case of N_2, and by a factor of 10^2 in the case of Ar. But once sufficient pressure is reached, molecules are inserted into sites 4 and the gate is 'blocked'. This is not to say that the dynamic gate opening oscillations cease entirely. Previously published literature[31] shows that they likely continue, but with lower amplitude and around the 'gate open' positions. This level of gas dose, beyond which 'gate blocking' occurs is also in broad agreement with previous theoretical predictions[26-28, 30] for the 'static' gate opening surveyed in section 2.5.2; and it is the dose at which adsorption isotherms diverge for samples of different ZIF-8 crystal sizes reported by Fairen-Jimenez and co-workers[34] (reproduced in Figure 2.22 on p. 60).

This 'gate blocking' hypothesis is substantiated by the tunnelling spectra. Beyond full occupancy of sites 3 sudden transitions occur for both gases. By 48 molec/uc of N_2 the tunnelling peaks disappear, which is accompanied by a shift of all NPD peaks to higher d-spacing values, corresponding to a 1.4% volumetric expansion of the unit cell. This absence

of tunnelling peaks persists to 51 molec/uc, at which sites 5 begin to be occupied, and at which the NPD pattern remains unchanged. The tunnelling is likely hampered by N_2 molecules in sites 4, which are in close proximity to the methyl groups. The classical argument for the unit cell expansion is swelling because of molecules entering the pores, but chemical effects are likely at play as in the case of Ar-triggered contraction. Both phenomena, however, are difficult to explain without novel *ab initio* modelling.

For Ar, increasing the dose to 45 molec/uc results in a small shift of the 'dosed' tunnelling peak to a lower energy, accompanied by a small shift of NPD peaks to marginally higher d-spacing. Moreover, a third tunnelling peak appears at 45 molec/uc of Ar at an even higher energy than the 'dosed' Ar tunnelling peak, indicating that a third species of methyl rotor appears in the sample. These phenomena arise from Ar molecules in sites 4-6 interacting with the quantum rotors, but it is not possible to further expand on them without new *ab initio* modelling of these processes.

At 71 molec/uc of Ar, a tunnelling peak at the 'empty' energy level reappears, the third species tunnelling peak is diminished but does not disappear, and NPD peaks at the 'empty' d-spacing values reappear accompanied by a decrease in intensity of the 'loaded' NPD peaks. This dose of Ar is above full capacity of ZIF-8 pores, so the extra 5 molec/uc, or more, likely reside on the outside surfaces of the crystals or on the walls of the Al sachet containing the sample.

7.5 N_2 vs Ar: mixing the diatomic homonuclear and the noble gases inside ZIF-8 pores

The above discussion delves into the effects of single gases, finding that despite being unreactive at the conditions employed in these experiments, the gases have clear chemical effects – the most striking manifestation of these are the unit cell expansions and contractions seen in NPD data. Both N_2 and Ar therefore interact chemically with ZIF-8 pores, but which has stronger interactions – the diatomic homonuclear N_2 or the noble Ar? Some experiments were performed to move towards answering this question by dosing ZIF-8 with one gas, taking INS and NPD spectra, and then dosing it with the other gas. The results are shown in Figure 7.7.

When Ar was loaded first, up to about 45 molec/uc, and N_2 followed (Figure 7.7a), the Ar dosed tunnelling peak first diminished (after 10 molec/uc of N_2) and then disappeared altogether (after 16 molec/uc of N_2). This shows that N_2 hampers the tunnelling even when Ar was already in the pores, and the tunnelling had a higher energy than in empty ZIF-8. At the same time, addition of N_2 triggers an expansion of the unit cell to levels as in the case of dosing with N_2 only. This is a dramatic shift, considering that there is three times more Ar than N_2 inside the sample when it occurs.

When N_2 was loaded first, only up to 10 molec/uc so as not to inhibit the tunnelling excessively, and Ar followed (Figure 7.7b), Ar still raised the energy of some rotors, but with a broader tunnelling peak than in the case of pure Ar. Moreover, this peak reached as high in energy (0.52 meV) as the second 'dosed' peak seen when ZIF-8 is dosed with Ar beyond 44 molec/uc. At the same time the NPD data shows that Ar acts to contract the unit cell, but the effect is diminished by the presence of N_2, making the contraction smaller than in the case of pure Ar dosing.

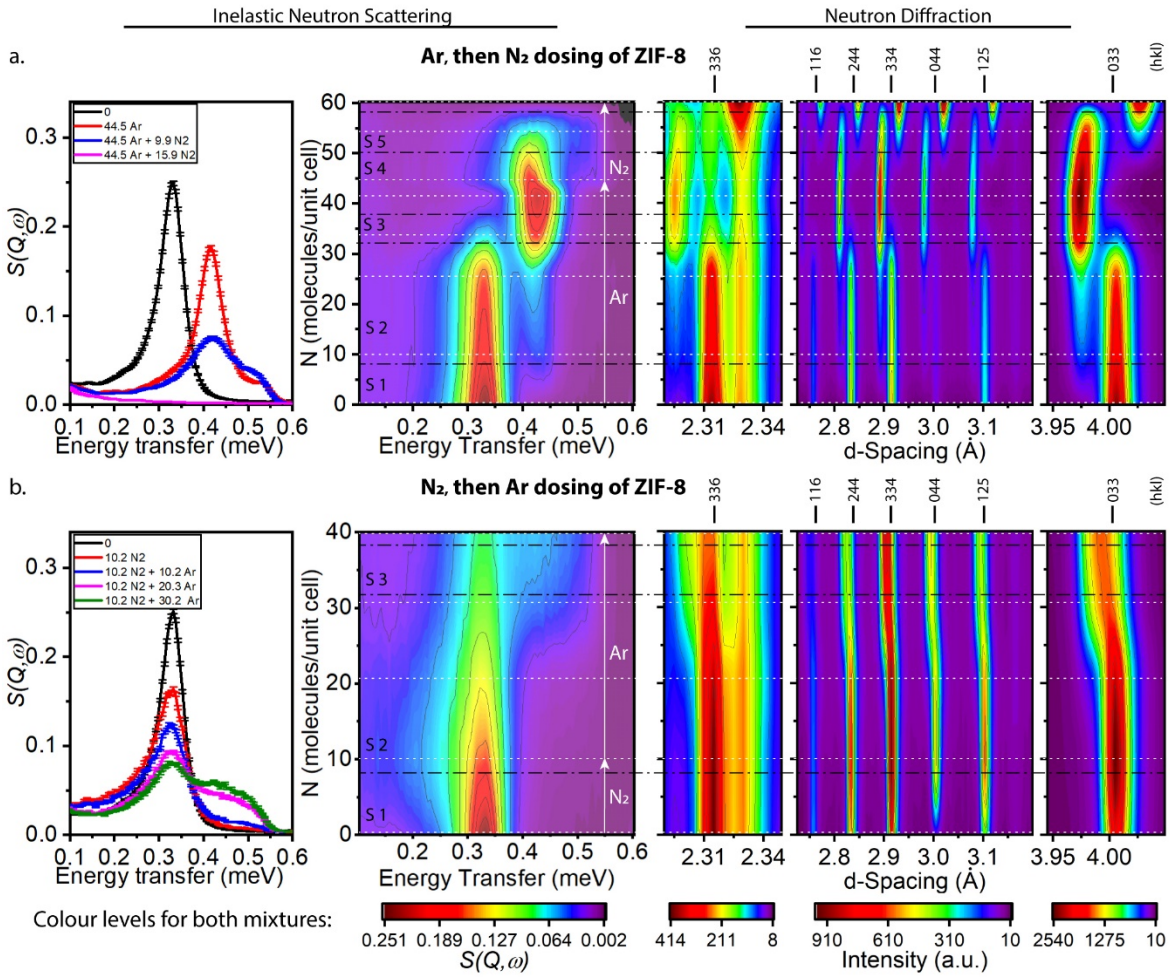

Figure 7.7 Dosing with (a) Ar first, followed by N_2, and (b) N_2 first, followed by Ar. Individual spectra (left) are interpolated (as described in section 3.6.4.2) and plotted as 2D projections of 3D surfaces. Black dash-dot lines mark levels of full cumulative occupancy of adsorption sites (S1-S6); white dotted lines mark levels at which individual spectra were recorded. Note that individual spectra of Ar up to 44 molec/uc (see Figure 7.5) are not shown in (a) for clarity.

These interactions of N_2 and Ar mixtures are intriguing, and arguments can be put forward as to what adsorption sites could be responsible for the effects observed in INS and NPD data described above. But at this stage such arguments would be mere speculation. More experiments and new approaches to *ab initio* modelling of these interactions are required to further understand the physical phenomena behind these previously unobserved effects.

7.6 Summary and conclusions: quantum tunnelling evidence untangled

This chapter demonstrates that adsorbed gas molecules have a significant impact on the quantum tunnelling of -CH_3 rotors in ZIF-8. In other words, the -CH_3 rotors act as sensitive local probes of the potentials inside the ZIF-8 pores. The effects produced by guest gas molecules are cumulative: a sufficient number of local changes need to be induced before a shift in long-range order is triggered. This is true for both N_2 and Ar gases, but the two gases induce effects in opposite directions. N_2 lowers the energy of the tunnelling rotors, whereas Ar increases it. N_2 expands the ZIF-8 unit cell, Ar contracts it, and does so at a lower gas dose.

Despite these opposite effects, the reported[41] adsorption sites for the two gases are the same. The differences in the effects the two gases have are, therefore, due to the differences in the chemistry of the gases' interactions with those adsorption sites. To further understand these differences, new approaches to *ab initio* modelling are required. Until these are developed, the best evidence provided in this chapter for the two gases actually adhering to the reported adsorption sites and their hierarchy, is the full transition of the tunnelling peak from its 'empty' to its 'dosed' versions by 38 molec/uc of both gases. At this dose there are just enough molecules of gas to fully occupy all sites 1,2 and 3. When these are occupied, the environments of all -CH_3 rotors in the framework are identical, which agrees with the well-defined 'dosed' peaks, especially in the case of Ar. In the case of N_2, the broadness of the 'dosed' peak can be attributed to the scatter of possible orientations of the diatomic molecules to the adsorption sites.

It is further argued in this chapter that the vibrational modes of the framework are instrumental for guest gas molecules in reaching and occupying the adsorption sites. The dynamic gate opening mode in particular is argued to allow access to sites 3, located in the middle of the 'gate'. It is also postulated that this dynamic gate opening is responsible for

the reluctance of ZIF-8 to adsorb further molecules of gas beyond 38 molec/uc. Only when gas pressure is increased by a factor of 10 for N_2, and 10^2 for Ar, does the gas dose increase, and molecules are inserted into sites 4, located at either 'entrance' to the gate. These molecules block the gate: they prevent the gate from oscillating back to its 'closed' state. The static gate opening, first observed *via* single crystal XRD by Moggach, Bennett and Cheetham[25], is therefore argued to be more of a 'gate blocking' (GB).

The arguments and theories constructed in this Chapter fit well with the experimental results presented here. But in many cases the data is not sufficient for proving those theories. Further carefully designed experiments and new advanced *ab initio* theoretical calculations are required to further substantiate the claims put forward in this chapter. The intriguing results from sequential loading of both N_2 and Ar into the same sample give some indication of what exciting new experiments may reveal.

Chapter Eight

8 Summary of findings and outlook to future challenges

This thesis thrives to advance the development of metal-organic frameworks as practically useful materials by leveraging access to synchrotron and neutron sources in tandem with lab-based techniques. Three areas of applications are explored throughout the thesis: next generation dielectric materials, next generation catalysts and novel sensor materials. Chapter 2 explores the state-of-the-art in these fields and Chapters 4-7 present advancements based largely on results enabled by access to large-scale facilities – the Diamond Light Source synchrotron and the ISIS Neutron and Muon Source.

MOFs are highly promising candidates to hit the ITRS roadmap target for next generation of dielectric materials – keeping the real part of the dielectric function below 2 – due to their high porosity and tunability. Until now, however, studies reporting reliable data on dielectric properties of MOFs have been rare. Chapter 4 takes a step towards rectifying this issue by developing a technique for rapid probing of dielectric properties of MOF powders to screen candidate materials. This is based on the availability of broadband IR radiation from 5000 cm^{-1} down to about 40 cm^{-1} at the B22 MIRIAM beamline of Diamond Light Source. Access to this facility is admittedly difficult. However, tens of MOF variants can be screened during a single beamtime slot. Commercially available MIL-53(Al) powder is shown to contain a mixture of large and narrow pore phases, with the latter collapsing under uniaxially applied stress. This property of the LP phase enabled comparisons to be made between experimental data and theoretical predictions based on state-of-the-art *ab initio* calculations, which showed good agreement, indicating that developments in theoretical predictions are moving in the right direction. This possibility of verifying predictions is a significant step forward for the field, and the technique presented in

Chapter 3 can play a big role in further advancements – not least because information about vibrational modes of the materials under study is obtained together with values for the dielectric constants. To take full advantage of these possibilities, ways need to be established to infer lower frequency (GHz-kHz region) properties from the THz measurements achieved by FTIR spectroscopy. Work in this direction is already well under way.

MOFs have been shown as excellent hosts for catalytic Pd species, with the resulting Pd@MOF composites exhibiting excellent yields in various reactions. In most cases, however, these materials are difficult and expensive to synthesise. Chapter 5 presents the Pd@OX-1 catalytic MOF system with a straightforward and scalable synthesis route. The initial investigations of its catalytic properties in Suzuki coupling and Heck arylation reactions show that it is competitive with the previously reported systems. Moreover, the active sites for Pd attachment are not deactivated during the Heck reaction and even survive a complete transformation of the host framework during the Suzuki reaction. This makes OX-1 a robust host for active Pd species, which are found to consist of single Pd atoms and small clusters of Pd attached to the benzene rings of the BDC linkers when the material is first synthesised. These transform into larger nanoparticles as the material is used in catalytic reactions. Further development of Pd@OX-1 can expand the scope of reactions the material can catalyse, answering questions regarding Pd losses incurred during reaction cycles, and improving the stability of Pd species by further functionalising the already robust active sites on BDC linkers with, for example, amine groups. These avenues of research could clarify just how attractive Pd@OX-1 can be for industrial applications and take further steps towards novel heterogenous single-metal-site catalysts envisaged by Beller and co-workers[95].

Advancements in sensing volatile organic compounds can have an impact in non-invasive diagnostics. Management of Type 1 Diabetes Mellitus in particular can benefit from

advancements in sensing acetone concentrations in exhaled breath. Chapter 6 presents evidence suggesting that the ZnQ@OX-1 MOF is an excellent candidate to compete with metal oxide-based sensors – the current best performers. *In situ* acetone sensing experiments conducted at B22 MIRIAM beamline of Diamond Light Source provide a significant step forward in understanding this optochemical sensor. The previously observed optical response is translated into a response of the system's IR-active vibrational modes, and key modes responsible for the system's sensing functionality are identified. Significant investment into *ab initio* calculations is required to properly assign and interpret these vibrational modes – the results presented here can provide the justification to make that investment. The results also show that ZnQ@OX-1 can detect a little as 1.5 ppm of acetone in a carrier gas, and that its response likely scales according to some law of proportionality to acetone concentration. This sensitivity can likely be improved by carefully adjusting the ZnQ@OX-1 layer thickness used as the active material in the potentially forthcoming sensor device. But more importantly, questions pertaining to the material's stability and selectivity need to be addressed on the road to practical deployment.

More exotic 'sensors' – quantum tunnelling -CH_3 rotors – have long held promise to make an impact in advancing understanding of various materials' behaviours. These are found in the ZIF-8 MOF, where they are shown to be quasi-free – meaning that the tunnelling of individual -CH_3 groups is not coupled to other groups, thanks to the MOF's structure. ZIF-8 itself is a well-known and widely-studied material, due in part to its distinct adsorption isotherms, some features of which are attributed to the phenomenon of 'gate opening'. Chapter 2 explores in detail the literature published in relation to this phenomenon and distils a conflict of terminology between the 'static' gate opening observed by x-ray diffraction techniques and the 'dynamic' gate opening predicted as a vibrational mode by *ab initio* calculations and observed in different forms of spectroscopy in the THz domain. Chapter 7

tackles this duality by adding *operando* tunnelling spectroscopy coupled with neutron powder diffraction to the repertoire of techniques deployed to understand ZIF-8 behaviours. The results, when interpreted through the lens of the reported[41] hierarchy of adsorption sites inside ZIF-8 pores, strongly suggest that the widely explored 'static' gate opening is more of a 'gate blocking' phenomenon that occurs when the adsorption sites at the two 'entrances' to the 4-MRs ('gates') are occupied by adsorbed gas molecules. Until that happens, these gates oscillate between their 'closed' and 'open' configurations, which allows gas molecules to occupy the single adsorption site located in the middle of the 'gate'. This dynamic gate opening likely plays a key role in explaining the plateaus in ZIF-8 adsorption isotherms. The importance of the chemical interactions between the gases investigated here – N_2 and Ar – and the host framework, are evident from the contractions and expansions in the unit cell volume observed in neutron diffraction data. The interplay between these two gases when they are loaded into ZIF-8 one after the other further stresses the importance of the chemistry in these adsorption processes. To elucidate the mechanisms behind these interactions, novel approaches to *ab initio* modelling need to be developed, while further carefully designed tunnelling spectroscopy experiments can enrich understanding of these phenomena.

The diversity of the fields presented here – dielectrics, catalysis and sensing – is representative of the flexibility and vast potential of MOFs. OX-1 is a good example, demonstrated to act as an excellent host to both Pd species and ZnQ luminescent guests, resulting in two very different functionalities. At the same time, the techniques employed in studying MOFs for these varied experimental applications are very similar throughout the chapters of this thesis, which demonstrates the wide scope for the techniques' customisation. This thesis, then, both develops MOFs as practical materials and expands the toolbox of the scientist similarly engaged in this pursuit of applied Metal-Organic Frameworks.

Appendices

8.1 Appendix 1: Matlab code for the KKT transform from reflectance spectra to dielectric functions

This code is based on the Kramers-Kronig relations described in Section 3.6.1. It takes as input the far IR and mid IR specular reflectance spectra, together with some necessary parameters (given in the header instructions), and generates as output the smoothly joined reflectance spectra, the complex dielectric function and the complex refractive index. To use the code, copy-paste the below functions in the order they are presented into a Matlab editor window, save the file with the name KKTransform_Publish.m and follow the instructions given in the header to call the function from the command line within Matlab.

8.1.1 KKTransform_Publish.m – top level function to be called by user

```
% Inputs:
% njufar - wavenumber vector in FIR;
% njumid - wavenumber vector in MIR;
% Rfar - reflectance data in FIR;
% Rmid - reflectance data in MIR;
% lowcutindex - index at which to trim data at the low limit of FIR;
% joinnju1 - wavenumber at which to start the joint of FIR and MIR data
% joinnju2 - wavenumber at which to end the joint of FIR and MIR data
% lownjugain - factor increase of reflectance at low wavenumber, this will
% determine the constant straight line extrapolation to low wavenumbers.
% resolution - what resolution is the data? 1cm-1?2cm-1?4cm-1?etc.

% Outputs:
% njunju - the wavenumber vector for the whole range
% RR - the joined reflectance spectra
% n - the real part of the complex refractive index
% k - the imaginary part of the complex refractive index
% epsR - the real part of the complex dielectric function
% epsIm - the imaginary part of the complex dielectric function

function [njunju, RR, n, k, epsR, epsIm] =...
    KKTransform_Publish(njufar, njumid,Rfar, Rmid,...
    lowcutnju, joinnju1, joinnju2, lownjugain, resolution)
% How many pellets? m
[l, m] = size(Rfar);
% Trim the Far IR data at the lower end
i = 1;
while njufar(i) < lowcutnju
    i = i + 1;
end
```

```
njufar = njufar(i:end);
Rfar = Rfar(i:end,:);
% Data treatment: join and interpolate data
[RR, njunju] = treatdata(njufar,njumid,Rfar,Rmid,...
    joinnju1,joinnju2,lownjugain, resolution);
% Initialise vectors for refractive index outputs
n = zeros(size(RR));
k = zeros(size(RR));
% Compute the complex refractive index for each pellet
for j = 1:m
    [n(:,j), k(:,j)] = refrInd(njunju, RR(:,j));
end
% Compute the complex dielectric function
epsR = n.^2-k.^2;
epsIm = 2*n.*k;
% Trim the data at the lower end to match the measured range
njunju = njunju(i:end);
RR = RR(i:end,:);
n = n(i:end,:);
k = k(i:end,:);
epsR = epsR(i:end,:);
epsIm = epsIm(i:end,:);
% Plot the complex refractive index and the complex dielectric function
figure(1);
plot(njunju, n, njunju, k);
xlabel('cm-1');
ylabel('Imaginary (bottom) and Real (top) parts');
title('Complex Refractive Index');
figure(2);
plot(njunju, epsR, njunju,epsIm);
xlabel('cm-1');
ylabel('Imaginary (bottom) and Real (top) parts');
title ('Complex Dielectric Function');
end
```

8.1.2 Function to smoothly join data and interpolate to 0 wavenumber

```
function [RR, njunju] = treatdata(njuF,njuM,rF,rM,joinnju1,joinnju2,G, res)
% How many pellets? m
[l, m] = size(rF);
% set up the wavenumber vector, which will guide the sampling of the
% pchip algorithm sample at twice the experimental sampling rate
njunju = [0.2:res/2:njuM(end)]';
% set up the output reflectance matrix
RR = zeros(length(njunju),m);
% Determine the joint end index
if joinnju2 > njuM(1)
    i = 1;
    while njuM(i) < joinnju2
        i = i + 1;
    end
    rM = rM(i:end,:);
    njuM = njuM(i:end);
end
% Determine the joint start index
if joinnju1 < njuF(l)
```

```
    h = 1;
    while njuF(h)<joinnju1
        h = h+1;
    end
    rF = rF(1:h, :);
    njuF = njuF(1:h);
end
% Treat each pellet's data
for j=1:m
    % Interpolate the data to 0.5 cm-1
    njuExtra = (0.5:0.5:njuF(1)-5)';
    rExtra = ones(length(njuExtra),1)*rF(1,j)*G;
    % Put the extrapolation, FIR and MIR data into a single vector
    y = [rExtra;rF(:,j);rM(:,j)];
    x = [njuExtra; njuF;njuM];
    % Fit a pchip line to the data, sampling at wavenumbers specified by
    % njunju
    RR(:,j) = pchip(x,y,njunju);
end
% Plot the treated spectra
figure(3);
plot(njunju,RR);
xlabel('cm-1');
ylabel('Treated Reflectivity');
end
```

8.1.3 Function to calculate the phase shift

```
function phase = KKphase(nju, R)
% Use the KK-derived relation to calculate the phase shift of the IR signal
g = length(nju);
% Initialise output vector
phase = zeros(length(nju),1);
% Initialise holding vectors
a = zeros(length(nju),1);
b = zeros(length(nju),1);
% What's the wavenumber step?
dnju = nju(3)-nju(2);
% Assume R(infinity) = R(furthest we measured)
Rinf = R(g);
% calculate the first element of the phase shift vector
j = 1;
beta1 = 0;
for k = 2:g
    b(j) = beta1 + (0.5*log(R(k)/Rinf)/(nju(k)^2-nju(j)^2));
    beta1 = b(j);
end
phase(j) = (-2*nju(j)/pi)*b(j)*dnju;
% calculate the last element of the phase shift vector
j = g;
alpha1 = 0;
for k = 1:g-1
    a(j) = alpha1 + (0.5*log(R(k)/Rinf)/(nju(k)^2-nju(j)^2));
    alpha1 = a(j);
end
phase(j) = (-2*nju(j)/pi)*a(j)*dnju;
```

```
% loop the inner elements of the phase shift vector
for j = 2:g-1
    alpha1 = 0;
    beta1 = 0;
    for k = 1:j-1
        a(j) = alpha1 + (0.5*log(R(k)/Rinf)/(nju(k)^2-nju(j)^2));
        alpha1 = a(j);
    end
    for k = j+1:g
        b(j) = beta1 + (0.5*log(R(k)/Rinf)/(nju(k)^2-nju(j)^2));
        beta1 = b(j);
    end
    phase(j) = (-2*nju(j)/pi)*(a(j)+b(j))*dnju;
end
end
```

8.1.4 Function to calculate the complex refractive index

```
function [n, k] = refrInd(nju, R)
n = zeros(length(nju),1);
k = zeros(length(nju),1);

phase = KKphase(nju, R);
for i = 1:length(nju)
    n(i) = (1-R(i))/(1+R(i)-2*(R(i).^0.5).*cos(phase(i)));
    k(i) = (2*(R(i).^0.5).*sin(phase(i)))/(1+R(i)-2*(R(i).^0.5)...
        .*cos(phase(i)));
end
end
```

8.2 Appendix 2: Mathematica code for Schrödinger equation calculations

The code given in this appendix calculates the energies of excited states of a -CH_3 quantum tunnelling rotor based on the single particle model presented in section 3.6.3. The code can be pasted into a new Mathematica notebook, and when evaluated will produce a Matlab file eigenvalues.m containing a matrix of energy values for the first eight excited states of the methyl tunnelling rotor.

```
SetDirectory[NotebookDirectory[]];
B = 1;
ω=1;
V =0;
U[x_]:=V (1-Cos[3 x])/2;
Plot[U[x],{x,0,2π}X]
solutions=NDEigensystem[{-B ψ''[x]+U[x] ψ[x],ψ[0]==ψ[2 π]},ψ,{x,0,2 π},8]
energies = solutions[[1]];
entrans1 = {(energies[[2]] - energies[[1]])*0.655}
entrans2 = {(energies[[4]] - energies[[2]])*0.655}
Vlist = {V*0.655};
eigenvalues = energies;
While[V<50, V = V+0.1; Vlist = Join[Vlist, {V*0.655}];
 solutions=NDEigensystem[{-B ψ''[x]+U[x] ψ[x],ψ[0]==ψ[2 π]},ψ,{x,0,2 π},8];
energies = solutions[[1]];
 transone = (energies[[2]] - energies[[1]])*0.655; transtwo = (energies[[4]] -
energies[[2]])*0.655;
 entrans1 = Join[entrans1, {transone}];entrans2 = Join[entrans2, {transtwo}];
 eigenvalues = Join[eigenvalues, energies];];
entransfer1matrix = {Vlist,entrans1};
entransfer2matrix = {Vlist,entrans2};
eigenvaluesmatrix  = Partition[eigenvalues,8];
ListPlot[entrans1]
ListPlot[entrans2]
Export["entr1.mat", entransfer1matrix]
Export["entr2.mat", entransfer2matrix]
        Export["eigenvalues.mat", eigenvaluesmatrix]
```

8.3 Appendix 3: Matlab code for FTIR data handling and plotting

This appendix gives the code referred to in section 3.6.4. The amount of data collected during the *in situ* acetone dosing experiments was immense: more than 500 individual spectra were collected for some of the analysed dosing runs. Handling this data manually is simply intractable. The below code deals with this problem: it takes a matrix of spectra (`data`), whose first column is the wavenumber vector and all subsequent columns are individual spectra, which are assumed to be collected at regular intervals (`dt`) in the far or mid IR (`region`). What it also facilitates is isolating single doses of acetone by selecting the relevant range of spectra numbers (`runs`) as written down in the logbook during the experiment. Finally, it saves a file with a chosen name (`filename`) to be imported into Origin, which contains data in the relevant wavenumber regions for quickly and easily producing 3D plots, as well as full individual spectra. The code plots all the different bits of data that it exports to Origin, so that one does not need to go through the plotting in Origin to find out that something went wrong with the code.

```
% Fit a smooth surface, plot pieces of it, save a file to Plot in Origin
function [OriginDat] = analyseIRdat(data, dt, region, runs, filename)
% extract the relevant data
nju = data(:, 1);
absorb = data(:,(runs(1)+2):(runs(2)+2));
% construct vectors for fitting
% here I fit along the time dimension, as will you.
[~,ntimepoints] = size(absorb);

time = [0:dt:(dt*(ntimepoints-1))]./60;%this is my construction of the time
vector assuming all the spectra were taken
%at intervals dt seconds, I have ntimepoints number of spectra, and I
%divide by 60 to convert to minutes from seconds.

timeS = [0:20/60:max(time)]; % this is the vector that will sample the time-
resolved data along the time dimension
njuS = [min(nju):0.1:max(nju)]; % this vector samples the individual spectra
along cm-1 to make it evenly spaced.

% Defining regions of interest in the data.
% For example, one of the peaks I was looking at is in Mid IR from 600 to
% 700cm-1, so that's the first one I defined in Mnju.
```

```
% Mnju =
[512,700;700,843;843,1123;1123,1249;1249,1335;1335,1421;1421,1514;1514,1643;1643,
1780];
Mnju = [606,700;720,930;1000,1165;1450, 1800];
% Mnju = [600, 700;700,850;850,920;1050,1165; 1250, 1320;1520, 1680];
% Mnju = [600, 1800];
Fnju = [121,228;228,338;338,480;480,610];
% Fnju = [121, 480; 480, 608];
% Fnju = [125, 223; 234, 330; 340, 480; ];
njuAcM = [500, 564; 1165, 1256; 1320, 1500; 1700, 1800];

% make file names for exporting to Origin depending on what region I'm
considering and which run numbers I'm taking
if region == 'F'
    njulim = Fnju;
    [numnames, ~] = size(njulim);
    for i = 1:numnames
        datnames{i} = strcat('runs',
num2str(runs(1)),'to',num2str(runs(2)),'peaks',num2str(njulim(i,1)),'to',num2str(
njulim(i,2)),'cm1');
    end
    datnames{numnames+1} = 'FullSpectrum';
elseif region == 'M'
    njulim = Mnju;
    [numnames, ~] = size(njulim);
    for i = 1:numnames
        datnames{i} = strcat('runs',
num2str(runs(1)),'to',num2str(runs(2)),'peaks',num2str(njulim(i,1)),'to',num2str(
njulim(i,2)),'cm1');
    end
    datnames{numnames+1} = 'FullSpectrum';
elseif region == 'AM'
    njulim = njuAcM;
    [numnames, ~] = size(njulim);
    for i = 1:numnames
        datnames{i} = strcat('runs',
num2str(runs(1)),'to',num2str(runs(2)),'peaks',num2str(njulim(i,1)),'to',num2str(
njulim(i,2)),'cm1');
    end
    datnames{numnames+1} = 'FullSpectrum';
end
% fitting lines to construct the smooth surface

% first fit individual spectra along cm-1
absorbN = zeros(length(njuS),length(time));
for i = 1:length(time)
    absorbN(:,i) = pchip(nju, absorb(:,i), njuS);
end

% now fit through the individual spectra along the time dimension
absorbS = zeros(length(njuS), length(timeS));
for i = 1:length(njuS)
    absorbS(i,:) = pchip(time, absorbN(i,:), timeS);
end
% absorbS now has your Z data, with each column containing a single
```

```
% spectrum along cm-1 at a particular point in time. Time increases as you
% go through the columns.
% absorbS is a matrix, of course.

% calling a function that does all the plotting
plotSurfCont(njuS, absorbS,timeS,njulim);

% constructing xyz data for Origin plots
[k, ~] = size(njulim);
for q = 1:k
    roinju = njuS>njulim(q,1) & njuS<njulim(q,2);
    % here OriginDat is called a 'structure' read about structures in
    % Matlab - they are very useful ways of collected various data under a
    % single variable name.
    % Also read about matrices and cells.
    OriginDat.(datnames{q}) = [NaN, timeS; njuS(roinju)', absorbS(roinju,:)];
end
OriginDat.(datnames{k+1}) = [njuS', absorbS];
% saving the file, which will be imported into Origin. This has all the
% pieces of the surfaces that I want to plot
save(strcat(filename,'.mat'),'OriginDat');

end

% Plotting all the surfaces I want to see before going to Origin
% it takes these variables:
% nju - wavenumber vector
% spectra - the z data as a matrix as fitted before
% time - the time vector
% limnju - a matrix with pairs of limits between which I want to plot
% limtime - start and end times I want to look at

% The rest you can figure out. Google is your friend.
function [] = plotSurfCont(nju, spectra, time, limnju, limtime)
if nju(1) > nju(end)
    nju = flipud(nju);
    spectra = flipud(spectra);
end
switch nargin
    case 5
        [npeaks, ~] = size(limnju);

        njui = findindex(nju, limnju);
        timei = findindex(time, limtime);

        for q = 1:npeaks
            figure(10+q);

meshc(time(timei(1):timei(2)),nju(njui(q,1):njui(q,2)),spectra(njui(q,1):njui(q,2
),timei(1):timei(2)));
            xlabel('t /min');
            ylabel('Wavenumber /cm-1');
        end
        figure(20); plot(nju,spectra);
    case 4
```

```
        [npeaks, ~] = size(limnju);

        njui = findindex(nju, limnju);

        for q = 1:npeaks
            figure(10+q);
            meshc(time,nju(njui(q,1):njui(q,2)),spectra(njui(q,1):njui(q,2),:));
            xlabel('t /min');
            ylabel('Wavenumber /cm-1');
        end
        figure(20); plot(nju,spectra);

    case 3
        figure(10);
            meshc(time,nju,spectra);
            xlabel('t /min');
            ylabel('Wavenumber /cm-1');
        figure(20); plot(nju,spectra);
end
end
% Bad way of finding indexes
% This function is actually a very clunky way of finding indexes of
% particular values, or a range of values in a vector.
% Use 'find' instead. Google 'find Matlab'
% But since I wrote the analyseIRdat function before I found out how to do
% this, I'm not getting rid of this clunky way. It works for this code, so
% it's fine.
function indexes = findindex(data, values)
[npeaks, ~] = size(values);
i = ones(npeaks, 1);
for q = 1:npeaks
    while data(i(q)) < values(q,1)
        i(q) = i(q)+1;
    end
end
j = ones(npeaks, 1);
for q = 1:npeaks
    while data(j(q)) < values(q,2)
        j(q) = j(q)+1;
    end
end
indexes = [i, j];
end
```

Publications

Titov, K.; Eremin, D. B.; Kashin, A. S.; Boada, R.; Souza, B. E.; Kelley, C. S.; Frogley, M. D.; Cinque, G.; Gianolio, D.; Cibin, G.; Rudić, S.; Ananikov, V. P.; Tan, J. C. OX-1 Metal–Organic Framework Nanosheets as Robust Hosts for Highly Active Catalytic Palladium Species. *ACS Sustainable Chemistry & Engineering* **2019,** *7*, 5875-5885.

Titov, K.; Zeng, Z.; Ryder, M. R.; Chaudhari, A. K.; Civalleri, B.; Kelley, C. S.; Frogley, M. D.; Cinque, G.; Tan, J. C. Probing Dielectric Properties of Metal-Organic Frameworks: MIL-53(Al) as a Model System for Theoretical Predictions and Experimental Measurements via Synchrotron Far- and Mid-Infrared Spectroscopy. *Journal of Physical Chemistry Letters* **2017,** *8*, 5035-5040.

Titov, K.; Tan, J.C. Facile Patterning of Electrospun Polymer Fibers Enabled by Electrostatic Lensing Interactions. *APL Materials* **2016,** *4*. (Not included in this thesis.)

Babal, A.S.; Donà L.; Ryder, M.R.; **Titov, K.**; Chaudhari, A.K.; Zeng, Z.X.; Kelley, C.S.; Frogley, M.D.; Cinque, G.; Civalleri, B.; and Tan, J.C. Impact of pressure and temperature on the broadband dielectric response of the HKUST-1 metal-organic framework. *Journal of Physical Chemistry C* **2019,** Accepted Manuscript.

Souza, B. E.; Rudic, S.; **Titov, K.**; Babal, A. S.; Taylor, J. D.; Tan, J. C. Guest-host interactions of nanoconfined anti-cancer drug in metal-organic framework exposed by terahertz dynamics. *Chemical Communications* **2019,** *55*, 3868-3871.

Ryder, M. R.; Zeng, Z.; **Titov, K.**; Sun, Y.; Mahdi, E. M.; Flyagina, I.; Bennett, T. D.; Civalleri, B.; Kelley, C. S.; Frogley, M. D.; Cinque, G.; Tan, J. C. Dielectric Properties of Zeolitic Imidazolate Frameworks in the Broad-Band Infrared Regime. *Journal of Physical Chemistry Letters* **2018,** *9*, 2678-2684.

Flyagina, I. S.; Mahdi, E. M.; **Titov, K.**; Tan, J. C. Thermo-mechanical properties of mixed-matrix membranes encompassing zeolitic imidazolate framework-90 and polyvinylidine difluoride: ZIF-90/PVDF nanocomposites. *APL Materials* **2017,** *5*.

Manuscripts in preparation

Titov, K.; Ryder M. R.; Zeng Z.; Chaudhari, A.K.; Taylor, J.; Mahdi, E.M.; Mukhopadhyay, S.; Rudic, S.; Fernandez-Alonso, F.; Tan, J. C. Quantum Tunnelling Rotors Sensing Guests in a Metal-Organic Framework.

Titov, K.; Zeng, Z.; Souza, B. E.; Babal, A. S.; Chaudhari, A. K.; Frogley, M. D.; Cinque, G.; Tan, J. C. Acetone Sensing Behaviour of ZnQ@OX-1 via in situ synchrotron transmission FTIR spectroscopy.

References

1. Chaudhari, A. K.; Kim, H. J.; Han, I.; Tan, J. C. Optochemically Responsive 2D Nanosheets of a 3D Metal-Organic Framework Material. *Advanced Materials* **2017,** *29*.

2. Prager, M.; Heidemann, A. Rotational Tunneling and Neutron Spectroscopy: A Compilation. *Chemical Reviews* **1997,** *97*, 2933-2966.

3. Zhou, W.; Wu, H.; Udovic, T. J.; Rush, J. J.; Yildirim, T. Quasi-free methyl rotation in zeolitic imidazolate framework-8. *Journal of Physical Chemistry A* **2008,** *112*, 12602-6.

4. Furukawa, H.; Cordova, K. E.; O'Keeffe, M.; Yaghi, O. M. The chemistry and applications of metal-organic frameworks. *Science* **2013,** *341*, 1230444.

5. Chem CommunSenkovska, I.; Kaskel, S. Ultrahigh porosity in mesoporous MOFs: promises and limitations. *Chemical Communications* **2014,** *50*, 7089-98.

6. Wharmby, M. T.; Henke, S.; Bennett, T. D.; Bajpe, S. R.; Schwedler, I.; Thompson, S. P.; Gozzo, F.; Simoncic, P.; Mellot-Draznieks, C.; Tao, H.; Yue, Y.; Cheetham, A. K. Extreme Flexibility in a Zeolitic Imidazolate Framework: Porous to Dense Phase Transition in Desolvated ZIF-4. *Angewandte Chemie - International Edition* **2015,** *54*, 6447-51.

7. Ferey, G.; Serre, C. Large breathing effects in three-dimensional porous hybrid matter: facts, analyses, rules and consequences. *Chemical Society Reviews* **2009,** *38*, 1380-99.

8. Ryder, M. R.; Civalleri, B.; Bennett, T. D.; Henke, S.; Rudic, S.; Cinque, G.; Fernandez-Alonso, F.; Tan, J. C. Identifying the role of terahertz vibrations in metal-organic frameworks: from gate-opening phenomenon to shear-driven structural destabilization. *Physical Review Letters* **2014,** *113*, 215502.

9. Comotti, A.; Bracco, S.; Sozzani, P. Molecular Rotors Built in Porous Materials. *Accounts of Chemical Research* **2016,** *49*, 1701-10.

10. Ryder, M. R.; Civalleri, B.; Cinque, G.; Tan, J. C. Discovering connections between terahertz vibrations and elasticity underpinning the collective dynamics of the HKUST-1 metal-organic framework. *CrystEngComm* **2016,** *18*, 4303-4312.

11. Horike, S.; Shimomura, S.; Kitagawa, S. Soft porous crystals. *Nature Chemistry* **2009,** *1*, 695-704.

12. Stavila, V.; Talin, A. A.; Allendorf, M. D. MOF-based electronic and opto-electronic devices. *Chemical Society Reviews* **2014,** *43*, 5994-6010.

13. Stassen, I.; Burtch, N.; Talin, A.; Falcaro, P.; Allendorf, M.; Ameloot, R. An updated roadmap for the integration of metal-organic frameworks with electronic devices and chemical sensors. *Chemical Society Reviews* **2017,** *46*, 3185-3241.

14. Loiseau, T.; Serre, C.; Huguenard, C.; Fink, G.; Taulelle, F.; Henry, M.; Bataille, T.; Ferey, G. A rationale for the large breathing of the porous aluminum terephthalate (MIL-53) upon hydration. *Chemistry - A European Journal* **2004,** *10*, 1373-82.

15. Serre, C.; Millange, F.; Thouvenot, C.; Noguès, M.; Marsolier, G.; Louër, D.; Férey, G. Very Large Breathing Effect in the First Nanoporous Chromium(III)-Based Solids: MIL-53 or CrIII(OH)·{O2C−C6H4−CO2}·{HO2C−C6H4−CO2H}x·H2Oy. *Journal of the American Chemical Society* **2002,** *124*, 13519-13526.

16. Ferey, G. Hybrid porous solids: past, present, future. *Chem Soc Rev* **2008,** *37*, 191-214.

17. Kashin, A. S.; Ananikov, V. P. Catalytic C-C and C-heteroatom bond formation reactions: in situ generated or preformed catalysts? Complicated mechanistic picture behind well-known experimental procedures. *Journal of Organic Chemistry* **2013,** *78*, 11117-25.

18. Eremin, D. B.; Ananikov, V. P. Understanding active species in catalytic transformations: From molecular catalysis to nanoparticles, leaching, "Cocktails" of catalysts and dynamic systems. *Coordination Chemistry Reviews* **2017,** *346*, 2-19.

19. Pascanu, V.; Yao, Q.; Bermejo Gomez, A.; Gustafsson, M.; Yun, Y.; Wan, W.; Samain, L.; Zou, X.; Martin-Matute, B. Sustainable catalysis: rational Pd loading on MIL-101Cr-NH2 for more efficient and recyclable Suzuki-Miyaura reactions. *Chemistry* **2013,** *19*, 17483-93.

20. Pascanu, V.; Bermejo Gómez, A.; Ayats, C.; Platero-Prats, A. E.; Carson, F.; Su, J.; Yao, Q.; Pericàs, M. A.; Zou, X.; Martín-Matute, B. n. Double-supported silica-metal–organic framework palladium nanocatalyst for the aerobic oxidation of alcohols under batch and continuous flow regimes. *ACS Catalysis* **2014,** *5*, 472-479.

21. Carson, F.; Pascanu, V.; Bermejo Gomez, A.; Zhang, Y.; Platero-Prats, A. E.; Zou, X.; Martin-Matute, B. Influence of the Base on Pd@MIL-101-NH2 (Cr) as Catalyst for the Suzuki-Miyaura Cross-Coupling Reaction. *Chemistry* **2015,** *21*, 10896-902.

22. Pascanu, V.; Hansen, P. R.; Bermejo Gomez, A.; Ayats, C.; Platero-Prats, A. E.; Johansson, M. J.; Pericas, M. A.; Martin-Matute, B. Highly functionalized biaryls via Suzuki-Miyaura cross-coupling catalyzed by Pd@MOF under batch and continuous flow regimes. *ChemSusChem* **2015,** *8*, 123-30.

23. Yuan, N.; Pascanu, V.; Huang, Z.; Valiente, A.; Heidenreich, N.; Leubner, S.; Inge, A. K.; Gaar, J.; Stock, N.; Persson, I.; Martin-Matute, B.; Zou, X. Probing the Evolution of Palladium Species in Pd@MOF Catalysts during the Heck Coupling Reaction: An Operando X-ray Absorption Spectroscopy Study. *Journal of the American Chemical Society* **2018,** *140*, 8206-8217.

24. Rydosz, A. Sensors for Enhanced Detection of Acetone as a Potential Tool for Noninvasive Diabetes Monitoring. *Sensors* **2018,** *18*.

25. Moggach, S. A.; Bennett, T. D.; Cheetham, A. K. The effect of pressure on ZIF-8: increasing pore size with pressure and the formation of a high-pressure phase at 1.47 GPa. *Angewandte Chemie - International Edition* **2009,** *48*, 7087-9.

26. Fairen-Jimenez, D.; Moggach, S. A.; Wharmby, M. T.; Wright, P. A.; Parsons, S.; Duren, T. Opening the gate: framework flexibility in ZIF-8 explored by experiments and simulations. *Journal of the American Chemical Society* **2011,** *133*, 8900-2.

27. Ania, C. O.; Garcia-Perez, E.; Haro, M.; Gutierrez-Sevillano, J. J.; Valdes-Solis, T.; Parra, J. B.; Calero, S. Understanding Gas-Induced Structural Deformation of ZIF-8. *Journal of Physycal Chemistry Letters* **2012,** *3*, 1159-64.

28. Fairen-Jimenez, D.; Galvelis, R.; Torrisi, A.; Gellan, A. D.; Wharmby, M. T.; Wright, P. A.; Mellot-Draznieks, C.; Duren, T. Flexibility and swing effect on the adsorption of energy-related gases on ZIF-8: combined experimental and simulation study. *Dalton Transactions* **2012,** *41*, 10752-62.

29. Russell, B.; Villaroel, J.; Sapag, K.; Migone, A. D. O2 Adsorption on ZIF-8: Temperature Dependence of the Gate-Opening Transition. *The Journal of Physical Chemistry C* **2014,** *118*, 28603-28608.

30. Tanaka, H.; Ohsaki, S.; Hiraide, S.; Yamamoto, D.; Watanabe, S.; Miyahara, M. T. Adsorption-Induced Structural Transition of ZIF-8: A Combined Experimental and Simulation Study. *Journal of Physical Chemistry C* **2014,** *118*, 8445-8454.

31. Kolokolov, D. I.; Stepanov, A. G.; Jobic, H. Mobility of the 2-Methylimidazolate Linkers in ZIF-8 Probed by 2H NMR: Saloon Doors for the Guests. *The Journal of Physical Chemistry C* **2015,** *119*, 27512-27520.

32. Tan, N. Y.; Ruggiero, M. T.; Orellana-Tavra, C.; Tian, T.; Bond, A. D.; Korter, T. M.; Fairen-Jimenez, D.; Zeitler, J. A. Investigation of the terahertz vibrational modes of ZIF-8 and ZIF-90 with terahertz time-domain spectroscopy. *Chemical Communications* **2015,** *51*, 16037-40.

33. Casco, M. E.; Cheng, Y. Q.; Daemen, L. L.; Fairen-Jimenez, D.; Ramos-Fernandez, E. V.; Ramirez-Cuesta, A. J.; Silvestre-Albero, J. Gate-opening effect in ZIF-8: the first experimental proof using inelastic neutron scattering. *Chemical Communications* **2016,** *52*, 3639-42.

34. Tian, T.; Wharmby, M. T.; Parra, J. B.; Ania, C. O.; Fairen-Jimenez, D. Role of crystal size on swing-effect and adsorption induced structure transition of ZIF-8. *Dalton Transactions* **2016,** *45*, 6893-900.

35. Coudert, F. X. Molecular Mechanism of Swing Effect in Zeolitic Imidazolate Framework ZIF-8: Continuous Deformation upon Adsorption. *ChemPhysChem* **2017,** *18*, 2732-2738.

36. Knebel, A.; Geppert, B.; Volgmann, K.; Kolokolov, D. I.; Stepanov, A. G.; Twiefel, J.; Heitjans, P.; Volkmer, D.; Caro, J. Defibrillation of soft porous metal-organic frameworks with electric fields. *Science* **2017,** *358*, 347-351.

37. Tanno, T.; Watanabe, Y.; Umeno, K.; Matsuoka, A.; Matsumura, H.; Odaka, M.; Ogawa, N. In Situ Observation of Gas Adsorption onto ZIF-8 Using Terahertz Waves. *Journal of Physical Chemistry C* **2017,** *121*, 17921-17924.

38. Chaplais, G.; Fraux, G.; Paillaud, J. L.; Marichal, C.; Nouali, H.; Fuchs, A. H.; Coudert, F. X.; Patarin, J. Impacts of the Imidazolate Linker Substitution (CH3, CI, or Br) on the Structural and Adsorptive Properties of ZIF-8. *Journal of Physical Chemistry C* **2018,** *122*, 26945-26955.

39. Formalik, F.; Fischer, M.; Rogacka, J.; Firlej, L.; Kuchta, B. Effect of low frequency phonons on structural properties of ZIFs with SOD topology. *Microporous and Mesoporous Materials* **2018**.

40. Hobday, C. L.; Bennett, T. D.; Fairen-Jimenez, D.; Graham, A. J.; Morrison, C. A.; Allan, D. R.; Duren, T.; Moggach, S. A. Tuning the Swing Effect by Chemical Functionalization of Zeolitic Imidazolate Frameworks. *Journal of the American Chemical Society* **2018,** *140*, 382-387.

41. Hobday, C. L.; Woodall, C. H.; Lennox, M. J.; Frost, M.; Kamenev, K.; Duren, T.; Morrison, C. A.; Moggach, S. A. Understanding the adsorption process in ZIF-8 using high pressure crystallography and computational modelling. *Nature Communications* **2018,** *9*, 1429.

42. Gonzalez-Nelson, A.; Coudert, F. X.; van der Veen, M. A. Rotational Dynamics of Linkers in Metal(-)Organic Frameworks. *Nanomaterials (Basel)* **2019,** *9*.

43. Usman, M.; Mendiratta, S.; Lu, K. L. Metal-Organic Frameworks: New Interlayer Dielectric Materials. *ChemElectroChem* **2015,** *2*, 786-788.

44. Lew, C. M.; Cai, R.; Yan, Y. Zeolite thin films: from computer chips to space stations. *Accounts of Chemical Research* **2010,** *43*, 210-9.

45. ITRS Roadmap (www.itrs2.net).

46. Fox, M. *Optical Properties of Solids*. Oxford University Press Oxford; 2010.

47. Anderson, J. C. *Dielectrics*. Chapman and Hall Ltd.: London; 1964.

48. Chung, D. L. *Functional Materials: Electrical, Dielectric, Electromagnetic, Optical and Magnetic Applications* World Scientific Publishing Co Pte Ltd: Singapore; 2010.

49. Zagorodniy, K.; Seifert, G.; Hermann, H. Metal-organic frameworks as promising candidates for future ultralow-k dielectrics. *Applied Physics Letters* **2010,** *97*, 251905.

50. Eslava, S.; Zhang, L. P.; Esconjauregui, S.; Yang, J. W.; Vanstreels, K.; Baklanov, M. R.; Saiz, E. Metal-Organic Framework ZIF-8 Films As Low-kappa Dielectrics in Microelectronics. *Chemistry of Materials* **2013,** *25*, 27-33.

51. Usman, M.; Lee, C. H.; Hung, D. S.; Lee, S. F.; Wang, C. C.; Luo, T. T.; Zhao, L.; Wueg, M. K.; Lu, K. L. Intrinsic low dielectric behaviour of a highly thermally stable Sr-based metal-organic framework for interlayer dielectric materials. *Journal of Materials Chemistry C* **2014,** *2*, 3762-3768.

52. Redel, E.; Wang, Z. B.; Walheim, S.; Liu, J. X.; Gliemann, H.; Woll, C. On the dielectric and optical properties of surface-anchored metal-organic frameworks: A study on epitaxially grown thin films. *Applied Physics Letters* **2013,** *103*, 091903.

53. Warmbier, R.; Quandt, A.; Seifert, G. Dielectric Properties of Selected Metal-Organic Frameworks. *Journal of Physical Chemistry C* **2014,** *118*, 11799-11805.

54. Kuc, A.; Enyashin, A.; Seifert, G. Metal-organic frameworks: structural, energetic, electronic, and mechanical properties. *Journal of Physical Chemistry B* **2007,** *111*, 8179-86.

55. Warmbier, R.; Quandt, A.; Seifert, G. Dielectric Properties of Selected Metal–Organic Frameworks. *The Journal of Physical Chemistry C* **2014,** *118*, 11799-11805.

56. Eslava, S.; Zhang, L.; Esconjauregui, S.; Yang, J.; Vanstreels, K.; Baklanov, M. R.; Saiz, E. Metal-Organic Framework ZIF-8 Films As Low-κ Dielectrics in Microelectronics. *Chemistry of Materials* **2012,** *25*, 27-33.

57. Wang, M.; Zhang, X.; Chen, Y.; Li, D. How Guest Molecules Stabilize the Narrow Pore Phase of Soft Porous Crystals: Structural and Mechanical Properties of MIL-53(Al)⊃H2O. *The Journal of Physical Chemistry C* **2016,** *120*, 5059-5066.

58. Yot, P. G.; Vanduyfhuys, L.; Alvarez, E.; Rodriguez, J.; Itie, J. P.; Fabry, P.; Guillou, N.; Devic, T.; Beurroies, I.; Llewellyn, P. L.; Van Speybroeck, V.; Serre, C.; Maurin, G. Mechanical energy storage performance of an aluminum fumarate metal-organic framework. *Chemical Science* **2016,** *7*, 446-450.

59. Beurroies, I.; Boulhout, M.; Llewellyn, P. L.; Kuchta, B.; Ferey, G.; Serre, C.; Denoyel, R. Using Pressure to Provoke the Structural Transition of Metal-Organic Frameworks. *Angewandte Chemie - International Edition* **2010,** *49*, 7526-7529.

60. Yot, P. G.; Yang, K.; Guillerm, V.; Ragon, F.; Dmitriev, V.; Parisiades, P.; Elkaim, E.; Devic, T.; Horcajada, P.; Serre, C.; Stock, N.; Mowat, J. P. S.; Wright, P. A.; Ferey, G.; Maurin, G. Impact of the Metal Centre and Functionalization on the Mechanical Behaviour of MIL-53 Metal-Organic Frameworks. *European Journal of Inorganic Chemistry* **2016,** *2016*, 4424-4429.

61. Yaghi, O. M.; O'Keeffe, M.; Ockwig, N. W.; Chae, H. K.; Eddaoudi, M.; Kim, J. Reticular synthesis and the design of new materials. *Nature* **2003,** *423*, 705-14.

62. Balanta, A.; Godard, C.; Claver, C. Pd nanoparticles for C-C coupling reactions. *Chemical Society Reviews* **2011,** *40*, 4973-85.

63. Trzeciak, A. M. *Pd Nanoparticles for Coupling Reactions and Domino/Tandem Reactions*. Wiley-VCH: Weinheim, Germany: 2016.

64. Bugaev, A. L.; Guda, A. A.; Lazzarini, A.; Lomachenko, K. A.; Groppo, E.; Pellegrini, R.; Piovano, A.; Emerich, H.; Soldatov, A. V.; Bugaev, L. A.; Dmitriev, V. P.; van Bokhoven, J. A.; Lamberti, C. In situ formation of hydrides and carbides in palladium catalyst: When XANES is better than EXAFS and XRD. *Catalysis Today* **2017,** *283*, 119-126.

65. Bugaev, A. L.; Usoltsev, O. A.; Lazzarini, A.; Lomachenko, K. A.; Guda, A. A.; Pellegrini, R.; Carosso, M.; Vitillo, J. G.; Groppo, E.; van Bokhoven, J. A.; Soldatov, A. V.; Lamberti, C. Time-resolved operando studies of carbon supported Pd nanoparticles under hydrogenation reactions by X-ray diffraction and absorption. *Faraday Discussions* **2018,** *208*, 187-205.

66. Carosso, M.; Lazzarini, A.; Piovano, A.; Pellegrini, R.; Morandi, S.; Manzoli, M.; Vitillo, J. G.; Ruiz, M. J.; Lamberti, C.; Groppo, E. Looking for the active hydrogen species in a 5 wt% Pt/C catalyst: a challenge for inelastic neutron scattering. *Faraday Discussions* **2018,** *208*, 227-242.

67. Frenkel, A. I.; Yevick, A.; Cooper, C.; Vasic, R. Modeling the structure and composition of nanoparticles by extended X-ray absorption fine-structure spectroscopy. *Annual Review of Analytical Chemistry* **2011,** *4*, 23-39.

68. Lopes, C. W.; Cerrillo, J. L.; Palomares, A. E.; Rey, F.; Agostini, G. An in situ XAS study of the activation of precursor-dependent Pd nanoparticles. *Physical Chemistry Chemical Physics* **2018,** *20*, 12700-12709.

69. Ananikov, V. P.; Beletskaya, I. P. Toward the Ideal Catalyst: From Atomic Centers to a "Cocktail" of Catalysts. *Organometallics* **2012,** *31*, 1595-1604.

70. Fairlamb, I. J. S.; Lee, A. F. Fundamental Pd-0/Pd-II Redox Steps in Cross-coupling Reactions: Homogeneous, Hybrid Homogeneous-Heterogeneous to Heterogeneous Mechanistic Pathways for C-C Couplings. In *C-H and C-X Bond Functionalization: Transition Metal Mediation*, 2013; pp 72-107.

71. Trzeciak, A. M.; Ziółkowski, J. J. Monomolecular, nanosized and heterogenized palladium catalysts for the Heck reaction. *Coordination Chemistry Reviews* **2007,** *251*, 1281-1293.

72. Ranocchiari, M.; van Bokhoven, J. A. Catalysis by metal-organic frameworks: fundamentals and opportunities. *Physysical Chemistry Chemical Physics* **2011,** *13*, 6388-96.

73. Hendon, C. H.; Rieth, A. J.; Korzynski, M. D.; Dinca, M. Grand Challenges and Future Opportunities for Metal-Organic Frameworks. *ACS Central Science* **2017,** *3*, 554-563.

74. Yakukhnov, S. A.; Pentsak, E. O.; Galkin, K. I.; Mironenko, R. M.; Drozdov, V. A.; Likholobov, V. A.; Ananikov, V. P. Rapid “Mix-and-Stir” Preparation of Well-Defined Palladium on Carbon Catalysts for Efficient Practical Use. *ChemCatChem* **2018,** *10*, 1869-1873.

75. Hermes, S.; Schroter, M. K.; Schmid, R.; Khodeir, L.; Muhler, M.; Tissler, A.; Fischer, R. W.; Fischer, R. A. Metal@MOF: loading of highly porous coordination polymers host lattices by metal organic chemical vapor deposition. *Angewandte Chemie - International Edition* **2005,** *44*, 6237-41.

76. Li, H.; Eddaoudi, M.; O'Keeffe, M.; Yaghi, O. M. Design and synthesis of an exceptionally stable and highly porous metal-organic framework. *Nature* **1999,** *402*, 276-279.

77. Kobayashi, H.; Mitsuka, Y.; Kitagawa, H. Metal Nanoparticles Covered with a Metal-Organic Framework: From One-Pot Synthetic Methods to Synergistic Energy Storage and Conversion Functions. *Inorganic Chemistry* **2016,** *55*, 7301-10.

78. Li, B.; Ma, J. G.; Cheng, P. Integration of Metal Nanoparticles into Metal-Organic Frameworks for Composite Catalysts: Design and Synthetic Strategy. *Small* **2019**, e1804849.

79. Malouche, A.; Zlotea, C.; Szilagyi, P. A. Interactions of Hydrogen with Pd@MOF Composites. *ChemPhysChem* **2019,** *20*, 1282-1295.

80. Wang, N.; Sun, Q.; Yu, J. Ultrasmall Metal Nanoparticles Confined within Crystalline Nanoporous Materials: A Fascinating Class of Nanocatalysts. *Advanced Materials* **2019,** *31*, e1803966.

81. Yang, Q.; Xu, Q.; Jiang, H. L. Metal-organic frameworks meet metal nanoparticles: synergistic effect for enhanced catalysis. *Chemical Society Reviews* **2017,** *46*, 4774-4808.

82. Dong, W.; Zhang, L.; Wang, C.; Feng, C.; Shang, N.; Gao, S.; Wang, C. Palladium nanoparticles embedded in metal–organic framework derived porous carbon: synthesis and application for efficient Suzuki–Miyaura coupling reactions. *RSC Advances* **2016,** *6*, 37118-37123.

83. Huang, Y. B.; Gao, S. Y.; Liu, T. F.; Lu, J.; Lin, X.; Li, H. F.; Cao, R. Palladium Nanoparticles Supported on Mixed-Linker Metal-Organic Frameworks as Highly Active Catalysts for Heck Reactions. *ChemPlusChem* **2012,** *77*, 106-112.

84. Yuan, B.; Pan, Y.; Li, Y.; Yin, B.; Jiang, H. A highly active heterogeneous palladium catalyst for the Suzuki-Miyaura and Ullmann coupling reactions of aryl chlorides in aqueous media. *Angewandte Chemie - International Edition* **2010,** *49*, 4054-8.

85. Huang, Y.; Lin, Z.; Cao, R. Palladium nanoparticles encapsulated in a metal-organic framework as efficient heterogeneous catalysts for direct C2 arylation of indoles. *Chemistry* **2011,** *17*, 12706-12.

86. Hwang, Y. K.; Hong, D. Y.; Chang, J. S.; Jhung, S. H.; Seo, Y. K.; Kim, J.; Vimont, A.; Daturi, M.; Serre, C.; Ferey, G. Amine grafting on coordinatively unsaturated metal centers of MOFs: consequences for catalysis and metal encapsulation. *Angewandte Chemie - International Edition* **2008,** *47*, 4144-8.

87. Bugaev, A. L.; Guda, A. A.; Lomachenko, K. A.; Kamyshova, E. G.; Soldatov, M. A.; Kaur, G.; Oien-Odegaard, S.; Braglia, L.; Lazzarini, A.; Manzoli, M.; Bordiga, S.; Olsbye, U.; Lillerud, K. P.; Soldatov, A. V.; Lamberti, C. Operando study of palladium nanoparticles inside UiO-67 MOF for catalytic hydrogenation of hydrocarbons. *Faraday Discussions* **2018,** *208*, 287-306.

88. Dong, W.; Feng, C.; Zhang, L.; Shang, N.; Gao, S.; Wang, C.; Wang, Z. Pd@UiO-66: An Efficient Catalyst for Suzuki–Miyaura Coupling Reaction at Mild Condition. *Catalysis Letters* **2015,** *146*, 117-125.

89. Kardanpour, R.; Tangestaninejad, S.; Mirkhani, V.; Moghadam, M.; Mohammadpoor-Baltork, I.; Khosropour, A. R.; Zadehahmadi, F. Highly dispersed palladium nanoparticles supported on amino functionalized metal-organic frameworks as an efficient and reusable catalyst for Suzuki cross-coupling reaction. *Journal of Organometallic Chemistry* **2014,** *761*, 127-133.

90. Zhang, L.; Su, Z.; Jiang, F.; Zhou, Y.; Xu, W.; Hong, M. Catalytic palladium nanoparticles supported on nanoscale MOFs: a highly active catalyst for Suzuki–Miyaura cross-coupling reaction. *Tetrahedron* **2013,** *69*, 9237-9244.

91. Tahmasebi, S.; Mokhtari, J.; Naimi-Jamal, M. R.; Khosravi, A.; Panahi, L. One-step synthesis of Pd-NPs@Cu 2 (BDC) 2 DABCO as efficient heterogeneous catalyst for the Suzuki–Miyaura cross-coupling reaction. *Journal of Organometallic Chemistry* **2017,** *853*, 35-41.

92. Puthiaraj, P.; Ahn, W.-S. Highly active palladium nanoparticles immobilized on NH2-MIL-125 as efficient and recyclable catalysts for Suzuki–Miyaura cross coupling reaction. *Catalysis Communications* **2015,** *65*, 91-95.

93. Burrows, A. D.; Cassar, K.; Friend, R. M. W.; Mahon, M. F.; Rigby, S. P.; Warren, J. E. Solvent hydrolysis and templating effects in the synthesis of metal–organic frameworks. *CrystEngComm* **2005,** *7*.

94. Biemmi, E.; Bein, T.; Stock, N. Synthesis and characterization of a new metal organic framework structure with a 2D porous system: (H2NEt2)2[Zn3(BDC)4]·3DEF. *Solid State Sciences* **2006,** *8*, 363-370.

95. Cui, X. J.; Li, W.; Ryabchuk, P.; Junge, K.; Beller, M. Bridging homogeneous and heterogeneous catalysis by heterogeneous single-metal-site catalysts. *Nature Catalysis* **2018,** *1*, 385-397.

96. Fortea-Perez, F. R.; Mon, M.; Ferrando-Soria, J.; Boronat, M.; Leyva-Perez, A.; Corma, A.; Herrera, J. M.; Osadchii, D.; Gascon, J.; Armentano, D.; Pardo, E. The MOF-driven synthesis of supported palladium clusters with catalytic activity for carbene-mediated chemistry. *Nature Materials* **2017,** *16*, 760-766.

97. Kao, K. W.; Hsu, M. C.; Chang, Y. H.; Gwo, S.; Yeh, J. A. A sub-ppm acetone gas sensor for diabetes detection using 10 nm thick ultrathin InN FETs. *Sensors* **2012,** *12*, 7157-68.

98. Hu, Z.; Deibert, B. J.; Li, J. Luminescent metal-organic frameworks for chemical sensing and explosive detection. *Chemical Society Reviews* **2014,** *43*, 5815-40.

99. Kreno, L. E.; Leong, K.; Farha, O. K.; Allendorf, M.; Van Duyne, R. P.; Hupp, J. T. Metal-organic framework materials as chemical sensors. *Chemical Reviews* **2012,** *112*, 1105-25.

100. Eckert, J. Theoretical Introduction to Neutron-Scattering Spectroscopy. *Spectrochimica Acta Part A: Molecular and Biomolecular Spectroscopy* **1992,** *48*, 271-283.

101. Walton, K. S.; Snurr, R. Q. Applicability of the BET method for determining surface areas of microporous metal-organic frameworks. *Journal of the American Chemical Society* **2007,** *129*, 8552-6.

102. Howarth, A. J.; Peters, A. W.; Vermeulen, N. A.; Wang, T. C.; Hupp, J. T.; Farha, O. K. Best Practices for the Synthesis, Activation, and Characterization of Metal–Organic Frameworks. *Chemistry of Materials* **2016,** *29*, 26-39.

103. Pike_Technologies. *Installation and User Guide - VeeMAX II variable angle specular reflectance accessory*. PIKE Technologies, Inc.: 2012.

104. Parker, S. F.; Fernandez-Alonso, F.; Ramirez-Cuesta, A. J.; Tomkinson, J.; Rudic, S.; Pinna, R. S.; Gorini, G.; Castanon, J. F. Recent and future developments on TOSCA at ISIS. *Dynamics of Molecules and Materials-II* **2014,** *554*.

105. Colognesi, D.; Celli, M.; Cilloco, F.; Newport, R. J.; Parker, S. F.; Rossi-Albertini, V.; Sacchetti, F.; Tomkinson, J.; Zoppi, M. TOSCA neutron spectrometer: The final configuration. *Applied Physics A - Materials Science & Processing* **2002,** *74*, S64-S66.

106. Arnold, O.; Bilheux, J. C.; Borreguero, J. M.; Buts, A.; Campbell, S. I.; Chapon, L.; Doucet, M.; Draper, N.; Ferraz Leal, R.; Gigg, M. A.; Lynch, V. E.; Markvardsen, A.; Mikkelson, D. J.; Mikkelson, R. L.; Miller, R.; Palmen, K.; Parker, P.; Passos, G.; Perring, T. G.; Peterson, P. F.; Ren, S.; Reuter, M. A.; Savici, A. T.; Taylor, J. W.; Taylor, R. J.; Tolchenov, R.; Zhou, W.; Zikovsky, J. Mantid—Data analysis and visualization package for neutron scattering and μ SR experiments. *Nuclear Instruments and Methods in Physics Research Section A: Accelerators, Spectrometers, Detectors and Associated Equipment* **2014,** *764*, 156-166.

107. Pinna, R. S.; Rudic, S.; Parker, S. F.; Armstrong, J.; Zanetti, M.; Skoro, G.; Waller, S. P.; Zacek, D.; Smith, C. A.; Capstick, M. J.; McPhail, D. J.; Pooley, D. E.; Howells, G. D.; Gorini, G.; Fernandez-Alonso, F. The neutron guide upgrade of the TOSCA spectrometer. *Nuclear Instruments & Methods in Physics Research Section a-Accelerators Spectrometers Detectors and Associated Equipment* **2018,** *896*, 68-74.

108. Frick, B.; Demmel, F.; McPhail, D.; Crawford, J.; Maxwell, D.; Pokhilchuk, K.; Garcia-Sakai, V.; Mukhopadyay, S.; Telling, M. T. F.; Bermejo, F. J.; Skipper, N. T.; Fernandez-Alonso, F.; Koza, M. M.; Boehm, M.; Mutka, H. Opening the terahertz window on the OSIRIS spectrometer. *EPJ Web of Conferences* **2015,** *83*.

109. Calvin, S. *XAFS for Everyone*. CRC press: 2013.

110. Ravel, B.; Newville, M. ATHENA, ARTEMIS, HEPHAESTUS: data analysis for X-ray absorption spectroscopy using IFEFFIT. *Journal of Synchrotron Radiation* **2005,** *12*, 537-41.

111. Dent, A.; Cibin, G.; Ramos, S.; Smith, A.; Scott, S.; Varandas, L.; Pearson, M.; Krumpa, N.; Jones, C.; Robbins, P. In *B18: A core XAS spectroscopy beamline for Diamond*, Journal of Physics: Conference Series, IOP Publishing: 2009; p 012039.

112. Chalmers, J. M.; Griffiths, P. R. *Handbook of Vibrational Spectroscopy*. Wiley: 2002.

113. Lucarini, V.; Saarinen, J. J.; Peiponen, K. E.; Vartiainen, E. M. *Kramers-Kronig Relations in Optical Materials Research*. Springer: 2005.

114. Dovesi, R.; Orlando, R.; Erba, A.; Zicovich-Wilson, C. M.; Civalleri, B.; Casassa, S.; Maschio, L.; Ferrabone, M.; De La Pierre, M.; D'Arco, P.; Noël, Y.; Causà, M.; Rérat, M.; Kirtman, B. CRYSTAL14: A program for theab initioinvestigation of crystalline solids. *International Journal of Quantum Chemistry* **2014,** *114*, 1287-1317.

115. Grimme, S.; Antony, J.; Ehrlich, S.; Krieg, H. A consistent and accurate ab initio parametrization of density functional dispersion correction (DFT-D) for the 94 elements H-Pu. *Journal of Chemical Physics* **2010,** *132*, 154104.

116. Schafer, A.; Huber, C.; Ahlrichs, R. Fully Optimized Contracted Gaussian-Basis Sets of Triple Zeta Valence Quality for Atoms Li to Kr. *Journal of Chemical Physics* **1994,** *100*, 5829-5835.

117. Walker, A. M.; Civalleri, B.; Slater, B.; Mellot-Draznieks, C.; Cora, F.; Zicovich-Wilson, C. M.; Roman-Perez, G.; Soler, J. M.; Gale, J. D. Flexibility in a metal-organic framework material controlled by weak dispersion forces: the bistability of MIL-53(Al). *Angewandte Chemie - International Edition* **2010,** *49*, 7501-3.

118. De La Pierre, M.; Carteret, C.; Orlando, R.; Dovesi, R. Use of ab initio methods for the interpretation of the experimental IR reflectance spectra of crystalline compounds. *Journal of Computational Chemistry* **2013,** *34*, 1476-85.

119. Piecewise Cubic Hermite Interpolating Polynomial (PCHIP). https://uk.mathworks.com/help/matlab/ref/pchip.html#bvjbz1m-2 (accessed 5 June 2019).

120. Bennett, T. D.; Cheetham, A. K. Amorphous metal-organic frameworks. *Accounts of Chemical Research* **2014,** *47*, 1555-62.

121. Bennett, T. D.; Goodwin, A. L.; Dove, M. T.; Keen, D. A.; Tucker, M. G.; Barney, E. R.; Soper, A. K.; Bithell, E. G.; Tan, J. C.; Cheetham, A. K. Structure and properties of an amorphous metal-organic framework. *Physical Review Letters* **2010,** *104*, 115503.

122. Chapman, K. W.; Halder, G. J.; Chupas, P. J. Pressure-induced amorphization and porosity modification in a metal-organic framework. *Journal of the American Chemical Society* **2009,** *131*, 17546-7.

123. Mounfield, W. P., 3rd; Walton, K. S. Effect of synthesis solvent on the breathing behavior of MIL-53(Al). *Journal of Colloid and Interface Science* **2015,** *447*, 33-9.

124. Civalleri, B.; Napoli, F.; Noel, Y.; Roetti, C.; Dovesi, R. Ab-initio prediction of materials properties with CRYSTAL: MOF-5 as a case study. *CrystEngComm* **2006,** *8*, 364-371.

125. Zhao, F.; Bhanage, B. M.; Shirai, M.; Arai, M. Heck Reactions of Iodobenzene and Methyl Acrylate with Conventional Supported Palladium Catalysts in the Presence of Organic and/or Inorganic Bases without Ligands. *Chemistry - A European Journal* **2000,** *6*, 843-848.

126. Borja, G.; Monge-Marcet, A.; Pleixats, R.; Parella, T.; Cattoen, X.; Man, M. W. C. Recyclable Hybrid Silica-Based Catalysts Derived from Pd-NHC Complexes for Suzuki, Heck and Sonogashira Reactions. *European Journal of Organic Chemistry* **2012**, 3625-3635.

127. Genelot, M.; Dufaud, V.; Djakovitch, L. Carbonylative Sonogashira Coupling in the Synthesis of Ynones: A Study of "Boomerang" Phenomena. *Advanced Synthesis & Catalysis* **2013,** *355*, 2604-2616.

128. Gruttadauria, M.; Giacalone, F.; Noto, R. "Release and catch" catalytic systems. *Green Chemistry* **2013,** *15*, 2608-2618.

129. Giacalone, F.; Campisciano, V.; Calabrese, C.; La Parola, V.; Syrgiannis, Z.; Prato, M.; Gruttadauria, M. Single-Walled Carbon Nanotube-Polyamidoamine Dendrimer Hybrids for Heterogeneous Catalysis. *ACS Nano* **2016,** *10*, 4627-36.

130. Pentsak, E. O.; Kashin, A. S.; Polynski, M. V.; Kvashnina, K. O.; Glatzel, P.; Ananikov, V. P. Spatial imaging of carbon reactivity centers in Pd/C catalytic systems. *Chemical Science* **2015,** *6*, 3302-3313.

131. Li, Q.; Zaczek, A. J.; Korter, T. M.; Zeitler, J. A.; Ruggiero, M. T. Methyl-rotation dynamics in metal-organic frameworks probed with terahertz spectroscopy. *Chemical Communications* **2018,** *54*, 5776-5779.

132. Mehio, N.; Dai, S.; Jiang, D. E. Quantum mechanical basis for kinetic diameters of small gaseous molecules. *Journal of Physical Chemistry A* **2014,** *118*, 1150-4.